HELLENIC REPUBLIC
UNIVERSITY OF IOANNINA
SCHOOL OF ENGINEERING
DEPARTMENT OF MATERIALS SCIENCE AND ENGINEERING

"CHARACTERIZATION, CUTTING MECHANISMS AND MACHINABILITY OF LEAD-FREE BRASSES”

ANAGNOSTIS I. TOULFATZIS

DOCTORAL THESIS
IOANNINA
2019

ΕΛΛΗΝΙΚΗ ΔΗΜΟΚΡΑΤΙΑ
ΠΑΝΕΠΙΣΤΗΜΙΟ ΙΩΑΝΝΙΝΩΝ
ΠΟΛΥΤΕΧΝΙΚΗ ΣΧΟΛΗ
ΤΜΗΜΑ ΜΗΧΑΝΙΚΩΝ ΕΠΙΣΤΗΜΗΣ ΥΛΙΚΩΝ

«ΧΑΡΑΚΤΗΡΙΣΜΟΣ, ΜΗΧΑΝΙΣΜΟΙ ΚΟΠΗΣ ΚΑΙ ΚΑΤΕΡΓΑΣΙΜΟΤΗΤΑ ΜΗ ΜΟΛΥΒΔΟΥΧΩΝ ΟΡΕΙΧΑΛΚΩΝ»

ΑΝΑΓΝΩΣΤΗΣ Ι. ΤΟΥΛΦΑΤΖΗΣ

ΔΙΔΑΚΤΟΡΙΚΗ ΔΙΑΤΡΙΒΗ
ΙΩΑΝΝΙΝΑ
2019

Date of application Mr. Anagnostis Toulfatzis: 20/04/2012

Date of appointing Three Membered Advisory Committee: 26/04/2012 & 06/02/2013

Three Membered Advisory Committee:

Supervisor
Alkiviadis Paipetis: Professor of Department of Materials Science & Engineering, School of Engineering of the University of Ioannina.

Members
Nektaria-Marianthi Barkoula: Associate Professor of Department of Materials Science & Engineering, School of Engineering of the University of Ioannina.
Constantine David: Professor of Mechanical Engineering Department in Technological Education Institute of Central Macedonia.

Date of thesis definition: 26/04/2012

"Characterization, cutting processes and machinability of lead-free brasses”

SEVEN MEMBERED COMMITTEE ASSIGNATION: 23/01/2019

Alkiviadis Paipetis	Professor of Department of Materials Science & Engineering, School of Engineering of the University of Ioannina.
Nektaria-Marianthi Barkoula	Associate Professor of Department of Materials Science & Engineering, School of Engineering of the University of Ioannina.
Constantine David	Professor of Department of Mechanical Engineering, Faculty of Applied Technology, Technological Education Institute of Central Macedonia.
Dimitrios Manolakos	Professor of School of Mechanical Engineering in National Technical University of Athens.
Angeliki Lekatou	Professor of Department of Materials Science & Engineering School of Engineering of the University of Ioannina.
Pandora Psyllaki	Associate Professor of Department of Mechanical Engineering, School of Engineering of the University of West Attica.
Leonidas Gergidis	Assistant Professor of Department of Materials Science & Engineering, School of Engineering of the University of Ioannina.

Approval Dissertation with grade **"EXCELLENT"** on **01/03/2019**.

The President of the Department	**The Secretary of the Department**
Alkiviadis Paipetis **Professor**	**Maria Kontou**

Ημερομηνία αίτησης του κ. Τουλφατζή Αναγνώστη: 20/04/2012

Ημερομηνία ορισμού Τριμελούς Συμβουλευτικής Επιτροπής: 26/04/2012 & 06/02/2013

Μέλη Τριμελούς Συμβουλευτικής Επιτροπής:

Επιβλέπων:
Παϊπέτης Αλκιβιάδης: Καθηγητής του Τμήματος Μηχανικών Επιστήμης Υλικών της Πολυτεχνικής Σχολής του Πανεπιστημίου Ιωαννίνων.

Μέλη:
Μπάρκουλα Νεκταρία-Μαριάνθη: Αναπληρώτρια Καθηγήτρια του Τμήματος Μηχανικών Επιστήμης Υλικών της Πολυτεχνικής Σχολής του Πανεπιστημίου Ιωαννίνων.
Δαυΐδ Κωνσταντίνος: Καθηγητής του Τμήματος Μηχανολόγων Μηχανικών του Τεχνολογικού Εκπαιδευτικού Ιδρύματος Κεντρικής Μακεδονίας.

Ημερομηνία ορισμού θέματος: 26/04/2012

«Χαρακτηρισμός, μηχανισμοί κοπής και κατεργασιμότητα μη μολυβδούχων ορειχάλκων»

ΔΙΟΡΙΣΜΟΣ ΕΠΤΑΜΕΛΟΥΣ ΕΞΕΤΑΣΤΙΚΗΣ ΕΠΙΤΡΟΠΗΣ: 23/01/2019

Παϊπέτης Αλκιβιάδης	Καθηγητής του Τμήματος Μηχανικών Επιστήμης Υλικών της Πολυτεχνικής Σχολής του Πανεπιστημίου Ιωαννίνων.
Μπάρκουλα Νεκταρία-Μαριάνθη	Αναπληρώτρια Καθηγήτρια του Τμήματος Μηχανικών Επιστήμης Υλικών της Πολυτεχνικής Σχολής του Πανεπιστημίου Ιωαννίνων.
Δαυΐδ Κωνσταντίνος	Καθηγητής του Τμήματος Μηχανολόγων Μηχανικών της Σχολής Τεχνολογικών Εφαρμογών του Ανωτάτου Τεχνολογικού Εκπαιδευτικού Ιδρύματος Κεντρικής Μακεδονίας.
Μανωλάκος Δημήτριος	Καθηγητής της Σχολής Μηχανολόγων Μηχανικών του Εθνικού Μετσόβιου Πολυτεχνείου.
Λεκάτου Αγγελική	Καθηγήτρια του Τμήματος Μηχανικών Επιστήμης Υλικών της Πολυτεχνικής Σχολής του Πανεπιστημίου Ιωαννίνων.
Ψυλλάκη Πανδώρα	Αναπληρώτρια Καθηγήτρια του Τμήματος Μηχανολόγων Μηχανικών της Σχολής Μηχανικών του Πανεπιστημίου Δυτικής Αττικής.
Γεργίδης Λεωνίδας	Επίκουρος Καθηγητής του Τμήματος Μηχανικών Επιστήμης Υλικών της Πολυτεχνικής Σχολής του Πανεπιστημίου Ιωαννίνων.

Έγκριση Διδακτορικής Διατριβής με βαθμό « **ΑΡΙΣΤΑ** » στις **01/03/2019**.

Ο Πρόεδρος του Τμήματος
Αλκιβιάδης Παϊπέτης
Καθηγητής

Η Γραμματέας του Τμήματος
Μαρία Κόντου

ABSTRACT

In recent years, the enforced stricter regulations concerning allowable lead content levels in products, especially for drinking water applications, have encouraged the invention and utilization of innovative solutions, such as the development of lead-free brass alloys.

This study was focused on the material characterization, cutting mechanisms (chip breaking), as well as the assessment of the machinability of leaded and lead-free brass alloys, widely used in industrial applications for the fabrication of final brass component (bolts, nuts, hydraulic fittings, valves etc.) by machining.

Initially, the influence of microstructure and lead presence on dynamic and static mechanical behaviour was studied. The main purpose of this study was the identification of the emergent microscopic fracture mechanisms, for the better interpretation of cutting behaviour during brass rods’ turning.

In addition, a statistical non-parametric study was implemented for the improvement of the quality characteristics of machining process (Chip Morphology, Power Consumption, Cutting Force and Surface Roughness) of the studied alloys.

Finally, a first attempt was pursued pertaining to the redesign of the production process flow, via the realization of experimental heat treatment procedures, which were applied for the alteration of microstructure in order to improve the machinability of the studied brass alloys.

ΠΕΡΙΛΗΨΗ

Προσφάτως, λόγω της αυστηρότερης νομοθεσίας σχετικά με τα επιτρεπόμενα ποσοστά μολύβδου, κυρίως στα προϊόντα/εξαρτήματα στις εγκαταστάσεις πόσιμου νερού, απαιτείται η χρήση καινοτόμων λύσεων, που αφορούν στην ανάπτυξη και βελτιστοποίηση μη μολυβδούχων ορειχάλκων-υψηλής κατεργασιμότητας, ώστε να αποφευχθούν οι επικίνδυνες επιπτώσεις του μολύβδου στον άνθρωπο και το περιβάλλον.

Η εν λόγω διατριβή εστιάζεται στον χαρακτηρισμό, τους μηχανισμούς κοπής (chip breaking) καθώς και την κατεργασιμότητα μολυβδούχων και μη μολυβδούχων ορειχάλκων που χρησιμοποιούνται ευρέως στη βιομηχανία για την κατασκευή εξαρτημάτων (κοχλίες, περικόχλια, υδραυλικοί σύνδεσμοι, βαλβίδες κλπ) μέσω μηχανουργικών κατεργασιών. Αρχικώς, μελετήθηκε η επίδραση που έχει η μικροδομή και η παρουσία του μολύβδου στα αποτελέσματα των δυναμικών και στατικών μηχανικών δοκιμών. Στόχος των παραπάνω δοκιμών είναι η καταγραφή των κυρίαρχων τύπων θραύσης, η οποία πρόκειται να συμβάλλει στην κατανόηση της συμπεριφοράς των ορειχάλκινων ράβδων κατά την κοπή.

Στην συνέχεια πραγματοποιήθηκε στατιστική μη παραμετρική μελέτη της κατεργασιμότητας μεταξύ των εξεταζόμενων κραμάτων, για την αριστοποίηση των ποιοτικών χαρακτηριστικών της κατεργασίας (Μορφολογία Αποβλίττου Κοπής, Ισχύς Κοπής, Δύναμη Κοπής και Τραχύτητα Επιφάνειας Κατεργασμένου Δοκιμίου).

Τέλος, γίνεται μία πρώτη προσπάθεια ανασχεδιασμού της παραγωγικής διαδικασίας, μέσω πραγματοποίησης κατάλληλων θερμικών κατεργασιών, των μη μολυβδούχων κραμάτων, με στόχο την τροποποίηση της μικροδομής τους προκειμένου να βελτιστοποιηθεί η κατεργασιμότητα σε κοπή.

This Dissertation is dedicated to my wife, my parents and my brother

ACKNOWLEDGMENTS

This PhD study was fulfilled in the frame of a project sponsored by ELKEME S.A. and FITCO S.A. I am indebted to the management teams of the above companies for their continuous support and assistance during this period.

I have to express my sincere gratitude to Professor Alkiviadis Paipetis for his kind supervision during all the stages of the PhD study. Furthermore, his trustworthiness, motivation and profound knowledge offered to me valuable guidance which is highly appreciated.

Also, I would like to acknowledge the contribution of the two other members of the advisory committee: Professor Constantine David and Associate Professor Nektaria-Marianthi Barkoula for their insightful comments and kind involvement.

Moreover, I am grateful to my business advisor and colleague Dr. George Pantazopoulos. His encouragement, active participation and mentorship are fully recognized.

Special thanks are also addressed to Dr. George Besseris for his contribution to the application of complicated statistical techniques, as well as to Dr. Dimitrios Sagris and Mr. Ioannis Evelzaman for their contribution to the realization of the machining experiments.

Many thanks are also addressed to my colleagues Dr. Athanasios Vazdirvanidis and Mr. Andreas Rikos, for their assistance in metallographic sample preparation and examination as well as for the spontaneous offer of valuable technical advice.

Last but not least, I would like to thank my family for all their love and encouragement. My parents Ιωσήφ and Χρυσαυγή together with my brother Αντώνιος assisted me spiritually throughout writing this thesis and in my life, in general. And to my loving, supportive and patient wife Αλεξάνδρα, whose faithful understanding during the final stages of this PhD thesis is so appreciated.

TABLE OF CONTENTS

Introduction

The stricter environmental, health and safety regulations address the harmful effects of lead and provide the motivation for the development and evaluation of new environmental friendly brass alloys. Conventional leaded brass rods are widely used in several manufacturing sectors (i.e. fabrication of hydraulic components, fittings, valves, etc.) due to their workability in extrusion and drawing, as well as their superior machinability. The understanding of the mechanical behavior/microstructure interaction is critical in order to successfully tailor candidate lead-free brass alloys for improved machinability without compromising the reliability of manufactured components.

The innovation of the present research work is based on the evaluation, development and optimization of the new generation environmental-friendly brass alloys, aiming to improve their machinability behaviour. More specifically, the individual objectives of this research work, towards alloy performance improvement, are allocated to the following areas:

a) Characterization and optimization of the machining process of the “initial condition” (extruded and drawn) lead-free brass alloys (CW510L, CW511L and C27450), compared to a reference leaded brass alloy (CW614N), employing a multi-non-parametric statistical technique (DOE).
b) Experimental development of novel production routes to improve the machinability performance of the above lead-free brass alloys, aiming at microstructural modification, by means of post-processing (extrusion and drawing) heat treatment cycles.
c) Study of the fracture resistance properties for the extruded and drawn as well as for the experimentally developed (heat treated) brass alloys. This was focused on the examination of heat treatment influence on the fracture mechanics properties.

In *Chapter 1*, an extensive literature survey was performed concerning the study of microstructure, mechanical properties as well as the machinability performance of leaded and lead-free brass alloys.

In *Chapter 2*, the mechanical behavior under static and dynamic loading of the lead-free brass alloys (at the extruded and drawn condition) in comparison to a conventional leaded brass alloy was studied. Fractographic analysis was performed to identify the involved fracture mechanisms and their relation to the alloy microstructure.

In *Chapter 3*, the machinability of the extruded and drawn brass alloys was evaluated. Machinability parameters such as chip morphology and power consumption, used as quality characteristics, were optimized. The optimum cutting parameters such as speed, feed and depth of cut as a multi-criterion plain turning problem were defined and experimentally confirmed, using a non-linear design of experiments approach. The main objective was to concurrently screen and optimize one qualitative and one quantitative characteristic (chip morphology and power consumption), using multilevel Taguchi experimental designs and nonparametric data analysis.

In *Chapter 4*, two additional quality characteristics, such as cutting force and surface roughness, of the brass alloys, were evaluated in turning mode. A design of experiments (DOE) technique (Taguchi orthogonal array methodology), as well as analysis of variance (ANOVA), were employed in order to identify the critical-to-machinability parameters and to obtain their optimum values for high-performance machining. The experimental design consisted of four factors (cutting speed, depth of cut, feed rate and alloy) with four levels for each factor, using the "smaller-the-better" criterion for quality characteristics' optimization.

In *Chapter 5*, a final heat treatment study was elaborated, aiming to improve the microstructure and the subsequent machinability of lead-free brasses. Twenty seven heat treatment protocols were applied in order to optimise the heat treatment process conditions. The mechanical behavior (tensile and hardness testing) was evaluated, for all the performed process conditions, in order to determine the structure/properties relationships and check the conformance to the applicable specification requirements.

In *Chapter 6*, the fracture resistance assessment of lead-free brass alloys (CW510L and CW511L), after the optimum final heat treatment, was studied under different loading regimes. This was achieved by employing fracture mechanics testing techniques, such as impact toughness (Charpy) and Crack-Tip-Opening-Displacement (CTOD).

In *Chapter 7*, the influence of the optimum heat treatment conditions on the attained machinability performance of the three lead-free brasses, was studied. Chip morphology, power consumption, cutting force and surface roughness were assessed before and after heat treatment to highlight the influence of the modified microstructure on the evolution of machinability quality parameters.

Finally, in *Chapter 8*, the final conclusions as well as the suggested further research work were presented.

The structure of this dissertation is illustrated schematically by means of the flowchart presented in Figure 1. The Materials and Experimental Methods are analytically described in Appendix A (p.174) while the Robust Design Methods are referred in Appendix B (p.193).

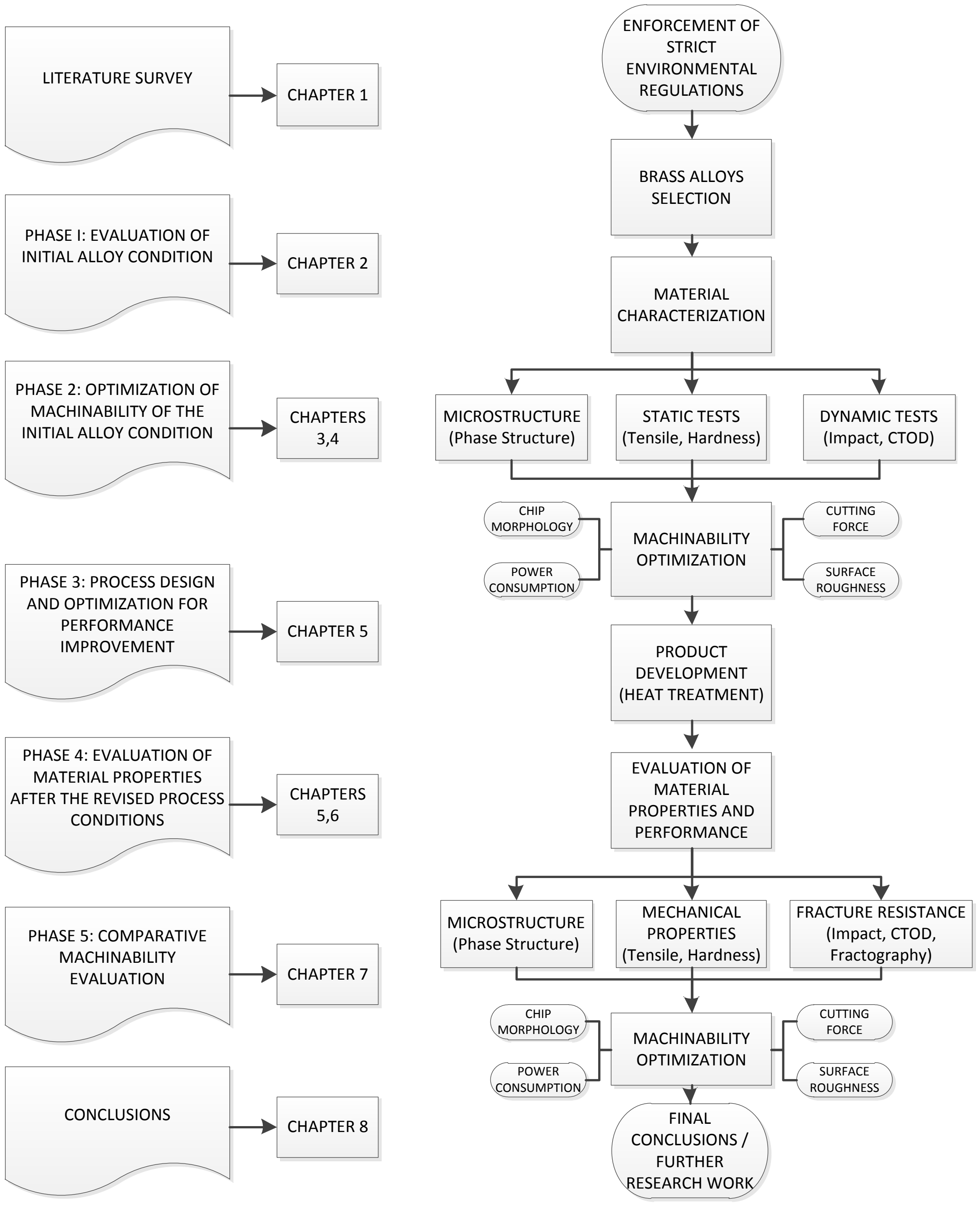

Fig. 1: Schematic illustration of the dissertation.

Chapter 1: Literature Survey

Overview

Cu–Zn alloys (brasses) are widely used industrial materials because of their superior properties such as high corrosion resistance, non-magnetism, good plastic deformability (forgeability) and machinability [1]. Lead is commonly added to brass alloys to ensure pressure tightness and improve machinability. Lead due to its low solidification temperature acts as a filler for micropores that form during casting. In addition, lead improves machinability by acting as a lubricant and promoting the formation of small discontinuous chips [2]. Improving the machinability of the material directly improves cutting-tool life [3].

However, the health hazards invoked by lead, resulted in the implementation of stricter regulations for allowable lead content levels in products and provided the driving force for the development of lead-free brasses [4]. From a purely manufacturing-economic standpoint, substitution of lead-containing brass with a lead-free alternative does not appear to be an economically viable option, but it is technically possible, satisfying the requirements of the enforced legislation [5].

The principal microstructural features of conventional and modern brass rods were highlighted and discussed in relation to behaviour during machining [6]. Chip size, cutting tool wear, cutting force and surface roughness are indicative parameters that may be employed for the optimization of cutting processes in terms of time and cost. In this direction, optimization algorithms have been applied to investigate the optimal number of passes and corresponding parameters such as speed, feed and depth of cut in each pass for multi-pass and multi-criterion plain turning problems [7].

This optimization could be achieved by fractional factorial designs and could prevent any potential complication arising from the use of analysis of variance (ANOVA) even in small samples [8]. The methodology of Taguchi through the use of orthogonal arrays is very efficiency in statistics at small sampling rates and creates an optimization technique for improving reliability [9]. Fractional factorials in robust design methodology designs have been extensively reviewed by Arvidsson and Gremyr [10]. The fundamental principle of robust design is to improve the quality of a product by minimizing the effect of the causes of variation, without eliminating the causes [11]. This can be achieved by optimizing the product and process, making its performance minimally sensitive to the various causes of variation.

Also, as was reported by Manna and Bhattacharyya, these causes were affected by the noise factors by way of parameter design [11]. In their work, the signal to noise factor is used as a measure of the quality, and orthogonal arrays were used to study many design parameters simultaneously. Many scientific works of practical design of experiments (DOE) methodology have been published in the last years [12]. In these works, the size of the experiments, the applied design, the number of factors that influenced the response variable and the sector of application of the design were analyzed. Viles et al., presented a real case of design of experiments focusing on the preliminary stages of experimentation, e.g. how to choose the best response analysis, how to evaluate the crucial factors and what the data sample collection should be [13].

Engineers may encounter key barriers in their trial to use design of experiments methodologies, so an exhaustive literature review was performed in order to classify these barriers [14]. The 16 barriers which were outlined were classified in 3 categories: business, educational and technical barriers. Numerous scientific articles, have verified that there is a gap between theoretical development of DOE and its effective application in industry [15]. Therefore, a simple methodology was proposed in order to facilitate the implementation of DOE in companies, through a framework that follows the traditional DMAIC (Define – Measure – Analyze – Improvement – Control) steps of ‘Six Sigma’ as a generic problem solving methodology. In this review, conventional leaded (Pb-ed) as well as modern lead-free (Pb-free) brass alloys were investigated. The elemental chemical analysis of these alloys and the related references are listed in Table 1.

Table 1.1: Chemical composition of leaded and lead-free brass rods (expressed in percent mass per mass).

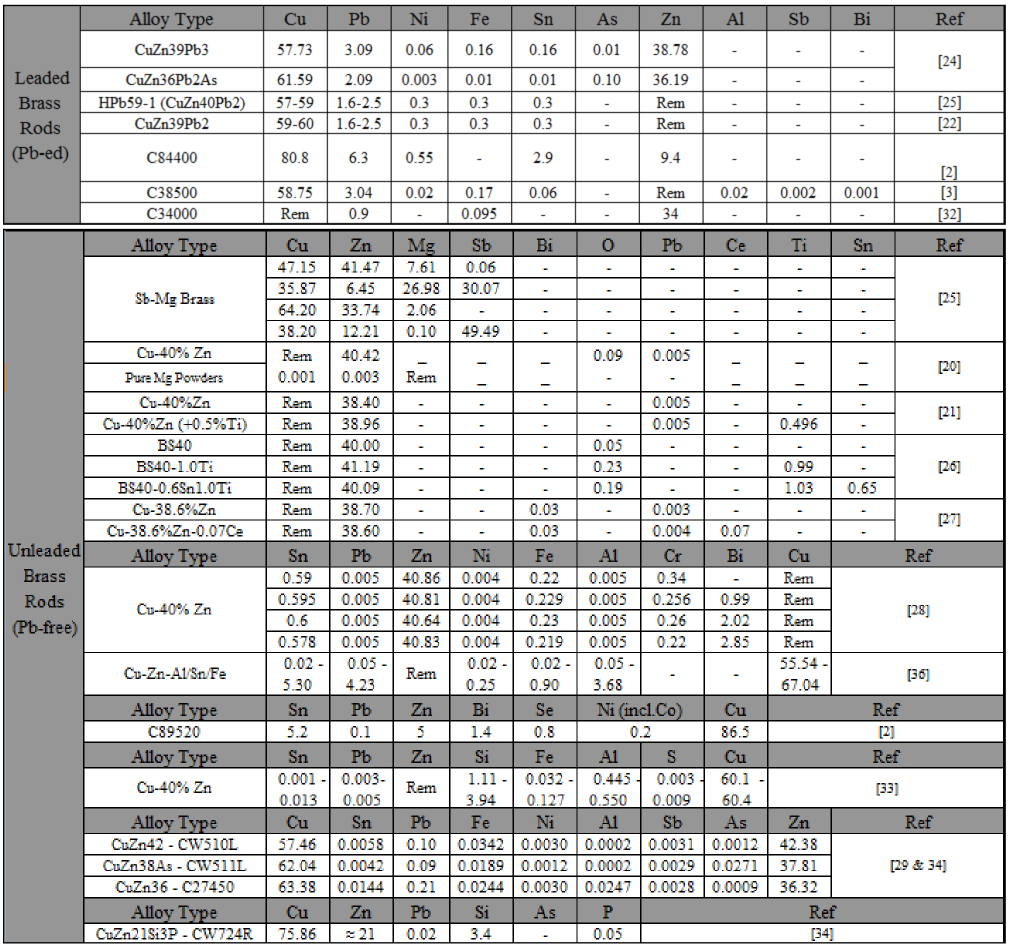

	Alloy Type	Cu	Pb	Ni	Fe	Sn	As	Zn	Al	Sb	Bi	Ref
Leaded Brass Rods (Pb-ed)	CuZn39Pb3	57.73	3.09	0.06	0.16	0.16	0.01	38.78	-	-	-	[24]
	CuZn36Pb2As	61.59	2.09	0.003	0.01	0.01	0.10	36.19	-	-	-	
	HPb59-1 (CuZn40Pb2)	57-59	1.6-2.5	0.3	0.3	0.3	-	Rem	-	-	-	[25]
	CuZn39Pb2	59-60	1.6-2.5	0.3	0.3	0.3	-	Rem	-	-	-	[22]
	C84400	80.8	6.3	0.55	-	2.9	-	9.4	-	-	-	[2]
	C38500	58.75	3.04	0.02	0.17	0.06	-	Rem	0.02	0.002	0.001	[3]
	C34000	Rem	0.9	-	0.095	-	-	34	-	-	-	[32]
Unleaded Brass Rods (Pb-free)	**Alloy Type**	**Cu**	**Zn**	**Mg**	**Sb**	**Bi**	**O**	**Pb**	**Ce**	**Ti**	**Sn**	**Ref**
	Sb-Mg Brass	47.15	41.47	7.61	0.06	-	-	-	-	-	-	[25]
		35.87	6.45	26.98	30.07	-	-	-	-	-	-	
		64.20	33.74	2.06	-	-	-	-	-	-	-	
		38.20	12.21	0.10	49.49	-	-	-	-	-	-	
	Cu-40% Zn	Rem	40.42	–	–	–	0.09	0.005	–	–	–	[20]
	Pure Mg Powders	0.001	0.003	Rem	–	–	-	-	–	–	–	
	Cu-40%Zn	Rem	38.40	-	-	-	-	0.005	-	-	-	[21]
	Cu-40%Zn (+0.5%Ti)	Rem	38.96	-	-	-	-	0.005	-	0.496	-	
	BS40	Rem	40.00	-	-	-	0.05	-	-	-	-	[26]
	BS40-1.0Ti	Rem	41.19	-	-	-	0.23	-	-	0.99	-	
	BS40-0.6Sn1.0Ti	Rem	40.09	-	-	-	0.19	-	-	1.03	0.65	
	Cu-38.6%Zn	Rem	38.70	-	-	0.03	-	0.003	-	-	-	[27]
	Cu-38.6%Zn-0.07Ce	Rem	38.60	-	-	0.03	-	0.004	0.07	-	-	
	Alloy Type	**Sn**	**Pb**	**Zn**	**Ni**	**Fe**	**Al**	**Cr**	**Bi**	**Cu**		**Ref**
	Cu-40% Zn	0.59	0.005	40.86	0.004	0.22	0.005	0.34	-	Rem		[28]
		0.595	0.005	40.81	0.004	0.229	0.005	0.256	0.99	Rem		
		0.6	0.005	40.64	0.004	0.23	0.005	0.26	2.02	Rem		
		0.578	0.005	40.83	0.004	0.219	0.005	0.22	2.85	Rem		
	Cu-Zn-Al/Sn/Fe	0.02 - 5.30	0.05 - 4.23	Rem	0.02 - 0.25	0.02 - 0.90	0.05 - 3.68	-	-	55.54 - 67.04		[36]
	Alloy Type	**Sn**	**Pb**	**Zn**	**Bi**	**Se**	**Ni (incl.Co)**		**Cu**			**Ref**
	C89520	5.2	0.1	5	1.4	0.8	0.2		86.5			[2]
	Alloy Type	**Sn**	**Pb**	**Zn**	**Si**	**Fe**	**Al**	**S**	**Cu**			**Ref**
	Cu-40% Zn	0.001 - 0.013	0.003- 0.005	Rem	1.11 - 3.94	0.032 - 0.127	0.445 - 0.550	0.003 - 0.009	60.1 - 60.4			[33]
	Alloy Type	**Cu**	**Sn**	**Pb**	**Fe**	**Ni**	**Al**	**Sb**	**As**	**Zn**		**Ref**
	CuZn42 - CW510L	57.46	0.0058	0.10	0.0342	0.0030	0.0002	0.0031	0.0012	42.38		[29 & 34]
	CuZn38As - CW511L	62.04	0.0042	0.09	0.0189	0.0012	0.0002	0.0029	0.0271	37.81		
	CuZn36 - C27450	63.38	0.0144	0.21	0.0244	0.0030	0.0247	0.0028	0.0009	36.32		
	Alloy Type	**Cu**	**Zn**	**Pb**	**Si**	**As**	**P**					**Ref**
	CuZn21Si3P - CW724R	75.86	≈ 21	0.02	3.4	-	0.05					[34]

1.1. Microstructure Evolution: Processing condition dependencies and influence on mechanical properties

1.1.1. Microstructure

I) Leaded Brasses

As aforementioned, Pb in conventional brass alloys serves in improving their machinability. Lead preferred accumulation sites are mainly the α/β interphase boundaries. Depending upon the casting and thermomechanical process parameters, lead in molten condition during metal forming, tends to reduce its surface energy by obtaining a spherical shape [6]. Furthermore, lead globules coalescence result in formation of bigger lead islands, arranged at the α/β interfaces and minimizing the interfacial energy.

Lead coalescence increases mean particle size and reduces the Pb particle density, with an adverse effect on machinability [6]. Fine and uniform lead distribution facilitates machining processes through better chip fracturing and less tool wear, while excess lead or non-uniform lead distribution may cause surface cracking during hot working due to hot-shortness [16]. Hot shortness results from over-heating because the temperature of the extrusion is increased by billet-container friction. The phase structure of leaded brass alloys is governed by a variety of mechanisms. The α/β interphase boundaries are high interfacial energy sites and, hence, potential lead distribution centres [17]. When machined, an (α+β)-brass has better chip breaking properties than a pure α alloy, while machinability is improved by increasing the size of interphase boundaries, which in its turn is affected by the β-phase content and the size of α-phase crystals. Higher β-phase volume fraction and finer α-crystals (for a constant α-phase content) tend to create longer interphase boundaries, which form Pb distribution sites (Fig. 1.1) [17].

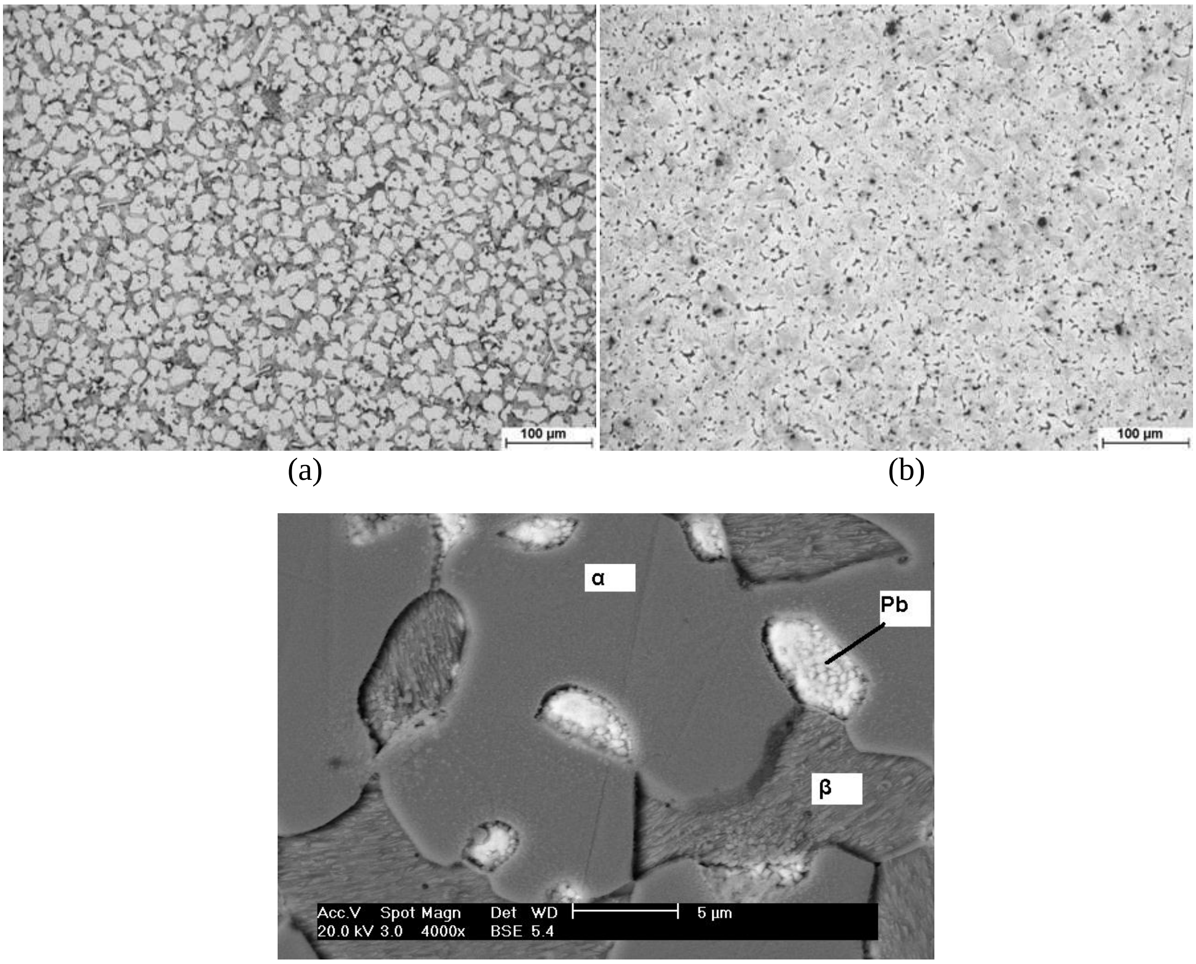

(a) (b)

(c)

Fig. 1.1: Optical micrographs showing the phase structure of (a) CuZn39Pb3 brass – a higher β-phase structure, (b) CuZn36Pb2As brass – a lower β-phase structure ($FeCl_3$ etching, 10s) and (c) SEM micrograph showing a typical phase structure of the CuZn39Pb3 brass; note the presence of lead islands concentrated at α/β interface boundaries and the plate-like morphology of the β-phase [17].

As Pb is precipitated at the end of solidification, its size and distribution is primarily affected by casting and solidification conditions, while the phase structure (volume fractions, grain size) is mainly influenced by extrusion conditions (e.g. temperature, extrusion ratio, speed and cooling rate) [18]. The sawing performance of brass bars (CuZn39Pb3) and its relationship to lead size and distribution and phase structure was reported in a previous study [18]. In this work the presence of β-phase lowers the overall ductility of the alloy and therefore enhances the segmentation of machining chips. Holler et al. examined the influence of extrusion parameters on the phase structure in CuZn40Pb2 [19]. They showed that the percentage of β-phase was decreased with increasing billet temperature and increasing extrusion ratio, while grain size decreased with decreasing billet temperature and increasing extrusion ratio. Both grain size and β-phase fraction are less influenced by the extrusion speed.

According to Pantazopoulos and Vazdirvanidis, beta (β) phase appeared in CuZn39Pb3 microstructure exhibits a characteristic plate-like type morphology possessing different orientation among the various grains [6]. This layered type morphology exhibited by β-phase may be considered beneficial for chip-breaking during machining. Chandra et al. investigated the intergranular and interphase cavitation in binary alpha/beta brass in tension at 600°C under conditions of superplastic deformation [20]. The process of cavitation was associated with grain boundary sliding. Cavity nucleation occurred at points of stress concentrations and was favored at the sliding interfaces on α-β boundaries rather than on α-α and β-β interfaces [21].

II) Unleaded Brasses (Pb-free)

In contrast, the absence of Pb as alloying element and/or the potential presence of other alloying constituents directly affects the microstructure of Pb-free brass. Atsumi et al. investigated high-strength brass (Cu-40% Zn) alloy with magnesium (Mg) which was fabricated via a powder technology process as well as the effect of the additive Mg element on microstructural properties of extruded brass alloys with α-β duplex phases [22]. In this work pre-mixed Cu-40% Zn alloy powder with 0.5-1.5 mass% pure Mg powder (Cu-40% Zn+ Mg) was consolidated using spark plasma sintering (SPS). SPSed Cu-40% Zn+Mg specimens consisted of α-β duplex phases containing $Mg(Cu_{1-x}Zn_x)_2$ intermetallic compounds (IMCs) with a mean particle size of 10-30 μm in diameter. The IMCs were completely dissolved in the α-β duplex phases by a heat-treatment at 973K for 15 min; thus, in order to disperse fine IMCs on α-β duplex phase matrix, the SPSed Cu-40% Zn +Mg specimens were pre-heated at the solid solution condition and immediately extruded [21]. The extruded specimen exhibited fine α-β duplex phases, containing very fine precipitates of the above Mg $(Cu_{1-x}Zn_x)_2$ IMCs with 0.5-3.0 μm in diameter [21].

Atsumi et al. also investigated the microstructural properties of the Cu-40Zn-0.5Ti ternary alloys via solid solution treatment [22]. The extruded specimen which was pre-heated at 973K for 15 min and then extruded consisted of fine and uniform α-β duplex phase structures having an average grain size of 2.14 μm in diameter. Furthermore, fine precipitates with a mean particle sizes of 0.5 μm diameter resulting from the precipitation of the solid solution Ti element, were densely dispersed in the matrix [22].

Fontaine and Keast, compared a lead-free brass (EnviroBrass C89520) to a conventional brass C84400 [2]. In this work, the large difference in grain size was attributed to the dependence of grain growth on alloy chemistry, while the excess concentration of Sn around the particles and at the grain boundaries was due to 'coring', a well-documented phenomenon. However, the presence of Sn prevented the segregation of Bi to the grain boundaries and inhibited hot-tearing phenomena during processing attributed to Bi segregation. It was not clear at this stage how the presence of Sn prevented the segregation of Bi; either the wetting behaviour of Bi was different in a Cu-Sn alloy than in pure copper or the excess number of Sn atoms at the boundaries prevented the segregation of Bi. Sn is a reasonably large atom and filled all the available grain boundary sites. EDS in the STEM did not trace Bi segregation at the boundaries in the brass, even though bismuth segregates strongly in pure copper alloys [2].

1.1.2. Mechanical Properties

I) Leaded Brasses

Hentati et al. investigated cracking of CuZn39Pb2 during hot forging [23]. The forgeability of the alloy is significantly affected by the work hardening capacity. Decrease of the ductility is observed as a result of work hardening and α-phase size reduction during hot stamping process at 750°C. Microhardness tests confirmed that stamping increased the brass hardness, while the size of α-phase was also decreased, as shown in Figure 1.2.

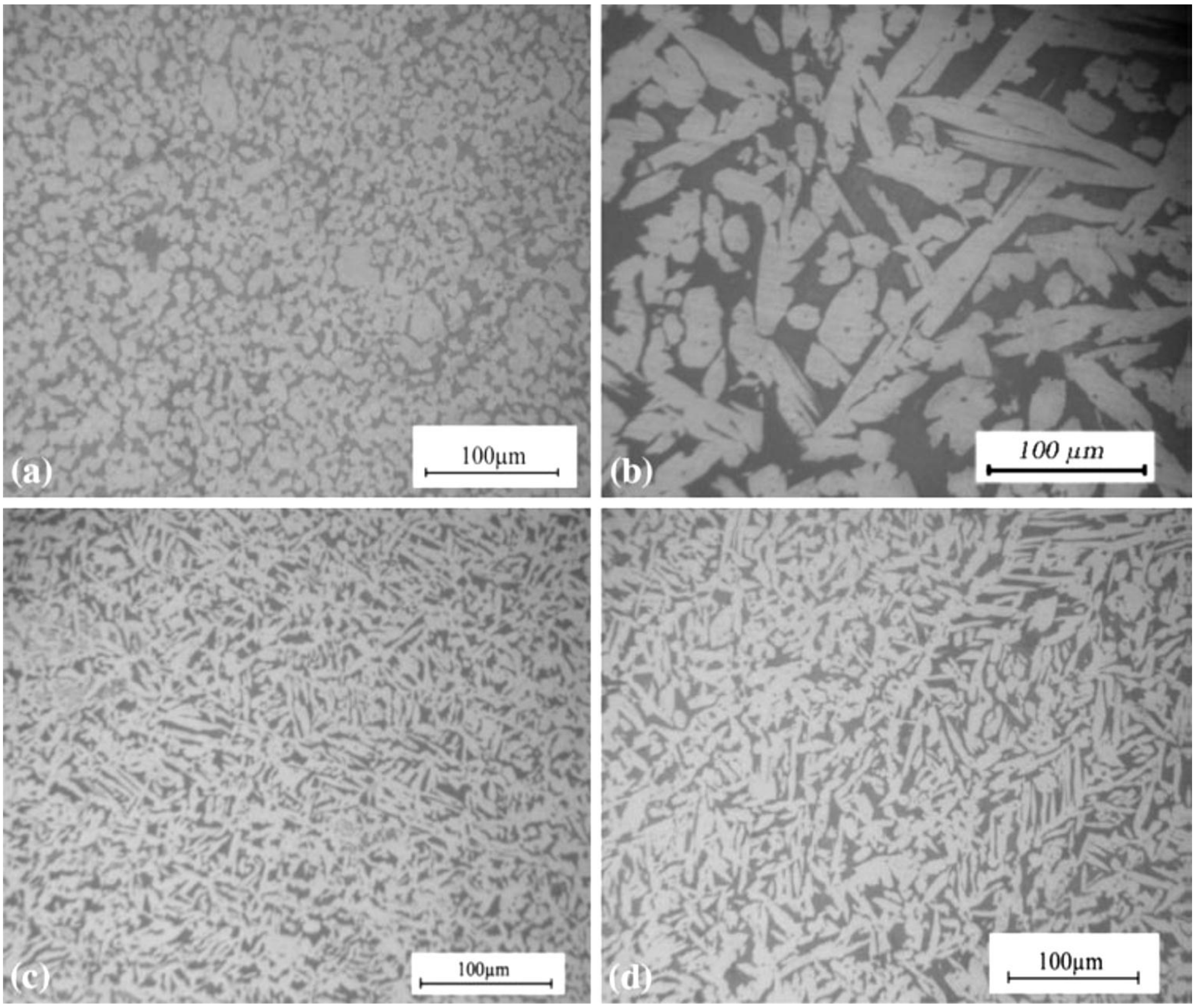

Fig. 1.2: Optical micrographs of CuZn39Pb2 brass: (a) virgin brass, (b) preheated brass at 750°C, (c) hot-stamped brass and (d) hot-stamped brass followed by annealing at 300°C [23].

Reduction of α-crystal size and subsequent hardness increase degrade material ductility causing cracks during stamping. Cracks could have been caused as the result of residual stresses developed during stamping. The application of heat treatment at 300^{o}C for 1h has a favourable effect in the solution of cracking problem, while tensile testing indicated an increase of strain up from 22% to 28% [23].

Blaz et al. showed that the reduction of the flow stress during hot deformation of CuZn39Pb3 alloy resulted from dynamic recovery and dynamic recrystallization which had operated above ~950 K [24]. Fine lead particles did not fully protect the grain coarsening in the course of dynamic recrystallization at high deformation temperatures. During hot deformation above ~1000 K, $\alpha \rightarrow \beta$ phase transformation was found to overlap with the aforementioned structural softening process and result in effective grain coarsening followed by effective flow stress reduction. Pantazopoulos and Toulfatzis, studied the mechanical behaviour and fracture mechanisms of conventional leaded brasses [25].

CuZn39Pb3 brass contained much higher percentage of β-intermetallic phase than CuZn36Pb2As brass. Beta (β)-phase (CuZn), an ordered-type intermetallic phase, possessing a body-centred cubic crystal structure was harder and less ductile than α-phase (face-centred cubic crystal structure) which refers to (Cu) solid solution. Consequently, CuZn39Pb3 brass, a dual phase (α + β) brass, containing ~35% β-phase, a much higher percentage than that existed in CuZn36Pb2As brass (<5%), exhibits higher strength, hardness and lower total elongation. Toulfatzis et al. found that CuZn39Pb3 brass had higher proof strength and tensile strength but lower elongation compared to CuZn36Pb2As brass (Fig. 1.3) [17].

The side views of the fractured specimens in tension, indicated typical ductile fracture morphology in both alloys (Fig. 1.4). The reduction of area was also higher in CuZn36Pb2As brass as compared to CuZn39Pb3, indicating that post-uniform elongation—as observed in the necking area— was more pronounced for the CuZn36Pb2As brass [17]. Higher reduction of area in case of CuZn36Pb2As brass was a result of greater extent of non-uniform elongation and was indicative of pronounced post-necking deformation during tensile testing. The metallurgical condition of CuZn36Pb2As brass, consisting of a relatively uniform microstructure, with a small percentage of β-phase, was found to be more resistant to micro-void growth and coalescence under tri-axial stress state leading to substantially higher post-uniform elongation and higher reduction of area during necking [25].

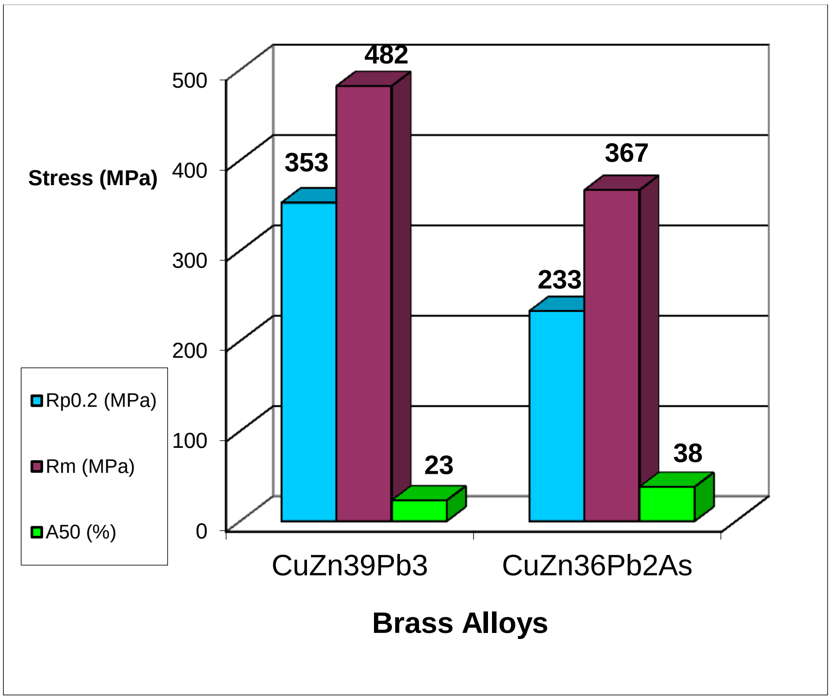

Fig. 1.3: Histograms showing proof strength, tensile strength and A_{50} fracture elongation [17].

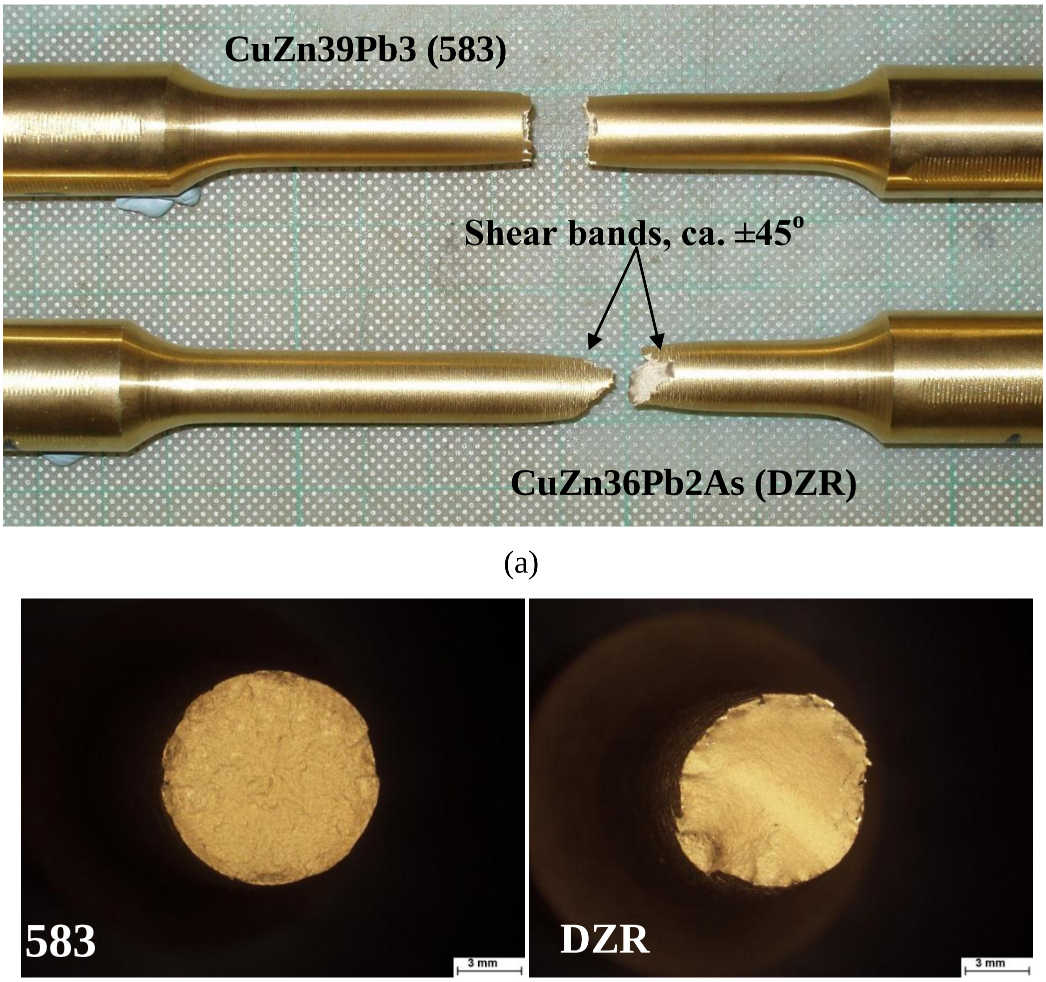

(a)

(b) (c)

Fig. 1.4: (a) Macroscopic side views of the fractured samples after tensile test and optical stereomicrographs showing the tensile fracture surfaces of (b) CuZn39Pb3 (583) and (c) CuZn36Pb2As (DZR) brass rods [17].

Hardness measurements indicated a more homogeneous hardness profile (lower hardness gradient) to CuZn39Pb3 brass as compared to CuZn36Pb2As brass [17]. In this research, CuZn39Pb3 alloy was characterized by higher hardness values (core ~136 to surface ~149 HV) as compared to CuZn36Pb2As (core ~104 to surface ~136 HV). The topographic features of tensile fracture surfaces of CuZn39Pb3 and CuZn36Pb2As alloys were studied with Scanning Electron Microscopy (Fig. 1.5) [25]. In this study, a mixed-mode fracture combining dimple formation and planar faceted fracture induced by a quasi-cleavage process was identified in the case of CuZn39Pb3 alloy (Fig. 1.5a, b).

On the other hand, the CuZn36Pb2As alloy exhibited a typical ductile fracture consisting of fine equiaxed dimples (Fig. 1.5c, d). Pantazopoulos investigated the mechanical properties of C38500 leaded brass [3].

Appreciable ductility was observed prior to fracture by the formation of localized neck, the subsequent fracture was primarily ductile, and the resultant matched surfaces were sufficiently rough, consisting of interconnected shear cracks. The final metal forming process, cold drawing, led to hardness inhomogeneities due to heterogeneous plastic deformation between the surface and core [3].

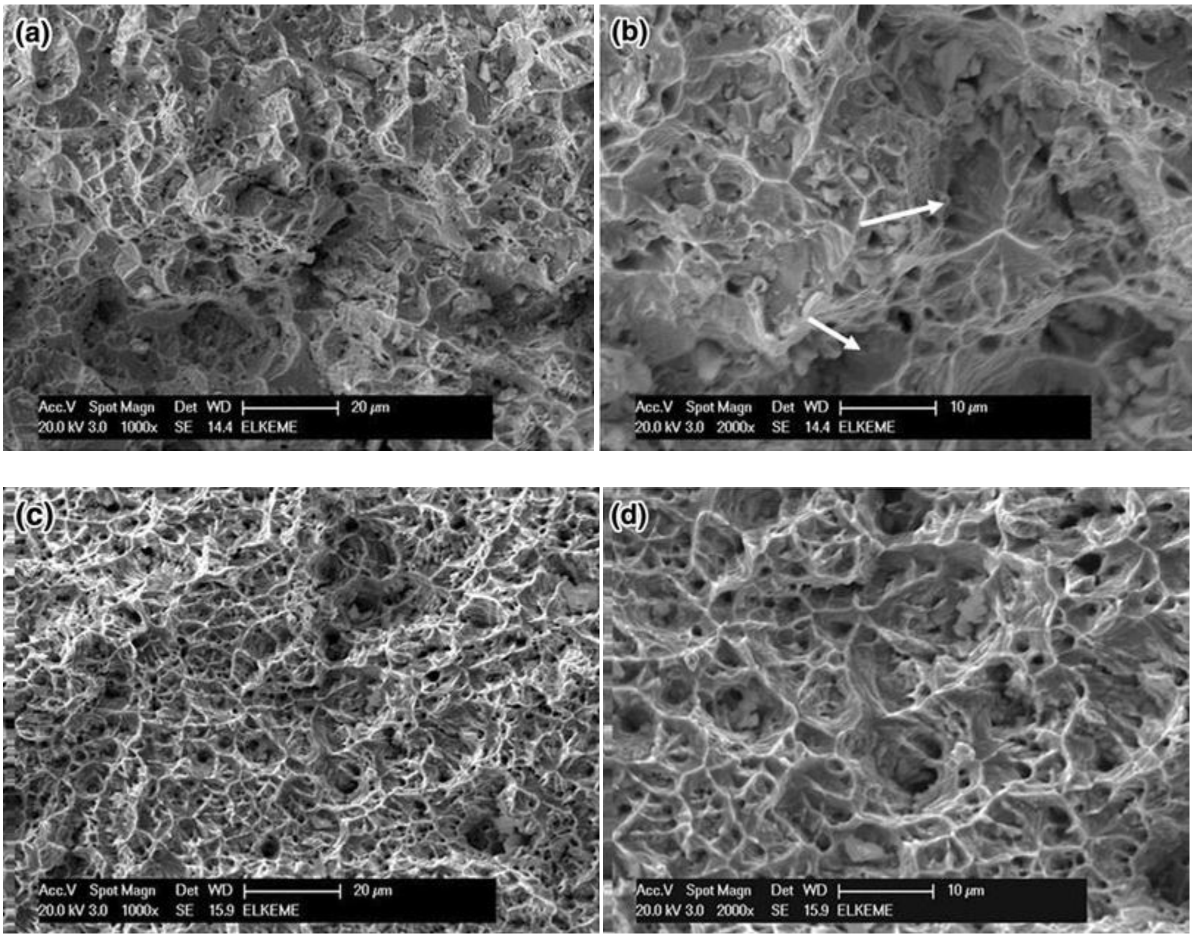

Fig. 1.5: SEM micrographs showing tensile fracture surface features of (a) CuZn39Pb3 brass rod, (b) detail of (a) at higher magnification (white arrows indicate presence of planar regions on fracture surface which constitute quasi-cleavage fractures), (c) CuZn36Pb2As brass rod, (d) detail of (c) at higher magnification [25].

II) Unleaded Brasses (Pb-free)

Quan Li et al. showed that the microstructure of the hot extruded Sb-Mg lead-free brass was composed of α, β phases and Sb-Mg containing intermetallic compounds [26]. In this research, the developed Sb-Mg brass was compared with the HPb59-1 brass (CuZn40Pb2) in terms of its mechanical properties and was found to have the potential to replace it in order to reduce cost and environment impact.

Atsumi et al. studied the tensile properties of the extruded Cu-40% Zn +1.0% Mg and reported an average value of yield strength (YS) 328 MPa, ultimate tensile strength (UTS) 553 MPa and elongation of 25% [21]. The extruded Cu-40% Zn +1.0% Mg alloy outperformed the conventional binary brass alloy with 229 MPa yield strength (YS) and 464 MPa ultimate tensile strength (UTS), while the strengthening mechanism of this wrought brass alloy was attributed to the grain refinement because of a pinning effect by the fine Mg $(Cu_{1-x} Zn_x)_2$ precipitated at the boundaries of each phase. In Figure 1.6, SEM micrographs of the tensile fractured surface of extruded Cu-40% Zn and Cu-40% Zn +1.5% Mg specimens are shown [21].

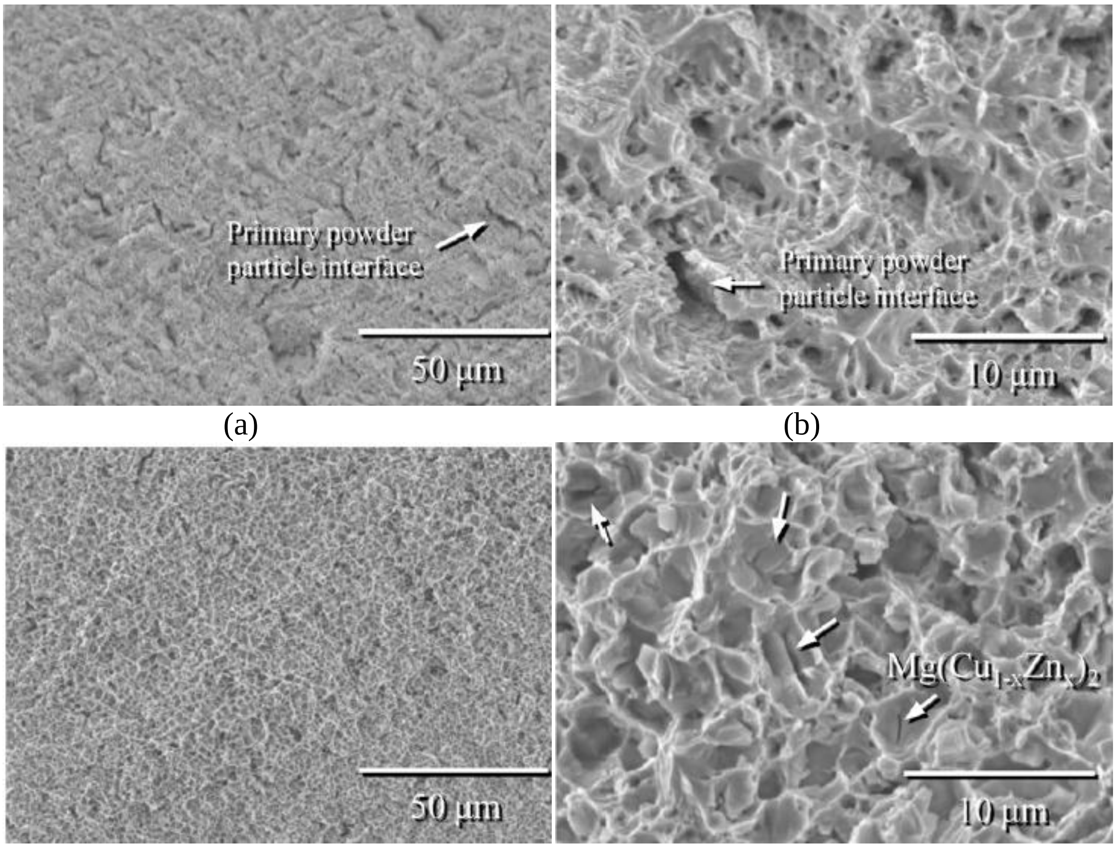

(a) (b)

(c) (d)

Fig. 1.6: SEM observation on fractured surface of tensile specimens of (a),(b) Cu-40% Zn and (c),(d) Cu-40% Zn +1.5% Mg [21].

Both extruded specimens showed fine dimples with size consistent to low overall ductility, as both extruded specimens consisted of extremely fine α-β duplex phase structures. Furthermore, the hills and valleys of extruded Cu-40% Zn specimen indicated that the crack paths preferentially follow the primary powder particle interface region. On the other hand, the hills and valleys were never observed in the extruded Cu-40% Zn +1.5% Mg specimen, except for some fine particles which were observed on the fracture surface [21].

In another study, Atsumi et al. reported that the extruded Cu-40%Zn-0.5Ti alloy had an average value of yield strength of 304 MPa, ultimate tensile strength of 543 MPa and elongation of 44% [22]. Cu-40%Zn-0.5Ti brasses revealed satisfactory strength and good ductility. The high strengthening mechanism of the wrought brass alloy was mainly due to the grain refinement of α and β phases by the fine precipitates derived from solid solution of Ti elements in the matrix [22]. In a previous research effort, Li et al. was reported that remarkable grain-refinement and strengthening effects were achieved by the addition of Ti to 60/40 brass in the powder metallurgy process route [27]. However, Ti was found to be readily segregated in the primary particle boundaries at elevated temperatures, which significantly deteriorated the mechanical properties of the BS40–1.0Ti (Fig. 1.7).

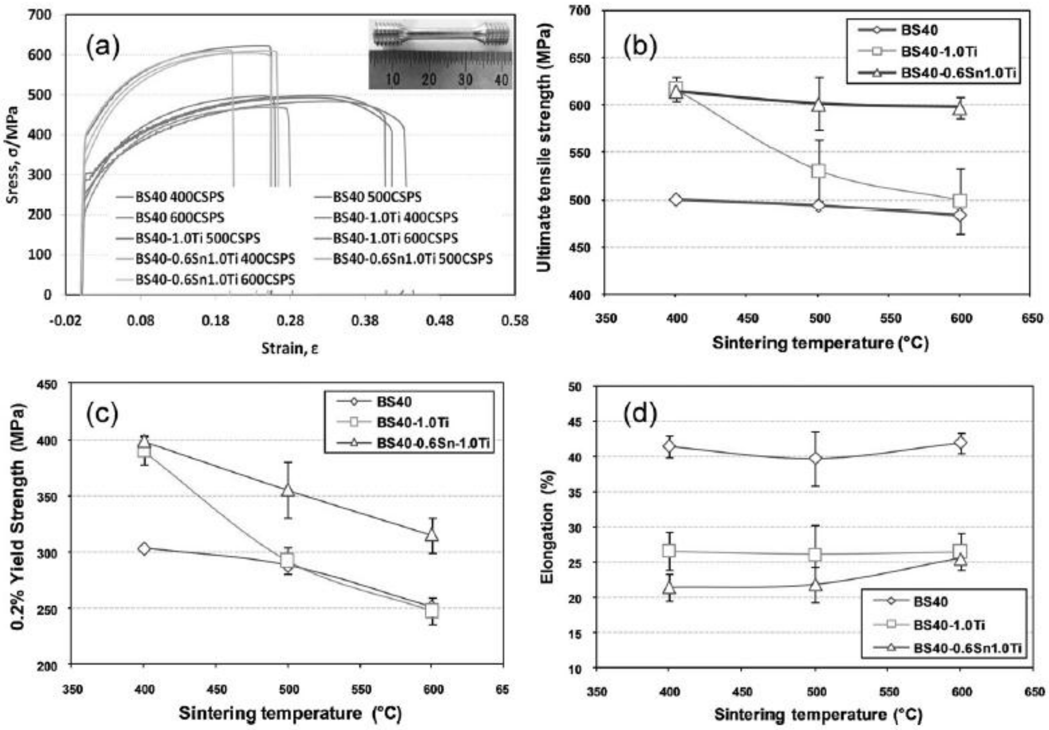

Fig. 1.7: (a) The true stress–strain curves of the extruded brasses (BS40 / BS40-1.0Ti / BS40-0.6Sn1.0Ti) as a function of sintering temperature. Influence of sintering temperature on (b) ultimate tensile strength, (c) yield strength and (d) elongation [27].

To inhibit the segregation behavior of the Ti in the BS40–1.0Ti, Sn was proposed as an additive. Also, in this work Ti was found to precipitate in the form of $CuSn_3Ti_5$ in grain boundaries, rather than segregate at the primary particle boundaries, leading to significant grain refinement and mechanical strengthening effects on the BS40–0.6Sn1.0Ti brass. These results showed that the introduction of Sn via powder metallurgy to BS40–1.0Ti brass can effectively impede the segregation of Ti and stabilize the mechanical properties at high processing temperatures [27]. Chandra et al. found that the ductility as well as the flow stress of α-β brass is significantly affected by the addition of cerium [28].

This effect resulted from the fact that cerium decreased the solubility of zinc in the α (fcc) phase at 475 to 675°C and consequently shifted the α/α+β boundary of the phase diagram to lower zinc concentrations reducing α-phase fraction. More specifically, the addition of small amount of cerium of 0.07% decreased the α/β ratio from 70:30 to 55:45 and modified the mechanical properties by improving the ductility and decreasing the flow stress up to a factor of 3, at the tested temperature range. Moreover, the hindering effect of Ce addition on Zn solubility, indirectly contributed to an expected increase of stacking fault energy (SFE) of α-phase, improving dislocation mobility, such as dislocation climb and cross slip.

Atsumi et al. investigated the mechanical properties of high-strength, Pb-free machinable α-β duplex phase brass Cu–40Zn–Cr–Fe–Sn–Bi alloys [29]. The extruded Cu–40Zn–Cr–Fe–Sn–Bi alloys consisted of α-β phases containing the fine, uniform Cr–Fe IMCs and Bi particles. The average yield strength (YS) and ultimate tensile strength (UTS) of the extruded Cu–40Zn–Cr–Fe–Sn–Bi alloys were 288 MPa and 601 MPa, respectively. Theses alloys exhibited YS and UTS that were 29% and 40% higher than conventional machinable brass Cu–40Zn–Pb alloy. The extruded Cu–40Zn–Cr–Fe–Sn–Bi alloys also maintained 75% of the machinability of the Cu–40Zn–Pb alloy [29].

Toulfatzis et al. studied the fracture behavior of lead-free brass alloys for machining applications [30]. In this work, the mechanical behavior under static and dynamic loading of three lead-free brass alloys CuZn42 (CW510L), CuZn38As (CW511L) and CuZn36 (C27450) lead-free brass alloys in comparison to the conventional CuZn39Pb3 (CW614N) leaded brass alloy was studied. The fractographic evaluation was performed on impact tested brass samples to identify the involved fracture mechanisms and their relation to the alloy microstructure. The action of dimpled fracture mechanism was evident to all the studied alloys; however, the dimple size and distribution exhibited a considerable variation signifying differences in the evolved plastic deformation prior to failure.

The largest dimples were detected in the case of CW511L and C27450 alloys, which is consistent to their higher values of impact energy and fracture toughness. In this study, it was also shown that the CuZn42 (CW510L) lead-free brass alloy is a potential candidate in replacing the conventional CuZn39Pb3 (CW614N) leaded brass, combining high tensile strength and tolerable fracture toughness, due to the high presence of β-phase in the alloy microstructure.

1.2. Machinability Evaluation

1.2.1. Chip Formation and Tool Wear

I) <u>Leaded Brasses</u>

Toulfatzis et al. investigated the machinability of CuZn39Pb3 and CuZn36Pb2As brasses [17]. In this research, machinability was assessed qualitatively and quantitatively by evaluating the chip size and morphology and the corresponding cutting tool wear land, employing a single point turning technique according to ISO 3685 [31]. Experimental results indicated that the most critical factors affecting the chip formation quality during brass bars machining, were the type of copper alloy used (CuZn39Pb3 and CuZn36Pb2As alloys) and the cutting speed, while it was not found to be sensitive to depth of cut and feed rate variations [17]. Characteristic forms of chip formation produced under various turning conditions are shown in Figure 1.8. It was evident that a significant variety of chip morphology was produced by changing the turning conditions: Single needle (Fig. 1.8c), feathery (Fig. 1.8d) and continuous helical (Fig. 1.8e) were representative forms that constituted a qualitative indicator of the machining process performance [17].

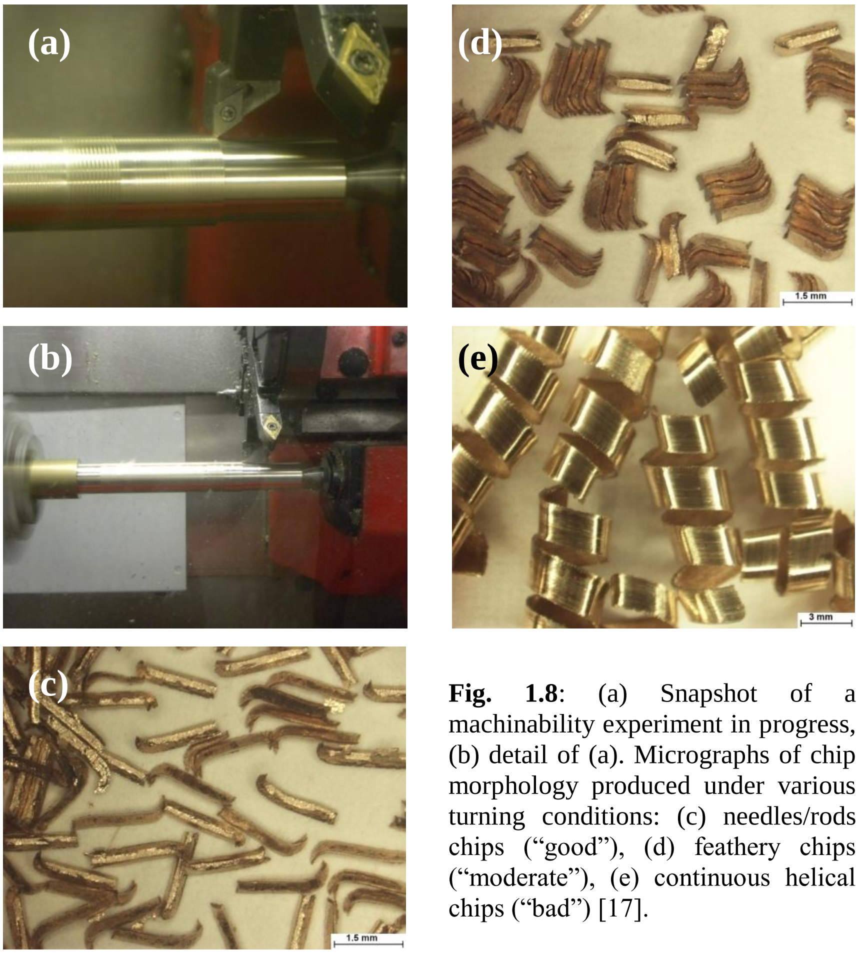

Fig. 1.8: (a) Snapshot of a machinability experiment in progress, (b) detail of (a). Micrographs of chip morphology produced under various turning conditions: (c) needles/rods chips (“good”), (d) feathery chips (“moderate”), (e) continuous helical chips (“bad”) [17].

The formation of shorter chips resulted in better surface finish, lower tool wear and ease of operation allowing higher cutting speeds, while chip fracturing and removal led to the reduction of tool/chip contact, minimizing the risk of built-up edge formation [17]. Gane has shown that the addition of a small quantity of Pb to brass was very effective in reducing friction, both in cutting experiments and in simple sliding-friction experiments [32]. In addition, the ductility of brass was substantially reduced when lead was present. Both these factors contributed to the considerable improvement in machining properties observed in lead-containing alloys.

The reduced friction on the rake face of the tool decreased the specific cutting energy by a factor of about 2; as a result, the tool temperature decreased and the tool life improved [32]. As the Pb particle distribution became finer (less than 5 μm) and more homogeneous, chip-breaking during cutting became more pronounced, and, as a result, machinability improved.
The chip fracture in short pieces had the following advantages: ease of machining operation; maximum productivity, lower cutting forces, better surface finish of the workpiece, closer tolerances of the final component and less tool wear; longer tool life [32].

Preliminary machinability tests were performed by Pantazopoulos, in turning operation [3]. The turning speed was up to 395 rpm (the linear speed was up to 0.165 m/s) using cemented tungsten carbide insert as a cutting tool. The chip size tended to increase by increasing the depth of cut, while no appreciable changes were recorded by changing the feed rate. The depth of cut was constant within the turning cycle (i.e., 0.4, 1.0, or 3.0 mm). The horizontal advancement of the tool per revolution was defined as a function of the feed rate (0.25 or 0.50 mm/rev) [3].

Morphological observations of the produced chips, using optical metallography, indicated the absence of flow-zone (Fig. 1.9). Segmented chips with intense shear fractures were produced during turning as a result of dual phase microstructure ($\alpha+\beta$) and distribution of Pb particles at interphase boundaries. The presence of Pb decreased friction and temperature at the tool-workpiece interface, therefore increasing the tool life [3].

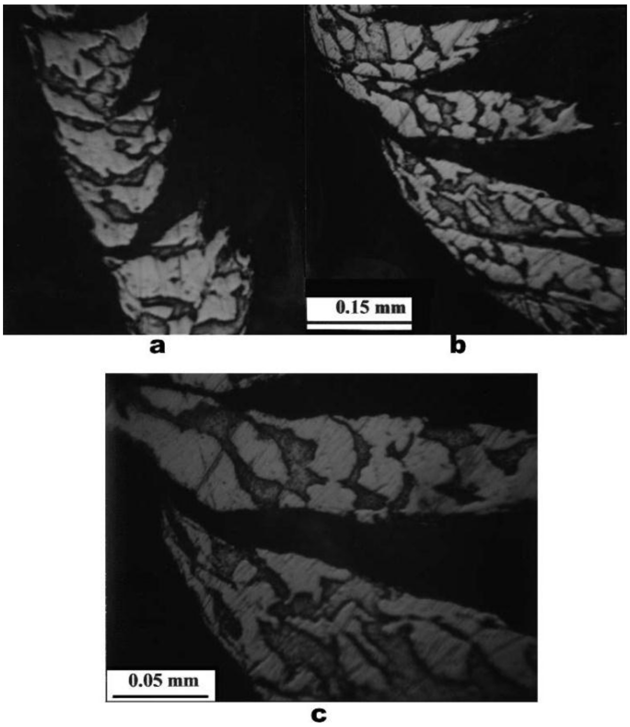

Fig. 1.9: (a) Segmented and (b) intensively fractured chip morphology without characteristic flow zone; (c) detail of (b) in the vicinity of the shear zone (depth of cut: 3.0 mm, feed rate: 0.25 mm/rev, cutting speed: 0.165 m/s) [3].

As it was shown in a previous study, cutting tool wear was principally controlled mainly by the cutting speed and depth of cut used during machining experiments while it appeared to be less sensitive to feed rate or the type of copper alloy variations [17]. Adhesion and sticking of the workpiece debris on flank face was intensified at higher cutting speeds. Moreover, the flank zone revealed several typical wear features, such as abrasive marks and chipping (edge fracturing), with increasing severity as the cutting speed increased (from 2,000 to 4,000 rpm; see Figs. 1.10a, b) [17].

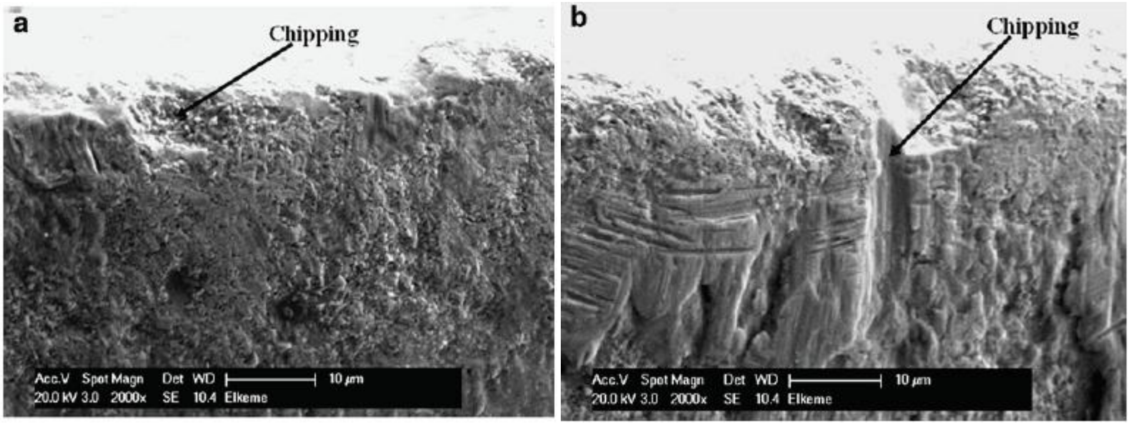

Fig. 1.10: SEM micrographs showing abrasive marks and chipping (edge fracturing): (a) cutting speed 2,000 rpm, (b) cutting speed 4,000 rpm [17].

Chipping caused edge fracture of machining tool, impairing cutting edge sharpness and leading to tool blunting. This type of tool failure increased cutting forces, resulting therefore in degradation of machining performance (longer chips, higher fluctuations and chattering, part distortion) and serious deficiencies in machined surface quality. Severe damage phenomena such as thermal cracking or flaking, were not observed in this study [17]. Toulfatzis et al. determined the optimum cutting conditions using non-parametric design of experiments methods applied in turning processes of leaded brass bars (CuZn39Pb3 and CuZn36Pb2As) for industrial applications [17].

Non-linear fractional factorial designs for the nine-run, three-level, four-factor saturated orthogonal array ($L_9=3^4$) were applied to collect sufficient data in order to investigate the multi-response optimization of two main machinability quality characteristics i.e. chip morphology and cutting tool wear.

The study outcomes were summarized as follows: i) concurrent multi-response optimization gave rise to no specific effect. Intermixing of the two studied quality characteristics led to blurring the dependence of alloy type on chip morphology by injecting a large variability in the unified response, ii) non-parametric analysis also demonstrated that no controlling factor influenced the behaviour of cutting tool wear; thus it was easy to base the final setting based on the performance of the chip morphology, iii) chip morphology was minimized using the following conditions: The optimal alloy type was the CuZn39Pb3 brass while pure practical considerations recommended cutting speed to be set at 2,000 rpm, a depth cut is set at 1.30 mm and feed rate locked at 0.1 mm/rev. The alloy type was the only parameter with an active effect in their study [17]. These optimal settings of the cutting parameters for chip morphology optimization suit right even for the cutting tool wear optimization (Fig. 1.11) and finally iv) confirmation experiments seem to verify the conclusion of this work [17].

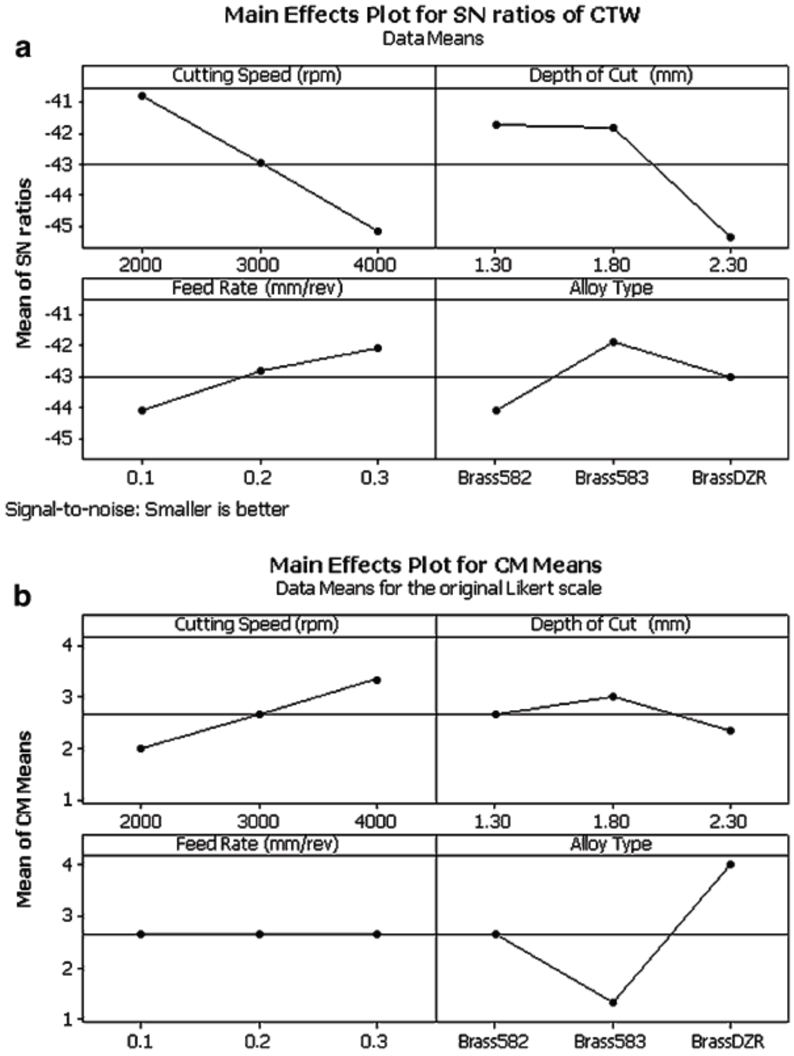

Fig. 1.11: (a) Response graph for signal-to-noise ratios of cutting tool wear, (b) response graph of means of chip morphology [17].

Hassan et al. evaluated the influence of cutting parameters i.e cutting speed, feed rate and depth of cut, in C34000 leaded brass, using ANOVA [33]. In this work, the purpose of the ANOVA was to identify the important parameters in predicting material removal rate. Feed rate was found to be the most significant factor and its contribution to material removal rate is 42.77 %. With 95% confidence interval, the feed rate was the most significant factor affecting the material removal rate.

The interaction between cutting speed and feed rate was found to be significant with a contribution of 7.75%. The best results for material removal rate were achieved when C34000 leaded brass was machined at cutting speed of 55 m/min, depth of cut of 0.2 mm, feed rate of 0.35 mm/rev.

II) Unleaded Brasses (Pb-free)

As the phase diagram indicates, both antimony and magnesium can be dissolved partly in copper, forming intermetallic compounds with copper [26]. If these intermetallic compounds were dispersively distributed in Cu-Zn system, these particles or strips would disturb the metallic matrix continuity, and make the chips rupture easily. Thus the cutting performance of the alloy can be improved without the addition of Pb. Also, the particles in the Sb-Mg brass are not expected to produce stress concentration during forming because they deformed plastically during extrusion, while improving the cutting performance and alloy's mechanical properties [26].

The development of a suitable grain and phase structure (the presence of α, β or γ phases in Cu-Zn system), through various metallurgical methods, e.g., alloying, forming, heat treating, etc. exerts a major influence on fracture behaviour and, consequently, on chip-breaking properties and machinability performance [34-35]. A scientific research revealed the benefits of the recycled bismuth-tin solder addition in lead-free brass alloy (Cu-38Zn-0.5Si) by reducing the chip-size morphology [36]. The improvement of chip-breaking efficiency was attributed to the presence of κ-phase in CuZn21Si3P, as opposed to the effect of α-phase in CuZn38As brass. Likewise, the high percentage of β-phase in the microstructure of CuZn41.5 resulted in the reduction of chip morphology [37].

The influence of the coating type (TiN, TiAlN, TiB2 and DLC on carbide tools) as well as the use of polycrystalline diamond (PCD) tools on chip formation and workpiece quality, was analyzed for the evaluation of machinability in three low-lead brass alloys (CuZn38As, CuZn42 and CuZn21Si3P). The machining problems were diminished using a diamond-like carbon coating, especially by the reduction of the friction in the secondary shear zone [38]. A machinability comparison between leaded (CuZn39Pb3) and lead-free brass (CuZn21Si3P) alloys was implemented in a relevant work concerning tool wear during machining. Machining of the lead-free brass alloy (CuZn21Si3P) resulted in longer chip size and, eventually, higher tool-wear rates using cemented carbides. The use of coating on carbide tools [e.g., (Ti, V, Zr, Hf, Nb, Ta) N], was recommended as a possible solution for overcoming excessive tool-wear rates [39].

Li et al. studied the influence of Ti addition on lead-free brasses [27]. They showed that BS40-2.2Bi alloy exhibited an excellent machinability compared to the Cu40Zn3.2Pb conventional leaded brass. The average drilling time increased with increasing Ti content from 0.3 wt. % to 1.0 wt. %. BS40-2.2Bi with 1.0 wt. % Ti addition could not be penetrated by drilling for more than 180 sec.

The different chip morphologies obtained during drilling operations were used to evaluate the machinability of the alloys produced (Fig. 1.12). Comparing with the chip shape of the conventional leaded brass (Cu40Zn3.2Pb), BS40-2.2Bi exhibited a different morphology, due to the facts that (i) the substantial brittleness of Bi affected the fracture behavior of the chip and (ii) the Ti addition to BS40-2.2Bi affected considerably the chip geometry which transformed into a continuous spiral shape when the Ti content increased to 0.5 wt. % [27].

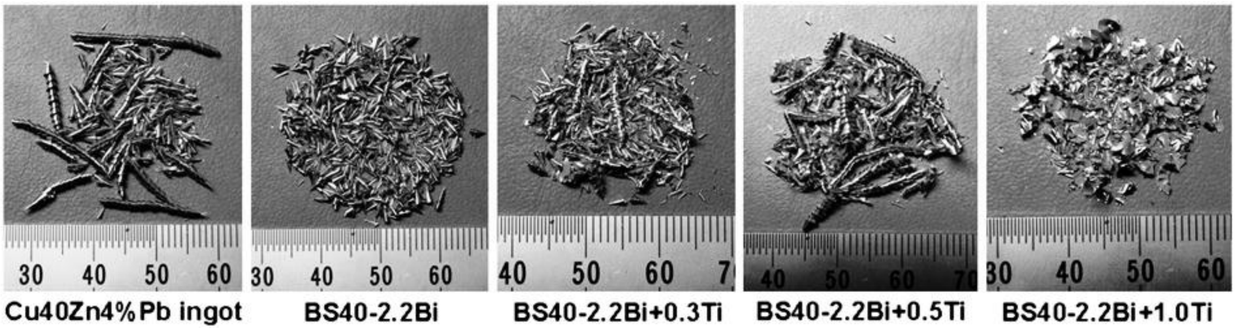

Fig. 1.12: Photographs of the chip types formed during drilling operation for leaded brass and BS40-2.2Bi alloy with different Ti addition [27].

Taha et al. showed that as the Si wt. % increased (from 0% to 1% Si) in modern lead-free brasses (CuZn40) tool wear slightly increased [40]. This was attributed to the decrease of the softer phase α and the respective increase of the harder phase β. In silicon brass alloys, the detrimental effect of β phase on tool wear was confirmed. The increase in silicon content (from 1% to 4% Si) led to moderate increase in tool wear due to the increase in volume fraction of brittle λ, η, and χ hard phases, albeit no significant effects of hardness and microstructure changes were observed. It was also indicated that cutting speed had a significant effect, as the chip changed from continuous to discontinuous type with decreasing cutting speed [40]. However, decrease of the cutting speed could not be recommended as a method to achieve the desirable discontinuous chip type due to lower productivity. By adding 4% Si to the unleaded CuZn40 brass, the chip changed from the undesirable continuous type to acceptable long bevel and cylindrical long types. It was clearly shown that the chip type was affected by the formation of hard secondary λ-phase precipitates rather than by the variation in mechanical properties [40].

Nobel et al. studied the machinability of various lead-free alloys, i.e. CW510L, CW511L and CW724R [41]. CW724R lead-free silicon brass, in comparison to other lead-free brasses, as CuZn42 (CW510L) and CuZn38As (CW511L), showed improved machinability concerning the chip formation. However, CW724R caused higher tool wear damage due to the abrasive action of Si-rich κ-phase against TiAlN coated carbide tool.

In this study, the CW510L machining performance using various cutting tools with different coatings (TiAlN, TiB_2, DLC, CVD-diamond) was investigated. Adhesive and abrasive wear was reduced by using DLC-coating among the tested PVD-coated tool systems. An additional improvement of cutting performance was achieved using CVD-diamond coating which exhibited exceptional abrasive wear resistance, while adhesion on the rake and flank face was minimized. Polycrystalline diamond tools (PCD) provide another alternative with significant abrasive wear resistance and low adhesion properties. However, the production demand for long tubular chips restricts the use of PCD tools and poses the need for the manufacture of such tools with favourable chip breaking geometry.

Experiments and simulations were implemented by Laakso et al. in order to investigate the effects of different cutting parameters on chip morphology of a low-lead brass [42]. This low-lead brass is not standardized, but it is close to standard CuZn38As (CW511L) lead-free brass. Based on these simulations and experiments, it was found that the use of a positive rake angle (+5°), high cutting speed (300 m/min) and low cutting feed rate (0.1 mm/rev) improves chip breakage from continuous chip to a chip of average length of 4 mm. High cutting speeds favour chip breakage by increasing chip brittleness, due to the suppression of softening effects at high strain rate conditions. Minimization of cutting force and friction force is achieved by using a positive rake angle (e.g. +5°). Reduction of friction could be realized by decrease of tool-chip contact area by decreasing feed rate and/or depth of cut. FEM simulation was in agreement to the above results.

Furthermore, in a very recent work, the influence of zinc equivalent on the evaluation of chip morphology and machining surface quality of free cutting silicon brasses was investigated, by adding Pb replacers (Si and Al elements). [43].

1.2.2. Cutting Force and Surface Roughness

Vilarinho et al. established several relationships concerning the influence of the chemical composition and the hardness on the different components of cutting forces [44]. The suggested empirical relationships took into account not only the well-established effect of lead in the machinability behaviour already shown by several authors, but also the effect of alloying elements usually present in brasses composition.

Conventional alloys (CuZn36Pb3 & CuZn39Pb3), with and without alloy additions, showed lower values of cutting forces (Fz) than the modern brass alloys of the studied ternary systems, Cu-Sn-Zn, Cu-Al-Zn and Cu-Fe-Zn [44]. However, in some cases, conventional alloys exhibited similar and higher values of feed and depth forces in relation to modern brasses.

The cutting forces applied for the machining of modern brass alloys of the ternary systems studied in this work were found to be affected by the type and content of alloying element. A scientific research revealed the benefits of the recycled bismuth-tin solder addition in lead-free brass alloy (Cu-38Zn-0.5Si) by reducing the required cutting forces in machining [36].

The influence of the coating type (TiN, TiAlN, TiB2 and DLC on carbide tools) as well as the use of polycrystalline diamond (PCD) tools on machining forces, was analyzed for the evaluation of machinability in three low-lead brass alloys (CuZn38As, CuZn42, and CuZn21Si3P). The machining problems were diminished using a diamond-like carbon coating, especially by the reduction of the friction in the secondary shear zone [38]. Machining of the lead-free brass alloy (CuZn21Si3P) resulted in higher cutting forces using cemented carbides. The use of coating on carbide tools [e.g., (Ti, V, Zr, Hf, Nb, Ta) N], was recommended as a possible solution for reducing the cutting forces [39].

In the alloys of the Cu–Sn–Zn system, the lowest values of cutting and feed forces (Fig. 1.13a) were obtained for tin contents that led to a β+γ structure. On the other hand, the presence of aluminium in alloys of the Cu-Al-Zn system had an opposite effect to that of tin, rising the cutting force as its content increased (Fig. 1.13b) [44]. In this ternary system, the highest values of cutting force Fz, were always obtained for alloys with a β+γ or only β structures.

Concerning Cu–Fe–Zn alloys, no relationship was found between the iron content and the machinability parameters. No significant correlations were found between the cutting forces and the chemical composition, when expressed in terms of effective copper content. However, a loose correlation of the feed force to the effective copper content on conventional alloys was found, although the authors indicate that further studies would be needed to elucidate this behavior [44].

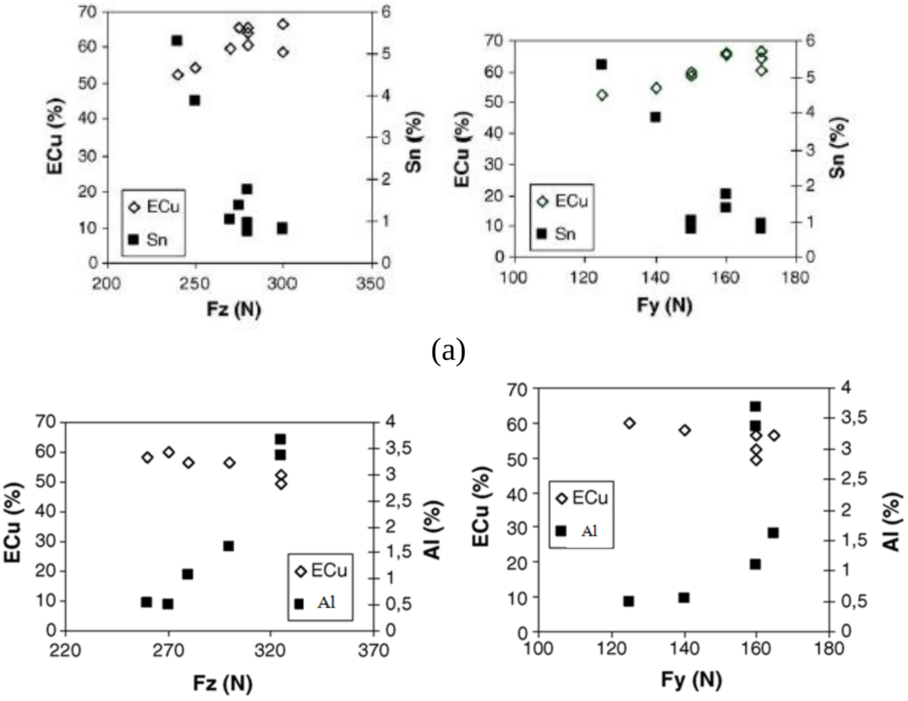

(a)

(b)

Fig. 1.13: (a) Cutting force (Fz) and Feed force (Fy) vs effective copper content and tin content, for the studied alloys of the Cu–Zn–Sn system, (b) Cutting force (Fz) and Feed force (Fy) vs. effective copper content and aluminium content, for the studied alloys of the Cu–Zn–Al system [44].

Gaitonde et al. employed Artificial Neural Networks (ANN) to study the effect of cutting speed, feed rate and different amount of minimum quantity of lubrication (MQL) on two aspects of machinability, namely, specific cutting force and surface roughness in turning of CuZn39Pb3 brass using a K10 carbide tool [45]. In their study, a multilayer feed forward ANN was employed trained by EBPTA (Error-Back Propagation-Training Algorithm). The training patterns required for input-output database were obtained through turning experiments conducted as per Full Factorial Design (FFD). 3D surface plots were generated to analyze the interaction effects of process parameters and the following conclusions were drawn from the present investigation: i) the minimum specific cutting force existed at high MQL (160–170 ml/h) with medium range of cutting speed (210–220 m/min), ii) the specific cutting force was also found to be minimal at a higher feed rate (0.20 mm/rev) with a low MQL (100 ml/h), iii) the specific cutting force was highly sensitive to feed rate variations for all values of MQL, iv) the minimum surface roughness resulted in high MQL (160–180 ml/h) with low cutting speed values and v) the surface roughness sharply increased with increasing feed rate irrespective of MQL [45].

Taha et al. investigated the machinability based on surface quality and cutting forces in lead-free silicon brass alloys [40]. In this work, the machinability based on machined surface quality was evaluated by measuring the machined average surface roughness (Ra) at selected cutting conditions using H20 and H123 tools. The results are shown in Figure 1.14a for Ra versus depth of cut keeping the feed and speed at 0.08 mm/rev and 104 m/min respectively. The effect of cutting feed and cutting speed on Ra is illustrated in Figure 1.14b and c respectively. As can be seen, for all Si brass alloys investigated, Ra was almost independent of depth of cut, while Ra increased as the cutting feed increased and gradually decreased as speed increased. Minimum values of Ra were observed for leaded brass, followed by (1% Si.) and (2% Si.) alloys, and finally the leaded brass C37700.

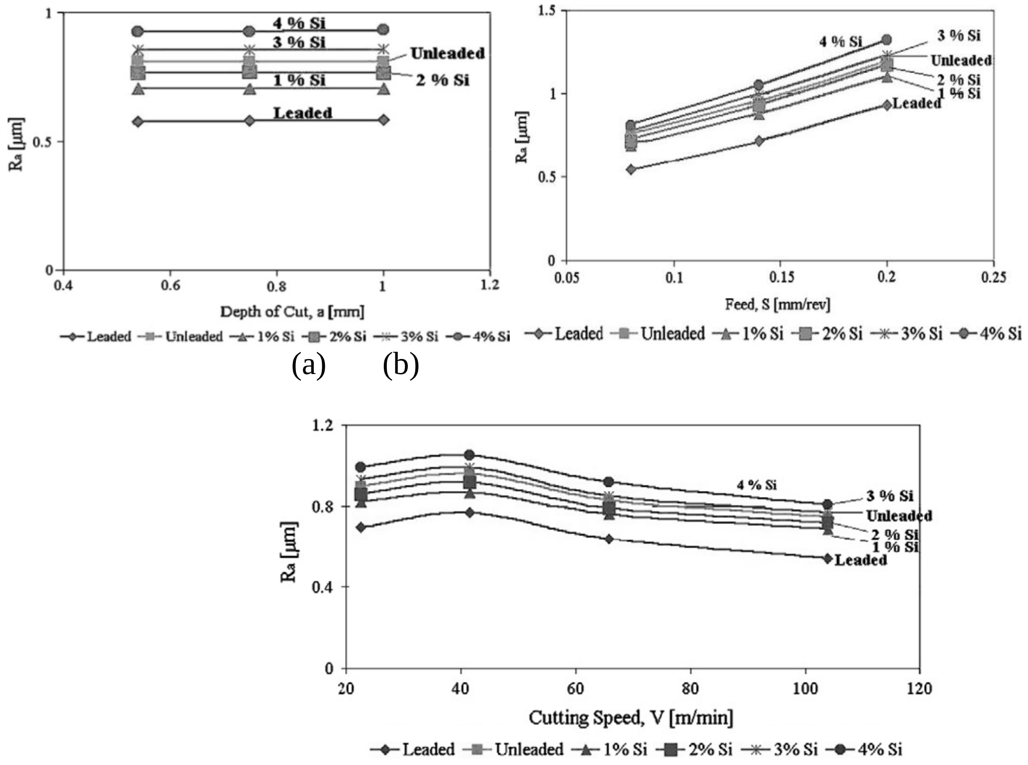

(a) (b)

(c)

Fig. 1.14: Variation of average machined surface roughness ‘‘Ra’’ of cast Pb-free Si brass alloys (Si up to 4 wt %) with (a) depth of cut, (b) feed of cut and (c) cutting speed [40].

Even higher Ra values were observed for (3% Si.) and (4% Si.) alloys [40]. The Ra was found to increase by 40% as the silicon content increased from 1 wt% to 4 wt% Si. For all leaded and unleaded alloys, cutting forces were proportional to the depth of cut. Figure 1.15a shows the linear incremental relationship between the cutting force and the cutting feed [40].

In both cases, the machining behavior was attributed to increased resistance of chip formation as a result of the increase of the volume of the material removal.

Figure 1.15b indicates that the cutting force increased with increasing cutting speed up to a maximum at 50 m/min. This was attributed to the increase of friction on the tool face caused by the chip flow. Further increase in speed led to the decrease in cutting force, which was attributed to the increase of the cutting temperature at high speeds, which in its turn resulted in the decrease of the friction forces and shear strength of the material due to thermally induced softening. Moreover, leaded brass exhibited the lowest cutting force value due to the reduction of the coefficient of friction between the chip and the tool face caused by the lubricating effect of lead. The maximum cutting force was measured for 1% Si and was attributed to the highest alloy strength [40].

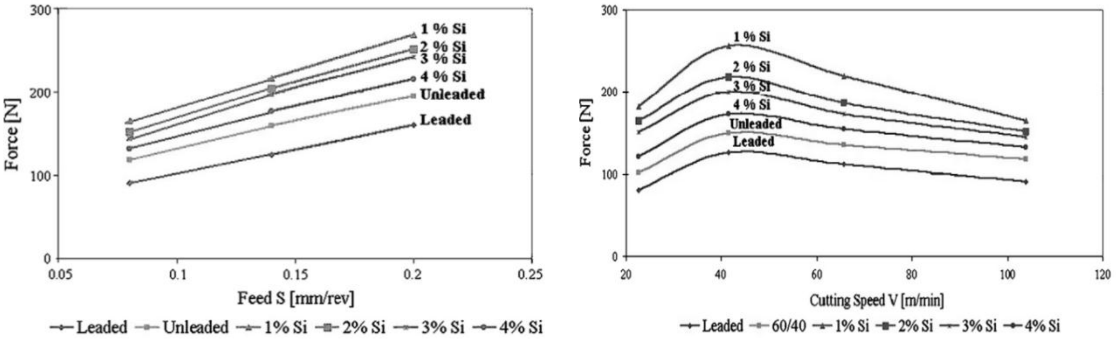

(a) (b)

Fig. 1.15: (a) Effect of cutting feed on the cutting force for the cast Pb-free Si brass alloys with different Si content up to 4 wt% (constant depth of cut of 0.5 mm and cutting speed of 104 m/min) and (b) Effect of cutting speed on the cutting force for the cast Pb-free Si brass alloys with different Si content up to 4 wt% (constant depth of cut of 0.5 mm and feed of 0.08 mm/rev) [40].

Gaitonde et al. employed the Taguchi method to determine the optimal process parameters for simultaneously minimizing the surface roughness and specific cutting force during turning of CuZn39Pb3 brass with K10 carbide tool [46]. In this work the optimum amount of MQL and the most appropriate cutting speed and feed rate were determined using Analysis of Means (ANOM) and the relative significance of the parameters was identified through ANOVA. From their study the following conclusions were drawn: i) the ANOM on multi-response S/N ratio indicated that optimum MQL of 200 ml/h, cutting speed of 200 m/min and a feed rate of 0.05 mm/rev was necessary to simultaneously minimize surface roughness and specific cutting force, ii) the ANOVA illustrated that feed rate was the most dominant parameter followed by MQL and cutting speed in optimizing the machinability characteristics, iii) the ANOVA also showed that the error contribution was 0.55%, which clearly indicated the absence of the interaction effects of process parameters on optimization of multiple performance characteristics and iv) the validation experiment confirmed that the additive model was adequate for determining the optimum quality characteristics at 95% confidence interval.

1.3. References

[1] H. Imai, Y. Kosaka, A. Kojima, S. Li, K. Kondoh, J. Umeda, H. Atsumi (2010) Characteristics and machinability of lead-free P/M Cu60–Zn40 brass alloys dispersed with graphite. Powder Technology 198: 417-421.

[2] A. La Fontaine, V.J. Keast (2006) Compositional distributions in classical and lead-free brasses. Materials Characterization 57: 424-429.

[3] G. Pantazopoulos (2002) Leaded brass rods C 38500 for automatic machining operations: A technical report. Journal of Materials Engineering and Performance 11: 402-407.

[4] S. Li, K. Kondoh, H. Imai, H. Atsumi (2011) Fabrication and properties of lead-free machinable brass with Ti additive by powder metallurgy. Powder Technology 205: 242-249.

[5] F. Schultheiss, C. Windmark, S. Sjöstrand, M. Rasmusson, J.E. Ståhl (2018) Machinability and manufacturing cost in low-lead brass. International Journal of Advanced Manufacturing Technology 99: 2101-2110.

[6] G. Pantazopoulos, A. Vazdirvanidis (2008) Characterization of the microstructural aspects of machinable α-β phase brass. Microscopy and Analysis 22: 13-16.

[7] D. B. Naik, A. K. Dave (1998) Multipass, multicriterion optimisation in turning. International Journal of Advanced Manufacturing Technology 14: 544-548.

[8] G.J. Besseris (2010) Non-linear nonparametric quality screening in low sampling testing, International Journal of Quality and Reliability Management 27: 893-915.

[9] G.J. Besseris (2010) A methodology for product reliability enhancement via saturated-unreplicated fractional factorial designs. Reliability Engineering and System Safety 95: 742-749.

[10] M. Arvidssson, I. Gremyr (2008) Principles of robust design methodology. Quality and Reliability Engineering International 24: 23-35.

[11] A. Manna, B. Bhattacharyya (2006) Taguchi and Gauss elimination method: A dual response approach for parametric optimization of CNC wire cut EDM of PRAlSiCMMC. International Journal of Advanced Manufacturing Technology 28: 67-75.

[12] L. Ilzarbe, M. J. Álvarez, E. Viles and M. Tanco (2008) Practical applications of design of experiments in the field of engineering: a bibliographical review. Quality and Reliability Engineering International 24: 417-428.

[13] E. Viles, M. Tanco, L. Ilzarbe, M.J. Alvarez (2009) Planning experiments, the first real task in reaching a goal. Quality Engineering 21: 44-51.

[14] M. Tanco, E. Viles, L. Ilzarbe, M.J. Alvarez (2009) Barriers faced by engineers when applying design of experiments. The TQM Journal 21: 565-575.

[15] M. Tanco, E. Viles, L. Ilzarbe, M.J. Alvarez (2009) Implementation of design of experiments projects in industry. Applied Stochastic Models in Business and Industry 25: 478-505.

[16] G. Pantazopoulos, A. Vazdirvanidis (2008) Failure analysis of a fractured leaded-brass (CuZn39Pb3) extruded hexagonal rod. Journal of Failure Analysis and Prevention 8: 218-222.

[17] A.I. Toulfatzis, G.J. Besseris, G.A. Pantazopoulos and C. Stergiou (2011) Characterization and comparative machinability investigation of extruded and drawn copper alloys using non-parametric multi-response optimization and orthogonal arrays. International Journal of Advanced Manufacturing Technology 57: 811-826.

[18] P. Garcia, S. Rivera, M. Palacios and J. Belzunce (2010) Comparative study of the parameters influencing the machinability of leaded brasses. Engineering Failure Analysis 17: 771-776.

[19] K. Holler, B. Reetz, K.B. Müller, A. Pyzalla and W. Reimers (2003) Microstructure and properties of hot extruded brass CuZn40Pb2. Materials Science Forum 426-432: 3667-3672.

[20] T. Chandra, J.J. Jonas, D.M.R. Taplin (1978) Grain-boundary sliding and intergranular cavitation during superplastic deformation of α/β brass. Journal of Materials Sciences 13: 2380-2384.

[21] H. Atsumi, H. Imai, S. Li, K. Kondoh, Y. Kousaka, A. Kojima (2012) Fabrication and properties of high-strength extruded brass using elemental mixture of Cu-40% Zn alloy powder and Mg particle. Materials Chemistry and Physics 135: 554-562.

[22] H. Atsumi, H. Imai, S. Li, K. Kondoh, Y. Kousaka, A. Kojima (2011) The effect of solid solutionizing Ti element on microstructural and mechanical properties of extruded Cu-40Zn-Ti ternary alloy. Transactions of JWRI 40: 67-71.

[23] N. Hentati, A. Makni, R. Elleuch (2012) Study of failure modes affecting a crimped nut related to forging process. Journal of Failure Analysis and Prevention 12: 130-138.

[24] L. Blaz, Z. Konior, T. Majda (2001) Structural aspects of α/β transformation in hot deformed CuZn-39Pb3 alloy. Journal of Materials Science 36: 3629-3635.

[25] G.A. Pantazopoulos, A.I. Toulfatzis (2012) Fracture modes and mechanical characteristics of machinable brass rods. Metallography, Microstructure and Analysis 1: 106-114.

[26] Z. QuanLi, W. WeiDong, L. KaiZhou, C. GengChun and C. WeiPing (2009) Study on microstructure and properties of brass containing Sb and Mg. Science in China Series E: Technological Sciences 52: 2172-2174.

[27] S. Li, H. Imai, H. Atsumi, K. Kondoh, A. Kojima, Y. Kousaka, K. Yamamoto, M. Takahashi (2012) The effects of Ti and Sn alloying elements on precipitation strengthened Cu40Zn brass using powder metallurgy and hot extrusion. Materials Science and Engineering A 535: 22-31.

[28] T. Chandra, J.J. Jonas, D.M.R Taplin (1976) The mechanical behavior of cerium-modified alpha-beta brass at high temperatures. Journal of Materials Science 11: 1843-1848.

[29] H. Atsumi, H. Imai, S. Li, K. Kondoh, Y. Kousaka, A. Kojima (2011) High-strength, lead-free machinable α-β duplex phase brass Cu–40Zn–Cr–Fe–Sn–Bi alloys. Materials Science and Engineering A 529: 275-281.

[30] A.I. Toulfatzis. G.A. Pantazopoulos and A.S. Paipetis (2014) Fracture behavior and characterization of lead-free brass alloys for machining applications. Journal of Materials Engineering and Performance 23: 3193-3206.

[31] ISO 3685: Tool-life testing with single-point turning tools. International Organization for Standardization (ISO), (1993).

[32] N. Gane (1981) The effect of lead on the friction and machining of brass. Philosophical Magazine A 43: 545-566.

[33] K. Hassan, A. Kumar, M.P. Garg (2012) Experimental investigation of material removal rate in CNC turning using Taguchi method. International Journal of Engineering Research and Applications 2: 1581-1590.

[34] H. Doostmohammadi, H. Moridshahi (2015) Effect of Si on microstructure, ordering transformation and properties of the Cu60Zn40 alloy. Journal of Alloys and Compounds 640: 401-407.

[35] Z. Rajabi, H. Doostmohammadi (2018) Effect of addition of tin on the microstructure and machinability of α-brass. Materials Science and Technology 34: 1218-1227.

[36] P. Suksongkarm, S. Rojananan, S. Rojananan (2017) Using recycled bismuth-tin solder in novel machinable lead-free brass. Materials Transactions 58: 1754-1760.

[37] C. Nobel, U. Hofmann, F. Klocke, D. Veselovac (2016) Experimental investigation of chip formation, flow, and breakage in free orthogonal cutting of copper-zinc alloys. International Journal of Advanced Manufacturing Technology 84: 1127-1140.

[38] F. Klocke, C. Nobel, D. Veselovac (2016) Influence of tool coating, tool material, and cutting speed on the machinability of low-leaded brass alloys in turning. Materials and Manufacturing Processes 31: 1895-1903.

[39] F. Schultheiss, D. Johansson, V. Bushlya, J. Zhou, K. Nilsson, J.E. Ståhl (2017) Comparative study on the machinability of lead-free brass. Journal of Cleaner Production 149: 366-377.

[40] M.A. Taha, N.A. El-Mahallawy, R.M. Hammouda, T.M. Moussa, M.H. Gheith (2012) Machinability characteristics of lead free-silicon brass alloys as correlated with microstructure and mechanical properties. Ain Shams Engineering Journal 3: 383-392.

[41] Nobel. C, Klocke. F, Lung. D, Wolf. S (2014) Machinability enhancement of lead-free brass alloys. 6th CIRP International Conference on High Performance Cutting: 95-100.

[42] S.VA Laakso, M. Hokka, E. Niemi and V-T. Kuokkala (2013) Investigation of the effect of different cutting parameters on chip formation of low-lead brass with experiments and simulations. Proc IMechE Part B: Journal of Engineering Manufacture 227 (11): 1620-1634.

[43] C. Yang, Z. Ding, Q.C. Tao, L. Liang, Y.F. Ding, W,W. Zhang, Q.L. Zhu (2018) High-strength and free-cutting silicon brasses designed via the zinc equivalent rule. Materials Science and Engineering A 723: 296-305.

[44] C. Vilarinho, J.P. Davim, D. Soares, F. Castro, J. Barbosa (2005) Influence of the chemical composition on the machinability of brasses. Journal of Materials Processing Technology 170: 441-447.

[45] V.N. Gaitonde, S.R. Karnik, J. P. Davim (2010) Study on the influence of MQL and cutting conditions on machinability of brass using Artificial Neural Network. International Journal of Materials and Product Technology 3: 155-172.

[46] V.N. Gaitonde, S.R. Karnik, J. P. Davim (2008) Selection of optimal MQL and cutting conditions for enhancing machinability in turning of brass. Journal of Materials Processing Technology 204: 459-464.

Chapter 2: Characterization of Microstructure and Mechanical Properties of Lead-Free Brass Alloys

2.1. Summary

Brass rods constitute an attractive class of engineering materials with a wide spectrum of applications. This is due to their satisfactory mechanical strength, high workability and superior corrosion and wear resistance. Machinable brass rods are used for the production of a broad range of products, such as bolts, nuts, electrical connectors, valve bodies, and hydraulic fittings. The machinability of those materials is a function of a complex combination of material parameters, such as phase and microstructure, second phase particle size and distribution and how these interact to define the macroscopical mechanical behaviour of the alloy. Improved machinability minimizes tool wear and allows the production of high precision components with superior surface finish. The interrelation of machinability/microstructure of typical brass alloys and their effect on mechanical properties has been assessed in previous research works [1-4].

The forthcoming application of environmental and health/safety regulations regarding the restriction of lead usage, instigates the development of eco-friendly lead-free brass alloys for the manufacturing of machine components (fluid distribution system, common machinery components, etc.). The study of these eco-friendly alloys as candidate materials for the substitution of conventional leaded brasses poses challenges which relate both to machinability and component reliability. For high risk applications in particular (e.g., tank valve components, adaptors for gas supply systems, etc), critical component failure may compromise the entire system.

The absence of lead is expected to substantially increase the ductility of the alloy, with the subsequent deterioration of its machinability. On the other hand, the control of the microstructure of brass alloys may be employed for the tailoring of the fracture behaviour towards the achievement of similar properties to leaded alloys [5]. The goal of this study is to study the performance of lead-free brasses as candidate replacement materials to conventional leaded brass alloys. This is driven by the demand coming from environmental regulations and industrial market sectors for new classes of machinable copper alloys, without the addition of Pb or other harmful elements. These new alloys should exhibit equivalent (i) machinability

for high productivity and (ii) performance for reliability and safety to their leaded counter parts. To this end, the interconnection of microstructural, mechanical and fracture results of lead-free brass rods was studied. Emphasis was placed on the mechanical behaviour under quasi-static and dynamic loading and its relation to microstructure with a view to identifying the dominant failure mechanisms of lead-free brass alloys.

Three lead-free brass rods (CW510L – CW511L – C27450) and a common leaded brass rod (CW614N), as a reference material, were examined. Quasi-static tensile, impact, as well as Crack Tip Opening Displacement (CTOD) tests were performed. CW510L which contains 60% β-phase, exhibited higher tensile strength (460 MPa) and slightly lower total elongation (41%) compared to CW511L (380 MPa, 42%) and C27450 (320 MPa, 48%). CW511L and C27450 exhibited the least percentages of β-phase volume percentage (5 and 2 %, respectively). Moreover, Charpy impact test and the critical CTOD values increased according to the following alloy order: CW614N (9 J and 0.02 mm respectively) < CW510L (47 J and 0.32 mm respectively) < CW511L (104 J and 0.71 mm respectively) < C27450 (109 J, CTOD measurement was not feasible).

Finally, the main fracture mechanisms and their relation to microstructure were assessed using Scanning Electron Microscopy (SEM). Dimpled ductile fracture was the dominant failure mechanism under impact loading for all tested brass alloys. However, the dimple size and distribution varied among the tested alloys suggesting different amounts of plastic deformation prior to impact failure. The impact fracture surfaces of CW614N leaded brass revealed the shallowest and finest shear dimples compared to lead-free brass alloys, while the largest and deepest dimples were observed in the case of CW511L and C27450 brass alloys which absorbed the highest impact energy.

All tensile, impact, and CTOD fracture toughness tests indicated that the CW510L lead-free brass alloy possessed a good combination of tensile strength and fracture toughness, similar to that of the conventional CW614N leaded brass. This suggests that CW510L lead-free brass is a strong candidate for the replacement of commonly used leaded brasses such as CW614N, combining high tensile strength and fracture toughness, due to the prevalence of the β-intermetallic phase in the alloy microstructure.

2.2. Microstructure

The chemical composition of the studied alloys has a major influence on microstructure, machinability and mechanical properties. More specifically, CW510L is the corresponding alloy to the existing CW614N, albeit without lead. The machinability of CW510L alloy is lower than that of CW614N alloy, but the high copper content guarantees an acceptable level of workability. CW511L is the corresponding lead-free alloy to the existing dezincification resistant leaded brass alloy CW602N. Due to relatively high copper content, the machinability of CW511L is lower than that of the CW602N. CW511L is widely used in applications which are in contact with drinking water; due to its higher Cu content, C27450 alloy has inferior machinability but higher cold workability in relation to CW510L and CW511L alloys. Metallographic evaluation showed that the phase structure of the brass alloys consisted of a mixture of α+β phases, as is typical for the Cu-Zn alloy system (Fig. 2.1).

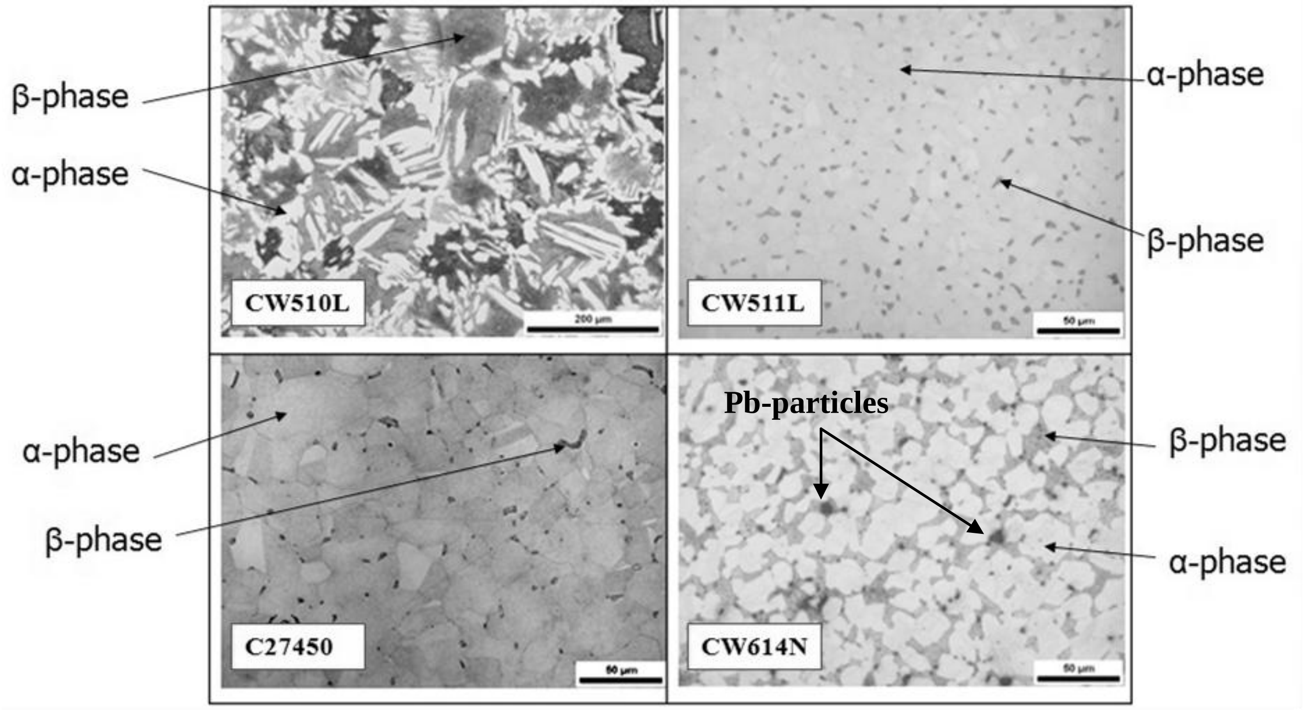

Fig. 2.1: Optical micrographs on longitudinal sections of studied lead-free and leaded brasses. Light areas represent α-phase and dark areas represent β-phase.

The α-phase is a Cu-Zn solid solution with a face-centered-cubic crystal lattice, which exhibits high cold workability. The β-phase is the ordered non-stoichiometric intermetallic compound CuZn which possesses a body-centered-cubic (bcc) lattice. As is well established [6], the presence of β-phase improves hot workability of brass alloys and at the same time contributes to its quasi-static strength.

More specifically, in binary Cu-Zn alloy systems, β-phase volume percentage is mainly controlled by Zn content and thermomechanical processing. As is expected under industrial manufacturing process conditions, β-phase percentage presented an incremental tendency with Zn content (Fig. 2.2). The higher volume percentage of the β-phase was attributed to non-equilibrium process conditions during cooling, which retarded diffusion processes and therefore favored β-phase to α-phase formation. Consequently, CuZn42 (CW510L) with 60% β-phase and CuZn39Pb3 (CW614N) with 33% β-phase exhibited higher strength, hardness and lower total elongation compared to CuZn38As (CW511L) and CuZn36 (C27450). As shown in Figure 2.2, CuZn38As (CW511L) and CuZn36 (C27450) exhibited the least percentages of β-phase volume percentage (5 and 2%, respectively). Together with the variation of β-phase volume percentage, a difference in phase morphology was also evident. In the case of CuZn42 (CW510L), a characteristic Widmanstätten structure consisting of α-intersecting acicular crystals in β-phase matrix was identified. A similar but coarser structure was observed in as-cast leaded brass alloys [2].

The presence of this morphology is typical for high-Zn brass alloys which have been subjected to relatively fast cooling from the β-phase domain. Hot extrudability is satisfactory in the β-phase field, hot work being usually followed by rapid cooling. This results in intra- and intergranular precipitation of α-phase crystals, once the β/α+β boundary is surpassed. High undercooling conditions lead to massive α-phase nucleation rates. However, growth kinetics is hindered by slow diffusion rates under at low temperatures. Figure 2.2 depicts the results for the β-phase volume percentage, as calculated by image analysis. CuZn42 (CW510L) contained significantly higher percentage of β-phase compared to the other alloys, mainly due to its higher Zn content.

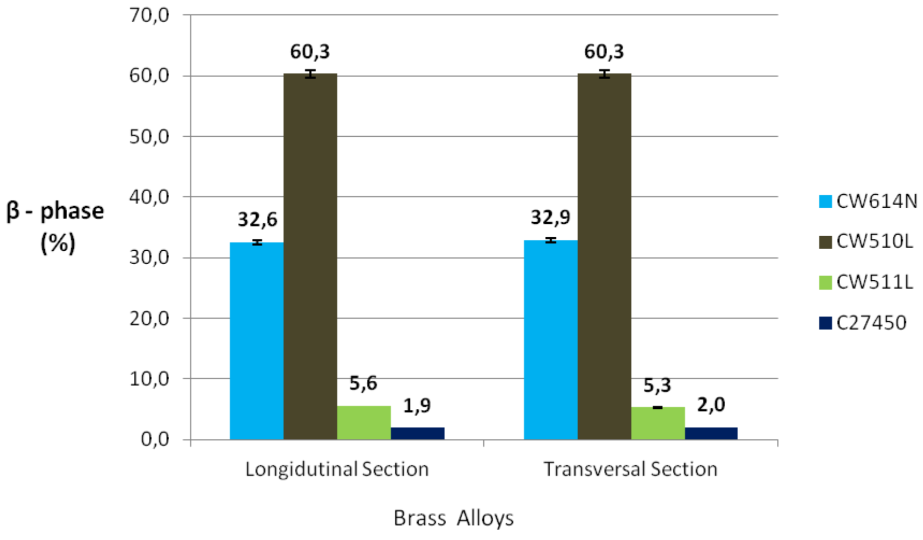

Fig. 2.2: β-phase volume percentage for each of the studied alloys.

2.3. Hardness and Tensile Properties

In Figures 2.3 to 2.5, the hardness and tensile properties of the studied alloys are presented. The tensile stress-strain curves (σ-ε) are presented in Figure 2.4. More specifically, CuZn42 (CW510L) and CuZn39Pb3 (CW614N) brasses exhibited higher yield strength and ultimate tensile strength but lower uniform elongation (A_g) and total elongation (A_{50}) as compared to CuZn38As (CW511L) and CuZn36 (C27450) brass (Fig. 2.5). CW510L lead-free brass alloy exhibited the highest ultimate tensile strength R_m (460 MPa). Lead-free CW510L brass alloy presented almost equal 0.2% yield strength ($R_{p0.2}$) to CW511L (250 MPa), higher than C27450 (185 MPa) and lower than leaded CW614N (300 MPa).

Finally, lead-free CW510L brass alloy showed slightly lower total elongation A_{50} (41%) compared to the other lead-free alloys, i.e. C27450 (48%) and CW511L (42%), but significantly higher compared to the leaded CW614N (28%). In all cases, a hardness gradient from surface to core was observed (Fig. 2.3). This was attributed to plastic deformation processing (especially cold drawing), which resulted in non-uniform work hardening.

As can be seen, Vickers hardness is considerably higher for CuZn42 (CW510L) and CuZn39Pb3 (CW614N) compared to CuZn38As (CW511L) and CuZn36 (C27450). Lead-free CW510L brass exhibited the highest average hardness among lead-free brasses (CW511L and C27450), almost equal to the leaded CW614N brass (Fig. 2.3). Hardness and tensile properties were within the typical range of half hard temper brass rods (extruded and lightly cold drawn). In the case of CuZn39Pb3 (CW614N) leaded brass alloy, the Pb distribution in α/β phase boundaries led to the minimization of grain boundary energy and consequently to premature ductility loss.

This was also suggested by the total elongation values of CuZn39Pb3-CW614N (28%) compared to CuZn42-CW510L (41%). Pb particles acted as microvoid nucleation sites which promoted void growth and coalescence and therefore reduced the overall plastic deformation (Fig. 2.5b).

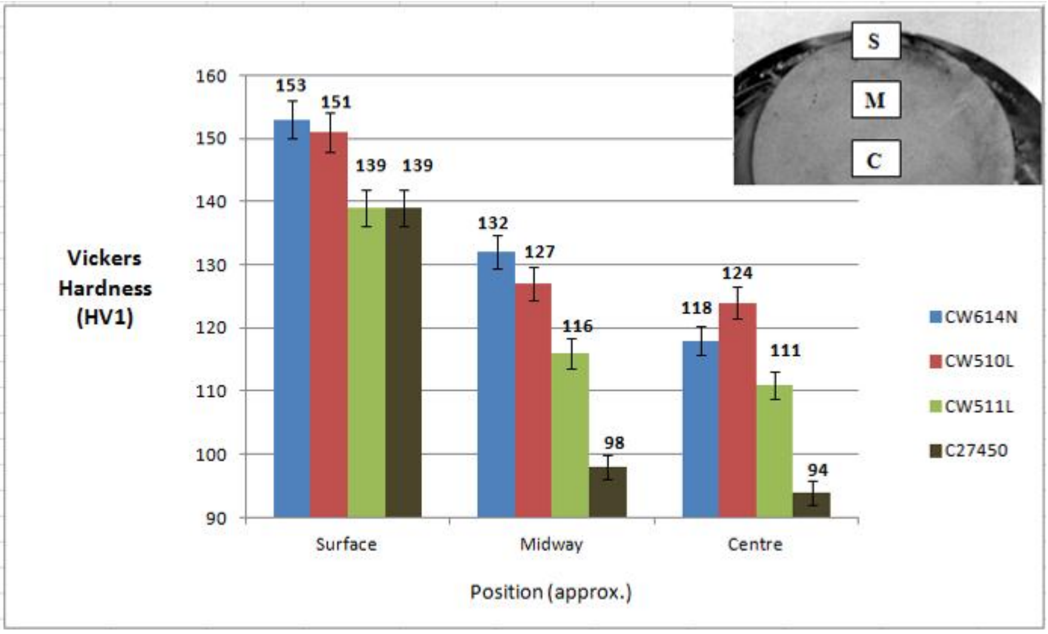

Fig. 2.3: Vickers hardness in surface, midway and centre of the studied alloys. Average values of three (3) specimens for each sample.

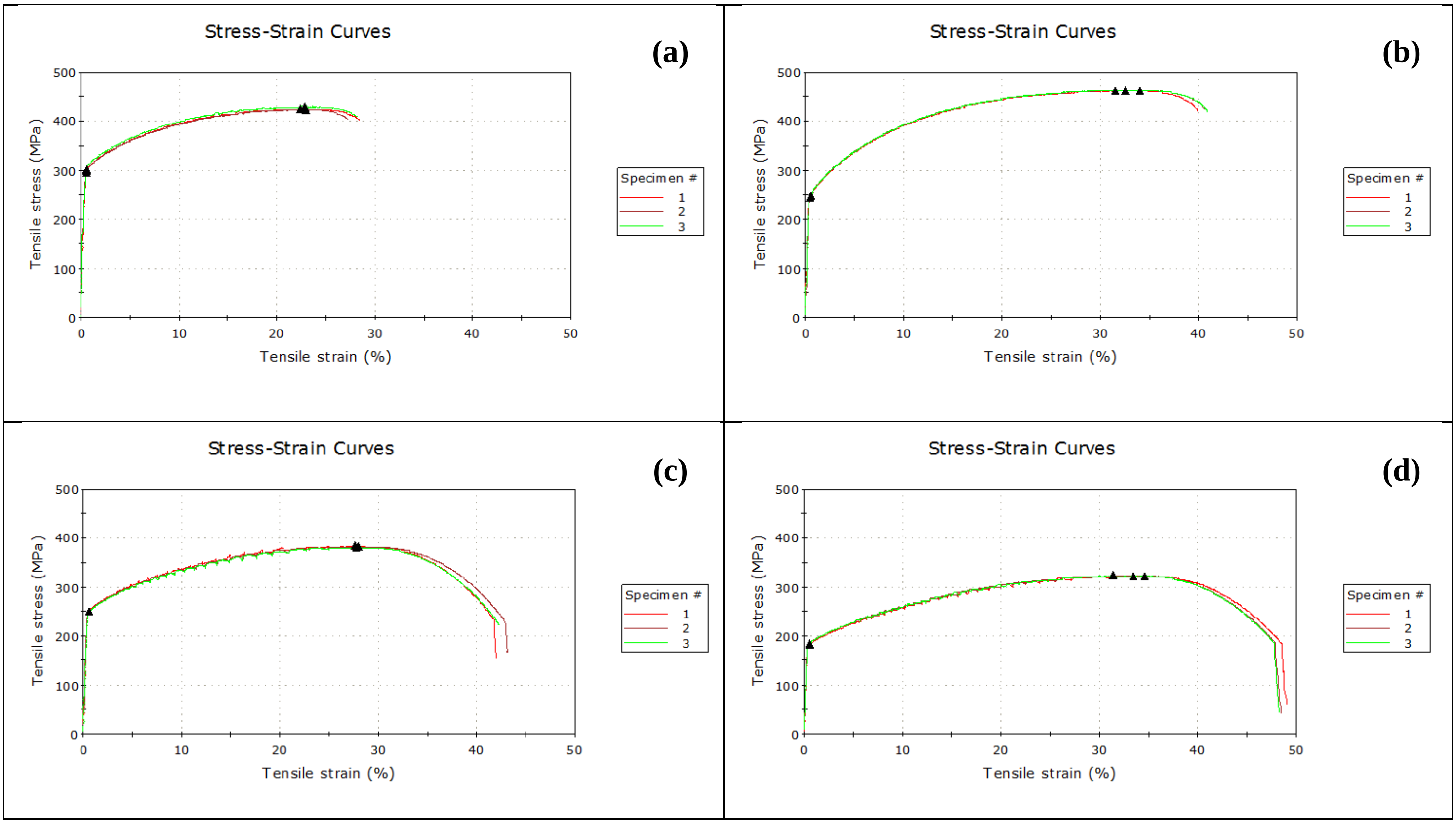

Fig. 2.4: Stress-strain curves for all studied alloys: (a) CW614N, (b) CW510L, (c) CW511L and (d) C27450, midway and centre of the studied alloys. Average values of three (3) specimens for each sample.

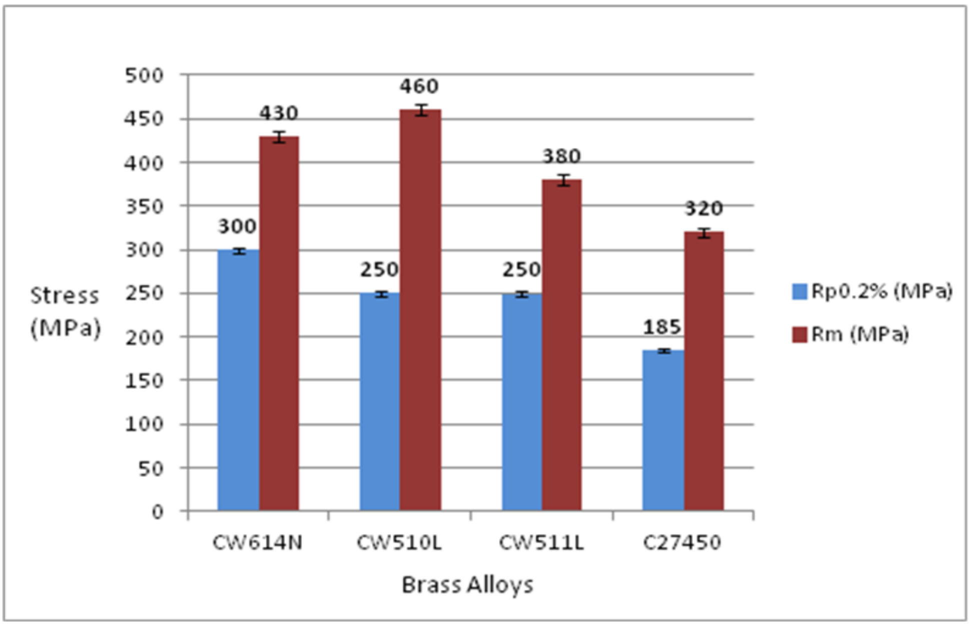

(a)

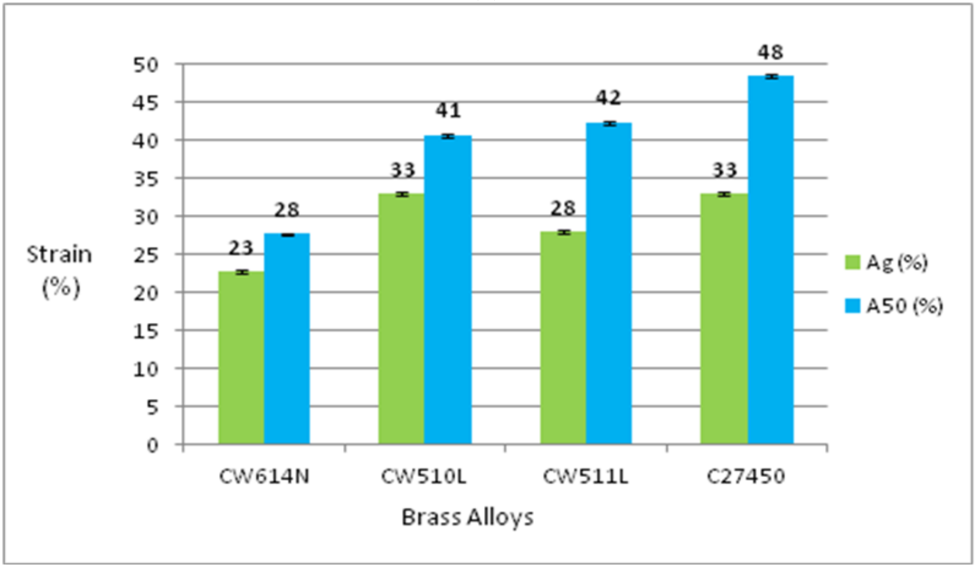

(b)

Fig. 2.5: Properties measured in tensile tests for each of the alloys under study: (a) proof stress, $Rp_{0.2}$; tensile strength, R_m, (b) uniform elongation, A_g; and fracture elongation, A_{50}. Average values of three (3) specimens for each sample.

In Figures 2.6 and 2.7, macroscopic images of side and top views of the tensile fractures are shown. These indicate the difference in area reduction exhibited by the studied alloys. As shown in Figure 2.8, the reduction of area (Z) was higher in C27450 (80%) and CW511L brass (70%) compared to CW510L (41%) and CW614N brass (32%). CuZn42 (CW510L) alloy showed the highest tensile strength/yield strength ratio ($R_m/R_{p0.2}$~1.8), indicating the highest work hardening potential among the tested brass alloys (Fig. 2.5a). This was consistent with the uniform elongation values (A_g) presented in Figure 2.5b. According to Considère’s criterion, for power law stress-strain relationships, the uniform true plastic strain is directly associated to the strain hardening exponent.

Thus, a threshold where the onset of plastic instability and necking initiates is established [7]. In metal working processes, high tensile strength/yield strength ratios ($R_m/R_{p0.2}$) are an indicator of workability safety, as extended uniform plastic deformation reduces the risk of fracture due to neck formation. The non-uniform elongation, which can be simply calculated by the difference A_{50}-A_g, increased according to the following alloy order: CW614N<CW510L<CW511L<C27450. This was also evident from the strain to failure (Fig. 2.5b) and stress-strain curves (Fig. 2.4). As expected, the identical alloy order was observed for reduction of area (Z), since post-uniform deformation corresponded to necking formation (Figs. 2.6-2.8).

Fig. 2.6: Optical stereomicrographs showing the side view of the tensile fracture surfaces of: (a) CuZn39Pb3 (CW614N) leaded brass as well as (b) CuZn42 (CW510L), (c) CuZn38As (CW511L) and (d) CuZn36 (C27450) lead-free brasses.

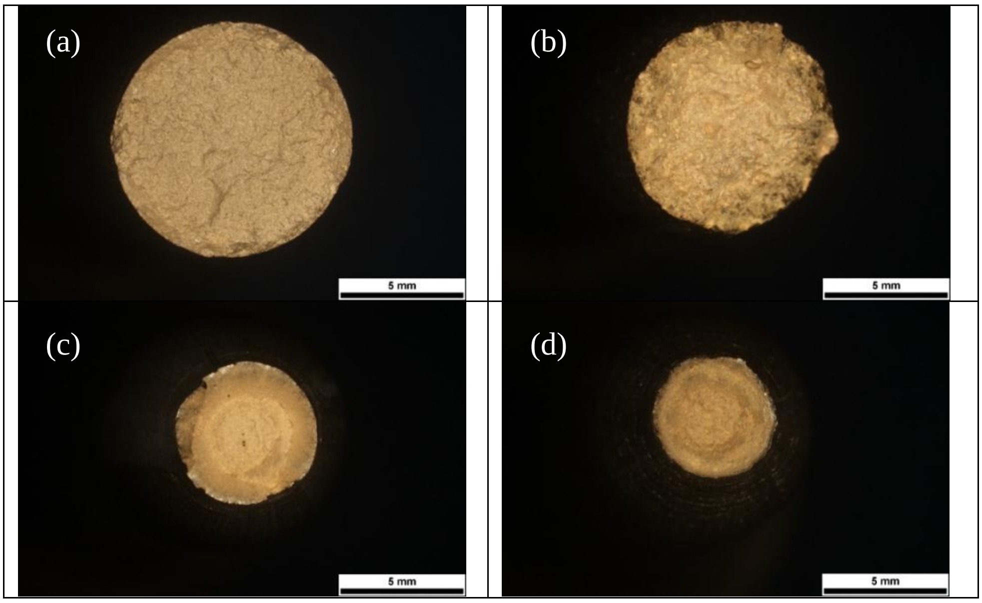

Fig. 2.7: Optical stereomicrographs showing the overall view of the fracture surfaces after the tensile test of (a) CuZn39Pb3 (CW614N) leaded brass as well as (b) CuZn42 (CW510L), (c) CuZn38As (CW511L) and (d) CuZn36 (C27450) lead-free brasses. Note the pronounced necking and reduction of area in the cases of CW511L and C27450 alloys.

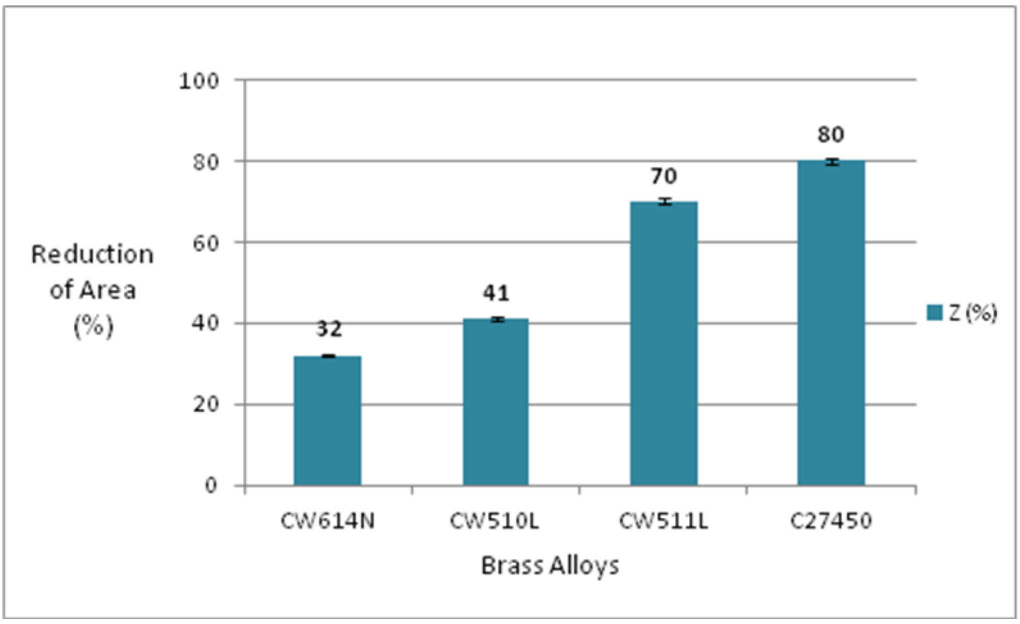

Fig. 2.8: Histogram showing the variation of area reduction in tensile specimens of the four studied alloys. Average values of three (3) specimens for each sample.

2.4. Impact Properties

The Charpy V-Notch at ambient temperature was employed for impact testing. The absorbed net energy results are presented in Figure 2.9. The impact toughness, expressed as absorbed net energy, decreased according to the following alloy order: C27450 > CW511L > CW510L > CW614N. The impact fracture surfaces are presented in Figure 2.10. High impact toughness was accompanied by significant shape distortion, demonstrated mainly by C27450 and CW511L alloys. As expected, these alloys exhibited higher energy absorption.

Together with impact energy, the percent of shear fracture and lateral expansion constitute common quantitative indicators of macroscopic fracture behaviour. Shear fracture percentage is related to the extent of the plastic deformation due to impact, while lateral expansion corresponds to the shape distortion expressed as the percentage of edge-size difference. The alloy order of the shear fracture and lateral expansion results coincided with the alloy order of impact toughness and shape distortion; measurements conducted on CW511L and C27450 fracture surfaces markedly exceeded the respective values obtained from CW510L and CW614N fractures (Fig. 2.11). CW511L and C27450 exhibited higher absorbed energy (104 J and 109 J, respectively) compared to those of CW510L and CW614N (47 J and 9 J, respectively).

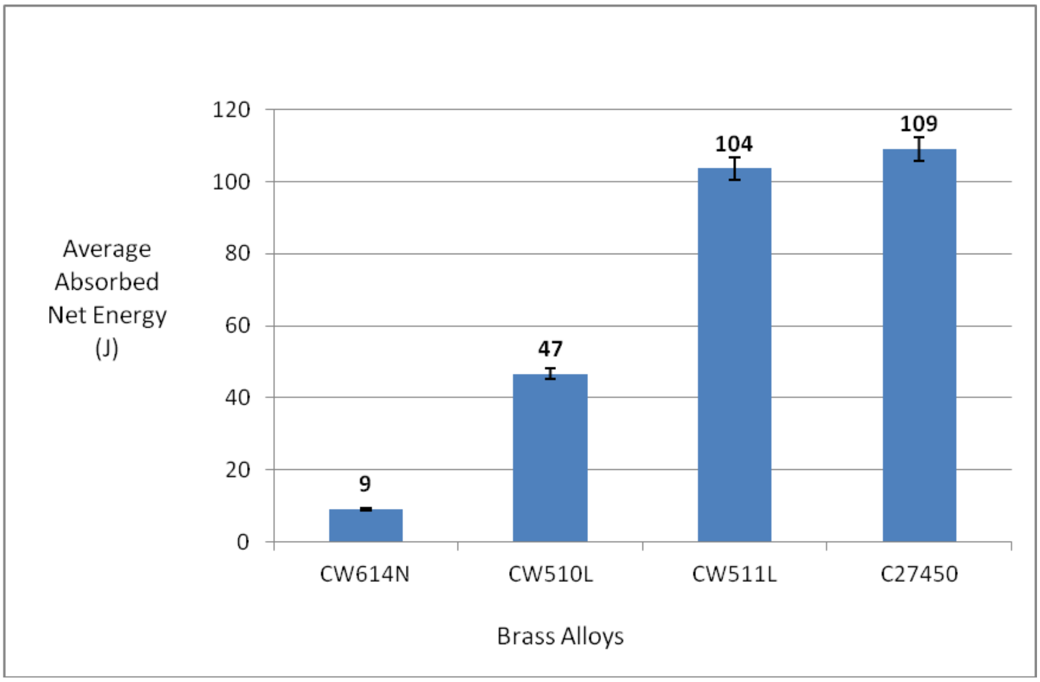

Fig. 2.9: Absorbed impact net energy results for lead-free CuZn42 (CW510L), CuZn38As (CW511L) and CuZn36 (C27450) lead-free brasses as well as for CuZn39Pb3 (CW614N) leaded brass. Average values of three (3) specimens for each sample.

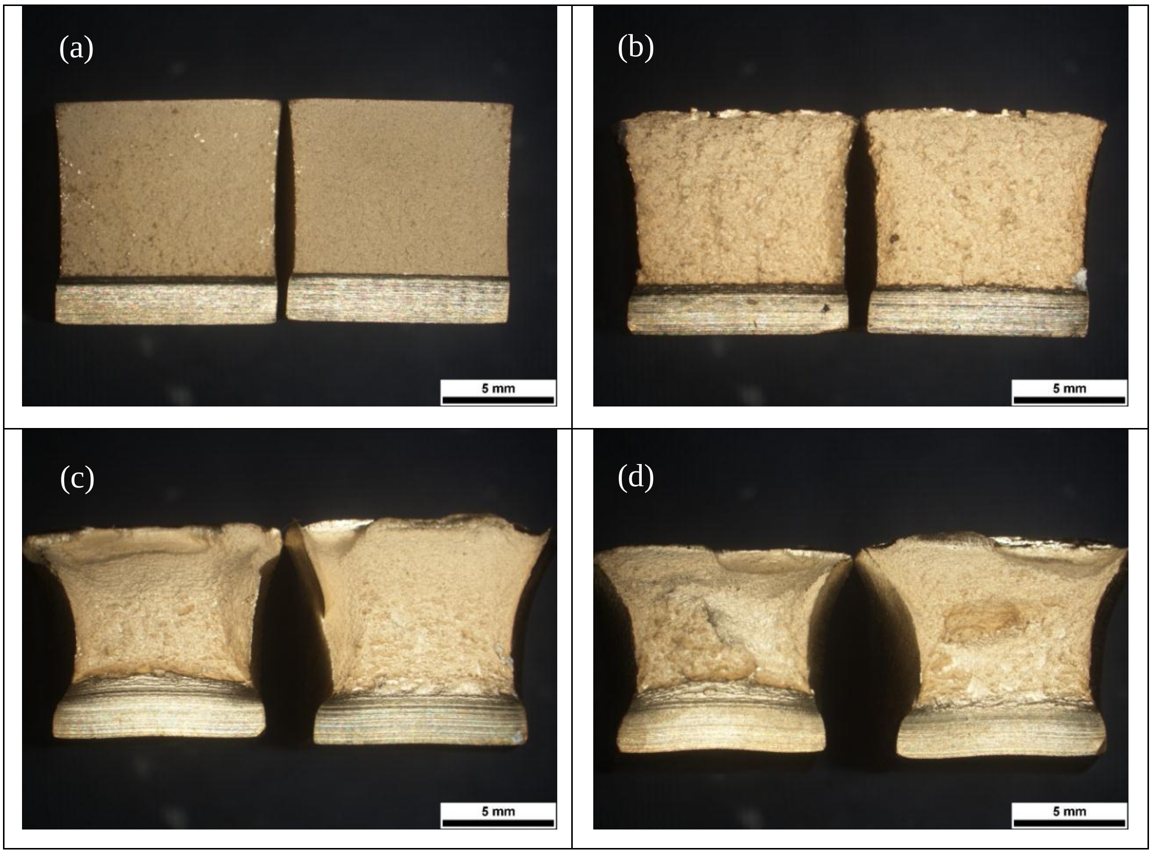

Fig. 2.10: Optical stereomicrographs showing the overall view of the fracture surfaces after the impact test of (a) CuZn39Pb3 (CW614N) leaded brass as well as (b) CuZn42 (CW510L), (c) CuZn38As (CW511L) and (d) CuZn36 (C27450) lead-free brasses.

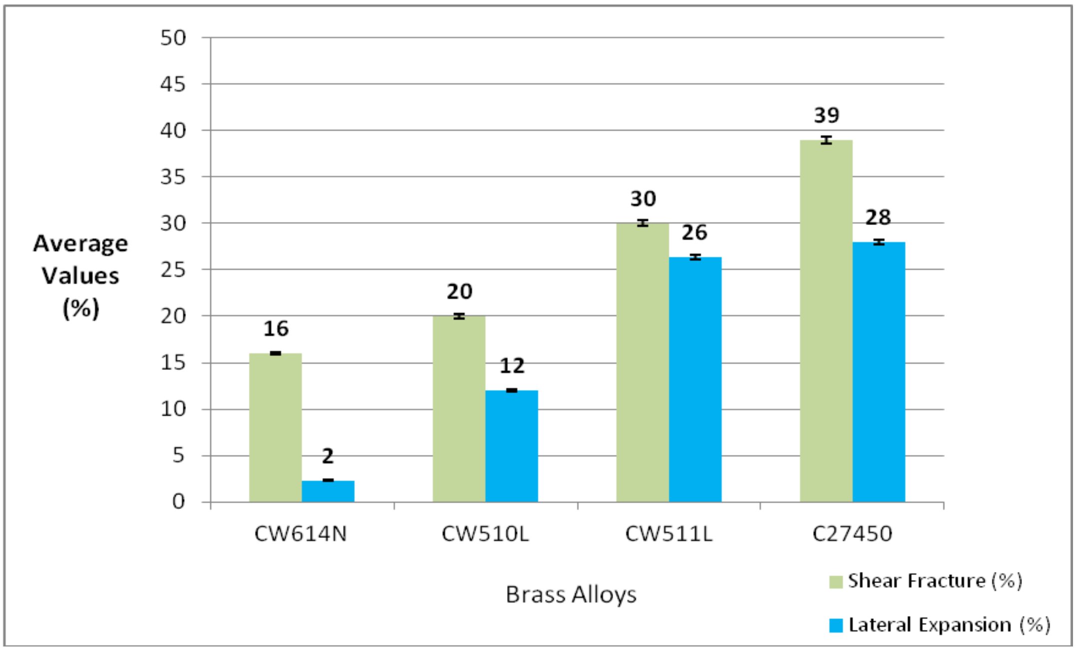

Fig. 2.11: Shear fracture and lateral expansion results for CuZn42 (CW510L), CuZn38As (CW511L), and CuZn36 (C27450) lead-free brasses as well as for CuZn39Pb3 (CW614N) leaded brass.

2.5. Fracture Toughness: CTOD Testing

CTOD tests, performed at room temperature, were employed to determine the critical crack length where unstable crack propagation occurs. The acquired load – displacement curves and the obtained CTOD values are presented in Figures 2.12 and 2.13, respectively. CTOD test fracture surfaces are shown in Figure 2.14. Crack length was a linear function of cycle number at the precracking stage. As expected, the constant crack growth rate was accompanied by constant stress intensity amplitude (ΔK) for the pre-cracking stage. In Figure 2.12, the load-extension curves correspond to the force evolution under monotonic loading as a function of crack “mouth” opening after the fatigue pre-cracking stage. Significant load increase vs. crack mouth opening suggested strain energy absorption ahead of the fatigue pre-crack tip and inherent resistance against unstable crack growth. Significant resistance to unstable crack growth was demonstrated by CW510L and CW511L brass alloys (Fig. 2.12b, c). Extensive load recovery was related to the retardation of the onset of unstable crack growth.

In the case of the ductile lead-free CuZn36 (C27450) brass, the high fracture resistance rendered the critical CTOD determination procedure invalid (Fig. 2.12d, 2.14d). Invalidities mainly stemmed from out-of plane crack extension and “exhaustive” plasticity phenomena which limited crack growth by continuous interaction and strain energy dissipation. This type of curve known as Type I, is typical for a wide range of ductile materials, where crack propagates under tearing mode with increasing force [7]. On the other hand, a sudden load drop until failure denotes fast and unstable crack growth.

This was observed in CW614N brass (Fig. 2.12a and 2.14a), where the generalized pop-in instability resulted in rapid crack propagation. This is commonly referred as a Type III curve and is typical of brittle materials. The above CTOD results were consistent with the results from the Charpy impact test and the critical CTOD values increased according to the following alloy order, see Figure 2.13: CW614N (0.02 mm) < CW510L (0.32 mm) < CW511L (0.71 mm). As aforementioned, the determination of a CTOD value for the ductile C27450 alloy was not feasible. The considerable plastic deformation until final fracture had a significant effect on the shape and geometry of the CTOD fracture. For all studied alloys, flat fracture surfaces corresponded to the initial fatigue pre-cracking stage, whereas deformed fracture textures developed during the secondary crack tearing process. This effect became more pronounced with increasing ductility (Fig. 2.14a-d).

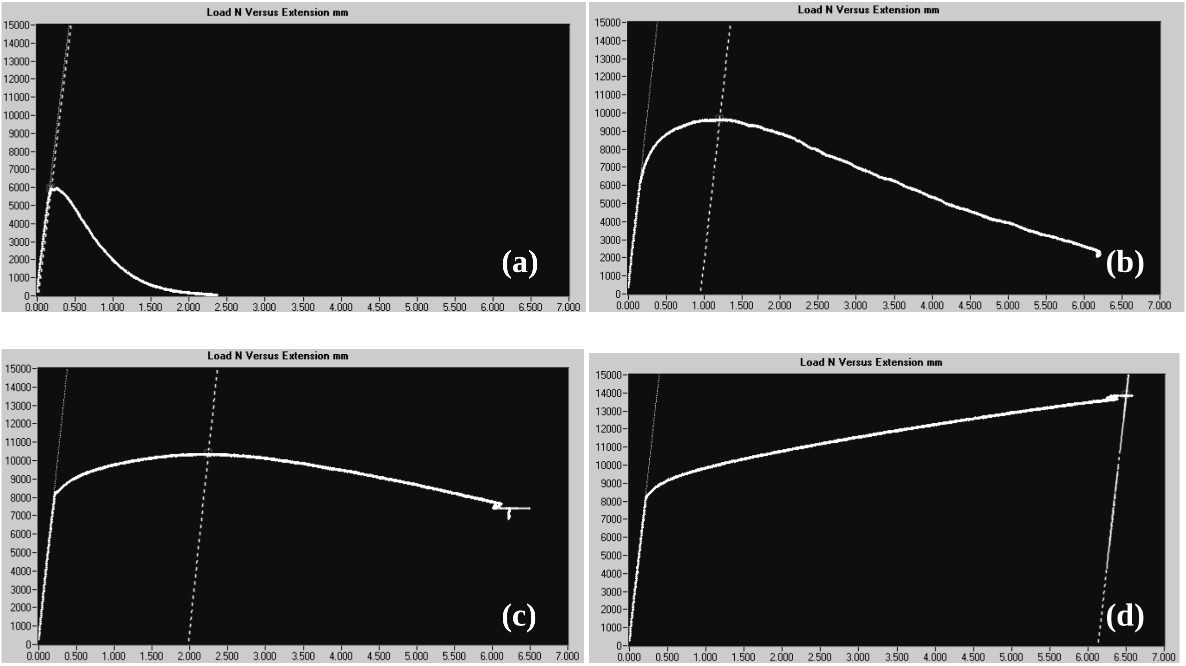

Fig. 2.12: Load (N)-extension (mm) graphs after CTOD test of (a) CuZn39Pb3 (CW614N) leaded brass as well as (b) CuZn42 (CW510L), (c) CuZn38As (CW511L) and (d) CuZn36 (C27450) lead-free brasses.

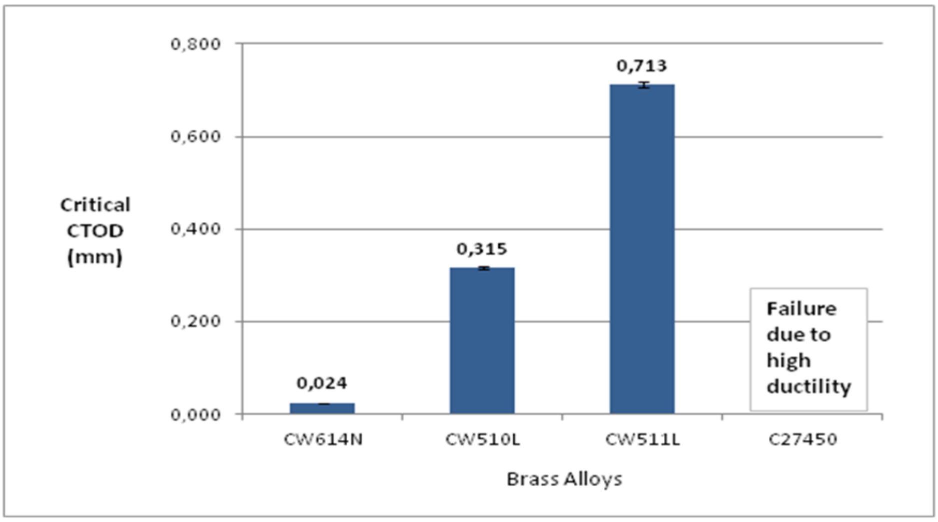

Fig. 2.13: Critical CTOD results for CuZn42 (CW510L), CuZn38As (CW511L) and CuZn36 (C27450) lead-free brasses as well as for CuZn39Pb3 (CW614N) leaded brass.

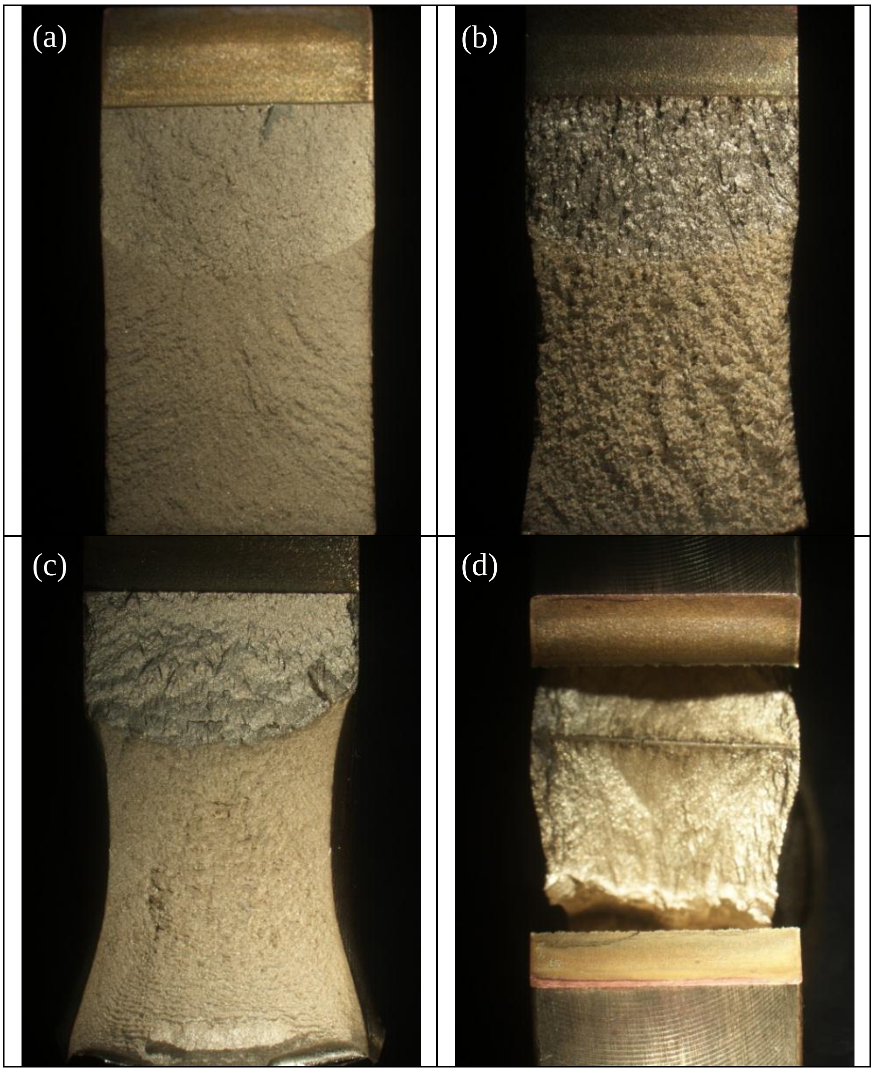

Fig. 2.14: Optical macrographs showing the overall view of the fracture surfaces after the CTOD test of (a) CuZn39Pb3 (CW614N) leaded brass as well as of (b) CuZn42 (CW510L), (c) CuZn38As (CW511L) and (d) CuZn36 (C27450) lead-free brasses.

2.6. SEM Fractographic Analysis

Scanning Electron Microscopy (SEM) under secondary and backscattered electron imaging was employed to study the impact fracture surfaces of all studied alloys. Dimpled fracture was the prevalent fracture mode for all the inspected fracture surfaces. However, dimple size and distribution was distinctly different among the tested alloys, suggesting that the amount of plastic deformation during impact was far from the same. More specifically, leaded brass (CW614N) exhibited the shallowest and finest shear dimples together with secondary intergranular and transgranular cracks which reduced the total absorbed energy (Figs. 2.15b and 2.16a). Some evidence of isolated transgranular fracture was observed (Fig. 2.16a). As is also reported in the literature [5], the presence of flat transgranular facets inhibited plastic deformation, reducing the impact energy.

The fracture surface of lead-free brass CW510L exhibited coarser and deeper shear dimples as well as higher plastic deformation compared to CW614N leaded brass (Fig. 2.15b, d). In the case of CW510L, secondary fine dimples were also evident (Fig. 2.15d, Fig. 2.16b). CW511L and C27450 brasses had the largest and deepest dimples. This was consistent with the high absorbed impact energies for both these alloys (Fig. 2.15e-h).The interior of coarse dimples showed a characteristic texture consisting of parallel lines, most probably related to crystallographic slip. This phenomenon is illustrated in Figure 2.16b for CW510L and in Figure 2.17 for CW511L, and C27450. As already stated, CW511L and C27450 lead-free brass exhibited larger shear dimple~~s~~ compared to lead-free brass CW510L (Fig. 2.15f-h). At higher magnification, CW511L (Fig. 2.17a) and C27450 (Fig. 2.17b-c) revealed shear bands and small secondary dimples, which were attributed to ductile tearing.

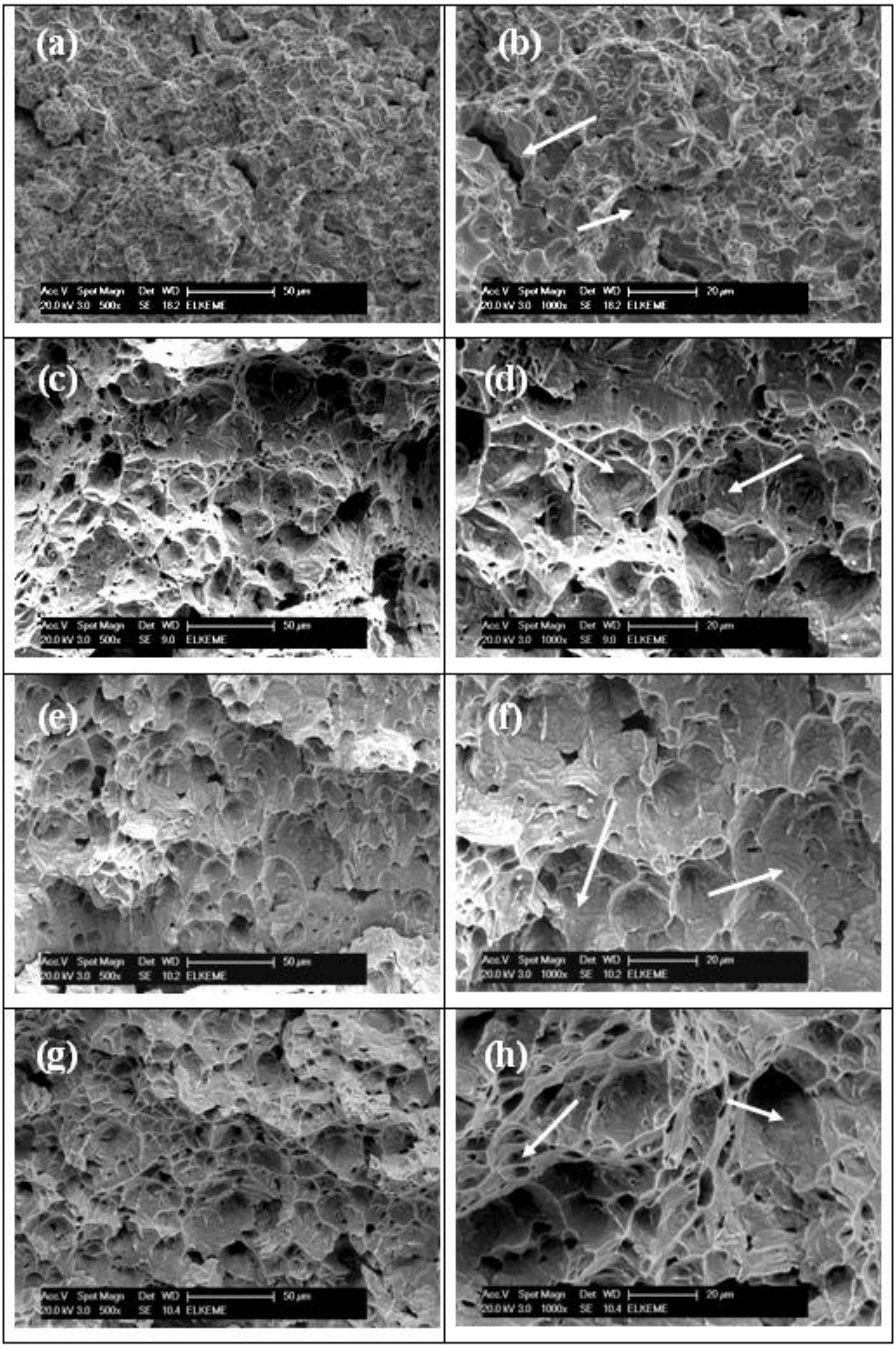

Fig. 2.15: SEM fractographs of impact samples: (a) and (b) CuZn39Pb3 (CW614N) leaded brass; (c) and (d) CuZn42 (CW510L) lead-free brass; (e) and (f) CuZn38As (CW511L) lead-free brass; and (g) and (h) CuZn36 (C27450) lead-free brass.

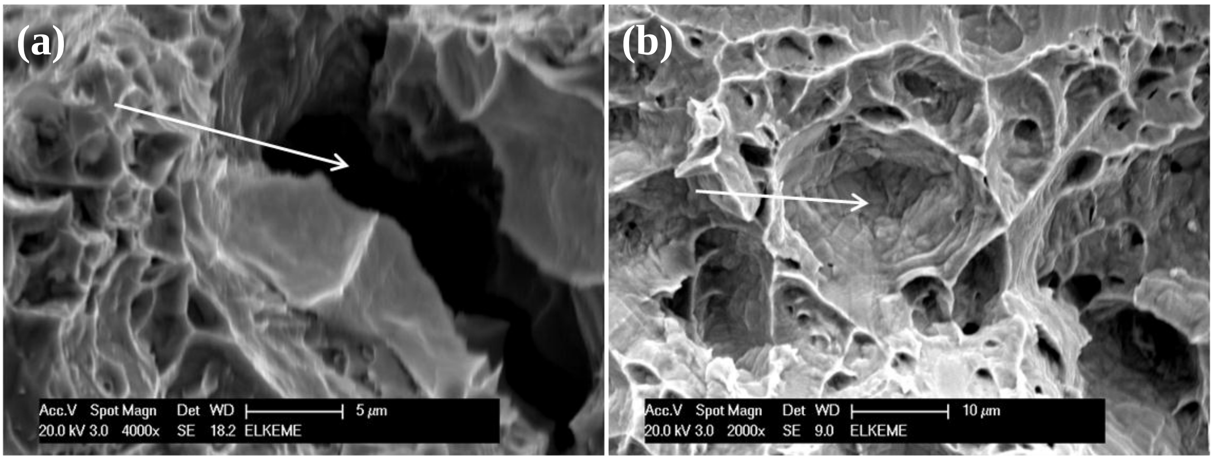

Fig. 2.16: SEM fractographs after impact tests: (a) Transgranular fracture in CW614N leaded brass; and (b) fine secondary dimples and slip lines (indicated by the white arrow) in CW510L lead-free brass.

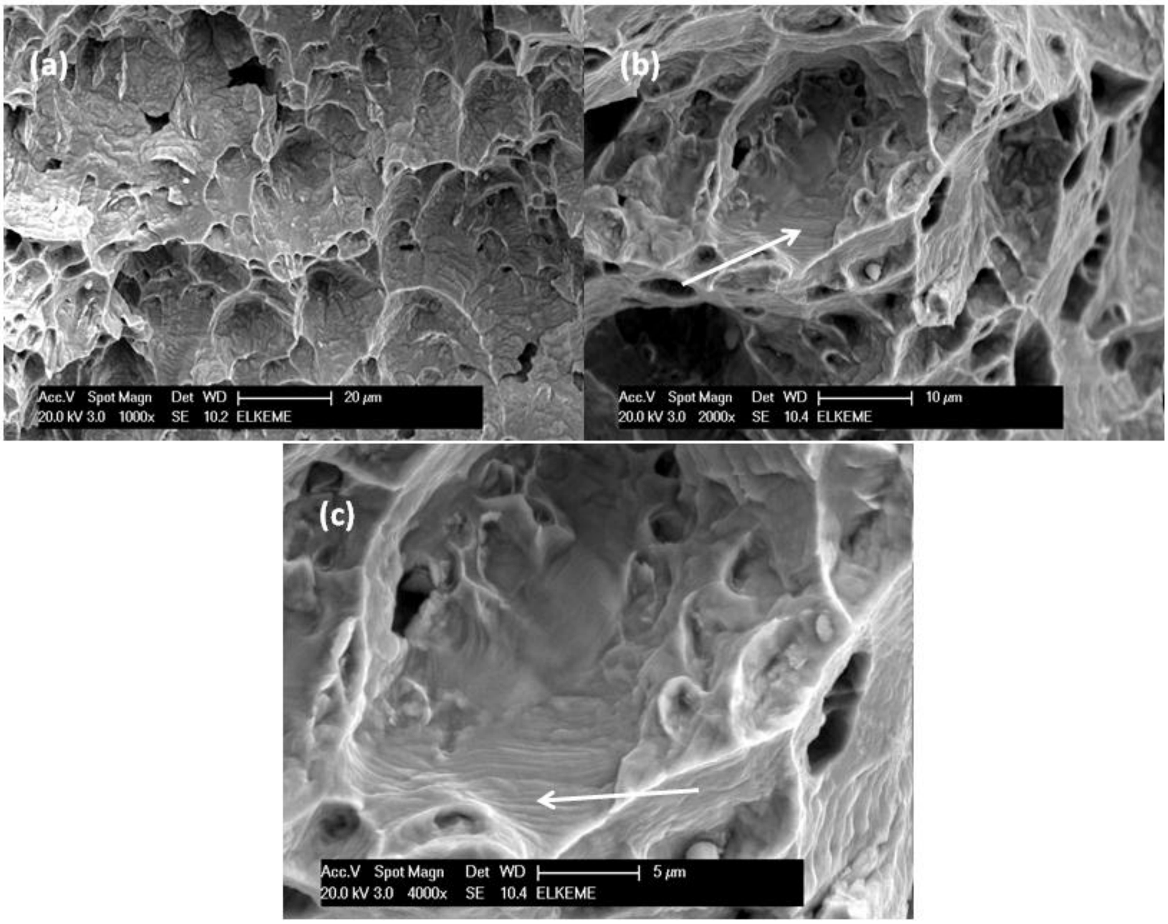

Fig. 2.17: SEM fractographs after impact tests: (a) shear dimples and slip lines in CW51lL lead-free brass; (b) slip steps (indicated by the arrow) and fine secondary dimples formed due to ductile tearing in C27450 lead-free brass during impact test; and (c) detail of (b) at higher magnification.

Backscattered electron imaging (BSE) was also employed to highlight composition or crystallographic differences that could be related to the prevalent fracture modes for each alloy (Fig. 2.18). In the case of CW614N leaded brass, the closely distributed bright areas corresponded to Pb islands (Fig. 2.18a), which promoted grain boundary decohesion and the subsequent brittle intergranular fracture, reducing thus the energy absorption efficiency. The presence of Pb particles may also have been the cause of the massive void nucleation and coalescence which resulted in the reduction of strain to failure. Low melting constituents such as lead (Pb), have often been reported to significantly affect the fracture process by inducing severe embrittlement of the material [8-12].

On the other hand, the absence of lead in brass alloys was found to promote plastic deformation and toughness, resulting in high impact energy absorption. As should be noted, traces of lead (Pb) phase were sparsely present on the fracture surface of C27450 alloy. CW511L and C27450 brass alloys exhibited the lowest β-phase fractions (~5% and ~2% respectively) together with higher plasticity and absorbed impact energy.

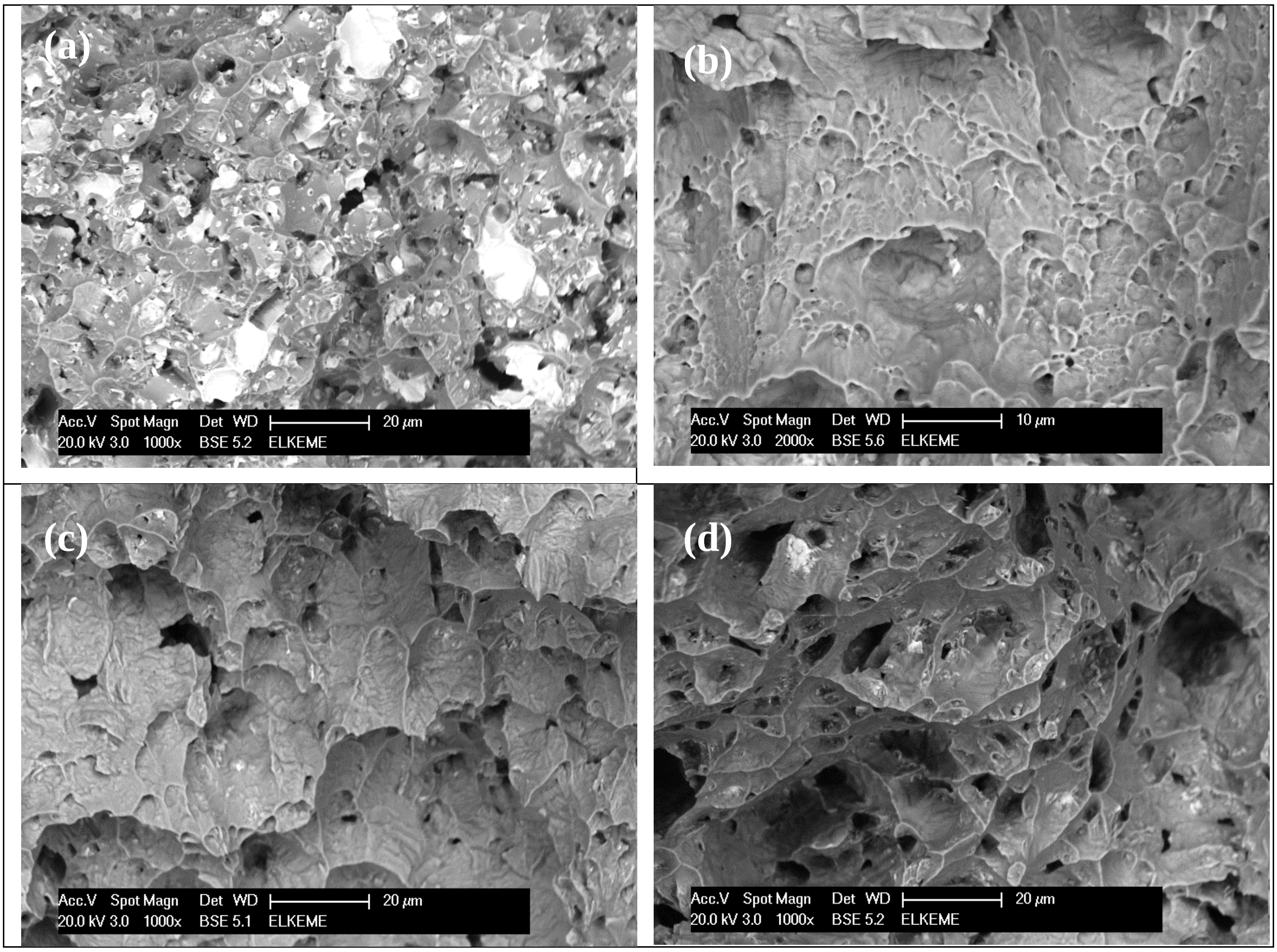

Fig. 2.18: SEM fractographs (BSE imaging) after impact testing: (a) CuZn39Pb3 (CW614N) leaded brass where the presence of a significant dispersion of Pb islands (white spots) is evident; and (b) CuZn42 (CW510L), (c) CuZn38As (CW511L), and (d) CuZn36 (C27450) lead-free brasses.

2.7. Correlation of Microstructure and Mechanical Properties

The microscopic observation of CW511L and C27450 alloys revealed a uniform microstructure with a relatively low percentage of β-phase. This microstructure is potentially more resistant to void growth and coalescence under a triaxial stress state, and results in a substantial post uniform elongation. Higher post uniform elongation is also related to higher strain-rate sensitivity and an improved resistance in the formation of incipient necking [13]. Higher lead percentage led to lower ductility and higher tensile strength. This was attributed to the fact that Pb particles, segregated in α/β phase boundaries, reduced the grain boundary surface energy and caused a ductility drop. This effect has been reported to be even more pronounced at higher and intermediate working temperatures [6,14].

Concerning the CTOD fracture modes, the CW614N leaded brass exhibited the lowest distortion compared to lead-free brass alloys (Fig. 2.14a). In this alloy, low ductility was mainly related to the microstructure and lead (Pb) phase distribution, as was also observed during SEM examination. CTOD fracture modes of lead-free brass CW511L (Fig. 2.14c) revealed a higher shape distortion and deformation in comparison to CW510L lead-free brass (Fig. 2.14b), as was anticipated by the respective critical CTOD values and load-displacement curves. As the SEM examination revealed, the CW511L alloy possesses a higher percentage of the ductile α-phase (solid solution). On the other hand, the harder β-intermetallic phase dominated the CW510L alloy microstructure. In other words, the prevalence of the β-intermetallic phase in the alloy microstructure may be regarded as an alternative to Pb, by inducing a similar mechanical behaviour. The most irregular fracture pattern was observed in the case of the ductile C27450 alloy, where crack divergence from the principal plane of crack propagation was observed (Fig. 2.14d). This was attributed to (i) the predominance of α-phase and (ii) the very low percentage of hard β-phase and the absence of lead.

2.8. Section Conclusions

CW510L alloy which contains 60% β-phase, exhibited higher tensile strength (460 MPa) and slightly lower total elongation (41%) compared to CW511L (380 MPa, 42%) and C27450 (320 MPa, 48%) alloys. CW511L and C27450 exhibited the least percentages of β-phase volume percentage (5 and 2%, respectively). Charpy impact test and the critical CTOD values at room temperature increased according to the following alloy order: CW510L (47 J and 0.32 mm respectively) < CW511L (104 J and 0.71 mm respectively) < C27450 (109 J, CTOD was not feasible due to enhanced plasticity behaviour). CW614N presented the minimum fracture mechanics properties (9 J and 0.02 mm respectively).

Dimpled ductile fracture was the dominant failure mechanism under impact loading for all tested brass alloys. However, the dimple size and distribution varied among the tested alloys suggesting different amounts of plastic deformation prior to impact failure. The impact fracture surfaces of CW614N leaded brass revealed the shallowest and finest shear dimples compared to lead-free brass alloys, while the largest and deepest dimples were observed in the case of CW511L and C27450 brass alloys which absorbed the highest impact energy. Static and dynamic tests indicated that the CW510L lead-free brass alloy possessed a good combination of tensile strength and fracture toughness, superior to that of the conventional CW614N leaded brass (especially concerning the fracture resistance). This suggests that CW510L lead-free brass is a strong candidate for the replacement of commonly used leaded brasses such as CW614N, at least as far as the mechanical properties are concerned.

2.9. References

[1] G. Pantazopoulos (2002) Leaded brass rods C38500 for automatic machining operations: a technical report. Journal of Materials Engineering and Performance 11: 402-407.

[2] A.I. Toulfatzis, G.J. Besseris, G.A. Pantazopoulos, C. Stergiou (2011) Characterization and comparative machinability investigation of extruded and drawn copper alloys using non-parametric multi-response optimization and orthogonal arrays. The International Journal of Advanced Manufacturing Technology 57: 811-826.

[3] P. Garcia, S. Rivera, M. Palacios, J. Belzunce (2010) Comparative study of the parameters influencing the machinability of leaded brasses. Engineering Failure Analysis 17: 771-776.

[4] G. Pantazopoulos, A. Vazdirvanidis (2008) Characterization of the microstructural aspects of machinable α-β brass. Microscopy and Analysis 22: 13-16.

[5] G.A. Pantazopoulos, A.I. Toulfatzis (2012) Fracture modes and mechanical characteristics of machinable brass rods. Metallography, Microstructure and Analysis 1: 106–114.

[6] K. Laue, H. Stenger (1981) Extrusion-Processes-Machinery-Tooling. American Society for Metals, 4th printing, Ohio.

[7] G.E. Dieter (1988) Mechanical Metallurgy. SI Metric Edition, McGraw-Hill, N.Y.

[8] “Fractography” (2012) ASM Handbook, 12, ASM International, OH USA.

[9] D. Hull (1999) Fractography, observing, measuring and interpreting fracture surface topography. Cambridge.

[10] S.P. Lynch, S. Moutsos (2006) A brief history of fractography, Journal of Failure Analysis and Prevention 6: 54-69.

[11] S.P. Lynch (2008) Failures of structures and components by metal-induced embrittlement. Journal of Failure Analysis and Prevention 8: 259-274.

[12] G.A. Pantazopoulos (2011) Damage assessment using fractography as failure surface evaluation: applications in industrial metalworking machinery. Journal of Failure Analysis and Prevention 11: 588-594.

[13] W.F. Hosford, R.M. Caddell (1983) Metal Forming: Mechanics and Metallurgy. Prentice Hall, Englewood Cliffs, New Jersey.

[14] D.J. Woley, A.G. Fox (1998) The embrittlement of leaded and unleaded α+β (60-40) brasses in the temperature range 300 to 500^{o}C. Journal of Materials Science Letters 7: 763-765.

Chapter 3: Machinability of Lead-Free Brass Alloys - Chip Morphology and Power Consumption Optimization

3.1. Summary

The limited referenced research work concerning the evaluation of machinability employing statistical tools and techniques and, more specifically, utilizing the screening methodology using a non-linear multifactorial profiler, provides a significant degree of innovation to the current study. The optimal cutting parameters such as speed, feed and depth of cut as a multi-criterion plain turning problem were defined and experimentally confirmed, using a non-linear design of experiments approach [1-3].

The main objective of this study was to concurrently screen and optimize one quality and one process characteristic—chip morphology and power consumption—against the four controlling factors—speed, feed, depth of cut and alloy type—using multilevel Taguchi experimental designs and nonparametric data analysis. To our knowledge, it is the first time that joint screening and optimization is accomplished using one numerical response (power consumption) and one nominal and ordinal response (chip morphology) using new-age, non-linear, and distribution free stochastics (the surrogate method) which is suitable for extracting information from saturated multifactorial OA-based datasets.

The attempted joint screening using a four-level orthogonal array revealed that the depth of cut and the alloy type were the two statistically predominant effects. The chip morphology and the power consumption in a balanced concurrent optimization effort, were optimal when the depth of cut was set at 0.5 mm for the alloy type CW614N chip morphology optimization. The optimal chip morphology response was split in equal chances to produce needle or arc chips. The predicted power consumption was confined in a range of values with an upper boundary at 65 W. The findings of the statistical evaluation were experimentally confirmed, validating the DOE approach.

3.2. Microstructure and Machinability Relationships

The microstructure of leaded and lead-free brass alloys and its relationship to mechanical properties, under quasi-static and dynamic loading conditions was studied extensively in previous studies [4-5]. Metallographic evaluation revealed a wide variation of microstructures among the leaded and lead-free brass alloys (Fig. 2.1). All the alloys consisted of a mixture of α and β phases with different volume fractions as a result of their chemical composition and manufacturing process conditions. Pb-particle distribution was readily identified in case of conventional machinable CW614N leaded alloy with a mean particle size up to 1.2 μm. In binary Cu-Zn alloy systems, β-phase volume fraction was mainly controlled by Zn content and thermomechanical processing. Consequently, CuZn42 (CW510L) exhibited the highest percentage of β-phase reaching up to 60%, while the lowest β-phase fraction (2%) was observed for CuZn36 (C27450) which showed an almost single phase structure (Figs. 2.1 and 2.2).

As shown in Figures 2.1 and 2.2, CuZn39Pb3 (CW614N) leaded alloy and CuZn38As (CW511L) lead-free alloy exhibited 33% and 5% β-phase fractions respectively. Together with the variation of β-phase volume percentage, a difference in phase morphology was observed among the studied brass alloys. In the case of CuZn42 (CW510L), a typical Widmanstätten structure consisting of α-intersecting coarse α-plates in β-phase matrix was identified. This microstructure is frequently detected to high-Zn brass alloys produced under fast cooling conditions which imply a suppressed growth rate of α-crystals mostly precipitated at β-phase boundaries. All the rest brass alloys exhibited an equiaxed and fine-and uniform grained structure. Isolated thermal (annealing) twins were located in the interior of α-crystals, principally in C27450 brass alloy (Fig. 2.1).

All brass alloys corresponded to half-hard metallurgical condition (extruded and lightly drawn). A hardness gradient from surface to core existed as a result of plastic deformation processing (especially cold drawing), which resulted in non-uniformstrain hardening (Fig. 2.3). As was evident, hardness was higher for CuZn42 (CW510L) and CuZn39Pb3 (CW614N) compared to CuZn38As (CW511L) and CuZn36 (C27450). This difference could be also attributed to the microstructural variation and more likely to the higher β-phase fraction exhibited by the former brass alloys (CW510L, CW614N) as compared to the latter ones (CW511L, C27450). However, it seemed that there was a “flattening” tendency of hardness differences, among the various brass alloys, mainly in outer surface regions, indicating that surface strain hardening became highly significant as a factor for strength development. Chip morphology studied under light optical microscopy revealed a wide spectrum of chip size and morphologies. The most representative patterns are depicted in Figure 3.1.

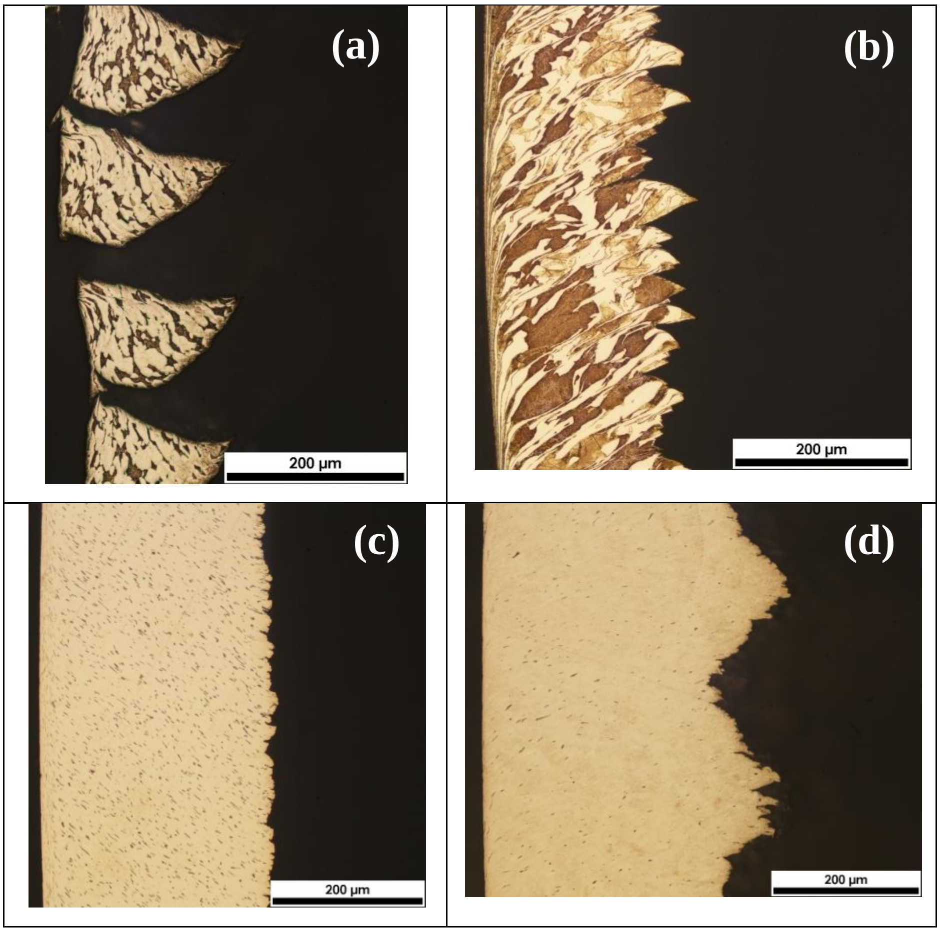

Fig. 3.1: Representative patterns of chip size and morphologies produced under various turning conditions: (a) Alloy: CW614N - Cutting Speed: 2250 rpm (247 m/min) - Depth of Cut: 1.50 mm - Feed Rate: 200 mm/min, (b) Alloy: CW510L - Cutting Speed: 1500 rpm (165 m/min) - Depth of Cut: 0.50 mm - Feed Rate: 150 mm/min, (c) Alloy: CW511L - Cutting Speed: 2000 rpm (220 m/min) - Depth of Cut: 1.50 mm - Feed Rate: 150 mm/min and (d) Alloy: C27450 - Cutting Speed: 2250 rpm (247 m/min) - Depth of Cut: 2.00 mm - Feed Rate: 150 mm/min.

As anticipated, the highest extent of chip segmentation accompanied by a low degree of plastic deformation on chip / rake face region was achieved in the case of conventional leaded brass alloy (CW614N), where the beneficial effect of Pb-particle distribution on chip size was confirmed (Fig. 3.1a), see also Ref. [6]. Among the lead free alloys, the highest tendency for chip fragmentation was observed for the CW510L brass alloy, outlining the potential favourable influence of intermetallic β-phase in machinability. The saw-tooth (“serrated”) chip morphology could be attributed to the formation of shear bands which facilitated prospective micro-crack initiation and propagation through α/β interfaces that promoted massive chip fracture (Fig. 3.1b). Plastic deformation of the chip/rake face region was encountered for the three lead-free brasses as a result of strain hardening potential, dictated by the strain hardening exponent (n) indicated by $R_m/R_{p0.2}$ ratio [5].

Further microhardness testing of the produced chips was employed to assess the hardness increase due to plastic deformation caused by the machining process. As is observed, weak chip fracturing may promote severe plastic flow while high machinability rating and intense chip breaking is accompanied by marginal or restricted plastic deformation attaining an almost superficial strain accommodation and absence of intense flow zones [6]. The use of deformation or “work hardening index” (WH) was introduced in order to quantitatively address and evaluate the hindrance of machining process realization (used as opposite term of machinability, i.e. ease of machining-chip fracturing):

$$WH = 100 \times \frac{(HV_{final} - HV_{initial})}{HV_{initial}} \tag{1}$$

Where,
WH: Work hardening index [%].
HV_{final}: the chip average hardness (assessed by Vickers indentation technique).
$HV_{initial}$: the initial surface hardness, as evaluated by the hardness of the brass rod surface (assessed by Vickers indentation technique).

The % difference in hardness was directly related to the severity of plastic deformation and hence the resistance against chip fracture and segmentation for the applied cutting conditions. A major factor contributing to the amelioration of machining efficiency was the alloy type, as has been also observed in other studies [1]. As should be noted, the schematic approach shown in Figure 3.2, was a only representative one for the applied machining conditions, implying a generic order of the assessed brass alloys which was deduced according to their chip breaking capability (in decreasing order):

$$\text{CW614N}<\text{CW510L}<\text{CW511L}\approx<\text{C27450} \tag{2}$$

This proposed series order indicated a marked difference in machinability, highlighting the superiority of CW614N grade among the studied alloys, followed by CW510L, while CW511L and C27450 grades exhibited the highest, though almost equivalent, index values, signifying comparable machinability characteristics in terms of chip breaking (low tendency).

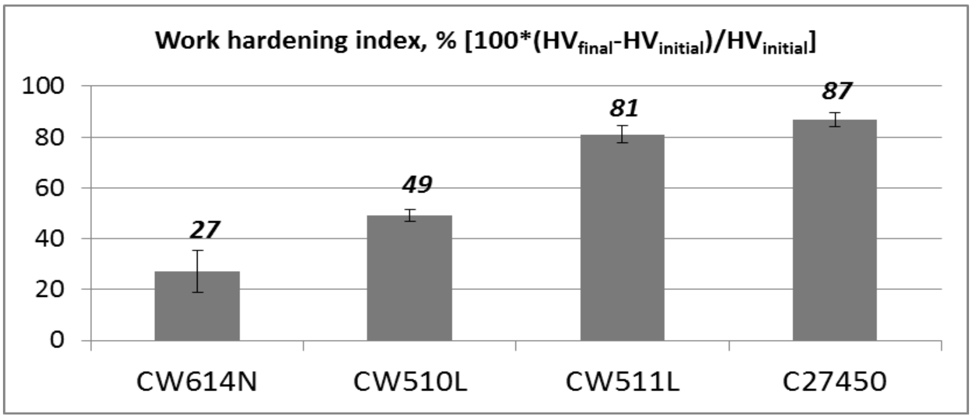

Fig. 3.2: Variation of “work hardening index” for the various studied brass alloys (error bars are calculated based on standard deviation interval, ±1s).

3.3. Machinability

During the machinability evaluation process, the two quality characteristics, chip morphology (CM) and the power consumption (P) were tracked. For consistency purposes, the experiments for the two quality characteristics were duplicated; see experimental results in Table 3.1 (noted as REP in Table 3.1). As seen in Table 3.1, the chip morphology and power consumption performance was perfectly repeatable for all sixteen recipes. Therefore, no additional trial runs were scheduled. The two replicates were linearly fitted in an one to one plot (Fig. 3.3). Although as seen by the coefficient of determination (R^2= 99.6%) for the perfect slope value of 1.00, several points were on or beyond the two confidence interval boundaries. This means that the complication of messiness was present in this type of response and thus it justified the decision to proceed to the data conversion step utilizing distribution-free stochastics [7].

At this stage, no additional experiments were required. The strong intermixing of the symmetrical and asymmetrical characters of the original dataset for the chip morphology and the power consumption at their respective investigated adjustments is shown in Figure 3.4 by summarizing the data behavior in terms of box plots. As is clear, the decision to follow a distribution-free framework in the subsequent data analysis instead of proceeding with ordinary ANOVA/MANOVA treatments that are heavily dependent on dataset symmetry was fully justified.

Table 3.1: Experimental Results of Chip Morphology **(**CM) and Power consumption (P).

Number of Experiment	Material	Quality Characteristics Results					
		*CM (class.) Rep 1	*CM (class.) Rep 2	*CM (class.) Average	P (W) Rep 1	P (W) Rep 2	P (W) Average
1	CW510L	4	4	4	240	240	240
2	CW511L	4	4	4	640	640	640
3	C27450	4	4	4	1240	1220	1230
4	CW614N	1	1	1	1240	1240	1240
5	C27450	2	2	2	240	240	240
6	CW614N	1	1	1	240	240	240
7	CW510L	2	2	2	1900	1900	1900
8	CW511L	3	3	3	1620	1580	1600
9	CW614N	1	1	1	240	220	230
10	C27450	2	2	2	1340	1440	1390
11	CW511L	5	5	5	840	820	830
12	CW510L	3	3	3	1220	1220	1220
13	CW511L	4	4	4	700	760	730
14	CW510L	2	2	2	740	740	740
15	CW614N	1	1	1	600	620	610
16	C27450	5	5	5	1040	1020	1030

*Chip Morphology (CM) classification: 1 needle chip, 2 arc chips, 3 conical helical chips, 4 washer-type helical chips, 5 ribbon chips.

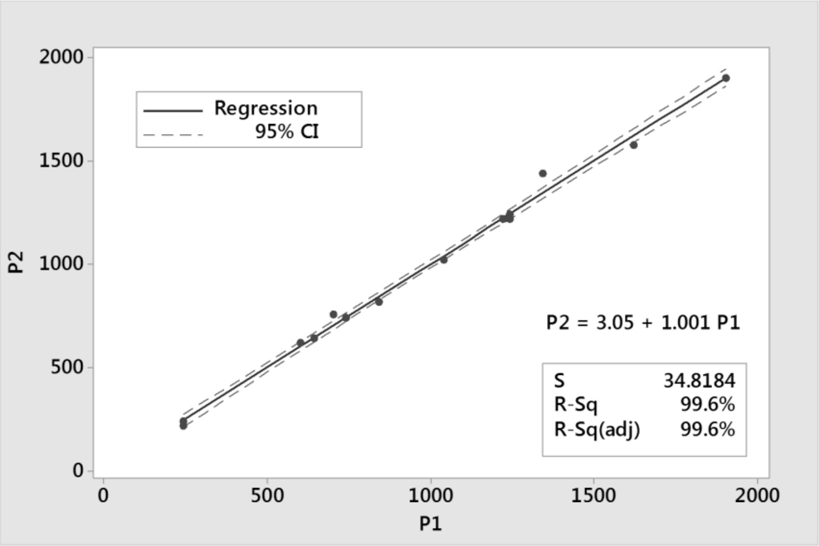

Fig. 3.3: Replication correlation test for power consumption (P) in W.

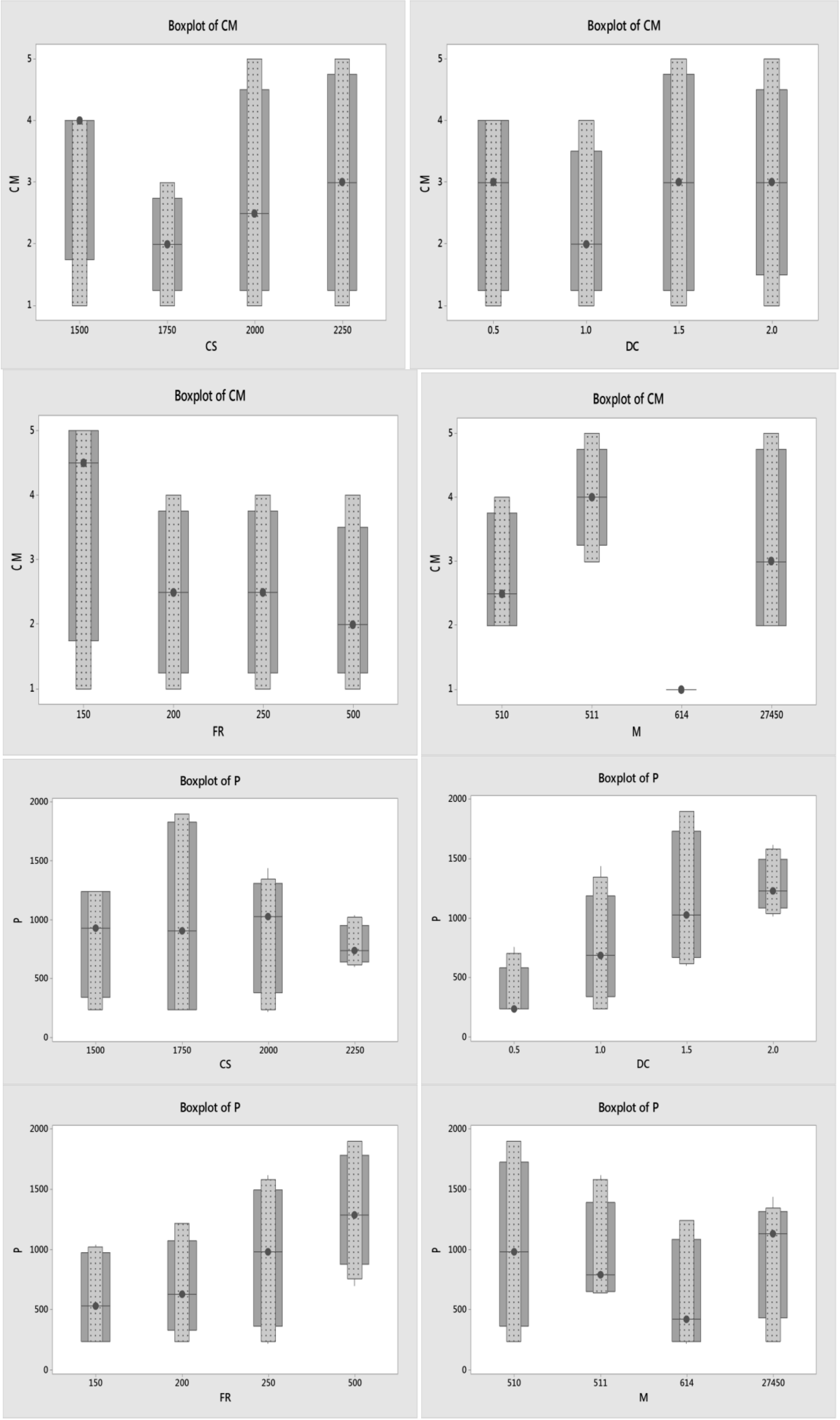

Boxplot of CM

Boxplot of CM

Boxplot of CM

Boxplot of CM

Boxplot of P

Boxplot of P

Boxplot of P

Boxplot of P

Fig. 3.4: Box plots of the four investigated effects for the responses of chip morphology (CM) and Power consumption (P).

3.4. Analysis of Chip Morphology

Characteristic forms of chip morphology resulted by the L_{16} orthogonal array experiments (Table B.2), produced under various turning conditions, are shown in Figure 3.5. The main effects plot for the data means of chip morphology response (Fig. 3.6) depicted a practical view of the relative strengths of the four effects as well as their optimal settings. It was evident that the type of material introduced the greatest variability in the measurements. The CW614N performed best in minimizing chip morphology. To provide a statistical support for this outcome, the nonparametric conversion of the CM dataset from Table 3.3 is tabulated in Table 3.5 following the published rank transformation procedures for multifactorial OA schemes [7-9].

The rank transformed replicates, CM1 and CM2 from Table 3.1, were cast respectively to the rank ordered responses rCM1and rCM2 which upon row addition created the sum of ranks of CM (srCM) response. Re-ranking the srCM column in Table 3.2 produced the rCM vector which contained homogenized information from both CM replicates. From Table 3.3, the Kruskal-Wallis H-statistic was statistical significant for rCM, at a level of 0.05, only for the alloy type. Surrogate error checking was estimated at a p value of 0.621 which supported the outcome of the nonparametric analysis [10].

Moreover, the lowest median rank (2.8) was identified with the brass alloy type CW614N which confirmed the result of the main effects plot for the CM. Thus, chip morphology was not sensitive to cutting speed, feed rate and depth of cut variations at a significance level of 0.05 (Table 3.3). Although CM was found to be in sensitive to all parameters other than the alloy type, this statistical observation relates to the choice level of significance and the type of the variable, i.e., a combination of nominal and ordinal categorical variable which assigned hierarchically chip morphology to five unique types. The outcome of this optimization obviously favored the manifestation of needle chips (Table 3.4).

Using the chip morphology criterion, machinability deteriorated for the studied materials in the following order: CW614N < CW510L < C27450 < CW511L, which was in close agreement to the series order proposed by using the "work hardening index" (WH). The marginal superiority of the C27450 against CW511L chips could be attributed to the slightly higher Pb content of C27450 alloy. The higher Pb content allowed for a higher degree of shear instability formation which in its turn was responsible for micro-crack generation and final chip fracture. Also, machining quality deteriorated in the following order of chip morphology: needle chips > arc chips > conical helical chips > washer-type helical chips > ribbon chips.

The formation of shorter chips resulted in better surface finish, lower tool wear and ease of operation, permitting therefore higher cutting speeds. As should be noted, chip morphology was more a qualitative and not a quantitative quality characteristic, a fact that limited the capability to accurately compare predicted with experimental results.

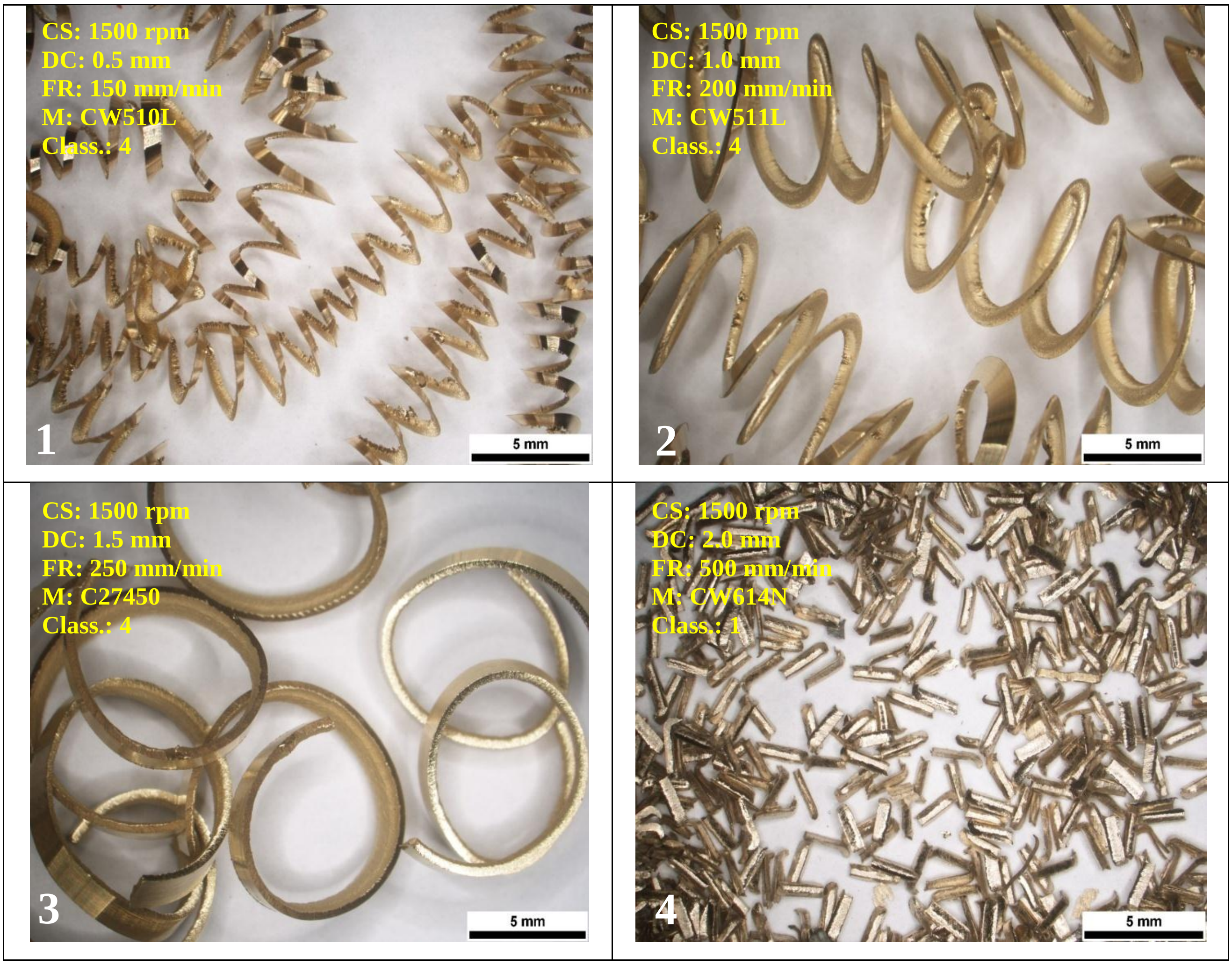

Fig. 3.5 Cont’ed


CS: 1750 rpm
DC: 0.5 mm
FR: 200 mm/min
M: C27450
Class.: 2
5
5 mm
CS: 1750 rpm
DC: 1.0 mm
FR: 150 mm/min
M: CW614N
Class.: 1
6
5 mm
CS: 1750 rpm
DC: 1.5 mm
FR: 500 mm/min
M: CW510L
Class.: 2
7
5 mm
CS: 1750 rpm
DC: 2.0 mm
FR: 150 mm/min
M: CW511L
Class.: 3
8
5 mm
CS: 2000 rpm
DC: 0.5 mm
FR: 250 mm/min
M: CW614N
Class.: 1
9
5 mm
CS: 2000 rpm
DC: 1.0 mm
FR: 500 mm/min
M: C27450
Class.: 2
10
5 mm

Fig. 3.5 Cont'd

Fig. 3.5: Characteristic forms of Chip Morphology (CM) produced under various turning conditions during the designed experiments (1-16).

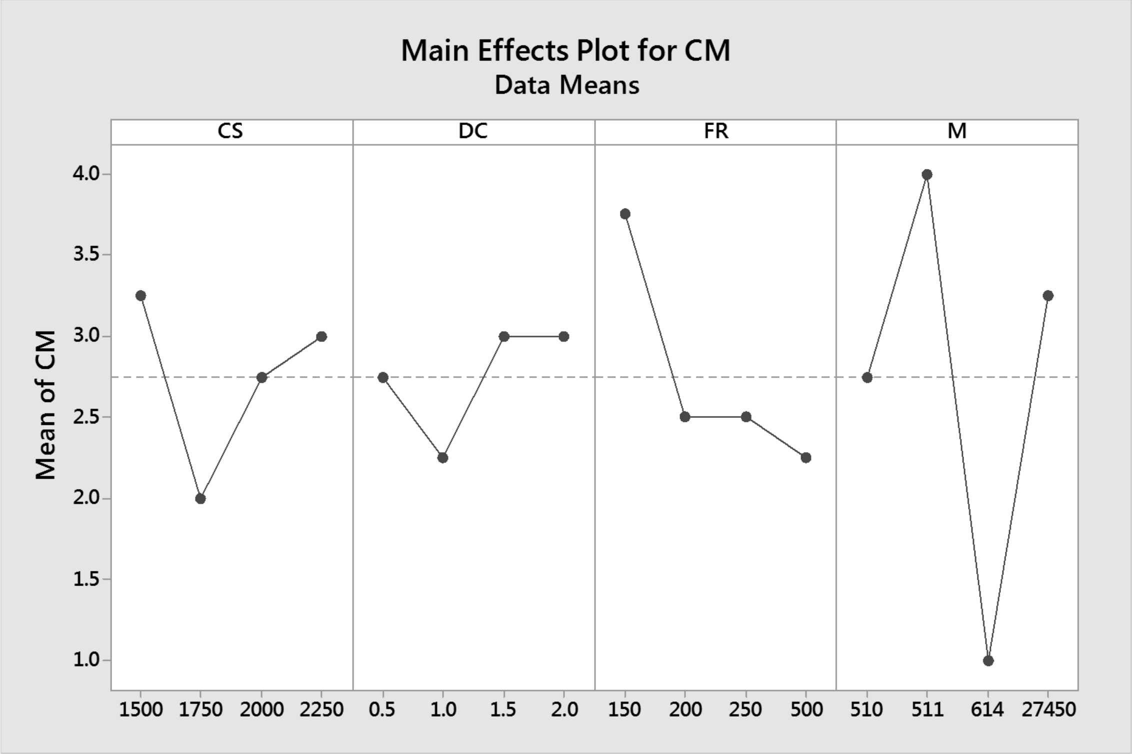

Fig. 3.6: Main effects plots for chip morphology (CM) versus cutting speed (CS), depth of cut (DC), feed rate (FR) and material (M).

Table 3.2: Rank consolidation of the two characteristics to a single master-response (MR).

Run no.	***rCM1***	***rCM2***	***rP1***	***rP2***	***srCM***	***srP***	***rCM***	***rP***	***ssRS***	***MR***
1	24.5	24.5	5	5	49	10	12.5	3	165.25	6
2	24.5	24.5	11.5	11.5	49	23	12.5	6	192.25	8
3	24.5	24.5	25	22	49	47	12.5	12	300.25	13
4	4.5	4.5	25	25	9	50	2.5	13	175.25	7
5	12.5	12.5	5	5	25	10	6.5	3	51.25	4
6	4.5	4.5	5	5	9	10	2.5	3	15.25	2
7	12.5	12.5	31.5	31.5	25	63	6.5	16	298.25	12
8	18.5	18.5	30	29	37	59	9.5	15	315.25	14
9	4.5	4.5	5	1	9	6	2.5	1	7.25	1
10	12.5	12.5	27	28	25	55	6.5	14	238.25	11
11	30.5	30.5	18	17	61	35	15.5	9	321.25	15
12	18.5	18.5	22	22	37	44	9.5	11	211.25	9
13	24.5	24.5	13	16	49	29	12.5	7.5	212.5	10
14	12.5	12.5	14.5	14.5	25	29	6.5	7.5	98.5	5
15	4.5	4.5	9	10	9	19	2.5	5	31.25	3
16	30.5	30.5	20	19	61	39	15.5	10	340.25	16

Table 3.3: Nonparametric analysis of chip morphology (rCM), power consumption (rP) and concurrent screening of both (MR).

Joint Response				**Chip Morphology**		**Power Consumption**	
Factor	Level	Median MR	H-statistic (p-value) (error p-value)	Median *rCM*	H-statistic (p-value) (error p-value)	Median *rP*	H-statistic (p-value) (error p-value)
DC	0.5	3.8	11.01 (**0.012**)	9.4	3.33 (0.344)	2.5	12.4 (**0.006**)
	1	5.5	0.402	4.9	0.179	7	0.717
	1.5	11.8		9.9		10.9	
	2	13		9.9		13.6	
CS	1500	10.8	2.25 (0.522)	12	6.83 (0.077)	8.6	1.62 (0.655)
	1750	6.8	0.485	3.8	0.85	9.9	0.692
	2000	9.8		8.5		9.5	
	2250	6.8		9.8		6	
FR	150	10.5	5.91 (0.116)	13.8	7.15 (0.067)	4.9	10.87 (**0.012**)
	200	4	0.766	6.6	0.179	5.1	0.44
	250	8		7.3		9.5	
	500	11.5		6.4		14.5	
M	510	7.8	10.52 (**0.015**)	8.4	11.08 (**0.011)**	9.8	8.67 (**0.034**)
	511	12.3	0.057	13.8	0.621	10.5	0.043
	614	2.5		2.8		2.5	
	27450	11.5		9.1		11.3	

Table 3.4: Median estimations of CM and P at all settings for the strong effects.

Factor	Level	mCM_M	mP_M (W)
M (alloy)	510	2.5	980
	511	4	790
	614^o	*1*	*420*
	27450	3	1130
		mCM_{DC}	mP_{DC} (W)
DC(mm)	*0.5^o*	*3*	*240*
	1	2	690
	1.5	3	1030
	2	3	1230
		M_{CM}^G	M_P^G (W)
Grand Median		2.5	790

^{o} Optimal setting from the joint screening

3.5. Measurements of Power Consumption

The histogram of power consumption, produced under various turning conditions is shown in Figure 3.7. The main effects plot for the data means of power consumption (Fig. 3.8) revealed that the P-response was more sensitive to the depth of cut and the feed rate. Similarly to the nonparametric analysis of the chip morphology described above, the rank ordering of the raw duplicated dataset of the P-response (Table 3.1) was homogenized to form the rank responses rP1 and rP2 (Table 3.2). Both then were added to form the sum of ranks srP response which upon a final re-ranking formed the uniform rP vector (Table 3.2). As seen in Table 3.3, it was confirmed statistically that the H-statistic was significant at a 0.05 level for both DC and FR. FR was obviously the controlling parameter for the minimization of power consumption at 150 mm/min (median rP=4.9) and DC was better controlled at the shallow cut of 0.5 mm (median rP=2.5). It was also observed that the brass alloy material could be a critical factor affecting the power consumption since its p value was significant at the 0.05 level.

However, its surrogate error turned out to be also significant at a level of 0.05, and this blurred the probable significance of the material selection in influencing the power consumption. Finally, as seen in Figure 3.8, the behavior of the two effects, DC and FR, could also have been predicted using a three-level OA-scheme at most, since they exhibited an almost linear tendency. In other words, it would also have been detected by experimenting on a three-setting schedule. The favored power consumption rates were predicted to be under 50 W.

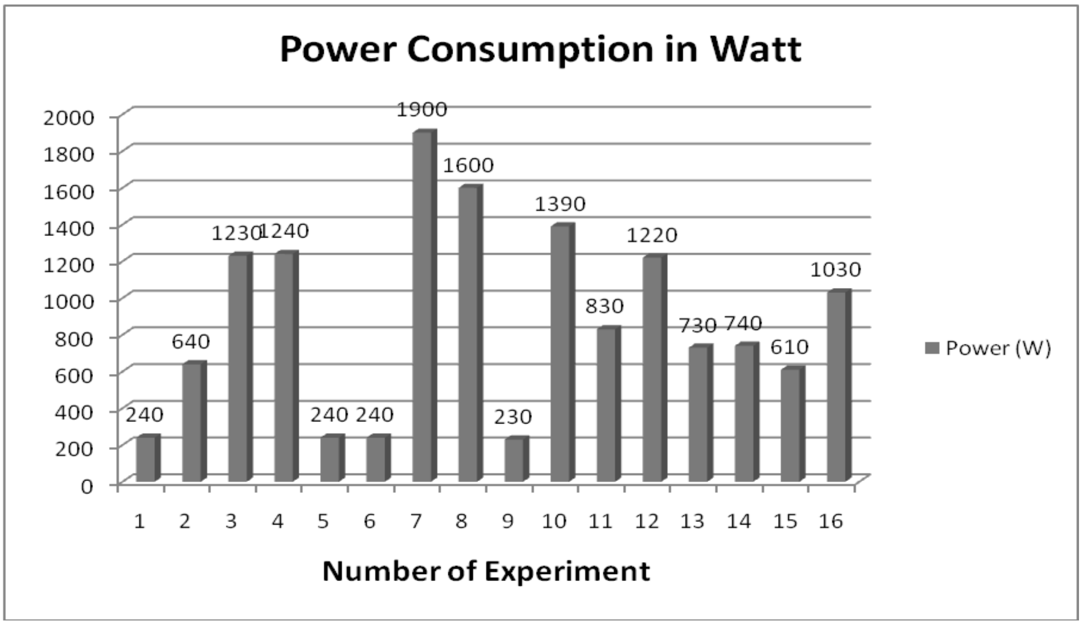

Fig. 3.7: Histogram showing the power consumption resulted under various turning conditions.

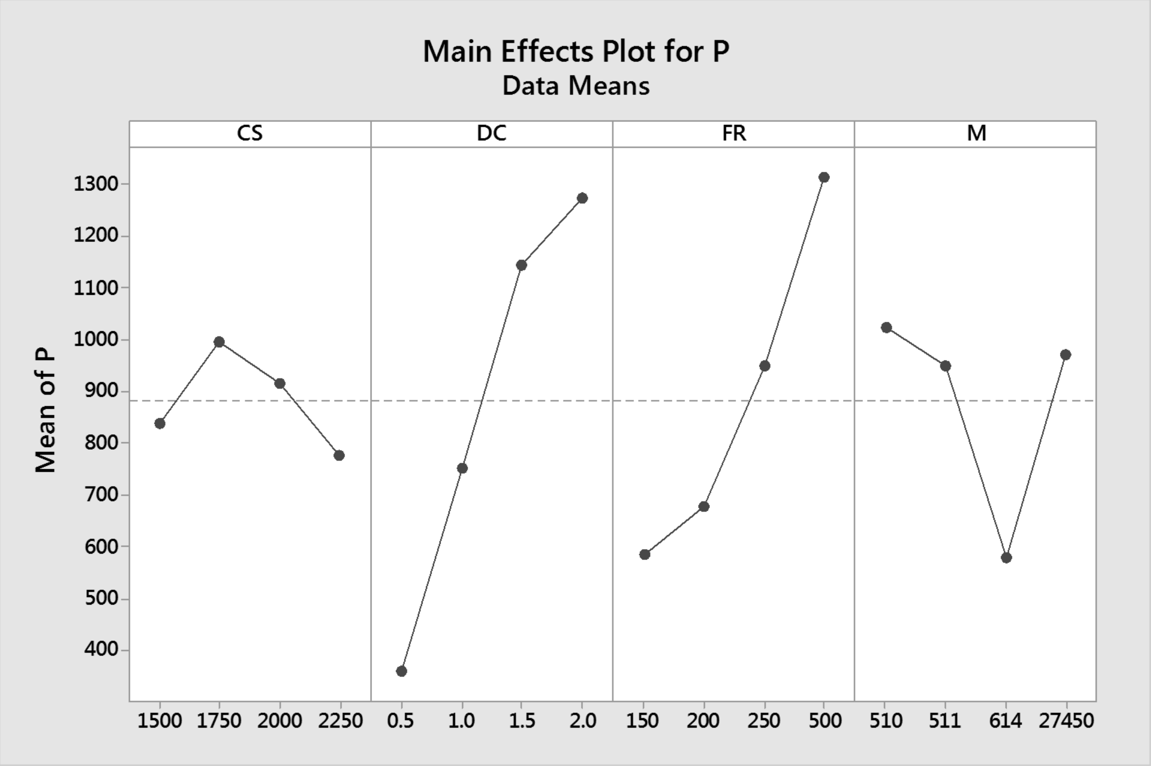

Fig. 3.8: Main effects plots for power consumption (P) versus cutting speed (CS), depth of cut (DC), feed rate (FR) and material (M).

3.6. Joint Screening of Chip Morphology and Power Consumption

To examine the simultaneous effect of the four investigated parameters on the two responses, CM and P, a concurrent nonparametric screening was performed. To achieve this, the homogenized responses, rCM and rP were squared and then added to form the sum of squared rank responses, ssRS (Table 3.2). Re-ranking the ssRS vector formed the master response (MR) which now contained in equal proportions the contributions due to both quality characteristics and their associated repeatability levels [8–12]. The main-effects plot of ssRS vector for the data means is depicted in Figure 3.9. It can easily be seen that DC, FR and M could influence the joint response. It was also observed that a three-level OA design would be capable to picking up the trends for DC and FR. The former effect could also be treated with a simpler (two-point) linear model. However, the latter effect was strongly convex upward, and thus it definitely required a non-linear treatment. The optimal settings for DC, FR and M, were identified from the main effects plot to be 0.5 mm, 200 mm/min, and CW614N, respectively. The available fifth (empty) column of the original L_{16} (4^5) OA—playing the role of an error contribution (ER)—was used to track down the potential presence of additional unknown influences [13].

Based on the main effects plot (Fig. 3.9), ER could not be considered to cause a significant disturbance in the conducted experiments and thus it was not examined any further. The outcomes from the joint nonparametric screening of both characteristics through the master response, MR (Table 3.3) revealed that the H-statistic values for two effects were significant at the 0.05 level. It was predicted stochastically that DC and M were the strong influences for the concurrent screening. Their respective settings were located at 0.5 mm (med MR= 3.8) and CW614N (med MR= 2.5). In both cases, the surrogate error was not significant at the 0.05 level. In accordance to Taguchi methodology, a confirmation test was performed. The predicted response values using the optimal levels of the statistically strong design parameters could be calculated in terms of median values as:

Chip morphology:

$$MCMG + (mCMDCo - MCMG) + (mCMMo - MCMG) = mCMDCo + mCMMo - MCMG$$

and

Power consumption:

$$MPG + (mPDCo - MPG) + (mPMo - MPG) = mPDCo + mPMo - MPG,$$

where MCMG and MPG are the grand median values of the original datasets for CM and P, respectively. Also, mCMDCo and mCMMo are the median values of CM at the optimal settings of DC and M, respectively. Similarly, mPDCo and mPMo are the median values of P at the optimal settings of DC and M, respectively.

The predictions for the optimal performance of CM and P were calculated to be 1.5 (±0.25) and 130 W. Hence, the median prediction for the power consumption was taken as zero at minimum with an estimated upper confidence bound at 65 W (at 95 %). The above quantities are tabulated in Table 3.4 for ease of reference. It was observed that three out of the four setting values of the responses were minimized, demonstrating the successful application of the concurrent screening method. Furthermore, while both the alloy type and the depth of cut independently contributed to the power consumption minimization; this was not the case for optimizing the chip morphology performance. As seen in Table 3.4, the alloy CW614N influenced the creation of very fine needle chips. However the best result that could be extracted from the depth of cut in term of chip morphology was arc chips, which was not predicted as the optimal setting. Instead the conical helical chips were predicted for the very shallow cut.

However, the joint screening offered a solution that gave a 50 % chance for the generation of either needle or arc chips. Table 3.5 shows the comparison of the estimated (predicted) and the measured (experimental) power consumption values using the optimal conditions. As can be seen, there is sufficient agreement between the predicted (< 65 W) and the experimental (70 W) power consumption values.

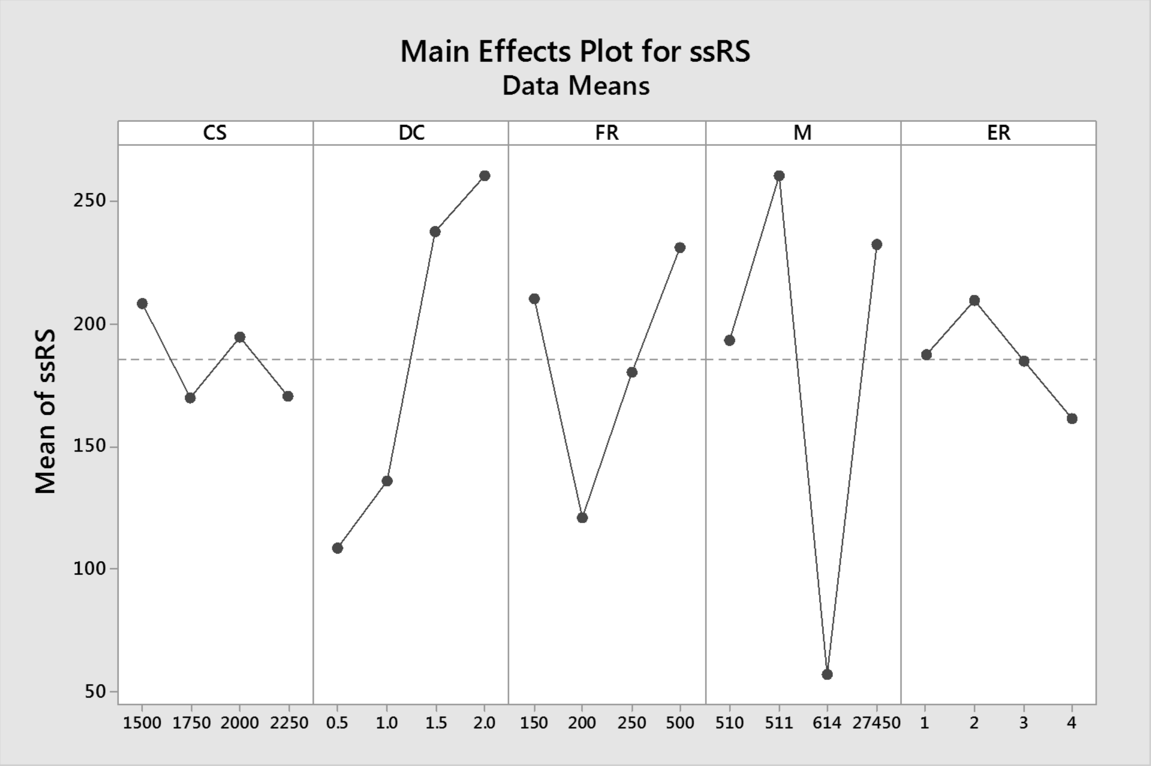

Fig. 3.9: Main effect plot for data means of the ssRS vector.

Table 3.5: Results of optimum values and confirmation experiments.

Quality Characteristic	Optimum Values				Confirmation Experiments	
	Cutting Speed (rpm)	Depth of Cut (mm)	Feed Rate (mm/min)	Material	Experimental Value	Predicted Value
Chip Morphology	1500 (165 m/min)	0.5	150	CW614N	Class. 1	Class.1 or 2
Power Consumption	1500 (165 m/min)	0.5	150	CW614N	70 W	0-65 W

3.7. Section Conclusions

Machinability assessment was performed to three lead-free brass alloys in comparison to a standard leaded brass alloy at the initial production condition (extruded and drawn). Chip size and morphology in brass alloys was principally influenced by the following microstructural constituents: Pb-particle and β intermetallic phase fractions. Chip fracturing was mainly controlled by the distribution of Pb particles, in conventional leaded brass alloys, while β-phase fraction exerted a major influence on shear band formation and micro-crack generation in lead-free alloys.

The use of chip "work hardening index (WH)" was attempted as a complementary estimator for quantitative evaluation of chip morphology based on chip fracturing promotion. It was shown that by utilizing this index, the inferred alloy series order was very close to the one deduced by statistical analysis. CW510L alloy which shows the minimum WH index among the lead-free alloys, stands as the optimum selection concerning chip morphology and power consumption quality characteristics.

Chip morphology and power consumption were concurrently optimized using the following conditions: the optimum alloy type was chosen to be CW614N, and the depth of cut was set at 0.50 mm. The cutting speed and the feed rate were statistically insignificant and their suitable settings were based on practical considerations. Thus, encouraging lower power consumption, the cutting speed and the feed rate were set at 1500 rpm (165 m/min) and 150 mm/min, respectively.

For the uni-response optimization case, the chip morphology was controlled only by the brass alloy type. It clearly favoured the alloy setting of CW614N ($p<0.05$). This favored the formation of needle chips. The uni-response optimization of power consumption resulted in two influencing parameters: (1) depth of cut, and (2) feed rate. Their respective settings were: (1) 0.5 mm, and (2) 150 mm/min ($p < 0.05$). This configuration favoured power consumption rates which are below 50 W.

Verification experiments confirmed the appearance of needle chips. The power consumption ranged at about 70 W which was in accordance to the optimum results predicted from the joint screening of the two characteristics.

3.8. References

[1] A. Toulfatzis, G. Besseris, G. Pantazopoulos, C. Stergiou (2011) Characterization and comparative machinability investigation of extruded and drawn copper alloys using non-parametric multi-response optimization and orthogonal arrays. International Journal of Advanced Manufacturing Technology 57: 811-826.

[2] K. Hassan, A. Kumar, M.P Garg (2012) Experimental investigation of material removal rate in CNC turning using Taguchi method. International Journal of Engineering Research and Applications 2: 1581-1590.

[3] N.M. Vaxevanidis, J.D. Kechagias, N.A. Fountas, D.E. Manolakos (2014) Evaluation of machinability in turning of engineering alloys by applying Artificial Neural Networks. The Open Construction and Building Technology Journal 8: 389-399.

[4] G. Pantazopoulos, A. Toulfatzis (2012) Fracture modes and mechanical characteristics of machinable brass rods. Metallography, Microstructure and Analysis 1: 106-114.

[5] A. Toulfatzis, G. Pantazopoulos, A. Paipetis (2014) Fracture behavior and characterization of lead-free brass alloys for machining applications. Journal of Materials Engineering and Performance 23: 3193-3206.

[6] G. Pantazopoulos (2002) Leaded brass rods C 38500 for automatic machining operations: A technical report. Journal of Materials Engineering and Performance 11: 402-407.

[7] Besseris, G.J (2015) Profiling multiple static and transient puff-pastry characteristics with a robust-and-intelligent processor. Journal of Food Engineering 164 (3): 40-54.

[8] G.J. Besseris (2015) Concurrent multi-response non-linear screening: Robust profiling of webpage performance. European Journal of Operational Research 241: 161-176.

[9] Besseris, G.J (2014) Multi-response non-parametric profiling using Taguchi’s qualimetric engineering and neurocomputing methods: Screening a foaming process in a solar collector assembly. Applied Soft Computing 22 (1): 222-237.

[10] G.J. Besseris (2014) A fast-and-robust profiler for improving polymerase chain reaction diagnostics. PLoS ONE 9: e108973. doi: 10.1371.

[11] G.J. Besseris (2012) Multi-response multi-factorial master ranking in non-linear replicated-saturated DOE for qualimetrics. Chemometrics and Intelligent Laboratory Systems 116: 47-56.

[12] G.J. Besseris (2013) Profiling effects in industrial data mining by non-parametric methods. European Journal of Operational Research 220: 147-161.

[13] G. Taguchi, S. Chowdhury, Y. Wu (2004) Quality Engineering Handbook. Wiley-Interscience, Hoboken, NJ.

Chapter 4: Machinability of Lead-Free Brass Alloys – Cutting Force and Surface Roughness Optimization

4.1. Summary

Surface quality is of major significance, and explicitly demanded in high-precision and productivity machining processes. Moreover, the use of high-speed cutting ensures increased productivity, workpiece dimensional accuracy and improved surface finish [1]. Cutting force is also another important machinability performance indicator, which constitutes a criterion for the selection of optimal process conditions, affecting tool lifetime significantly. Cutting forces could also be calculated using mathematical models and employing renowned machining theories (Oxley's machining theory) based on the determination of strain rates along the shear plastic zone and tool/chip interface [2-3]. Design of experiments (DOE) and genetic algorithm (GA) approaches are powerful and well-established techniques employed to investigate the optimization of cutting parameters such as cutting speed, feed rate, depth of cut, minimum quantity of lubrication (MQL) and alloy type [4-7].

Artificial neural networks (ANN) and response surface methodology (RSM) were used to determine the effect of cutting conditions (cutting speed, feed rate and depth of cut) on cutting force, surface roughness and tool wear during milling of Ti-6242S alloy [8]. In micromilling, tool wear and fracture as well as intense burr formation, and poor surface quality, are considered as the major quality problems. A relevant study investigated the effect of cutting path on the cutting force and surface quality in a micromilling process under different cooling conditions (e.g., dry, air blow, and flood-cooling agent) at fixed cutting parameters [9]. Cutting force and chip segmentation are also well reproduced using finite element method (FEM) (arbitrary Lagrangian-Eulerian and Lagrangian methods) and it was found that chip fragmentation can be correlated to the results of the cutting force development [10].

In this work, a first effort was made to optimize two quality characteristics, cutting force and surface roughness, during turning of the studied brass alloys. The methodology used for the optimization was supported by signal-to-noise ratio data means, as dictated by the Taguchi experimental design and ANOVA. This technique is an efficient and economical way to treat and optimize industrial processes [11-13]. The present work is an original contribution, pertaining to the optimization of machinability of environmentally friendly lead-free brass alloys (CuZn42, CuZn38As and CuZn36), in comparison to a conventional leaded-brass alloy (CuZn39Pb3).

The emergence of new legislation for the environment and health and safety (e.g., drinking-water regulations), together with the necessity to design and manufacture new lead-free machinable alloys, render this project as of high industrial significance. To the best of our knowledge, the present work is novel, since there is not any other published work in this specific area that provides an optimization guideline for cutting force and surface roughness during machining of these lead-free brass alloy classes. It reflects also the original experimental and statistical work performed by the authors, as a part and continuation of a long-term industrial research and development (R&D) project. The data means and signal-to-noise (S/N) responses indicated that the depth of cut and the feed rate were the most influential factors for the cutting force and surface roughness, respectively. The optimized machining parameters for cutting force (34.59 N) and surface roughness (1.22 μm) minimization were determined. Confirmation experiments (cutting force: 39.37 N and surface roughness: 1.71 μm) seem to show that they are in close agreement to the main conclusions, thereby validating the findings of the statistical evaluation performed.

4.2. Microstructure and Mechanical Properties

Metallographic evaluation revealed a duplex-phase microstructure consisting of a mixture of α-β phases of variable content, as anticipated in the Cu-Zn alloy system (Figs. 4.1 and 4.2). Moreover, the microstructure of the CW614N alloy contains ~3% Pb particles, which appeared as black dots (in optical micrographs), that are non-dissolved in α- or β-phase (Fig. 4.1a). Scanning electron microscopy (SEM) observations at higher magnification (×1000) confirmed the findings of the optical microscopy concerning the variation of β-phase content for each studied brass alloy (Fig. 4.2).

The tensile properties augmented significantly with the increase of β-phase volume fraction in brass alloys. More specifically, CW510L (60% β-phase) and CW614N (33% β-phase) exhibited the highest tensile strength (460 MPa and 430 MPa, respectively) and hardness (127 HV and 132 HV, respectively), while they show the lowest total elongation (41% and 28%, respectively), compared to CW511L and C27450 alloys, see also Figures 2.2, 2.3, 2.5 as well Figures 4.1 and 4.2 [14]. The β-phase content is inherently related to the machinability and most effectively to the chip breakability [15]. Chip breaking is mainly controlled by the distribution of Pb particles in conventional leaded brass alloys, while β-phase fraction exerts a major influence on shear band formation and micro-crack generation in lead-free alloys. In a previous research work, CW614N and CW510L possessed the optimum chip-breaking capability, followed by C27450 and CW511L alloys.

The C27450 was marginally superior compared with CW511L alloy, due to its slightly higher content of Pb, which promotes chip breaking [16]. Apart from chip-breaking capability, additional characteristics such as cutting force and surface roughness play an important role in ranking machinability performance. The respective results, pertaining to the optimization of the aforementioned characteristics, are discussed in the following sections.

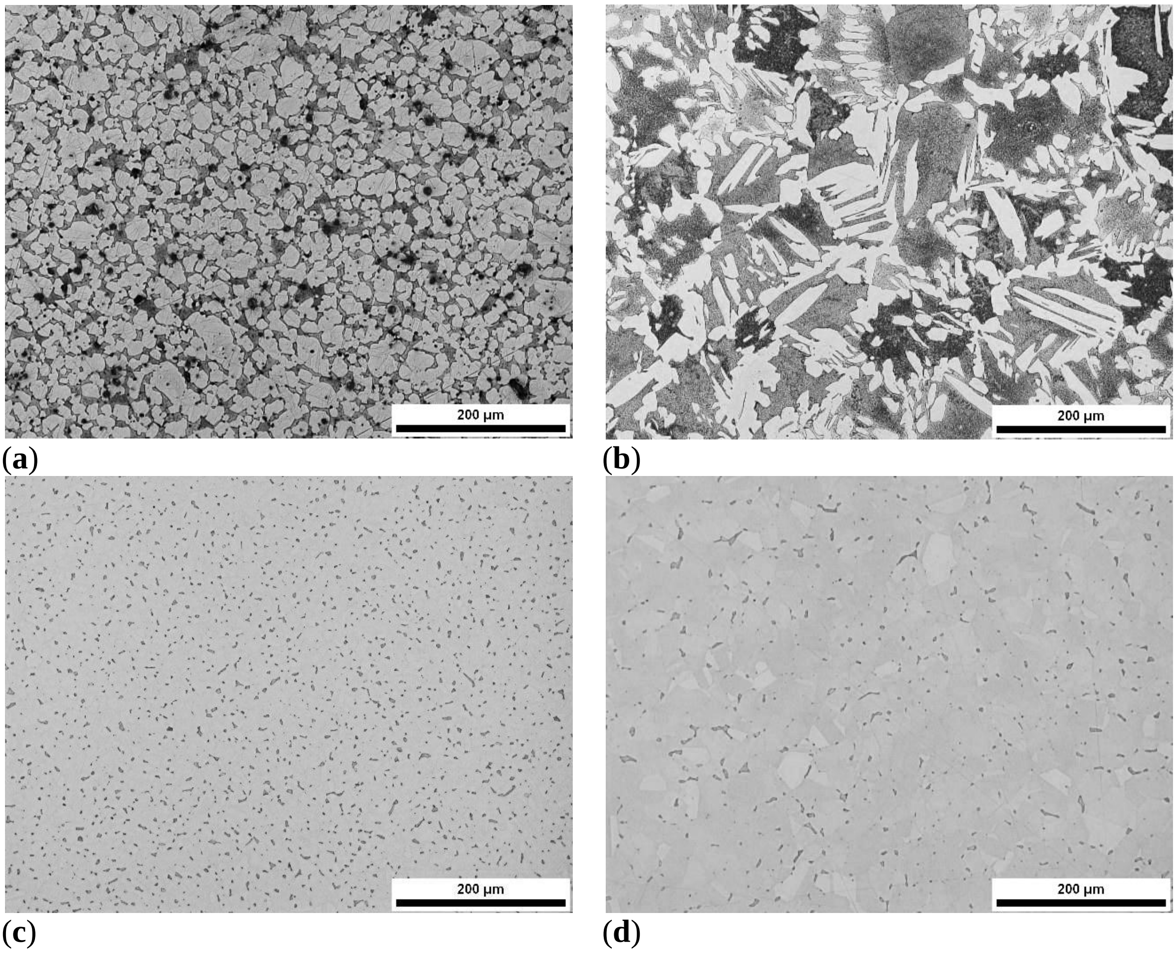

Fig. 4.1: Optical micrographs of the microstructure on transverse sections: (a) CuZn39Pb3 (CW614N) leaded brass as well as (b) CuZn42 (CW510L); (c) CuZn38As (CW511L) and (d) CuZn36 (C27450) lead-free brasses. Light areas represent α-phase and dark areas represent β-phase. In (a) there is an appreciable amount of Pb particles, which appeared as black dots.

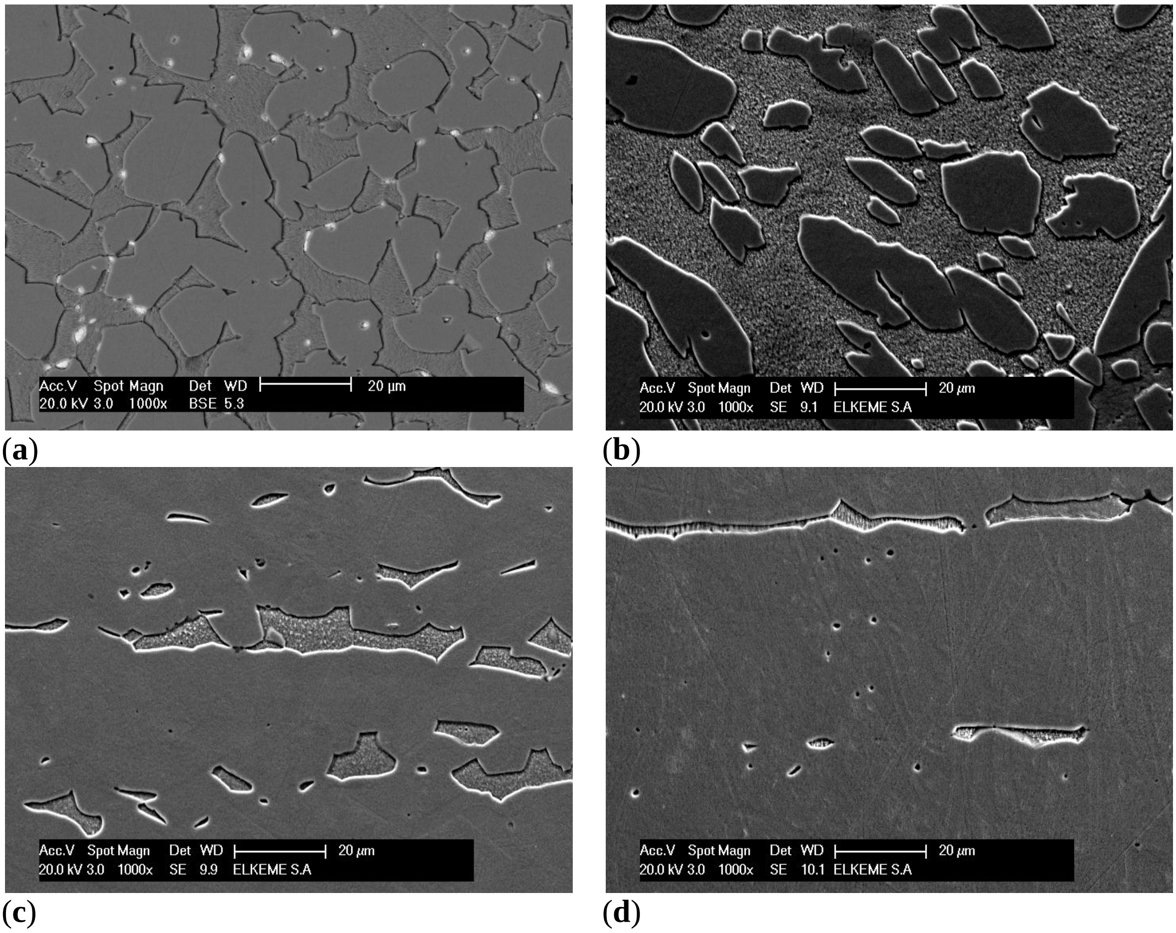

Fig. 4.2: Scanning electron microscopy (SEM) micrographs under secondary and backscattered electron imaging: (a) CuZn39Pb3 (CW614N) leaded brass as well as (b) CuZn42 (CW510L); (c) CuZn38As (CW511L) and (d) CuZn36 (C27450) lead-free brasses. White dots in (a) represent Pb particles in the α/β interfaces. The β-phase is located in the recess areas, as a result of its higher dissolution during chemical etching.

4.3. Machinability Evaluation

During the machinability evaluation, two quality characteristics were selected: the cutting force (CF) and the surface roughness (SR). For reliability reasons, the experiments for the two quality characteristics were repeated twice; see experimental results in Table 4.1 ("REP" stands for replicate). The particular quality characteristics, namely cutting force (CF) and surface roughness (SR), have to be minimized and hence the "smaller-the-better" type quality criterion has been selected for each of the data means and signal-to-noise responses. The governing Equation (1) for the signal-to-noise ratio (S/N) using the above criterion was:

$$[\mathrm{S/N}] = -10\log\left(\sum y_i^2 / n\right), \tag{1}$$

where y_i corresponds to the performance value of the *i*th experiment and *n* was the number of repetitions.

Table 4.1: Experimental results for cutting force (CF) and surface roughness (SR).

Number of Experiment	Material	Quality Characteristics Results					
		CF (N) REP 1	CF (N) REP 2	CF(N) AVERAGE	SR(µm) REP 1	SR(µm) REP 2	SR (µm) AVERAGE
1	**CW510L**	81	80	81	1.8	1.7	1.8
2	**CW511L**	214	223	219	2.1	2.2	2.1
3	**C27450**	344	348	346	2.9	2.7	2.8
4	**CW614N**	454	454	454	10.8	11.4	11.1
5	**C27450**	91	90	91	1.9	2.0	2.0
6	**CW614N**	86	87	87	2.1	2.2	2.2
7	**CW510L**	544	535	540	8.1	8.0	8.0
8	**CW511L**	441	450	446	2.2	2.5	2.3
9	**CW614N**	63	61	62	2.6	2.3	2.4
10	**C27450**	301	299	300	5.7	5.6	5.6
11	**CW511L**	202	215	209	1.8	1.8	1.8
12	**CW510L**	328	324	326	5.6	5.1	5.4
13	**CW511L**	122	129	126	4.4	4.3	4.3
14	**CW510L**	181	174	178	3.3	4.5	3.9
15	**CW614N**	131	131	131	2.1	2.1	2.1
16	**C27450**	242	245	244	4.7	5.8	5.3

4.4. Cutting-Force Optimization

Characteristic histograms of cutting force, produced under various turning conditions, are shown in Figure 4.3.

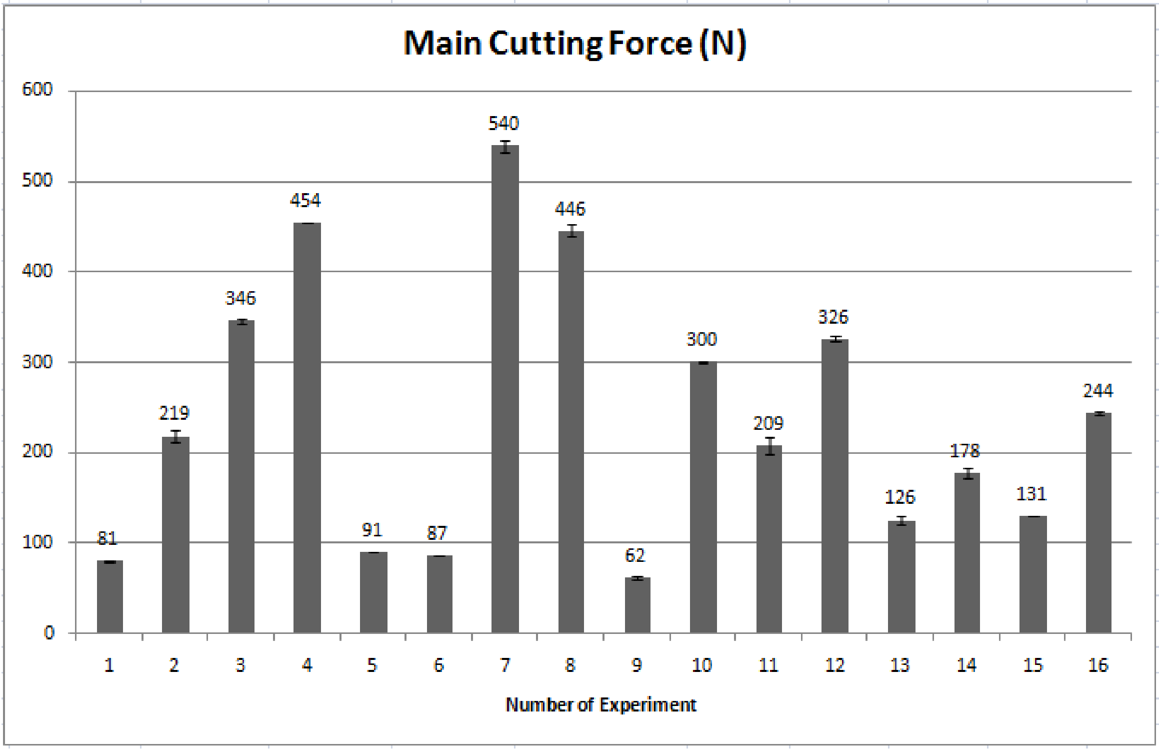

Fig. 4.3: Histogram showing the main cutting force (N) that resulted under various turning conditions.

The plots of main effects of S/N ratios (Fig. 4.4) and data means (Fig. 4.5) indicated that the optimum values of cutting parameters that minimize the cutting force were the following:

1. Alloy type: CW614N;
2. Cutting speed: 2250 rpm;
3. Depth of cut: 0.5 mm;
4. Feed rate: 150 mm/min.

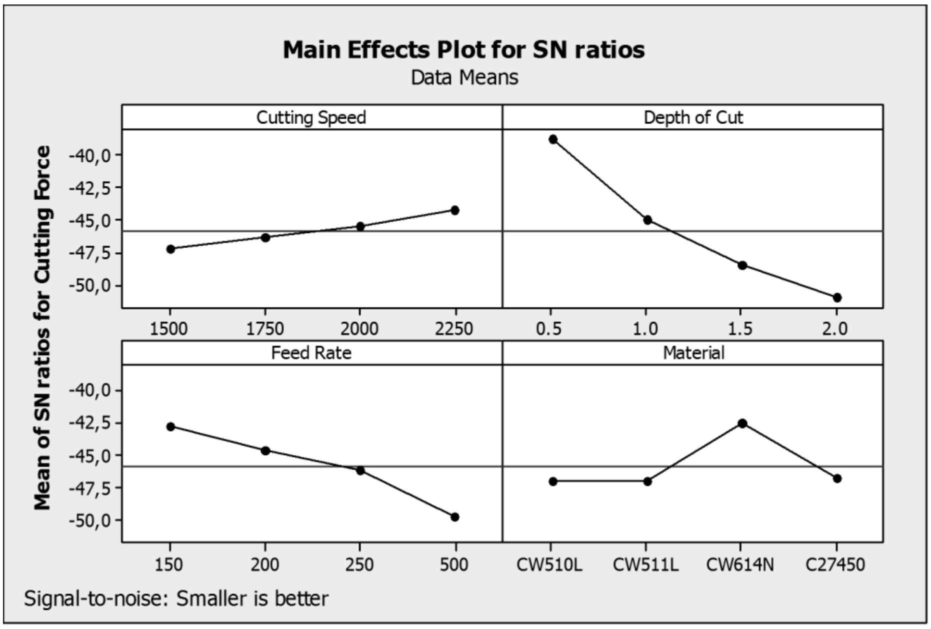

Fig. 4.4: Diagrams showing the variation of signal-to-noise (S/N) ratios for cutting force as a function of the cutting parameters (cutting speed, depth of cut, feed rate and material).

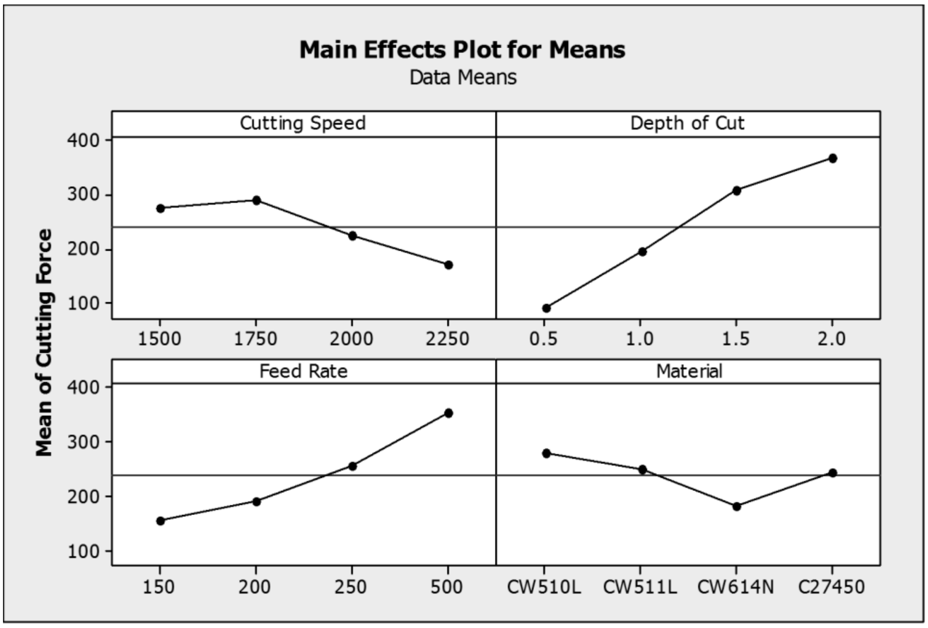

Fig. 4.5: Diagrams showing the data means for cutting force as a function of the cutting parameters (cutting speed, depth of cut, feed rate and material).

Experimental results indicated that the most critical factor affecting the cutting force (CF), during brass-bar machining, is the depth of cut, while the less influential factors for CF are the cutting speed and the type of brass alloy (Table 4.2). An important step in the Taguchi methodology is to perform confirmation experiments. The predicted S/N ratio using the optimal level of the design parameters can be calculated by the following equation [17]:

$$[S/N]_{\text{predicted}} = [S/N]_{\text{m}} + \sum_{i=1}^{n} ([S/N]_i - [S/N]_{\text{m}}), \tag{2}$$

where $[S/N]_{\text{m}}$ is the total mean S/N ratio, $[S/N]_i$ is the S/N ratio at the optimal level of the ith parameter, and n is the number of the main design parameters that affect the quality characteristic.

In the case of cutting force: $[S/N]_{\text{m}} = -45.8369$.

So, the predicted S/N ratio using the optimal parameters for cutting force (CF) is given below:

$$[S/N]_{\text{predicted}} = -30.78$$

From Equation (1) and substituting the [S/N] term with the predicted value (−30.78) this yields to:

$$y = \text{Predicted Cutting Force} = 34.59\ \text{N}$$

Table 4.2: Response table for signal-to-noise (S/N) ratios for cutting force.

Response Table	Cutting Speed (rpm)	Depth of Cut (mm)	Feed Rate (mm/min)	Material
Level 1	−47.21	−38.77	−42.74	−47.00
Level 2	−46.37	−45.01	−44.63	−47.03
Level 3	−45.51	−48.54	−46.15	−42.52
Level 4	−44.26	−51.03	−49.82	−46.80
Difference	2.95	12.26	7.08	4.51
Rank	4	1	2	3

Table 4.3 shows the comparison of the estimated (predicted) and the measured (experimental) cutting force values using the optimal conditions, where it has been deduced that there is sufficient agreement between the predicted (34.59 N) and the experimental cutting force (39.37 N) values.

In terms of cutting force, it seems that the conventional leaded alloy CW614N exhibits the highest machinability performance, signifying the dominant effect of the presence of Pb on cutting force reduction, as was also confirmed in case of chip breakability [16].

Table 4.3: Results of confirmation experiment.

Quality Characteristic	Cutting Speed (rpm)	Depth of Cut (mm)	Feed Rate (mm/min)	Material	Experimental Value	Predicted Value
Cutting Force	2250	0.5	150	CW614N	39.37 N	34.59 N
Surface Roughness	1750	0.5	150	CW511L	1.71 μm	1.22 μm

4.5. Surface-Roughness Optimization

Characteristic measurements of surface roughness, resulted by the L_{16} orthogonal array experiments (Table B.2), produced under various turning conditions, are shown in Figures 4.6 and 4.7.

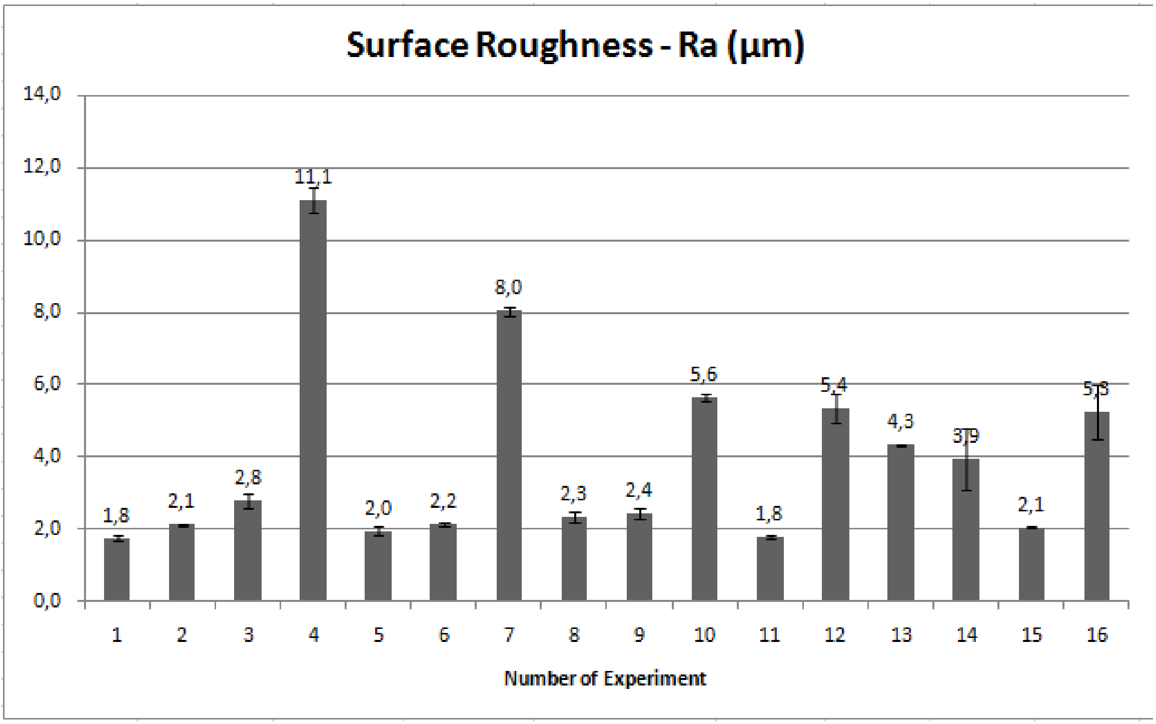

Fig. 4.6: Histogram showing the surface roughness—Ra (μm) that resulted under various turning conditions.

Exp.No	Surface Roughness (SR)
1	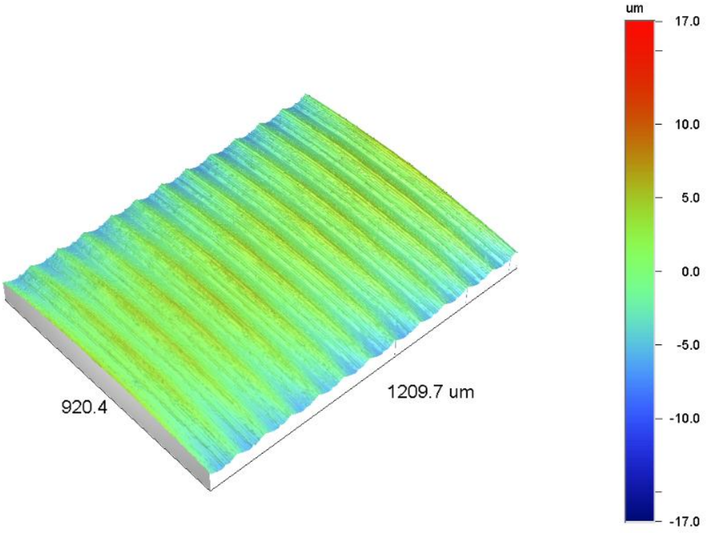 Cutting Speed (rpm): 1500 Depth of Cut (mm): 0.50 Feed Rate (mm/min): 150 Material: CW510L **Average Surface Roughness: 1.8 µm**
2	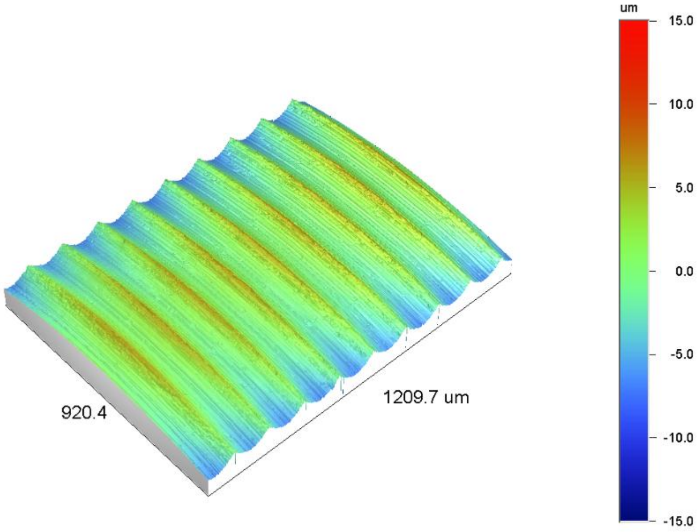 Cutting Speed (rpm): 1500 Depth of Cut (mm): 1.00 Feed Rate (mm/min): 200 Material: CW511L **Average Surface Roughness: 2.1 µm**
3	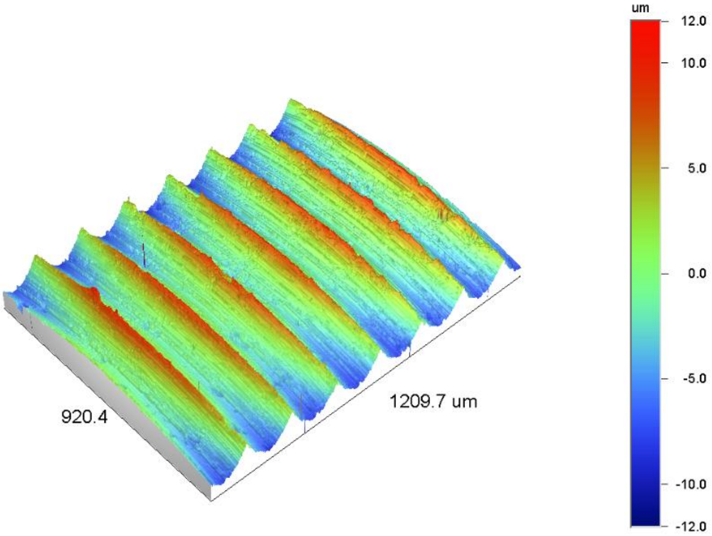 Cutting Speed (rpm): 1500 Depth of Cut (mm): 1.50 Feed Rate (mm/min): 250 Material: C27450 **Average Surface Roughness: 2.8 µm**

Fig. 4.7 Cont’ed

4	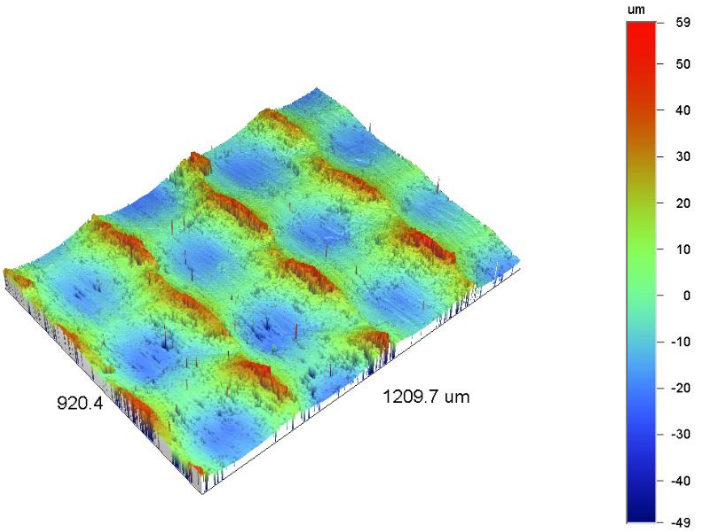 Cutting Speed (rpm): 1500 Depth of Cut (mm): 2.00 Feed Rate (mm/min): 500 Material: CW614N **Average Surface Roughness: 11.1 µm**
5	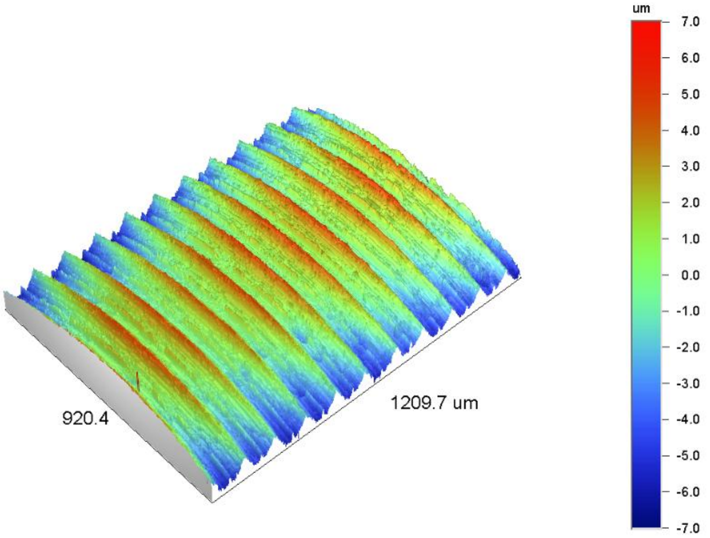 Cutting Speed (rpm): 1750 Depth of Cut (mm): 0.50 Feed Rate (mm/min): 200 Material: C27450 **Average Surface Roughness: 2.0 µm**
6	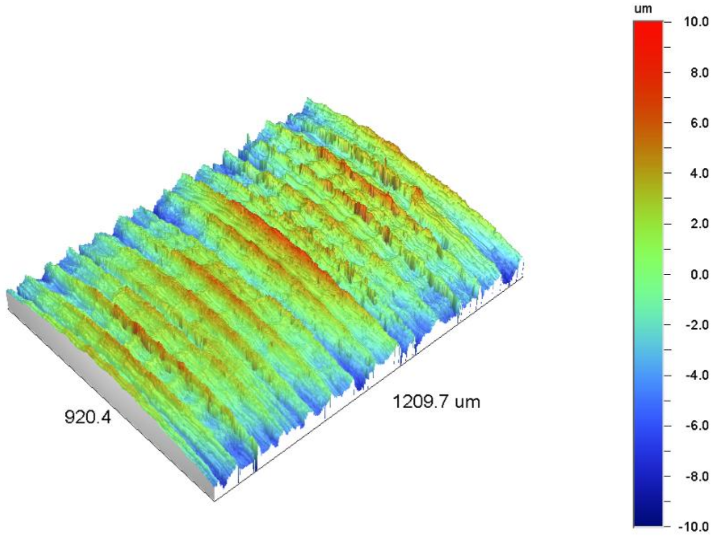 Cutting Speed (rpm): 1750 Depth of Cut (mm): 1.00 Feed Rate (mm/min): 150 Material: CW614N **Average Surface Roughness: 2.2 µm**

Fig. 4.7 Cont'ed

7	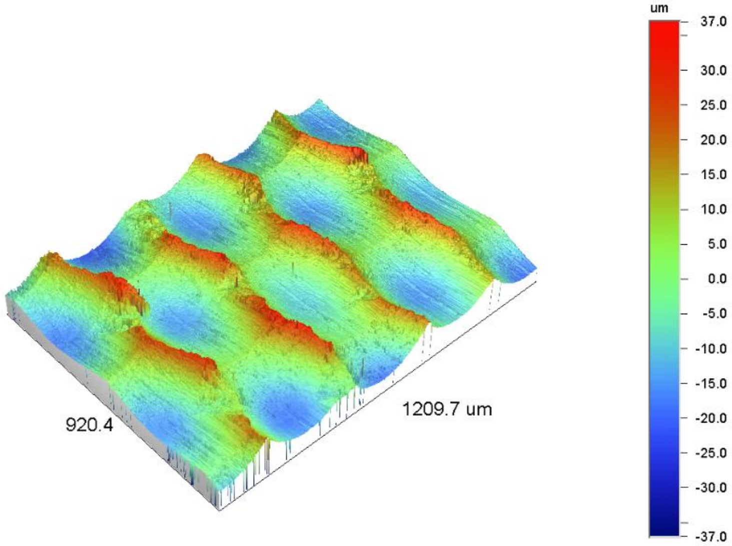 Cutting Speed (rpm): 1750 Depth of Cut (mm): 1.50 Feed Rate (mm/min): 500 Material: CW510L **Average Surface Roughness: 8.0 µm**
8	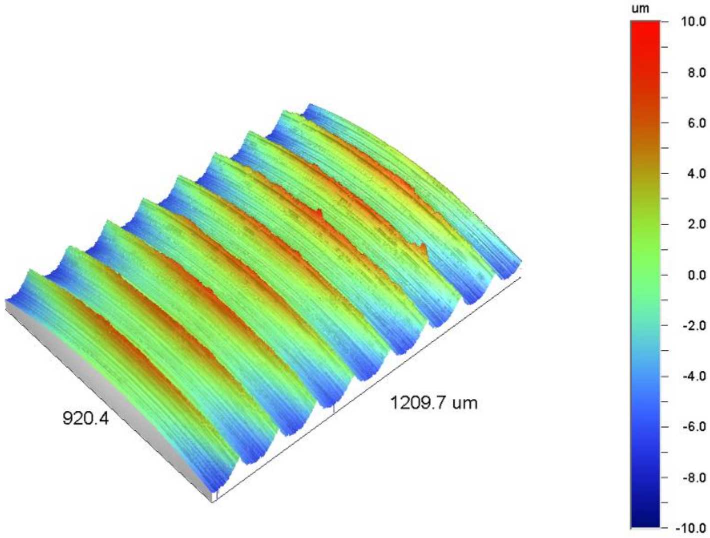 Cutting Speed (rpm): 1750 Depth of Cut (mm): 2.00 Feed Rate (mm/min): 250 Material: CW511L **Average Surface Roughness: 2.3 µm**
9	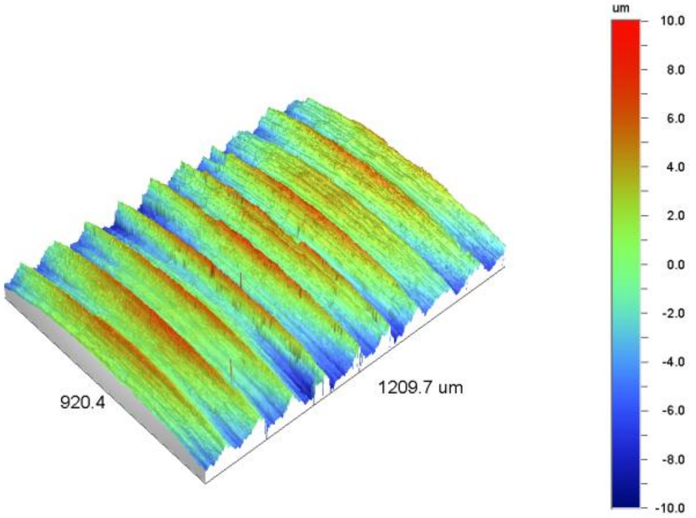 Cutting Speed (rpm): 2000 Depth of Cut (mm): 0.50 Feed Rate (mm/min): 250 Material: CW614N **Average Surface Roughness: 2.4 µm**

Fig. 4.7 Cont'ed

10	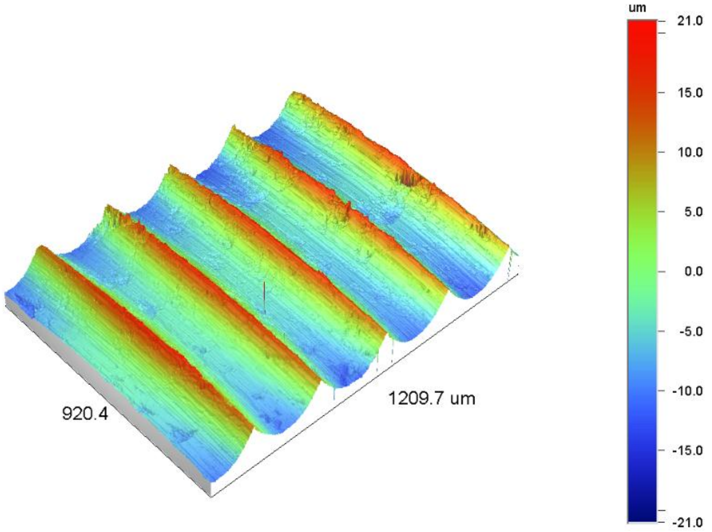	Cutting Speed (rpm): 2000 Depth of Cut (mm): 1.00 Feed Rate (mm/min): 500 Material: C27450 **Average Surface Roughness: 5.6 µm**
11	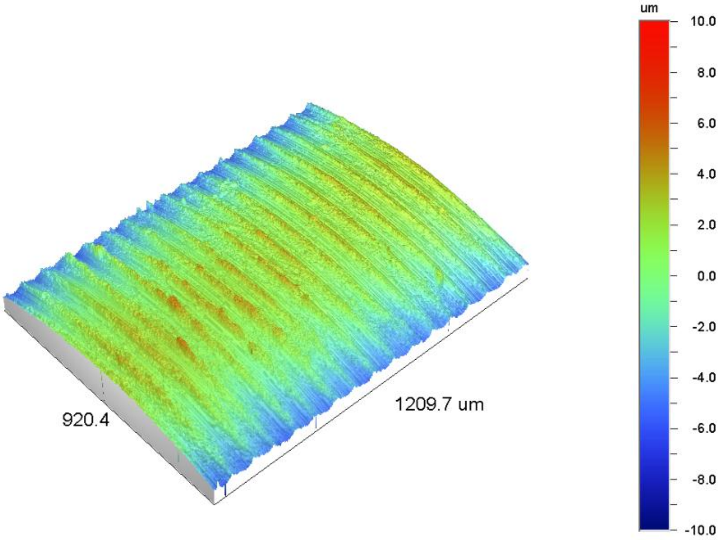	Cutting Speed (rpm): 2000 Depth of Cut (mm): 1.50 Feed Rate (mm/min): 150 Material: CW511L **Average Surface Roughness: 1.8 µm**
12	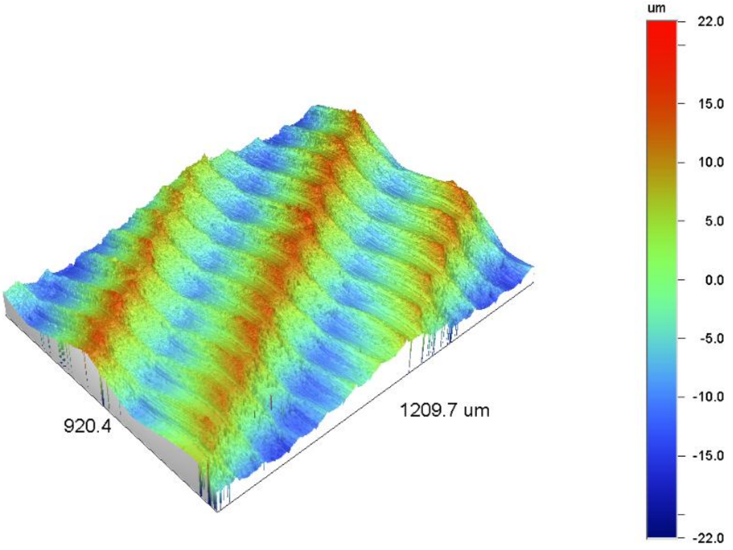	Cutting Speed (rpm): 2000 Depth of Cut (mm): 2.00 Feed Rate (mm/min): 200 Material: CW510L **Average Surface Roughness: 5.4 µm**

Fig. 4.7 Cont'ed

13	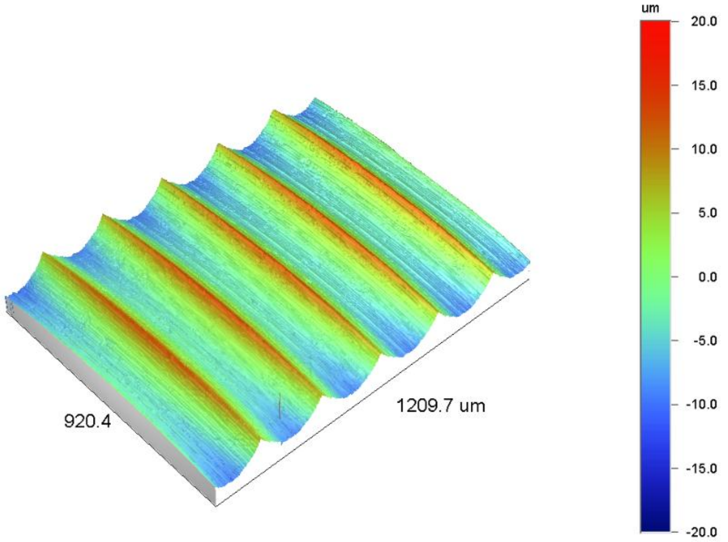	Cutting Speed (rpm): 2250 Depth of Cut (mm): 0.50 Feed Rate (mm/min): 500 Material: CW511L **Average Surface Roughness: 4.3 µm**
14	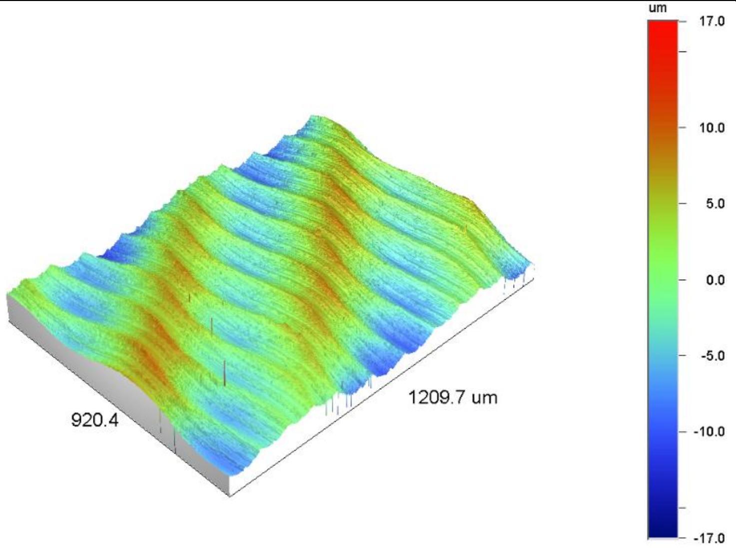	Cutting Speed (rpm): 2250 Depth of Cut (mm): 1.00 Feed Rate (mm/min): 250 Material: CW510L **Average Surface Roughness: 3.9 µm**
15	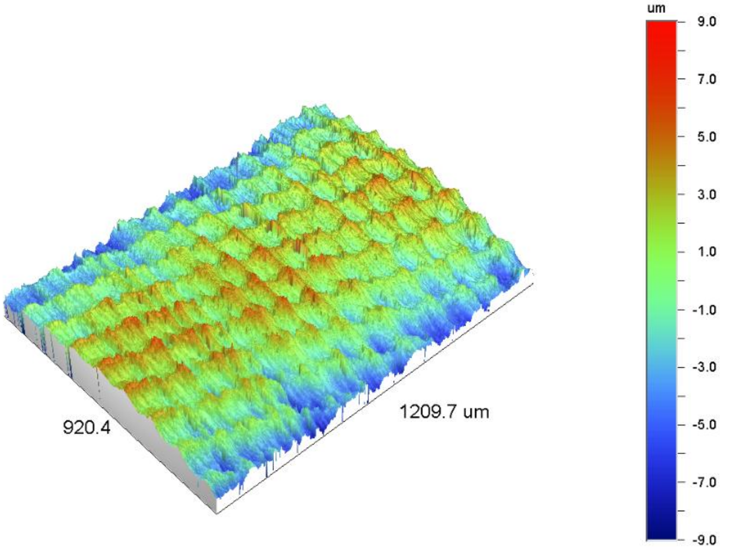	Cutting Speed (rpm): 2250 Depth of Cut (mm): 1.50 Feed Rate (mm/min): 200 Material: CW614N **Average Surface Roughness: 2.1 µm**

Fig. 4.7 Cont'ed

16

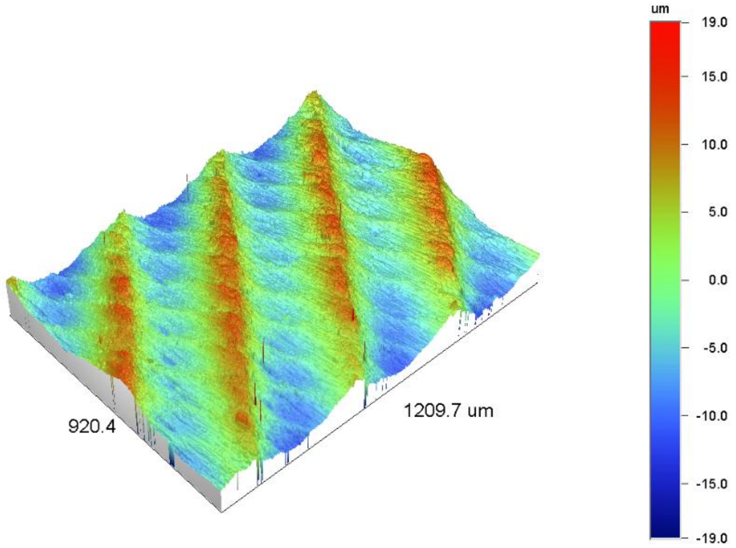

Cutting Speed (rpm): 2250
Depth of Cut (mm): 2.00
Feed Rate (mm/min): 150
Material: C27450

Average Surface Roughness: 5.3 µm

Fig. 4.7: Images showing the surface roughness (SR) measurements resulted under various turning conditions, during the designed experiments (1-16).

The graphs of the responses of S/N ratios (Fig. 4.8) and data means (Fig. 4.9) indicated that the values of cutting parameters which optimize the surface roughness were the following:

1. Alloy type: CW511L;
2. Cutting speed: 1750 rpm;
3. Depth cut: 0.50 mm;
4. Feed rate: 150 mm/min.

Experimental results indicated that the most critical factor affecting the surface roughness (SR), during brass-bar machining, is the feed rate, while SR seems to be not so highly sensitive to cutting speed and the type of brass alloy used varied (Table 4.4). In order to verify the adequacy of the Taguchi methodology, a confirmation test was performed. The predicted S/N ratio using the optimal level of the design parameters can be calculated by Equation (2).

Table 4.4: Response table for S/N ratios for surface roughness.

Response Table	Cutting Speed (rpm)	Depth of Cut (mm)	Feed Rate (mm/min)	Material
Level 1	−10.325	−7.819	−7.776	−12.368
Level 2	−9.496	−10.034	−8.315	−7.957
Level 3	−10.623	−9.603	−8.983	−10.396
Level 4	−11.331	−14.318	−16.700	−11.054
Difference	1.836	6.499	8.924	4.411
Rank	4	2	1	3

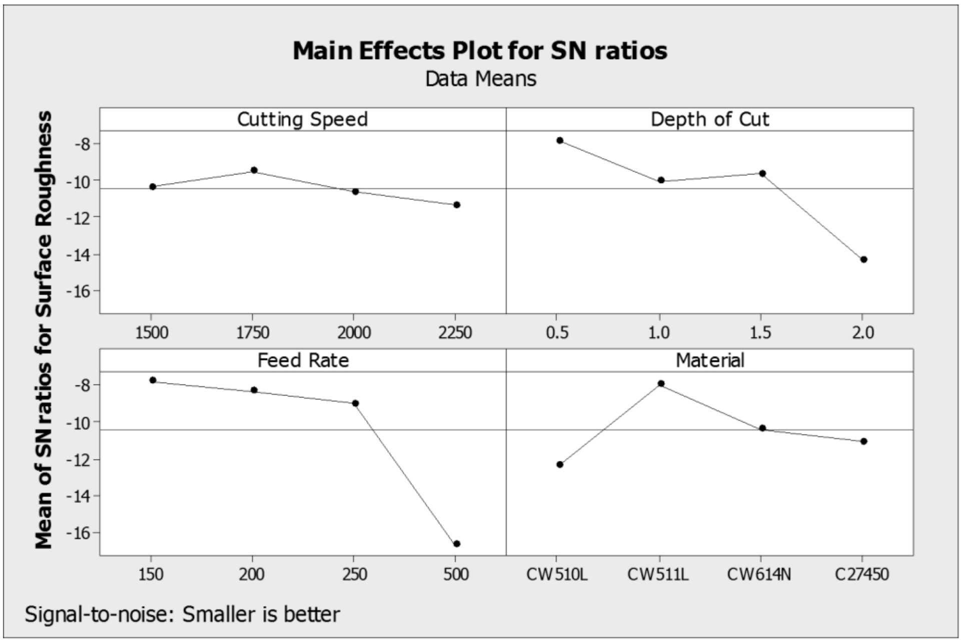

Fig. 4.8: Diagrams showing the variation of S/N ratios for surface roughness as a function of the cutting parameters (cutting speed, depth of cut, feed rate and material).

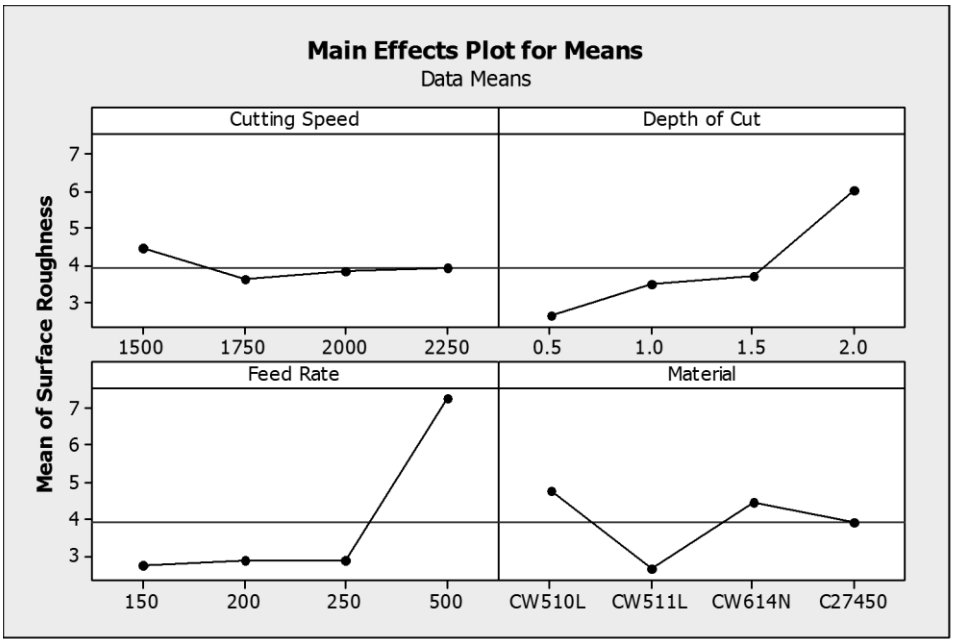

Fig. 4.9: Diagrams showing the data means for surface roughness as a function of the cutting parameters (cutting speed, depth of cut, feed rate and material).

In the case of surface roughness:

$$[S/N]_m = -10.4436$$

So, the predicted S/N ratio using the optimal parameters for surface roughness (SR) can be obtained and calculated as previously:

$$[S/N]_{predicted} = -1.72$$

Therefore, the predicted surface roughness, as calculated by Equation (1), is:

$$y = \text{Predicted Surface Roughness} = 1.22\ \mu\text{m}$$

Table 4.3 shows the comparison of the estimated (predicted) and the measured (experimental) surface roughness where it seems that there is a relative agreement between the predicted (1.22 μm) and the experimental (1.71 μm) surface-roughness values. Regarding surface roughness, the highest score was achieved by lead-free alloy CW511L, compared with the other lead-free alloys studied and a typical leaded one, which pinpoints a promising candidate whereby surface quality is considered as the most critical machinability criterion.

4.6. Analysis of Variance (ANOVA)

The contribution of each factor to the cutting force and surface roughness during the machining of lead-free brass alloys can be determined by performing ANOVA based on equations [17-19], which are listed below:

$$\mathrm{SS}_{\mathrm{T}} = \sum_{i}^{m} n_i^2 - \frac{1}{m}[\sum_{i=1}^{m} n_i]^2 \qquad \textit{Total Sum of Squares (}\mathrm{SS}_{\mathrm{T}}\textit{)} \tag{3}$$

$$\mathrm{SS}_{\mathrm{p}} = \sum_{j=1}^{t} \frac{(S_{nj})^2}{t} - \frac{1}{m}(\sum_{i=1}^{m} n_i)^2 \qquad \textit{Factorial Sum of Squares (}\mathrm{SS}_{\mathrm{p}}\textit{)} \tag{4}$$

$$V_{\mathrm{p}}(\%) = \frac{SS_{\mathrm{p}}}{D_{\mathrm{p}}} \times 100 \qquad \textit{Factorial Variance (}V_{\mathrm{p}}\textit{)} \tag{5}$$

$$\mathrm{SS'}_{\mathrm{p}} = SS_{\mathrm{p}} - D_{\mathrm{p}} V_{\mathrm{e}} \qquad \textit{Corrected Sum of Squares of a factor (}\mathrm{SS'}_{\mathrm{p}}\textit{)} \tag{6}$$

$$P_{\mathrm{p}}(\%) = \frac{SS'_{\mathrm{p}}}{SS_{\mathrm{T}}} \times 100 \qquad \textit{Percent Contribution (}P_{\mathrm{p}}\textit{)} \tag{7}$$

where m is the total number of the experiments, n_i is the S/N ratio at the ith test, S_{nj} the sum of the S/N ratio involving this factor and level j, D_{p} is the degree of freedom for each factor, and V_{e} is the error variance. The percent contribution (P_{p}) is used to evaluate the significance of the factorial change on the quality characteristic, i.e., cutting force and surface roughness [20].

The results of ANOVA for the cutting force and surface roughness are summarized in Tables 4.5 and 4.6 respectively. The data given in Tables 4.5 and 4.6 show the contribution of the four factors, i.e., cutting speed, depth of cut, feed rate and materials to the quality characteristics.

It is clear that, among the selected factors, the depth of cut and feed rate have the major influence on the cutting force and surface roughness, respectively. By ranking their relative contributions, the sequence of the four factors affecting the cutting force is the depth of cut, the feed rate, the material type and, finally, the cutting speed, while for surface roughness the corresponding sequence in decreasing order is the following: feed rate, depth of cut, material type and, finally, cutting speed. In the ANOVA analysis, the percentage error (P_e) contribution to the total variance is lower than 15% (0.43% and 10.50% for cutting force and surface roughness, respectively), showing that no important factor is missing in the experimental design [17].

Table 4.5: Analysis of variance (ANOVA) for the cutting force.

Factor	Degrees of Freedom	Sum of Squares (SS)	Corrected Sum of Squares (SS')	Variance	Percent Contribution P_p (%)	Rank
Cutting Speed	3	19.0425	18.8254	6.3475	3.5728	4
Depth of Cut	3	339.5408	339.3238	113.1803	64.3992	1
Feed Rate	3	108.0831	107.8660	36.0277	20.4715	2
Material	3	58.8660	58.6489	19.6220	11.1308	3
Error	19	1.3746	2.2428	0.0723	0.4257	
Total	31	526.9070	526.9070		100.0000	

Table 4.6: Analysis of variance (ANOVA) for the surface roughness.

Factor	Degrees of Freedom	Sum of Squares (SS)	Corrected Sum of Squares (SS')	Variance	Percent Contribution P_p (%)	Rank
Cutting Speed	3	7.3498	3.5422	2.4499	0.9460	4
Depth of Cut	3	91.6606	87.8530	30.5535	23.4625	2
Feed Rate	3	210.9051	207.0974	70.3017	55.3085	1
Material	3	40.4101	36.6025	13.4700	9.7753	3
Error	19	24.1149	39.3453	1.2692	10.5078	
Total	31	374.4404	374.4404		100.0000	

4.7. Section Conclusions

Machinability assessment was performed to three lead-free brass alloys in comparison to a standard leaded brass alloy at the initial production condition (extruded and drawn). Cutting force is optimized using the following conditions (using signal-to-noise and data means): the optimum alloy type is CW614N, cutting speed = 2250 rpm, depth cut = 0.5 mm and feed rate = 150 mm/min. ANOVA showed that the contributions of the above factors are 11.13%, 3.57%, 64.40% and 20.47%, respectively. The analysis coming from data means and S/N response tables indicated that the depth of cut is the most influential factor, while ANOVA proved that this parameter has the highest percent contribution (Pp = 64.40%) and, consequently, plays the most affecting role in the determination of cutting-force measurements. Also, since the percentage error (0.43%) contribution in ANOVA analysis is lower than 50%, no repetition of any experiment is needed.

Surface roughness is optimized using the following conditions (using signal-to-noise and data means): the optimum alloy type is CW511L, cutting speed = 1750 rpm, depth cut = 0.50 mm and feed rate = 150 mm/min. The contributions of the above factors are 9.78%, 0.95%, 23.46% and 55.31%, respectively, according to the ANOVA technique. The same ranking order was also achieved by the S/N method. Feed rate has the highest percentage contribution (Pp = 55.31%), as it was proven by ANOVA and it constitutes also the most influential factor according to data means and S/N response tables. Since the percentage error (10.51%) contribution deduced from ANOVA analysis is lower than 50%, no experimental repetition is required.

Confirmation experiments indicated that a considerable agreement leading to around 10% deviation was achieved for cutting force (predicted 34.59 N vs. experimental 39.37 N). Although surface-roughness experiments resulted in higher differences (predicted 1.22 μm vs. experimental 1.71 μm), the obtained values are considered comparable and of the same order of magnitude, taking into account the entire spectrum of the tested conditions. In terms of cutting-force optimization, the leaded alloy CW614N exhibited the highest machinability performance, while for surface roughness, the lead-free CW511L was appointed as the optimum alloy selection. Although leaded brasses still dominate in the machining industry, this result offers a hopeful perspective, expanding the horizons for further research towards machinability improvement through further alloy and microstructural design.

4.8. References

[1] S. Ekinovic, E. Begovic, A. Silajdzija (2007) Comparison of machined surface quality obtained by high-speed machining and conventional turning. Machining Science and Technology 11: 531-551.

[2] D. Huo, W. Chen, X. Teng, C. Lin, K. Yang (2017) Modeling the influence of tool deflection on cutting force and surface generation in micro-milling. Micromachines 188, doi: 10.3390/mi8060188.

[3] W. Jomaa, V. Songmene, P. Bocher (2017) Predictive analytical modeling of cutting forces generated by high-speed machining of ductile and hard metals. Machining Science and Technology 21: 335-361.

[4] A. Toulfatzis, G. Besseris, G. Pantazopoulos, C. Stergiou (2011) Characterization and comparative machinability investigation of extruded and drawn copper alloys using non-parametric multi-response optimization and orthogonal arrays. International Journal of Advanced Manufacturing Technology 57: 811-826.

[5] K. Hassan, A. Kumar, M.P. Garg (2012) Experimental investigation of material removal rate in CNC turning using Taguchi method. International Journal of Engineering Research and Applications 2: 1581-1590.

[6] N.M.Vaxevanidis, J.D. Kechagias, N.A. Fountas, D.E. Manolakos (2014) Evaluation of machinability in turning of engineering alloys by applying artificial neural networks. The Open Construction and Building Technology Journal 8: 389-399.

[7] V.N. Gaitonde, S.R. Karnik, J.P. Davim (2012) Optimal MQL and cutting conditions determination for desired surface roughness in turning of brass using genetic algorithms. Machining Science and Technology 16: 304-320.

[8] E. Kilickap, A. Yardimeden, Y.H. Çelik (2017) Mathematical modelling and optimization of cutting force, tool wear and surface roughness by using artificial neural network and response surface methodology in milling of Ti-6242S. Applied Sciences 7, 1064, doi: 10.3390/app7101064.

[9] U. Koklu, G. Basmaci (2017) Evaluation of tool path strategy and cooling condition effects on the cutting force and surface quality in micromilling operations. Metals 7, 426, doi: 10.3390/met7100426.

[10] B. Haddag, S. Atlati, M. Nouari, A. Moufki (2016) Dry machining aeronautical aluminum alloy AA2024-T351: Analysis of cutting forces, chip segmentation and built-up edge formation. Metals 6, 197, doi: 10.3390/met6090197.

[11] Y.S. Ahmed, H. Youssef, H. El-Hofy, M. Ahmed (2018) Prediction and optimization of drilling parameters in drilling of AISI 304 and AISI 2205 steels with PVD monolayer and multilayer coated drills. Journal of Manufacturing and Materials Processing 2, 16, doi: 10.3390/jmmp2010016.

[12] G.E.P. Box, W.G. Hunter, J.S. Hunter (2005) Statistics for experimenters: design, innovation, discover. 2nd Edition, Wiley: Hoboken.

[13] G. Taguchi (1986) Introduction to quality engineering. Asian Productivity Organization: Tokyo.

[14] A. Toulfatzis, G. Pantazopoulos, A. Paipetis (2014) Fracture behavior and characterization of lead-free brass alloys for machining applications. Journal of Materials Engineering and Performance 23: 3193-3206.

[15] G. Pantazopoulos, A. Vazdirvanidis (2008) Characterization of microstructural aspects of machinable α-β phase brass. Microscopy and Analysis 22: 13-16.

[16] A.I. Toulfatzis, G.A. Pantazopoulos, G.J. Besseris, A.S. Paipetis (2016) Machinability evaluation and screening of leaded and lead-free brasses using a non-linear robust multifactorial profiler. International Journal of Advanced Manufacturing Technology 86: 3241-3254.

[17] M. Yousefieh, M. Shamanian, A.R. Arghavan (2012) Analysis of design of experiments methodology for optimization of pulsed current GTAW process parameters for ultimate tensile strength of UNS S32760 welds. Metallography, Microstructure, and Analysis 1: 85-91.

[18] Y. Ma, H. Hu, D. Northwood, X. Nie (2007) Optimization of the electrolytic plasma oxidation processes for corrosion protection of magnesium alloy AM50 using the Taguchi method. Journal of Materials Processing Technology 182: 58-64.

[19] M. Yousefieh, M. Shamanian, A. Saatchi, (2011) Optimization of the pulsed current gas tungsten arc welding (PCGTAW) parameters for corrosion resistance of super duplex stainless steel (UNS S32760) welds using the Taguchi method. Journal of Alloys and Compounds 509: 782-788.

[20] A. Mariajayaprakash, T. Senthilvelan (2014) Optimizing process parameters of screw conveyor (sugar mill boiler) through failure mode and effect analysis (FMEA) and Taguchi method. Journal of Failure Analysis and Prevention 14: 772-783.

Chapter 5: Modification of Microstructure and Mechanical Properties by Final Heat Treatment

5.1. Summary

The present work is focused on the improvement of the machinability of lead-free brasses, aiming to increase and stabilize β-phase fraction, through the application of various heat treatment cycles. The increase of β-phase fraction, leads to an overall increase in the hardness and lower ductility - at ambient temperature for the lead-free brass alloy. As a result, increased β-phase leads to better chip breaking capability and consequently the developed alloy is expected to have improved machinability properties [1]. To this end, heat treatments with rapid water quenching were performed in brasses in order to increase β-phase fraction hindering the β to α phase transformation. For this purpose, three machinable lead-free brasses, namely CuZn42 (CW510L), CuZn38As (CW511L) and CuZn36 (C27450) were evaluated in relation to their microstructure and mechanical behaviour as a function of the imposed heat treatment, and the resulting increase in the β-phase fraction. This is hoped to improve machinability but is to be checked in further work.

To the authors' knowledge, no relevant literature is published concerning the tailoring of the alloy microstructure via thermal treatment, with a view to counterbalance the absence of lead and to optimize the machinability for lead free brass alloys.

The most successful heat treatment was chosen for each studied alloy according to the above criteria. More specifically:

- CW510L - HT 5 (775°C for 60 min): R_m=430 MPa, $R_{p0.2}$=175 MPa, A_{50}=14% (β-phase: 100%).
- CW511L - HT 18 (850°C for 120 min): R_m=396 MPa, $R_{p0.2}$=136 MPa, A_{50}=44% (β-phase: 35%)
- C27450 - HT 24 and HT 27 (850°C for 60 and 120 min respectively): R_m=361-364 MPa, $R_{p0.2}$=118 MPa, A_{50}=47-51% (β-phase: 20%)

The selected protocols led to a combination of β-phase augmentation with mechanical properties conforming to standards providing a promising ground for improved machinability performance.

5.2. Characterization of Microstructure after Heat Treatment

All the studied lead-free brass alloys exhibited a duplex phase microstructure of both α-and β-ordered phases (a.k.a β' phase, here the term β will be used for simplicity purposes), with a variable β-phase content. The α-phase is a solid solution of Cu and Zn rich in copper, possessing a face-centered-cubic (fcc) crystal lattice, and β-phase is a non-stoichiometric intermetallic phase corresponding to CuZn compound, possessing a body-centered-cubic (bcc) crystal lattice [1-2]. Figure 5.1 depicts three representative micrographs showing the microstructure of the CuZn42 (CW510L), CuZn38As (CW511L) and CuZn36 (C27450) lead-free brasses in the "as received" condition see also previous study reported in Ref. [3]. The percentages of β-phase are 60%, 5% and 2% respectively. The broad spectrum of β-phase content for the examined alloy bars implied high variability in terms of machinability behaviour. Along with the variation of β-phase volume fraction, substantial differences in phase morphology were also observed.

In the case of CuZn42 (CW510L), a characteristic Widmanstätten-type structure consisting of α-intersecting acicular crystals in β-phase matrix was observed. Formation of similar non-equilibrium structures were reported in Refs. [4] and [5] for CuZn40 and CuZn39Pb3 brass alloys.

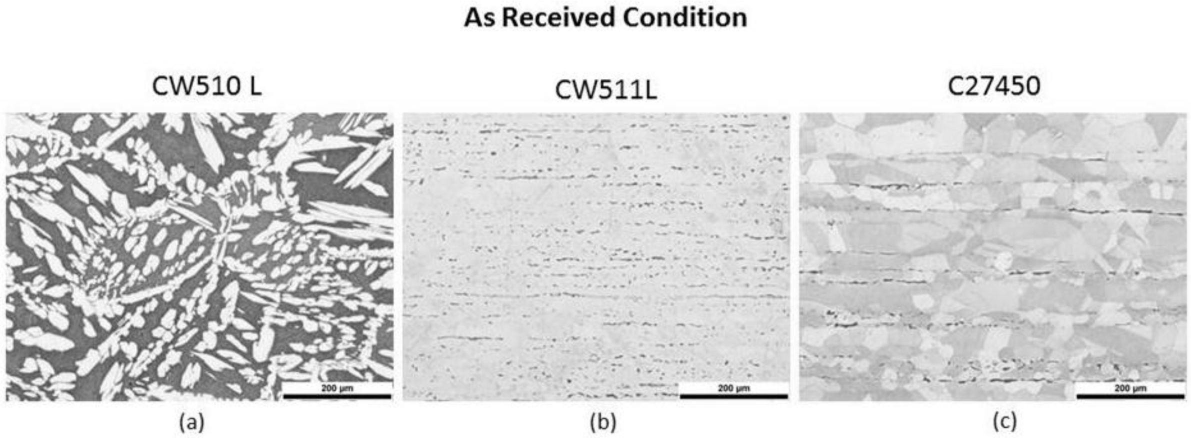

Fig. 5.1: Indicative optical micrographs showing the phase structure of longitudinal sections of "as received": (a) CuZn42 (CW510L), (b) CuZn38As (CW511L) and (c) CuZn36 (C27450) lead-free brasses, captured at x200 original magnifications and bright filed illumination. Note that bright areas represent α-phase and dark areas represent β-phase regions.

Heat treatment trials (Table 5.1) were performed, towards the alteration of the microstructure, by increasing the β-phase percentage. The material structure was effectively changed due to both dynamic recrystallization and the following water quenching effect which suppressed the β→α transformation.

Alloys possessing higher β-phase fractions demonstrated higher tensile strength and lower elongation values, expected to improve the machinability of lead-free brasses [6].

Table 5.1: Heat treatment schedule and obtained microstructure / mechanical testing results.

Heat Treatment	**Brass Alloy**	**Temperature (°C)**	**Soaking Time (min)**	**β-phase (%)**	**$Rp_{0.2}$ (MPa)**	**R_m (MPa)**	**A_{50} (%)**	**HV_1 Midway**
AR 510	CW510L	As Received		60	250	460	41	127
HT 1		700	15	85	156	469	34	130
HT 2		775	15	100	168	496	27	135
HT 3		850	15	100	145	197	2	128
HT 4		700	60	100	137	208	6	132
HT 5		775	60	100	175	430	14	138
HT 6		850	60	100	168	306	5	132
HT 7		700	120	100	168	293	5	132
HT 8		775	120	100	173	349	7	132
HT 9		850	120	100	159	220	4	135
AR 511	CW511L	As Received		5	250	380	42	116
HT 10		700	15	10	187	371	48	80
HT 11		775	15	25	151	402	44	93
HT 12		850	15	30	153	407	44	90
HT 13		700	60	15	116	383	59	83
HT 14		775	60	25	137	414	48	95
HT 15		850	60	30	153	414	41	98
HT 16		700	120	20	121	391	58	81
HT 17		775	120	30	140	416	44	94
HT 18		850	120	35	136	396	44	102
AR 27450	C27450	As Received		2	185	320	48	98
HT 19		700	15	2	148	319	46	67
HT 20		775	15	10	109	352	60	76
HT 21		850	15	10	116	350	51	80
HT 22		700	60	2	86	318	77	67
HT 23		775	60	15	104	356	63	84
HT 24		850	60	20	118	361	51	85
HT 25		700	120	2	88	317	72	68
HT 26		775	120	15	107	359	60	79
HT 27		850	120	20	118	364	47	88

Figure 5.2 depicts the evolution β-phase percentage of the studied lead-free brass alloys for the entire spectrum of thermal processing conditions (soaking temperature and holding time).

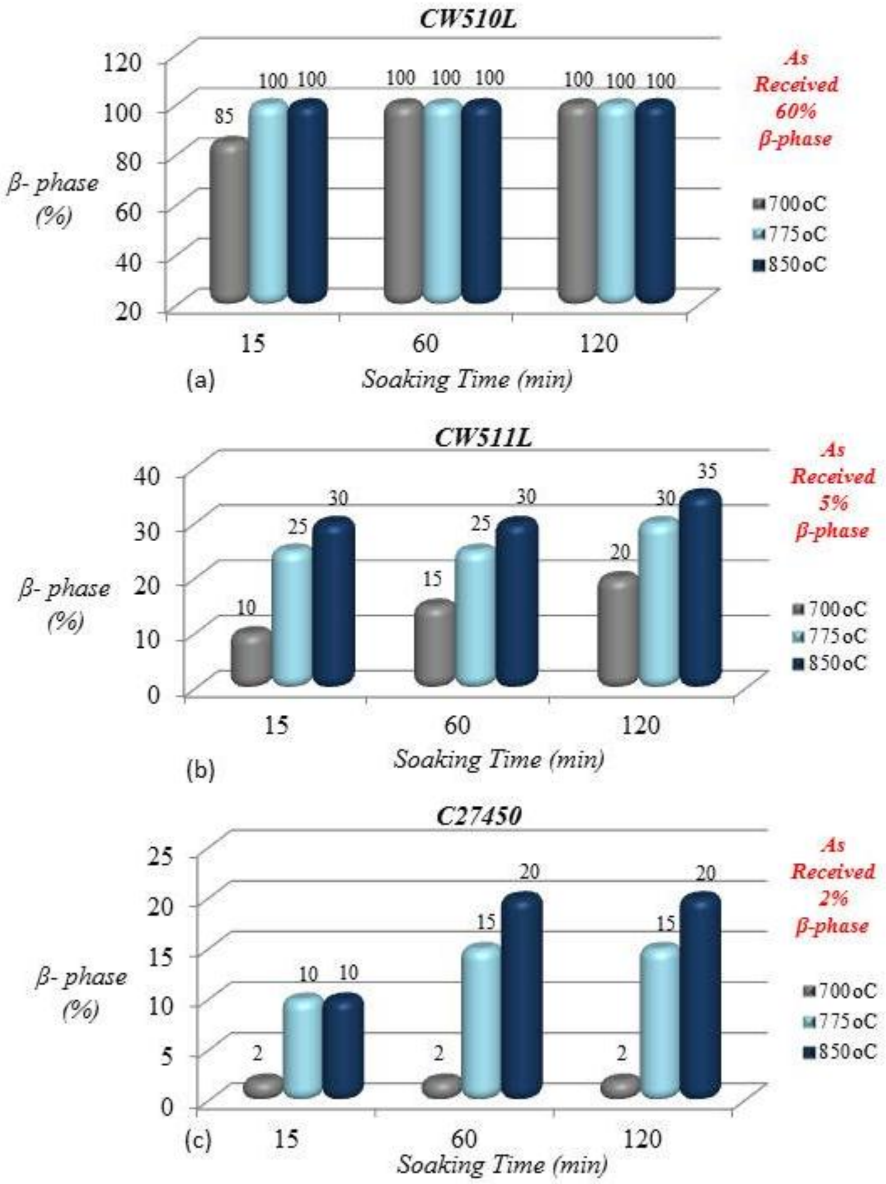

Fig. 5.2: Evolution of β-phase fraction as a result of heat treatment process to the studied alloy systems: (a) CuZn42 (CW510L), (b) CuZn38As (CW511L) and (c) CuZn36 (C27450).

The obtained microstructures are illustrated in Figures 5.3 - 5.5. The percentage of β-phase in the "as-received" lead-free brass CW510L was 60% (AR 510), while after heat-treatment varied from 85 to 100%, see Figures 5.2a and 5.3. More specifically, β-phase percentage was increased to 85% after annealing of HT 1 (Fig. 5.3a & Table 5.1). For the rest heat treatment cycles (HT 2 - HT 9), β-phase transformation was almost complete reaching a percentage up to approximately 100% (Fig. 5.3b-i & Table 5.1).

A general tendency of grain structure coarsening was also observed, as a result of grain growth due to prolonged heating, especially for HT 6 and HT 9 (Fig. 5.3f, i & Table 5.1).

The percentage of β-phase in the "as-received" lead-free brass CW511L was 5% (AR 511) while after heat-treatment, the β-phase fraction rose to a percentage which varied between 10 and 35% (HT 10 - HT 18) for the whole range of heat treatment conditions (Figs. 5.2b, 5.4 & Table 5.1). The β-phase fraction was almost stabilized to ~30% for heat treatment at 775 and 850^{o}C independently of soaking time. Soaking time was found to play a major role when the driving force was lower, i.e. for heat treatment temperature of 700^{o}C, where β-phase fraction doubled, as soaking duration changed from 15 min to 120 min (HT 10, HT 13 and HT 16). Furthermore, a coarsening tendency of the primary α-phase islands was observed with increasing holding temperature and soaking times, due to the thermally activated diffusion phenomena. Although rapid water cooling was subsequently applied, a secondary precipitation of acicular α-phase crystals took place within β-phase domains (Fig. 5.4f, i & Table 5.1).

The percentage of β-phase in the "as-received" lead-free brass C27450 was 2% (AR 27450) varied from 2 to 20% (HT 19 – HT 27) volume fraction after heat-treatment (Figs. 5.2c, 5.5 & Table 5.1). More specifically, β-phase percentage did not substantially change after annealing for HT 19, HT 22 and HT 25 respectively (Figs. 5.2c, 5.5a, d, g & Table 5.1). HT 20 and HT 21 resulted to an increase of β-phase percentage up to a 10% volume fraction (Figs. 5.2c, 5.5b, c & Table 5.1), while HT 23 and HT 26 resulted to a β-phase percentage up to 15% (Figs. 5.2c, 5.5e, h & Table 5.1). HT 24 and HT 27 yielded the maximum β-phase percentage, up to 20% volume fraction (Figs. 5.2c, 5.5f, i & Table 5.1). With regards to CW510L and CW511L alloys, the holding temperature had a more pronounced effect on β-phase formation kinetics than soaking time (principally for HT 23, HT 24, HT 26 and HT 27), while heat treatment duration mainly resulted to grain structure coarsening. Apart from α-phase grain growth, the effect of soaking time above 60 min and up to 120 min on β-phase volume fraction was negligible (Fig. 5.2c).

The precipitation of secondary acicular α-phase crystals in the β-phase interiors was more pronounced under higher holding temperature and soaking times due to their marked effect on driving force stimulus. Steep thermal gradients favoured the thermodynamics of nucleation processes, while prolonged time at high temperatures favoured the diffusion kinetics, promoting the formation of well defined α-phase crystals under the critical transformation temperature.

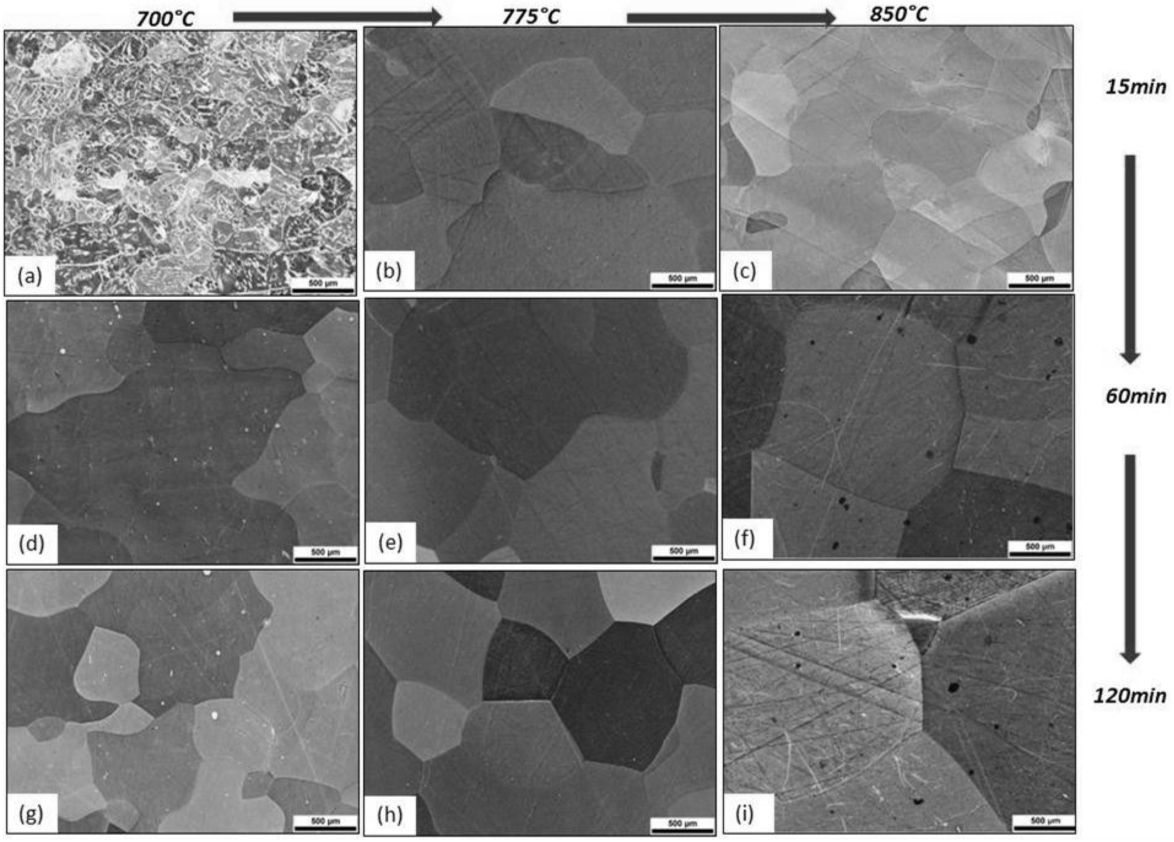

Fig. 5.3: Optical micrographs on longitudinal sections of CuZn42 (CW510L) lead-free brass after annealing in: (a) HT 1, (b) HT 2, (c) HT 3, (d) HT 4, (e) HT 5, (f) HT 6, (g) HT 7, (h) HT 8 and (i) HT 9.

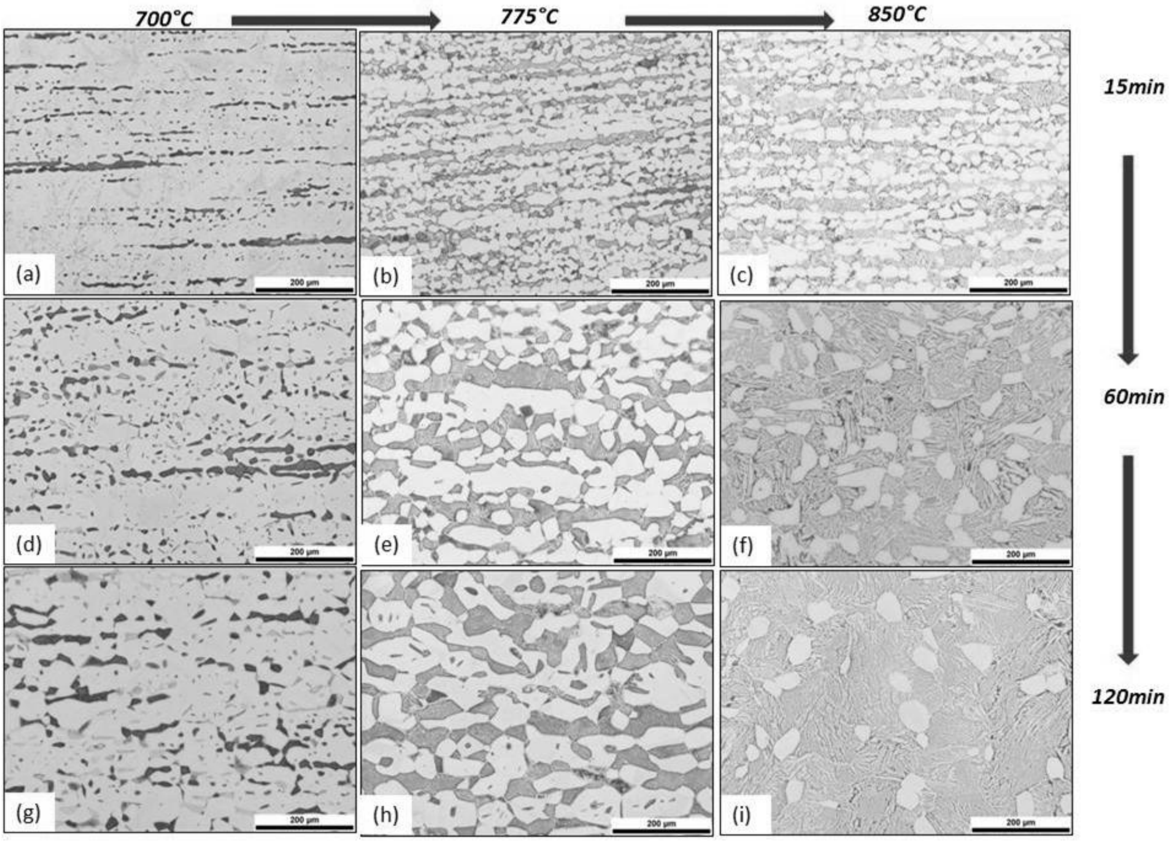

Fig. 5.4: Optical micrographs on longitudinal sections of CuZn38As (CW511L) lead-free brass after annealing in: (a) HT 10, (b) HT 11, (c) HT 12, (d) HT 13, (e) HT 14, (f) HT 15, (g) HT 16, (h) HT 17 and (i) HT 18. Note: Light areas represent α-phase and dark areas represent β-phase.

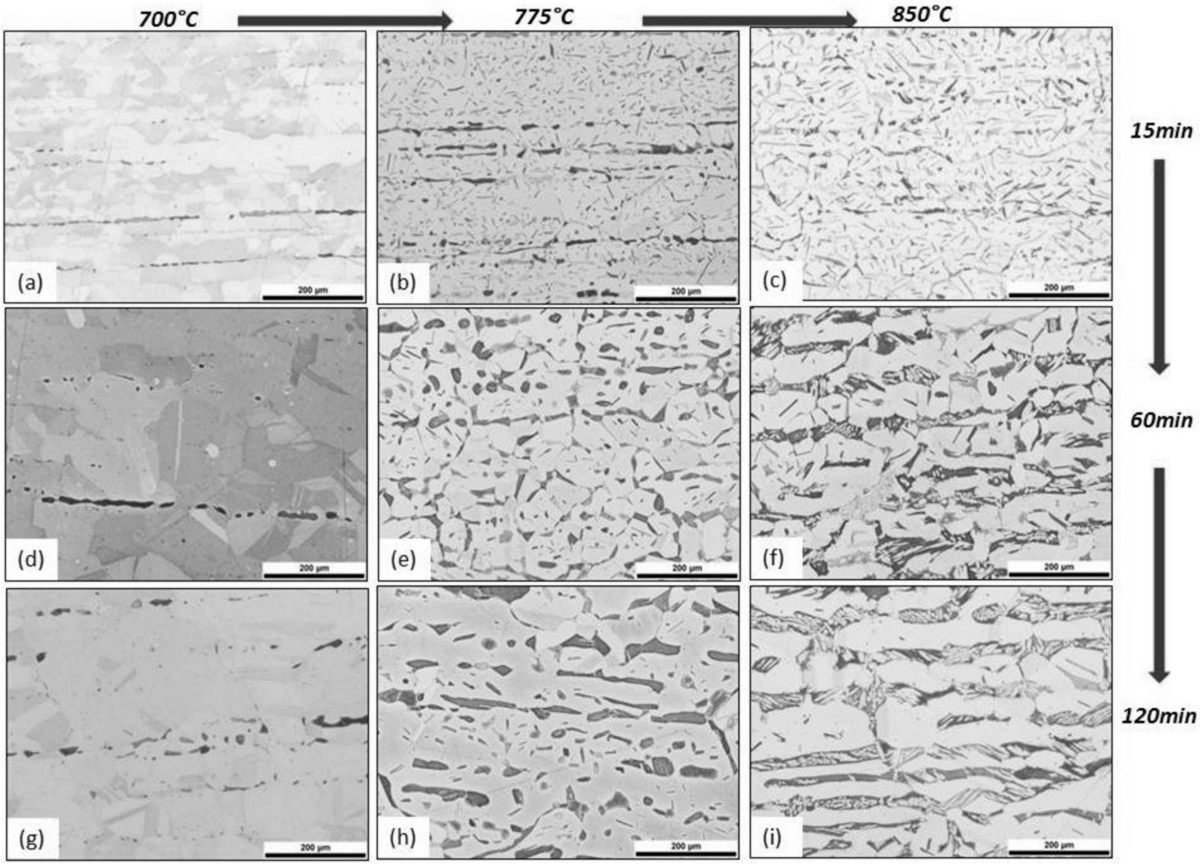

Fig. 5.5: Optical micrographs on longitudinal sections of CuZn36 (C27450) lead-free brass after annealing in: (a) HT 19, (b) HT 20, (c) HT 21, (d) HT 22, (e) HT 23, (f) HT 24, (g) HT 25, (h) HT 26 and (i) HT 27. Note: Light areas represent α-phase and dark areas represent β-phase.

Characteristic SEM micrographs showing the phase structure of the heat treated lead-free brass alloys under selected heat treatment conditions are presented in Figure 5.6. Apart from phase content difference, the variation in phase distribution and morphology was found to be significant, a fact that could potentially affect both the mechanical properties and machinability.

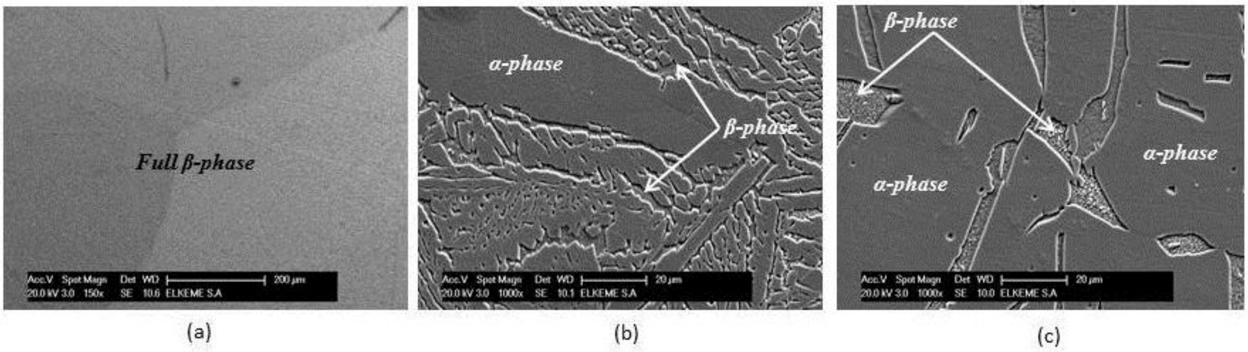

(a) (b) (c)

Fig. 5.6: SEM micrographs on longitudinal sections of (a) CuZn42 (CW510L), (b) CuZn38As (CW511L) and (c) CuZn36 (C27450), after representative heat treatment procedures.

5.3. Mechanical Properties after Heat Treatment

For each heat treatment cycle, three tensile test specimens were tested and the average value was presented. Error bars have not been included since the results' values presented negligible deviations and high repeatability. As was expected, all heat treatments influenced the mechanical process of CW510L, CW511L and C27450 lead-free brasses (Figs. 5.7-5.10). The transformation of the microstructure, and, more specifically, the increased percentage of β-phase and grain coarsening altered the proof stress, the tensile strength as well as elongation values in comparison with the mechanical properties of the "as received" lead-free brasses. The variation of CW510L mechanical properties as a function of the heat treatment parameters (temperature and soaking time) is shown in Figure 5.7.

Considering the machinable brass product standard (EN 12164), which dictates the specification limits, six out of nine heat treatment processes were rejected since they did not meet the minimum requirements. The acceptable values for tensile strength and total elongation, according to the EN12164 standard, for the CW510L were 430-500 MPa and minimum 10% respectively. As is shown in Figure 5.7 and Table 5.1, HT 1, HT 2 and HT 5 met the standard specifications as the tensile strength (469, 496 and 430 MPa) and the total elongation values (34, 27 and 14%) were found within the specifications limits for CW510L alloy. These three heat treatment cycles (HT 1, HT 2 and HT 5) were also found to increase β-phase percentage, while the mechanical properties remained within standards. As is shown in Figure 5.10a and Table 5.1, the annealing of CW510L for HT 5 resulted to the highest hardness measurement (138 HV1).

Grain structure coarsening, observed for HT 5, was also expected to contribute to this combination of tensile, yield strength and hardness, together with low elongation values. This combination is expected to promote chip breaking phenomena which in sequence may drastically affect machinability performance. As a result, this heat treatment process condition (HT 5) could be selected for further machinability performance evaluation for the CW510L lead-free brass alloy. Additionally, both HT 1 and HT 4 could have also a beneficial effect on machinability of CW510L brass alloy without compromising the mechanical properties. The predominance of β-phase together with its exaggerated grain size (>500 μm) were considered as the main reasons for the low ductility failures, observed during CW510L tensile testing (Fig. 5.3c, f, i, 5.7c and Table 5.1).

In the case of CW511L lead-free brass alloy, eight out of nine heat treatment processes were rejected, as both tensile strength (R_m>400 MPa) and hardness (HV1<95) did not meet the EN12164 standard (Figs. 5.8, 5.10 and Table 5.1). The increased values of tensile strength (402 - 416 MPa) were attributed to the enhanced β-phase fraction, which developed under specific heat treatment processes (HT 11, HT 12, HT 14, HT 15 and HT 17). Similar values of tensile strength and higher elongation values (371-396 MPa, 44-59%) and R_m/R_p ratios (due to lower proof strength), when compared to the “as received” condition (380 MPa, 42%), were obtained for the rest of heat treatment processes (HT 10, HT 13, HT 16 and HT 18).

These were associated to the annealing and restoration phenomena together with the coarsening of primary α-phase islands which are the prevalent strength controlling factors under those heat treatment conditions. HT 18 may be considered as a winning combination, which can be proposed for the improvement of machinability of CW511L, since β-phase percentage was increased in relation to the "as received" samples (35% vs. 5%), while the induced mechanical properties conformed to the standard specification requirements.

Finally, in the case of lead-free brass C27450, all the heat treatment processes (HT 19 - HT 27 complied with ASTM B927, since they resulted in acceptable values of tensile strength (R_m>295 MPa) and total elongation (A>15%), see Figure 5.9 and Table 5.1. HT 24 and HT 27 resulted in the highest values of tensile strength (361 and 364 MPa) exhibiting favourable machinability characteristics, in terms of the combination of hardness, tensile strength and β-fraction, see Figures 5.2c, 5.9b, 5.10c and Table 5.1. Strength and deformation capacity evolution (as reflected by high R_m/R_p ratios and elongation values) were governed by recrystallization and α-grain coarsening, dislocation annihilation softening mechanisms, similar to observed for CW511L.

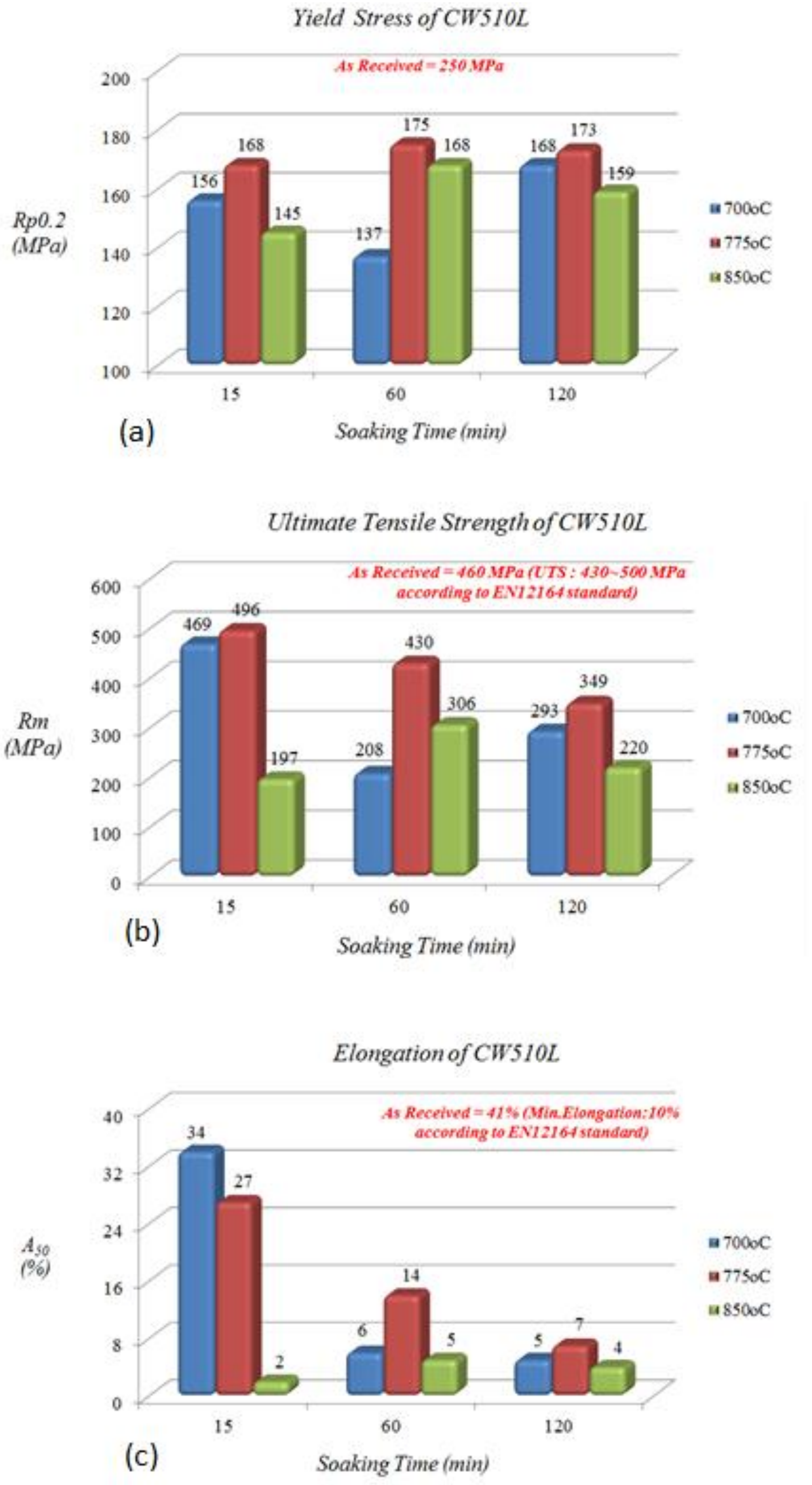

Fig. 5.7: Histograms showing the evolution of tensile properties of CuZn42 (CW510L) lead-free brass as a function of the heat treatment parameters: (a) $R_{p0.2}$, (b) R_m and (c) A_{50}.

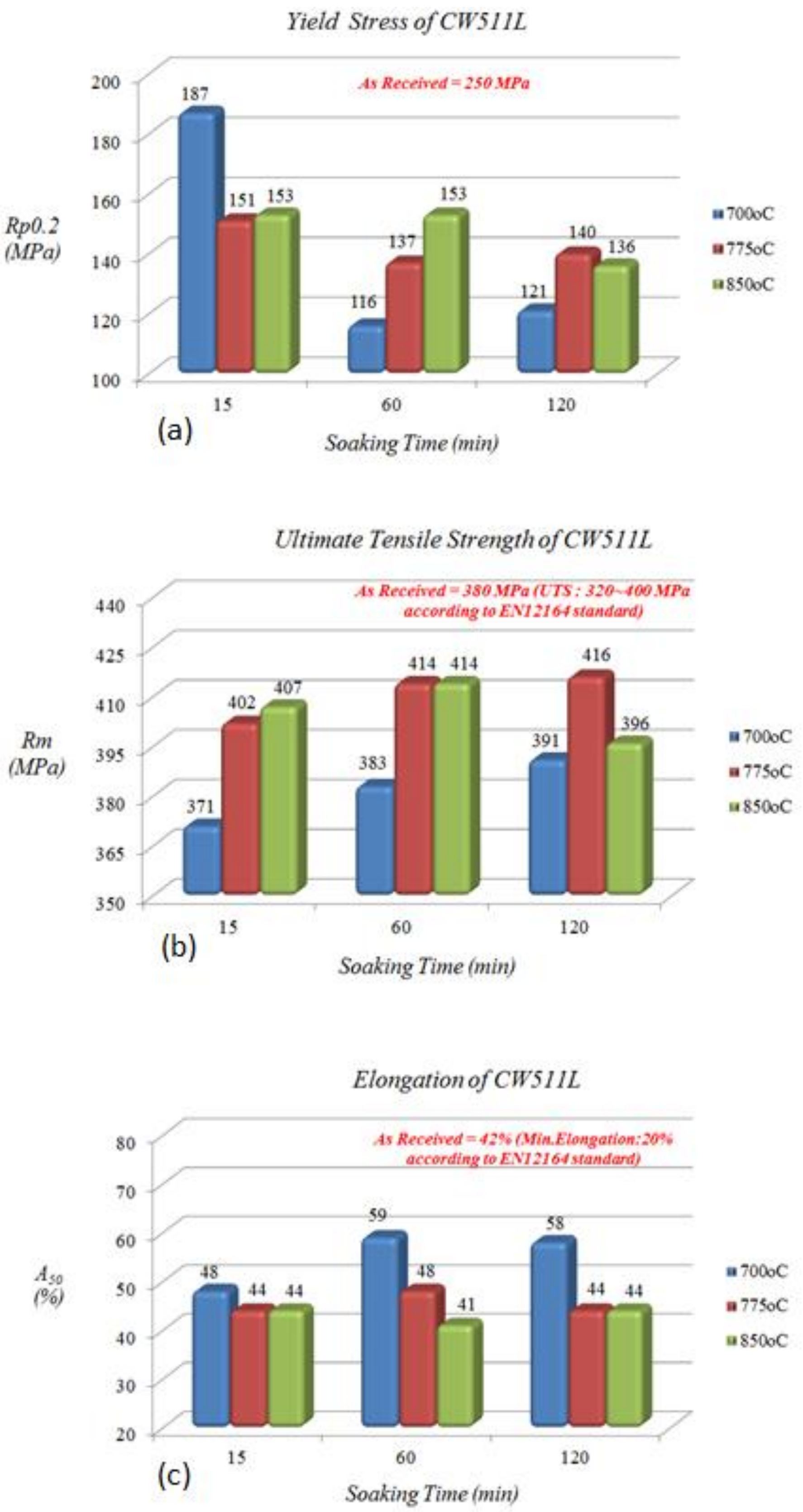

Fig. 5.8: Histograms showing the evolution of tensile properties of CuZn38As (CW511L) lead-free brass as a function of the heat treatment parameters: (a) $R_{p0.2}$, (b) R_m and (c) A_{50}.

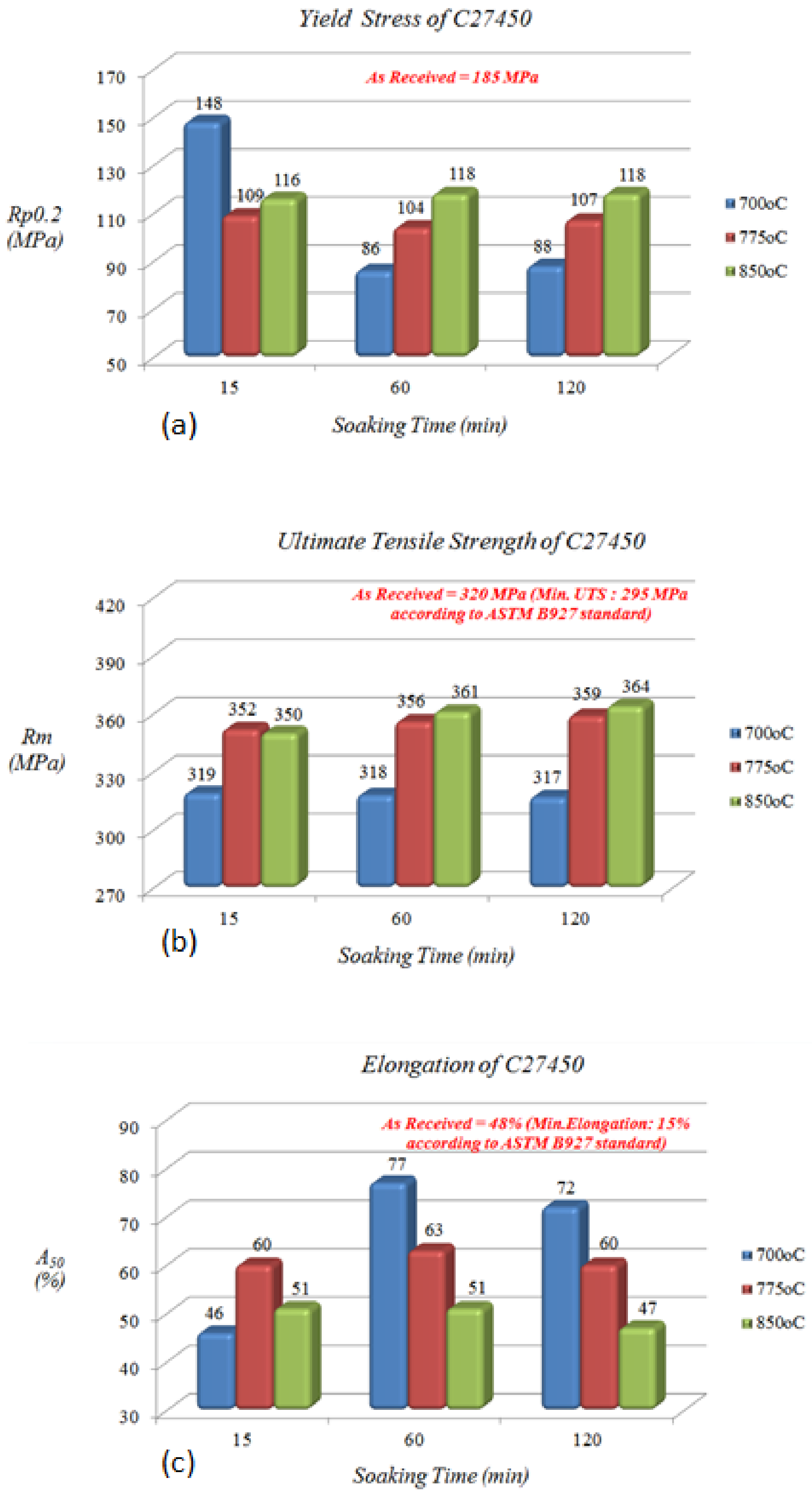

Fig. 5.9: Histograms showing the evolution of tensile properties of CuZn36 (C27450) lead-free brass as a function of the heat treatment parameters: (a) $R_{p0.2}$, (b) R_m and (c) A_{50}.

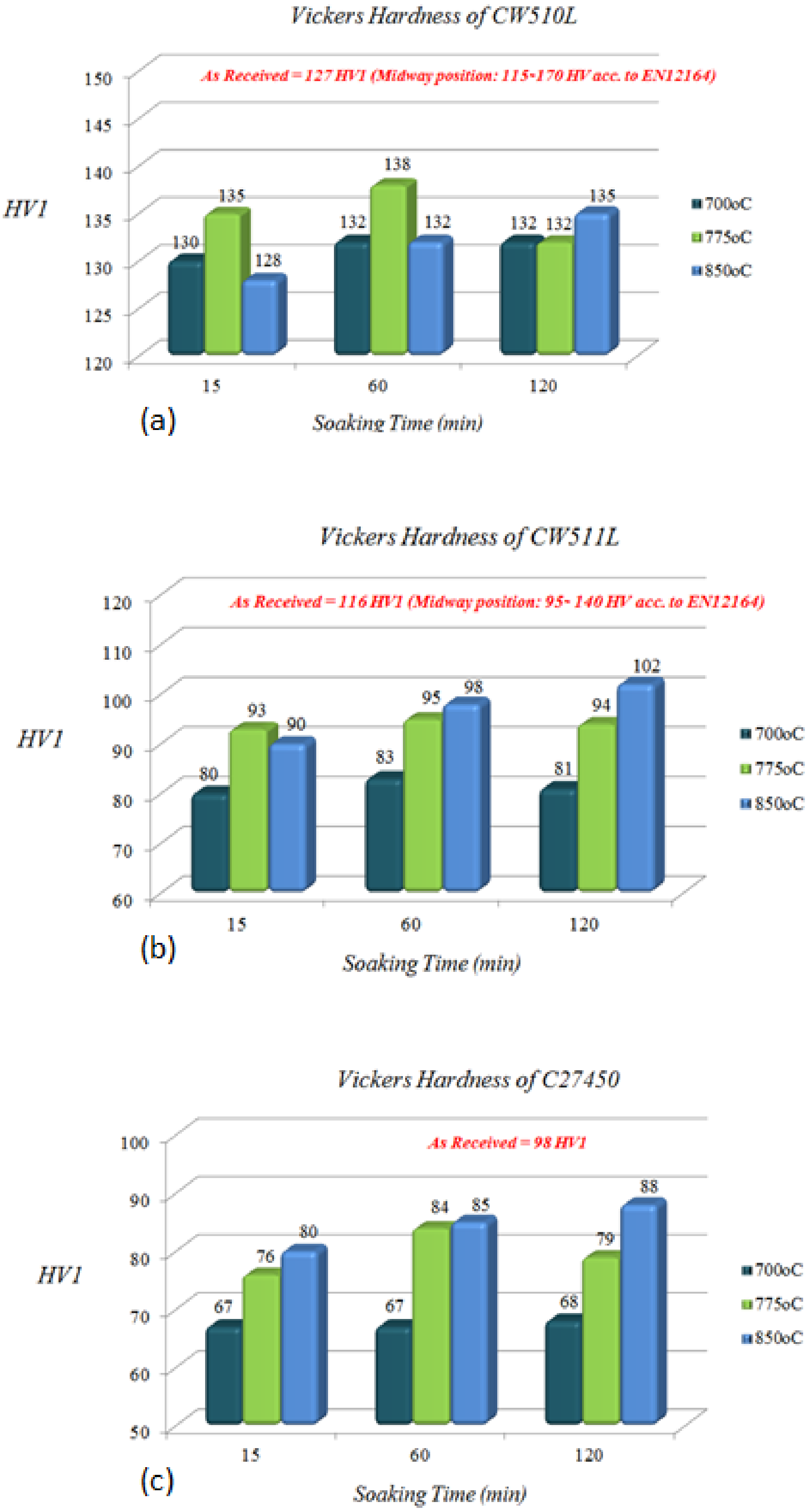

Fig. 5.10: Histograms showing the evolution of Hardness Vickers (HV1) results as a function of heat treatment parameters: (a) CuZn42 (CW510L), (b) CuZn38As (CW511L) and (c) CuZn36 (C27450).

5.4. Fractographic Examination

The fractographic investigation of the tensile failure surfaces of the alloys (CW510L, CW511L, C27450) was subsequently focused to the thermal treatment conditions (HT 5 for CW510L, HT 18 for CW511L and HT 27 for C27450), which were expected to favour machinability. Macroscopic views of the fracture surfaces after tensile tests, together with the corresponding σ-ε curves, are shown in Figure 5.11. Pronounced necking resulted to extensive reduction of area for both CW511L and C27450, while this effect was less pronounced for the CW510L lead-free brass alloy. CW510L exhibited a “shiny” and “granular” fracture surface which was typical of limited macroscopic post-uniform elongation. The granular appearance of CW510L fracture surface was also indicative of the coarse grain structure developed due to the thermal treatment (Fig. 5.3).

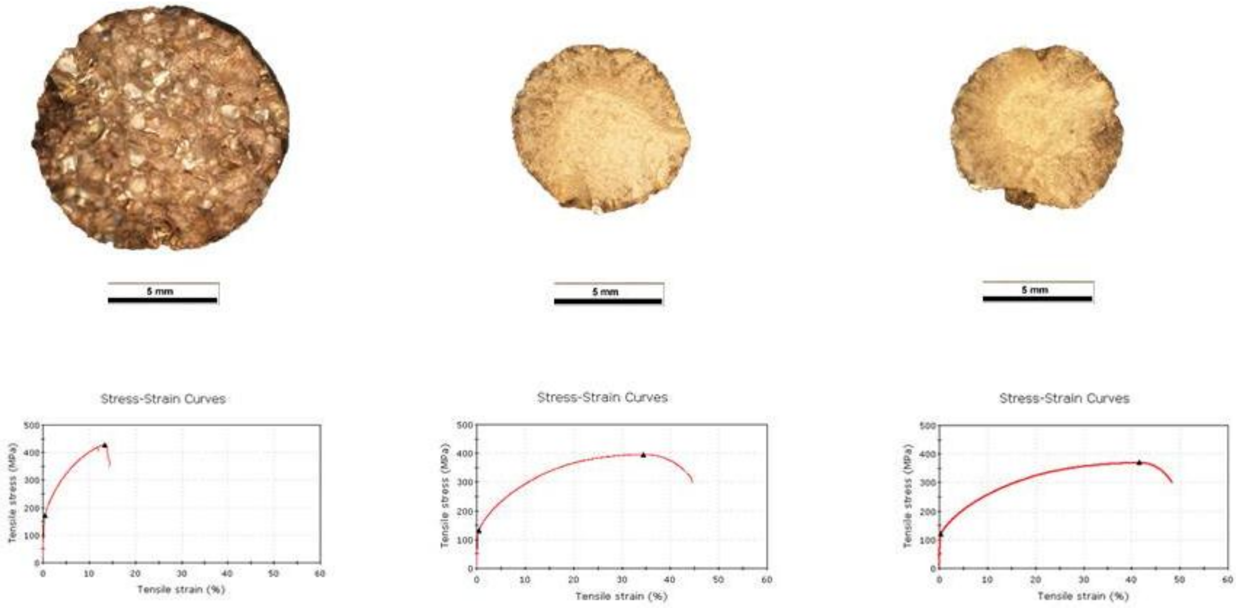

(a) (b) (c)

Fig. 5.11: Optical stereomicrographs, together with the corresponding σ-ε curves, showing the overall view of the fracture surfaces after the tensile test of (a) CW510L_HT 5, (b) CW511L_HT 18 and (c) C27450_ HT 27 lead-free brasses. Note the pronounced necking and reduction of area in the cases of CW511L and C27450 alloys

Secondary electron imaging Scanning Electron Microscopy was employed to examine the governing fracture micro-mechanisms activated during uniaxial tension (Figs. 5.12 - 5.14). The CW510L alloy under HT 5 exhibited a mixed failure mode with dominant intergranular fracture (Fig. 5.12a, b), while isolated “stepped” areas of transgranular fracture were also evidenced (Fig. 5.12c, d). Intergranular fracture was suggestive of the adverse effect of coarse β-grain structure on the strain accumulation during tensile testing. The decrease of stacking fault energy (SFE) potentially induced by dissolution of alloying elements and amplification of atom electron density along with phase transformation phenomena may be considered to impede the dislocation processes, favouring plastic deformation phenomena, such as cross-slip and climb, see also Refs. [7-8]. On the other hand, the β-phase typically a based centered cubic (bcc) crystal system possesses fewer active slip systems compared to the highly symmetric face centered cubic (fcc) lattice of the α-phase. Moreover, a dislocation reaction could result in the formation of immobile dislocations in the bcc lattice promoting crack nuclei and subsequently brittle fracture. In such a crystal plane which is not a close packed atomic plane [e.g. the (001) in the bcc lattice], brittle cleavage fracture propagates [9]. “Staircase”-type transgranular fracture areas were also identified. The creation of shear dimples denoting ductile tearing between shear ledges was evidenced (Fig. 5.12c and d). The presence of such transgranular fracture areas together with dimpled arrays, were considered as the main evidence for ductility, in case of β-phase CW510L heat treated brass and could be related to the change of crystallographic orientation among adjacent β-grains and/or inherent β-phase plate-like substructure on crack propagation [10]. The fractographic characteristics of CW510L heat treated alloy were also consistent to its poor fracture behaviour, yielding low CTOD (Crack-Tip-Opening-Displacement) values, as reported in [3].

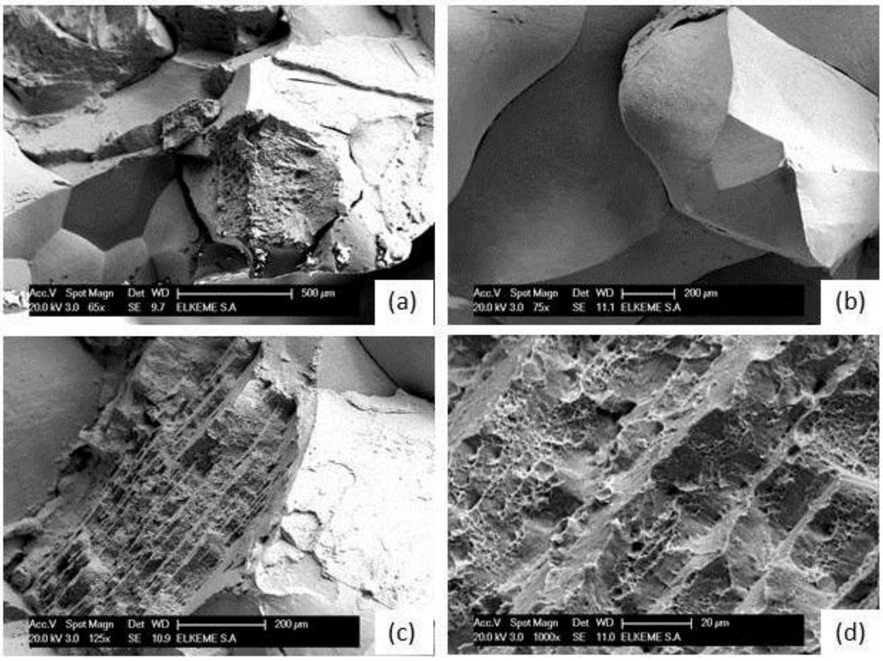

Fig. 5.12: SEM micrographs of CW510L_ HT 5, showing details of the fracture micro-mechanisms developed during uniaxial tension.

Both the tensile fracture surface of the CW511L and C27450 alloys exhibited similar failure modes with pronounced ductile dimpled fracture (Figs 5.13 and 5.14).In the case of C27450 heat treated alloy, the coarser size of the dimples was indicative of the higher post-uniform elongation compared to the CW511L heat treated alloy (Fig. 5.13d vs. Fig. 5.14d).The produced dimples resulting from microvoid growth and coalescence constituted the signature of ductile fracture. In the case of CW511L alloy (Fig. 5.13d), flat shear faceted areas were observed which are indicative of its brittle behaviour and could be attributed to the alteration of fracture micro-mechanisms caused by the distribution of β-phase in the microstructure, see also Ref. [2].

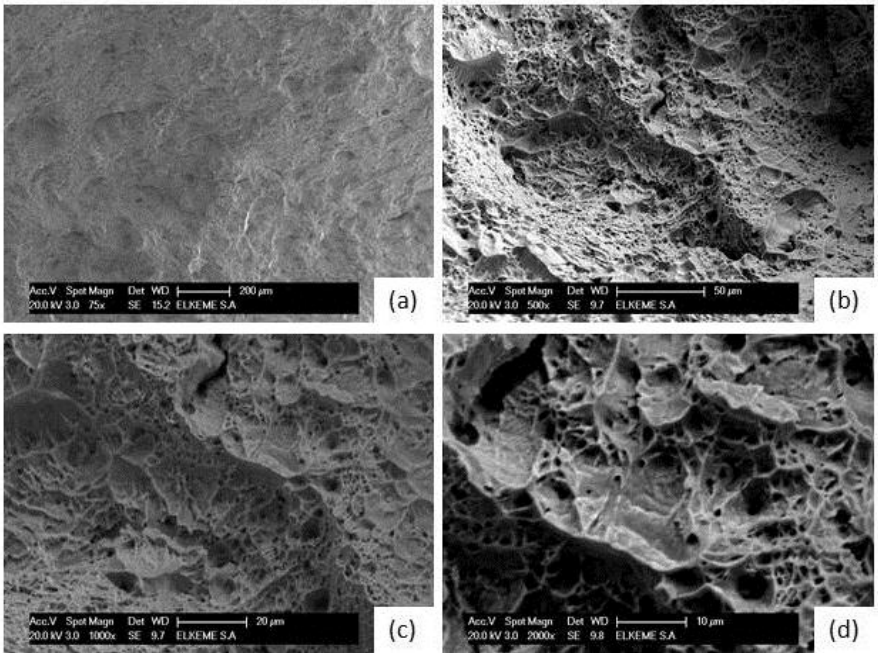

Fig. 5.13: SEM micrographs of CW511L_ HT 18, showing details of the fracture micro-mechanisms developed during uniaxial tension.

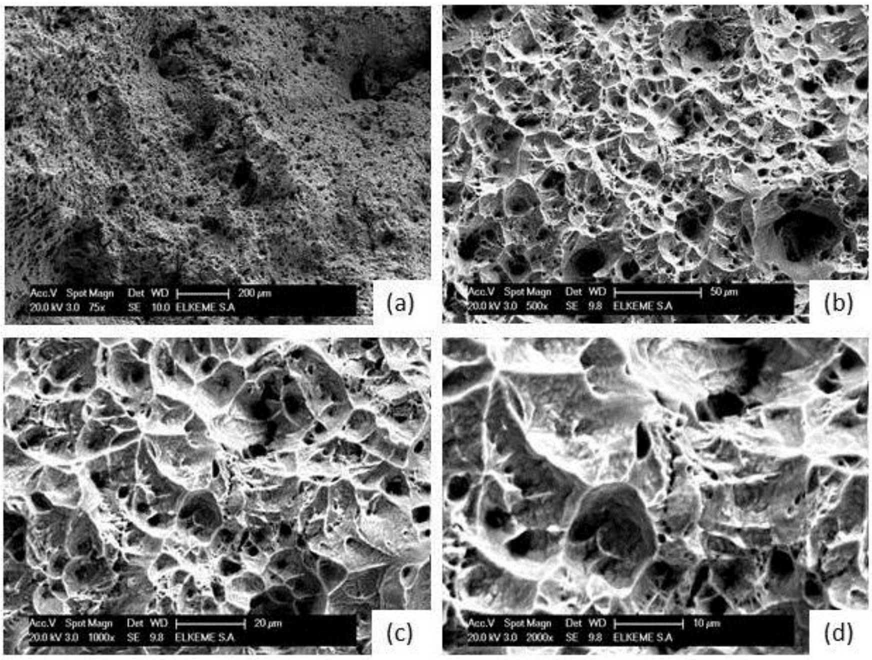

Fig. 5.14: SEM micrographs of C27450_ HT 27, showing details of the fracture micro-mechanisms developed during uniaxial tension.

5.5. Section Conclusions

Heat treatment (under selected process conditions) caused significant changes in phase structure, stabilising β-phase volume fraction at high concentration levels. The β-phase volume fraction, assessed through quantitative optical microscopy, was increased for all studied alloys. More specifically:
(i) For CW510L, β-phase volume fraction varied within 85-100% (initial vol. fraction 60%).
(ii) For CW511L, β-phase volume fraction varied within 10-35% (initial vol. fraction 5%).
(iii) For C27450, β-phase volume fraction varied within 2–20% (initial vol. fraction 2%).

The increase of β-phase fraction resulted to alloy strengthening and elongation reduction (in competition to grain coarsening), resulting in some cases to brittle fractures which did not conform to the relevant standards (especially for CW510L alloy). Mixed-mode tensile failure mechanisms were identified for the heat-treated CW510L alloy, which exhibited brittle intergranular and transgranular fracture showing restricted areas of shear dimpled fracture. After heat treatment, both CW511L and C27450 alloys, demonstrated almost completely ductile dimpled fracture. The deeper and coarser dimples were more pronounced for C27450 fracture surface, due to its extensive and homogeneous plastic deformation before tensile failure. The entire spectrum of the heat treatment conditions, allowed for a selection of heat treatment and alloy combinations to be considered as prominent candidates for improved machinability performance. The selection criteria were based on β-phase maximization, together with the establishment of acceptable mechanical properties, as dictated by the EN and ASTM standards.
The proposed optimum conditions were found to be as following:
(i) CW510L – HT 5 (775°C for 60 min): Rm = 430 MPa, Rp0.2 = 175 MPa,
A50 = 14% (β-phase: 100%).
(ii) CW511L – HT 18 (850°C for 120 min): Rm = 396 MPa, Rp0.2 = 136 MPa,
A50 = 44% (β-phase: 35%).
(iii) C27450 – HT 24 and HT 27 (850°C for 60 and 120 min respectively):
Rm = 361–364 MPa, Rp0.2 = 118 MPa, A50 = 47–51% (β-phase: 20%).

Although an additional heat treatment step would increase production cost, the potential improvement of quality (strength, machinability) could be considered as a balancing factor leading to even more beneficial results, provided that a thorough technological optimisation process will be implemented.

5.6. References

[1] H. Doostmohammadi, H. Moridshahi (2015) Effects of Si on the microstructure, ordering transformation and properties of the Cu60Zn40 alloy. Journal of Alloys and Compounds 640: 401-407.

[2] G. Pantazopoulos, A. Toulfatzis (2012) Fracture modes and mechanical characteristics of machinable brass rods. Metallography, Microstructure, and Analysis 1: 106-114.

[3] A.I. Toulfatzis, G.A. Pantazopoulos, A.S. Paipetis (2014) Fracture behavior and characterization of lead-free brass alloys for machining applications. Journal of Materials Engineering and Performance 23: 3193-3206.

[4] L. Blaz, Z. Konior, T. Majda (2001) Structural aspects of α/β transformation in hot deformed CuZn-39Pb3 alloy. Journal of Materials Science 36: 3629-3635.

[5] J. R. Davis (2001) ASM Specialty Handbook: Copper and Copper Alloys', ASM International.

[6] M.A. Taha, N. A. El-Mahallawy, R. M. Hammouda, T. M. Moussa, M. H. Gheith (2012) Machinability characteristics of lead free-silicon brass alloys as correlated with microstructure and mechanical properties. Ain Shams Engineering Journal 3: 383-392.

[7] O. Zurita, V. Di Graci (2012) Surface integrity in turning of annealed brass: Hardness prediction. Journal of Materials Engineering and Performance 21: 1534-1538.

[8] T. Chandra, J.J. Jonas, D.M.R. Taplin (1976) The mechanical behaviour of cerium-modified alpha-beta brass at high temperatures. Journal of Materials Science 11: 1843-1848.

[9] G.E. Dieter (1988) Mechanical Metallurgy. McGraw Hill.

[10] G. Pantazopoulos, A. Vazdirvanidis (2008) Characterization of the microstructural aspects of machinable α-β phase brass. Microscopy and Analysis 22: 13-16.

Chapter 6: Fracture Mechanics Properties and Failure Mechanisms of Heat-Treated Lead-Free Brass Alloys

6.1. Summary

In a recently published study, the effect of heat treatment of microstructure stabilization was attempted [1]. In the frame of this study, the enhancement of β-phase content was achieved, producing promising results concerning the potential improved machinability rating, especially for CW510L and CW511L lead-free brass alloys. The fracture behaviour of conventional leaded and lead-free brass alloys was comprehensively studied in Refs. [2-3]. The mechanical behaviour after heat treatment is greatly affected by the dominance of β-phase in the microstructure, which could further bring severe changes in strength and fracture resistance. Therefore, the assessment of fracture mechanics behaviour of lead-free brass alloys after heat treatment attracted special research interest, in view of the potential ductility loss and embrittlement phenomena that might occur and deteriorate the functionality and reliability of specially heat treated lead-free brass alloys [4]. In this sense, a rigorous characterization was performed, based on the notions of Elastic Plastic Fracture Mechanics (EPFM), using the Crack-Tip-Opening-Displacement (CTOD) approach and dynamic impact loading under Charpy test configuration. The fracture zone transitions were illustrated to shed profuse light to the emergent failure mechanisms and their influence exerted by the microstructure and the applied loading conditions.

This work is considered as original and novel, having high industrial significance and criticality for environmental-friendly machined brass components, destined as vital parts in hydraulic, mechanical and chemical industry installations (such as valves, fittings and connectors). Although EPFM CTOD approach was developed mainly for welded structures, it can be also used as a valuable comparison criterion to evaluate the crack resistance of solid (homogeneous, non-welded), non-ferrous materials, as in this case. The critical CTOD value which is the distance between the crack flanks (at the region of the crack tip) represents the amount of plastic strain at the onset of unstable fracture [5-7]. Furthermore, the observation of diverse fracture modes (in case of post-deformation heat treated brass alloys) for the various loading conditions (impact, fatigue and monotonic) revealed significant and original features regarding the imminent failure mechanisms and implied the elaboration of challenging interpretation hypotheses which have to be aligned with the prevailed grain- and phase-structure.

The aim of this study is focused on the examination of the heat treatment influence on the fracture mechanics properties, in order to provide helpful insight concerning the failure resistance, which is related to the required structural integrity of the lead-free brass components, operated under different loading regimes. The heat treatment procedure was described in detail in Ref. [1]. The optimum heat treatment conditions, which were selected according to machinability criteria, were the following:
(i) CW510L (CuZn42): 775 °C for 60 min soaking time.
(ii) CW511L (CuZn38As): 850 °C for 120 min soaking time.

The heat treated CW510L at 775^{o}C for 60 min exhibited an improvement of fracture toughness in terms of impact energy (from 47 J to 52 J) and critical CTOD (from 0.32 mm to 0.50 mm), while in case of CW511L heat treatment performed at 850^{o}C for 120 min caused a slight deterioration of fracture toughness in terms of impact energy (from 104 J to 84 J) and critical CTOD (from 0.71 mm to 0.54 mm). Moreover, fractographic analysis was comprehensively performed at the various transition fracture zones and the emergent failure mechanisms were identified and documented for both examined brass manufacturing conditions ("as received" and after "final heat treatment"). The compilation of fracture mechanics properties and the acquired fractographic information have resulted evidently in the formulation of salient interpretation and postulation of hypotheses concerning the influence of the dominant microstructure and loading regimes on crack propagation and the observed failure mechanisms.

6.2. Fracture mechanics properties

6.2.1. Impact properties

The Charpy impact test results are collectively presented in Figure 6.1. A marginal increase in impact energy of around 10% was observed in case of CW510L brass alloy (from 47 J to 52 J). Conversely, in case of CW511L brass alloy a 20% reduction in impact energy was observed (from 104 J to 84 J). The macro-fractographs showed sufficient ductility for all the examined cases, as it was marked qualitatively by the lateral expansion and shear fracture areas. In case of CW510L a rough and granular fracture surface topography was revealed, which is relevant and consistent to the variation of failure mechanism in conjunction to the prevailed coarse-grained β-phase structure. Similar observations were conducted pertaining to the tensile fractures of heat treated CW510L brass alloy, see Ref. [1].

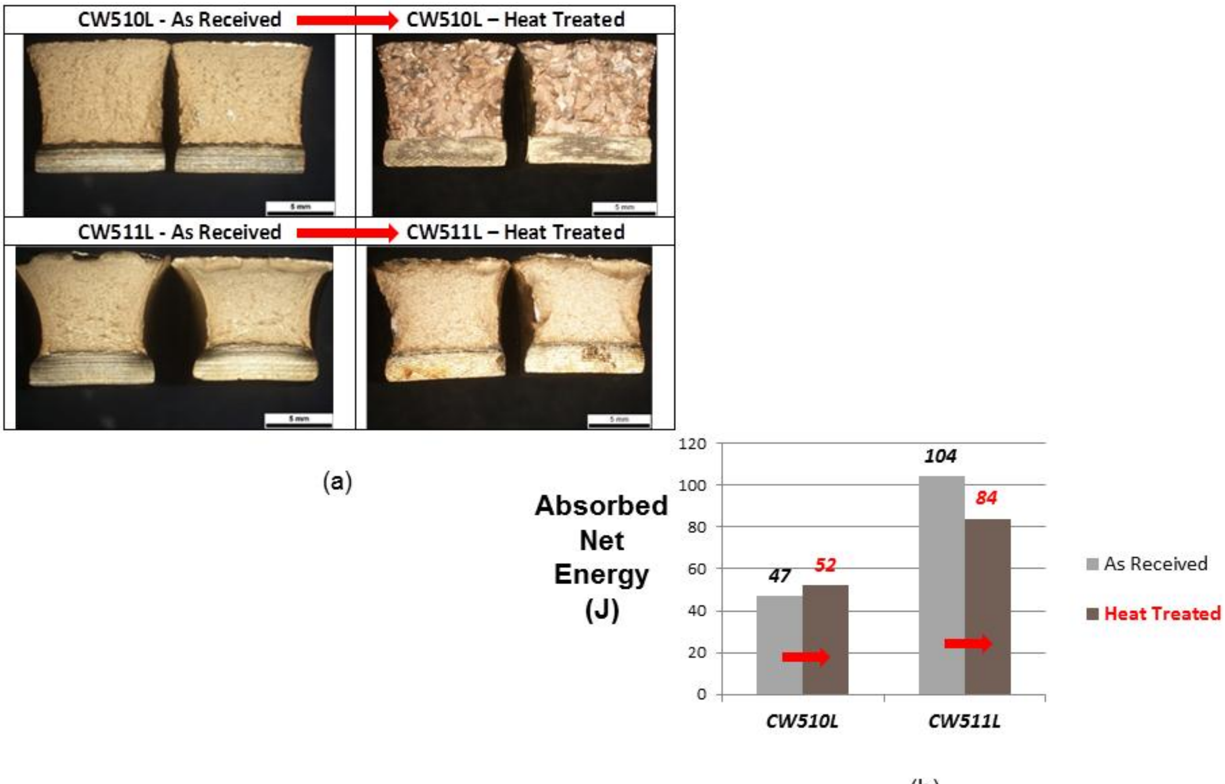

(a)

(b)

Fig. 6.1: Impact fracture toughness test (Charpy) results before and after heat treatment of CW510L and CW511L brass alloys: (a) Fracture surfaces after the impact test and (b) absorbed net energy bar chart. Average impact energy values are plotted.

6.2.2. Crack-Tip-Opening-Displacement (CTOD) properties

The CTOD test load-displacement curves together with the average values are collectively illustrated in Figure 6.2. It is noteworthy that the average value of critical CTOD for CW510L showed a marked increase (from 0.32 mm to 0.50 mm), while the opposite is shown in case of CW511L brass alloy (from 0.71 mm to 0.54 mm). This tendency is consistent to the trend observed for the corresponding impact properties (see Fig. 6.1b). The P-V curves for both alloys and metallurgical conditions examined belong to the “type 6” curves as classified by the relevant BS 7448-1 standard (Fig. 6.2a). P-V curves represent the variation of the following parameters: Load – Crack Mouth Opening Displacement (CMOD).

No signs of “pop-in”, i.e. localized instabilities accompanied by crack arrest were observed, while the maximum load (Pmax) has been attained showing fully plastic behaviour. Insets of macro-fractographic images, depicting qualitatively the overall area distortion and fracture surface texture and suggesting a massively ductile behaviour for all the examined cases, are shown in Figure 6.2a.

Similarities and analogies in macroscopic appearance of CTOD-fracture surfaces to the relevant impact fractures are also indicated here. The rough-granular appearance of heat treated CW510L CTOD-fracture was markedly illuminated as opposed to the smooth and fine texture of CW511L CTOD-fracture surface.

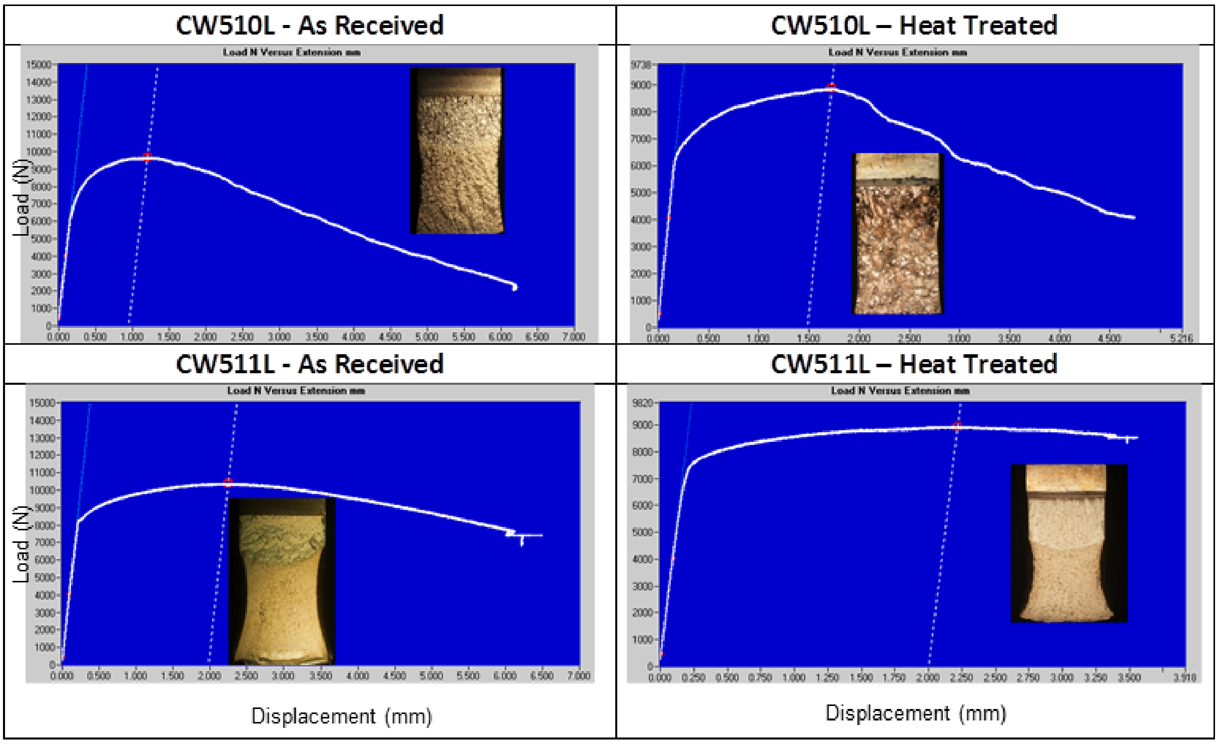

(a)

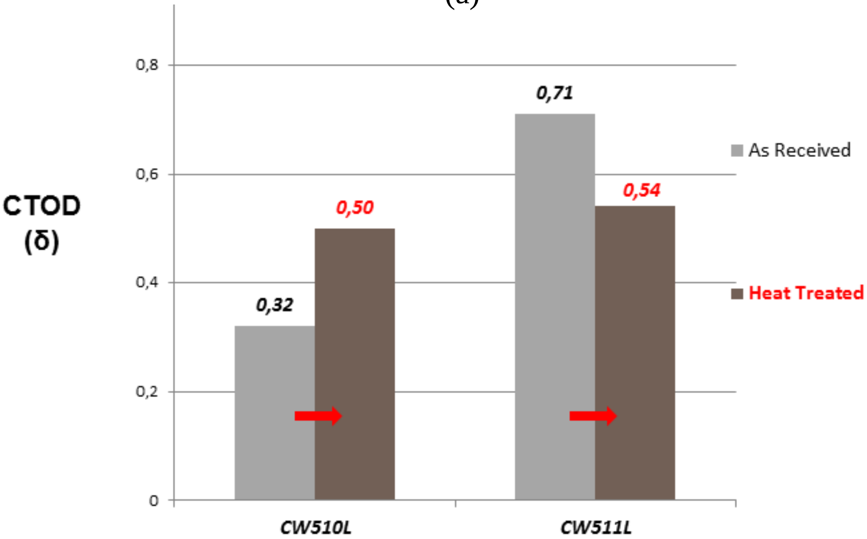

(b)

Fig. 6.2: Crack-Tip-Opening-Displacement (CTOD) test results according to BS 7448-1:1991. (a) Load-displacement curves before and after heat treatment of CW510L and CW511L brass alloy and (b) critical CTOD test values bar chart. Average critical CTOD values are plotted.

6.3. Fractographic examination

6.3.1. Impact failure mechanisms

After careful preservation and thorough alcohol ultrasonic cleaning, detailed views of the impact fractures were documented and the relevant failure mechanisms were investigated by employing high resolution FEG Scanning Electron Microscopy (see Figs. 6.3-6.5). CW510L brass alloy under the “as received condition” presented a classical ductile fracture failure mechanism and the relevant fracture surface was covered by multiple size dimples colonies (Fig. 6.3a). “After final heat treatment” CW510L brass alloy was almost entirely occupied by intergranular fracture topography, carrying minute dimple size population situated on the grain facets provoked by intergranular microvoid-coalescence (Figs. 6.3b and 6.4a, b). Isolated regions of final shear fracture expressed in terms of dimple tearing (Fig. 6.4c, d) and staircase fracture morphology showing shear ledges and tear ridges are also depicted in Figure 6.4e, f.

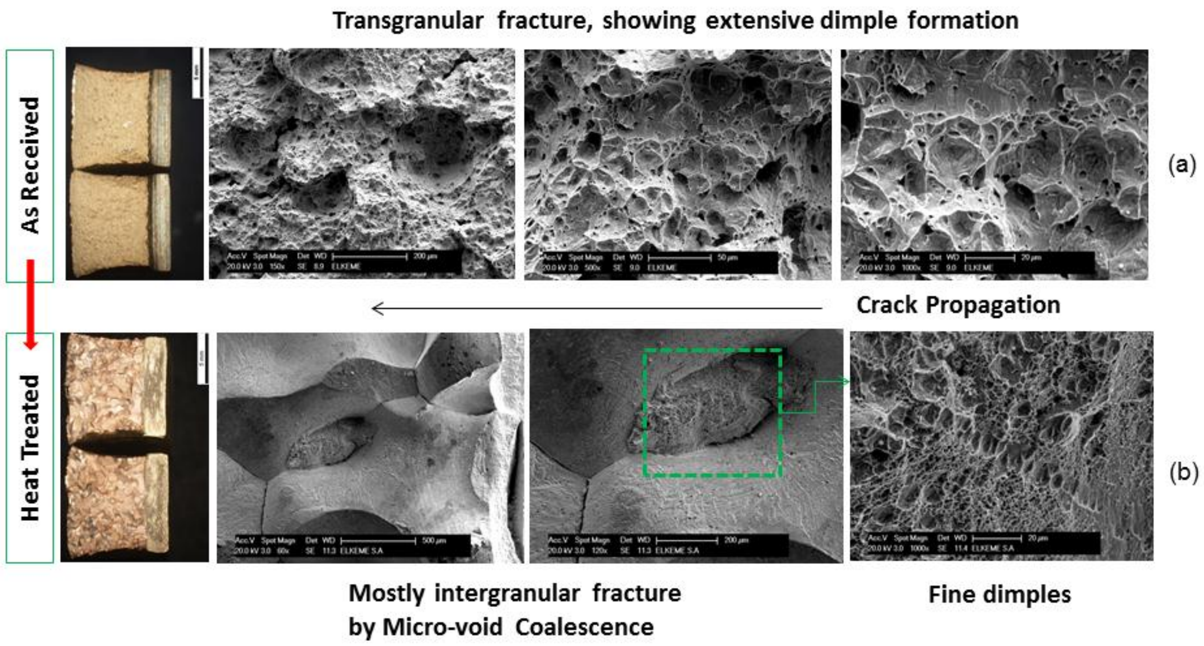

Fig. 6.3: Fractographic evaluation of CW510L impact fractures: (a) as received and (b) after heat treatment.

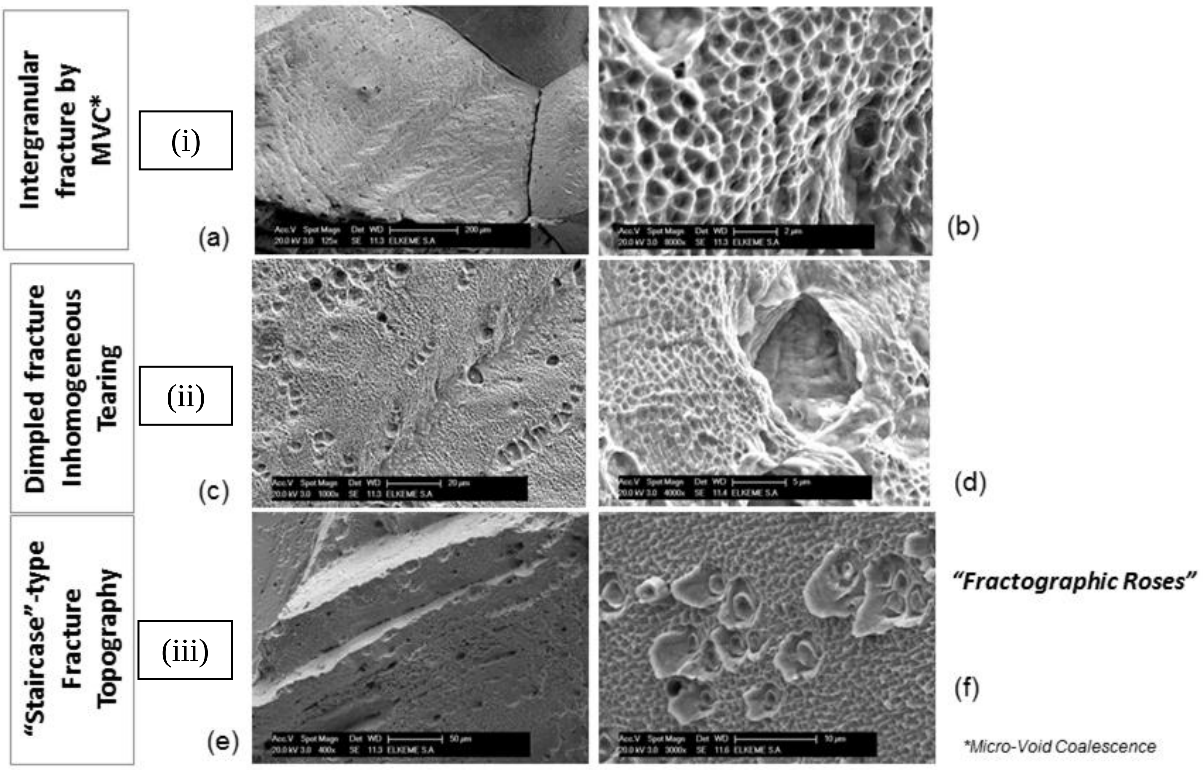

Fig. 6.4: Details of fracture surface of CW510L after heat treatment showing various damage mechanisms; (i) intergranular fracture, (ii) fine dimples on the grain boundary facets and (iii) transgranular "staircase"-type fracture mode.

A fully ductile behaviour is denoted in case of CW511L impact fracture, accompanied by dimple formation due to transgranular microvoid coalescence (Fig. 6.5). It is noteworthy that in the "as received" condition, the presence of multiple size dimples and large-deep voids advocated the greater amount of plastic strain accommodated during loading (Fig. 6.5a) as compared with the "final heat treatment" condition where finer and shallower dimples are evident (Fig. 6.5b). This result is consistent to the decrease of average impact energy indicated by the finally heat treated CW511L brass alloy.

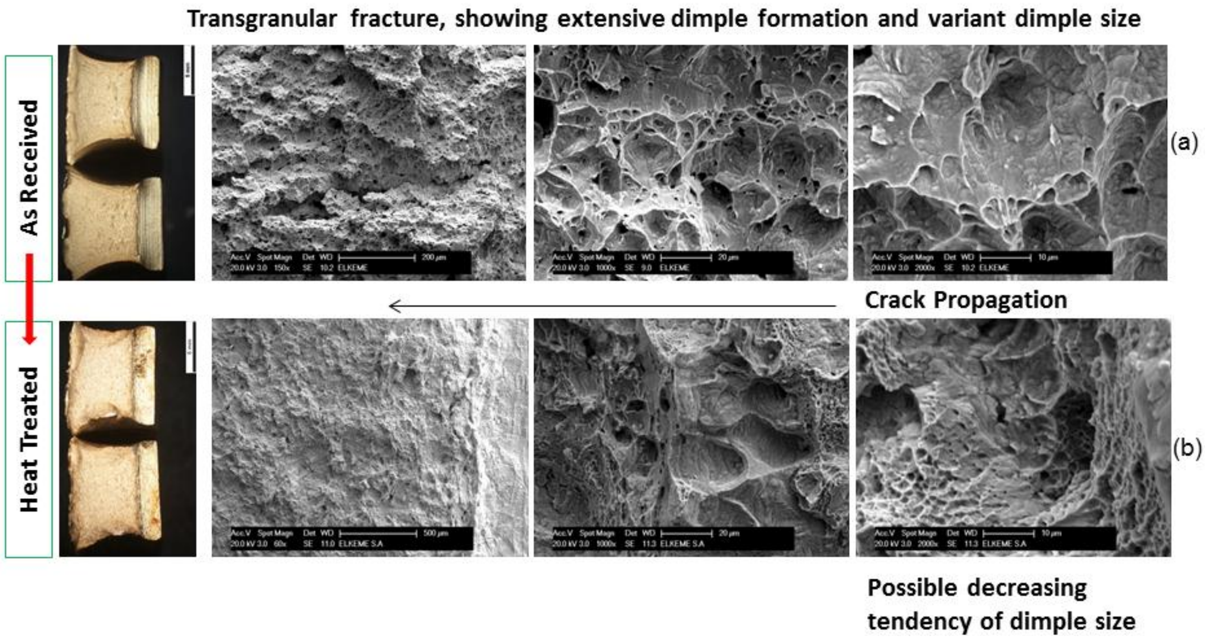

Fig. 6.5: Fractographic evaluation of CW511L impact fractures: (a) as received and (b) after heat treatment.

6.3.2. CTOD-complex failure mechanisms

The CTOD complex failure mechanisms consist of two principal fracture zones: (a) fatigue precracking (Fatigue Crack Propagation, FCP) zone and (b) monotonic or quasi-static loading zone. In-between, a narrow stretch zone appears joining the FCP and the monotonic zone (usually defined as stable crack extension). The main fractographic aspects of CTOD tested alloys CW510L and CW511L in the “as received” and after “final heat treatment” conditions are presented in Figures 6.6 - 6.13. In the case of ductile tearing the crack first undergoes blunting, i.e. it deforms plastically, until the crack extends by shearing off the metal links between the voids ahead of it.

The well-known stretch zone is formed due to the blunting at the onset of stable crack extension by void coalescence. Although this is usually not relevant with final failure, it provides useful information concerning fracture toughness and ductility [7]. Since the CTOD is defined by the distance between both crack faces in the vicinity of the crack tip, an ideal approximation could be that the critical CTOD value equals to almost two times the stretch zone width (SZW). CW510L brass alloy under the “as-received condition” presented a typical three-zone failure after CTOD testing: a fatigue precracking zone (FCP), an intermediate stretch zone and a ductile monotonic loading zone (Fig. 6.6). The last one consists of shallow dimples with flat terraces, indicating relatively limited plastic flow.

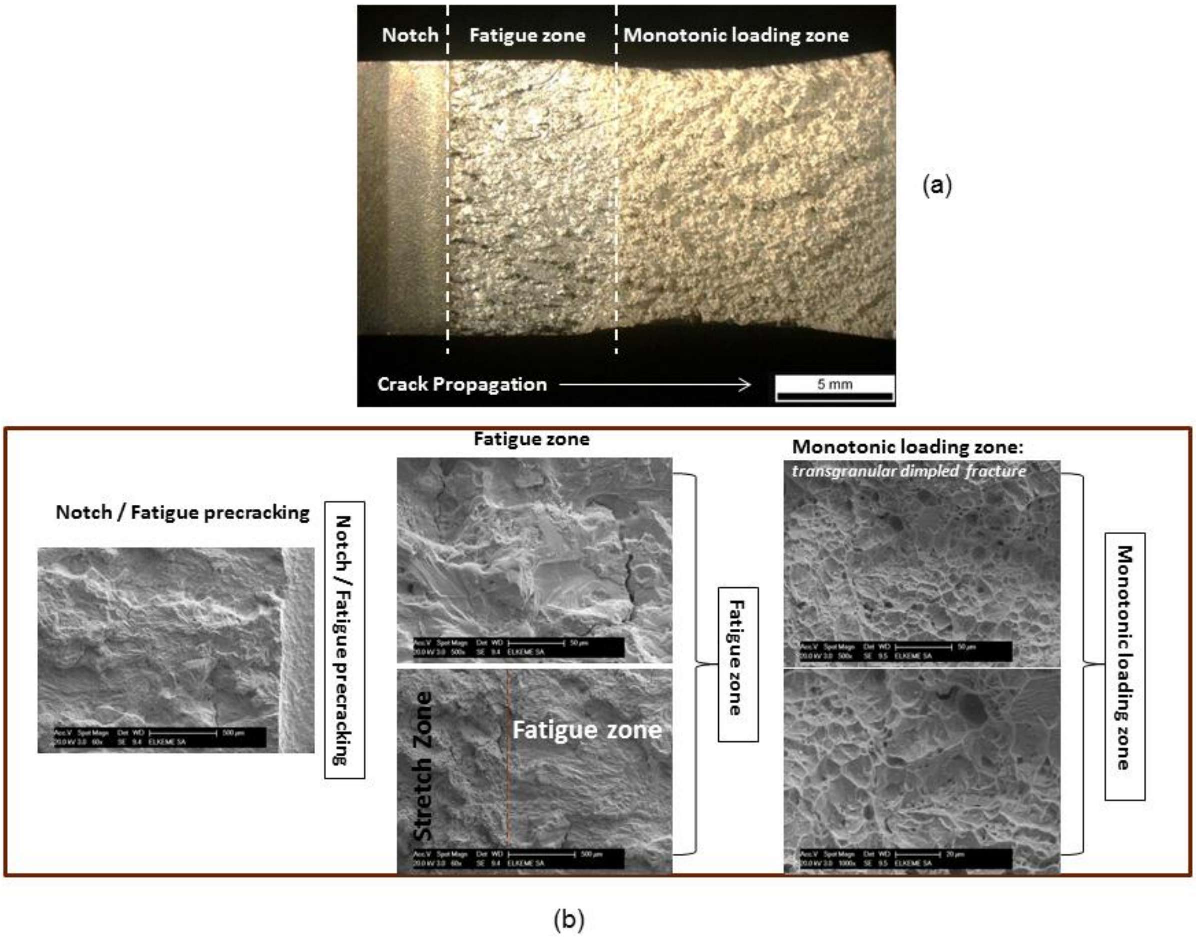

Fig. 6.6: Fractographic evaluation CTOD fracture of CW510L, as received condition: (a) optical stereomicrograph showing the entire fracture surface, (b) SEM micrographs showing details of the crack propagation history at the various transition zones (fatigue, stretch zone and monotonic loading).

In Figure 6.7, details of FCP zone are highlighted: fine and uniform fatigue striations indicated steady and continuous crack propagation with $d\alpha/dN \sim 0.7$ μm/cycle. The same alloy (CW510L) after “final heat treatment” showed a completely different failure mechanism; all the fracture zones are unified in a characteristic intergranular crack propagation fashion (Fig. 6.8).

Intergranular fatigue crack propagation was also evidenced, while fine fatigue striations were observed on the grain facets, denoting approximately a crack advancement rate ($d\alpha/dN$) equal to 0.8 μm/cycle (Fig. 6.9).

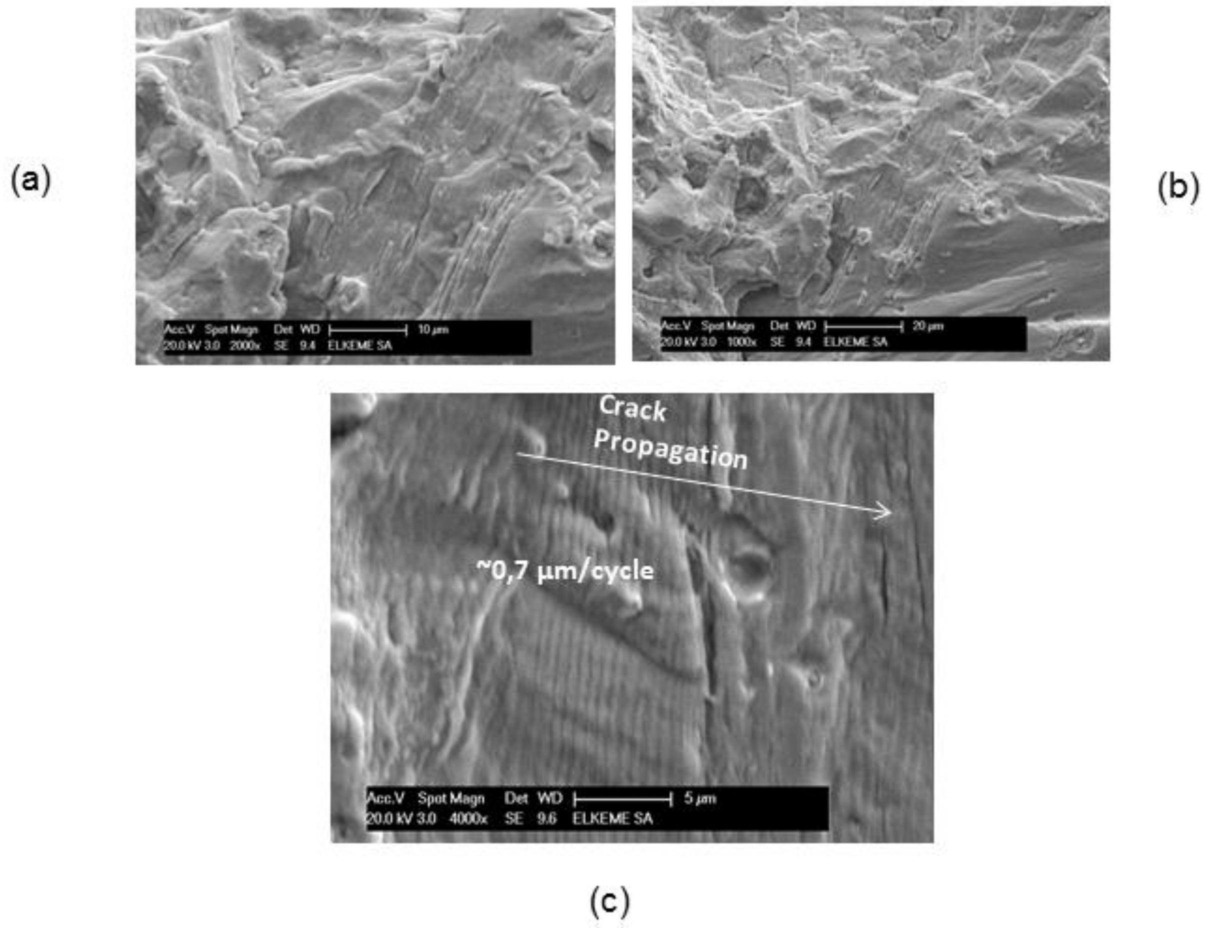

Fig. 6.7: Fractographic details of the fatigue crack propagation zone (CW510L, as received condition). Note the presence of typical fine fatigue striations denoting the localized *dα/dN*.

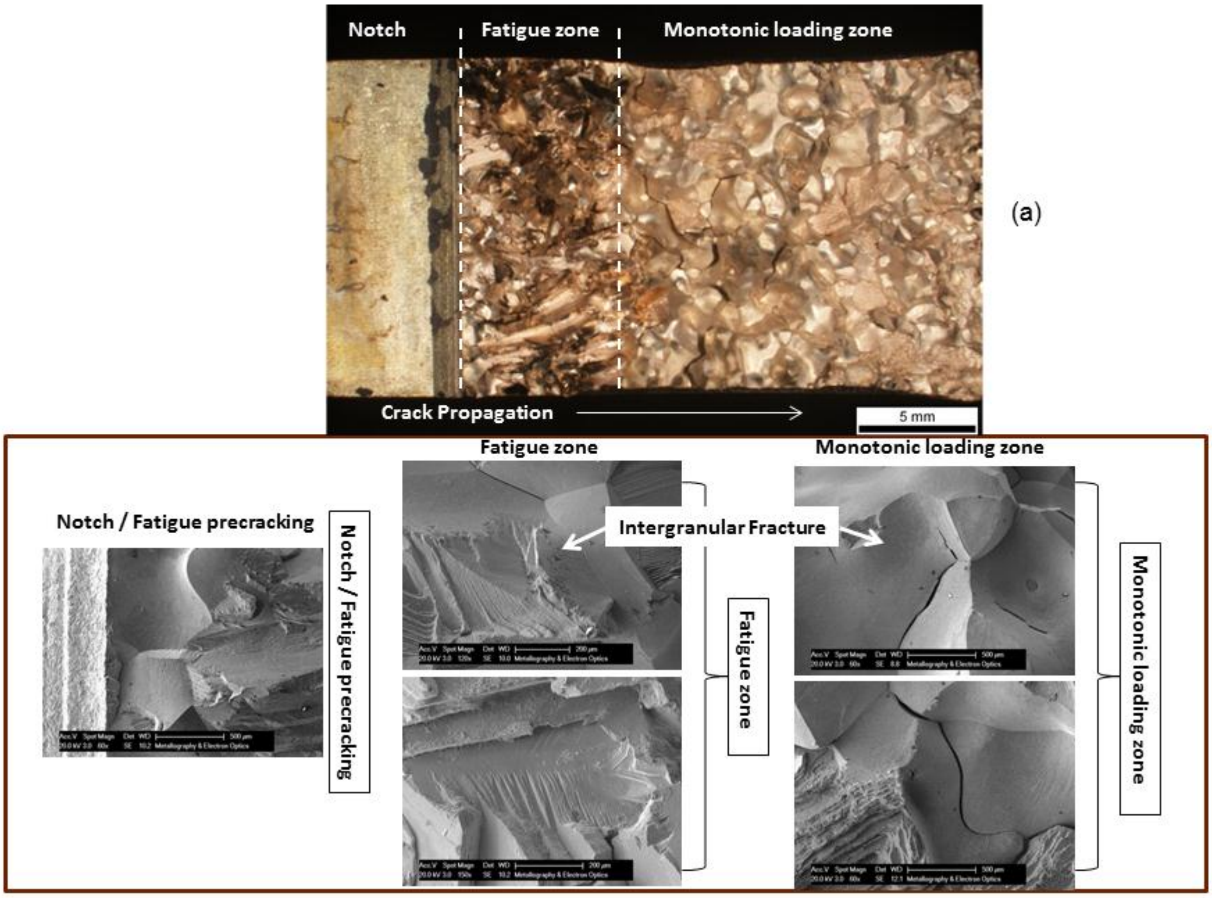

(a)

(b)

Fig. 6.8: Fractographic evaluation CTOD fracture of CW510L, after heat treatment: (a) optical stereomicrograph showing the entire fracture surface, (b) SEM micrographs showing details of the crack propagation history at the various transition zones (fatigue, stretch zone and monotonic loading).

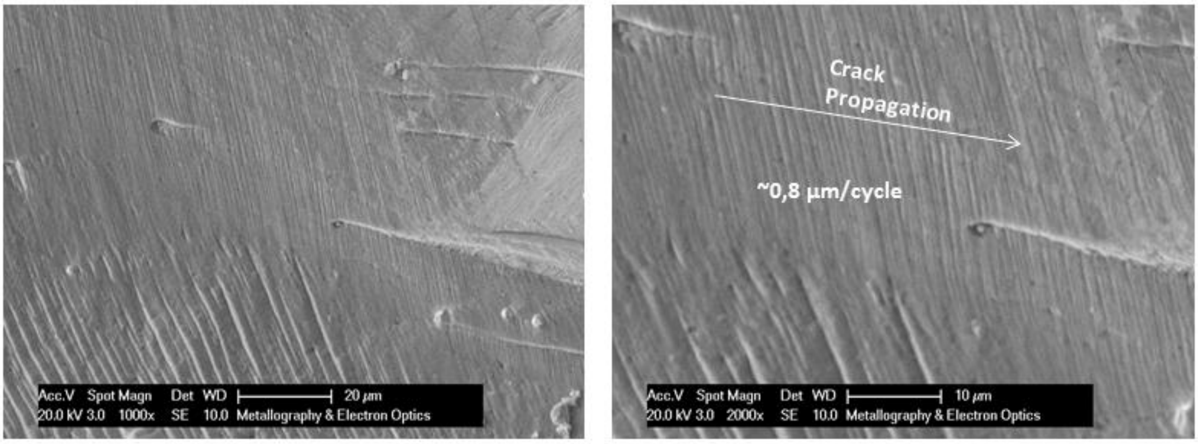

(a) (b)

Fig. 6.9: Fractographic details of the fatigue crack propagation zone (CW510L, after heat treatment). Note the presence of typical fine fatigue striations denoting the localized *dα/dN*.

CW511L brass alloy at the “as-received” condition presented a fully plastic behaviour recognized by the massive dimpled fracture surface in stretch zone and monotonic zone (Fig. 6.10). Fatigue precracking zone showed a wavy-serrated fracture surface which constituted signs of “fatigue ductility”, while a clear striation pattern is depicted with average crack propagation rate (*dα/dN*) approximately equal to 0.4 μm/cycle (Fig. 6.11).

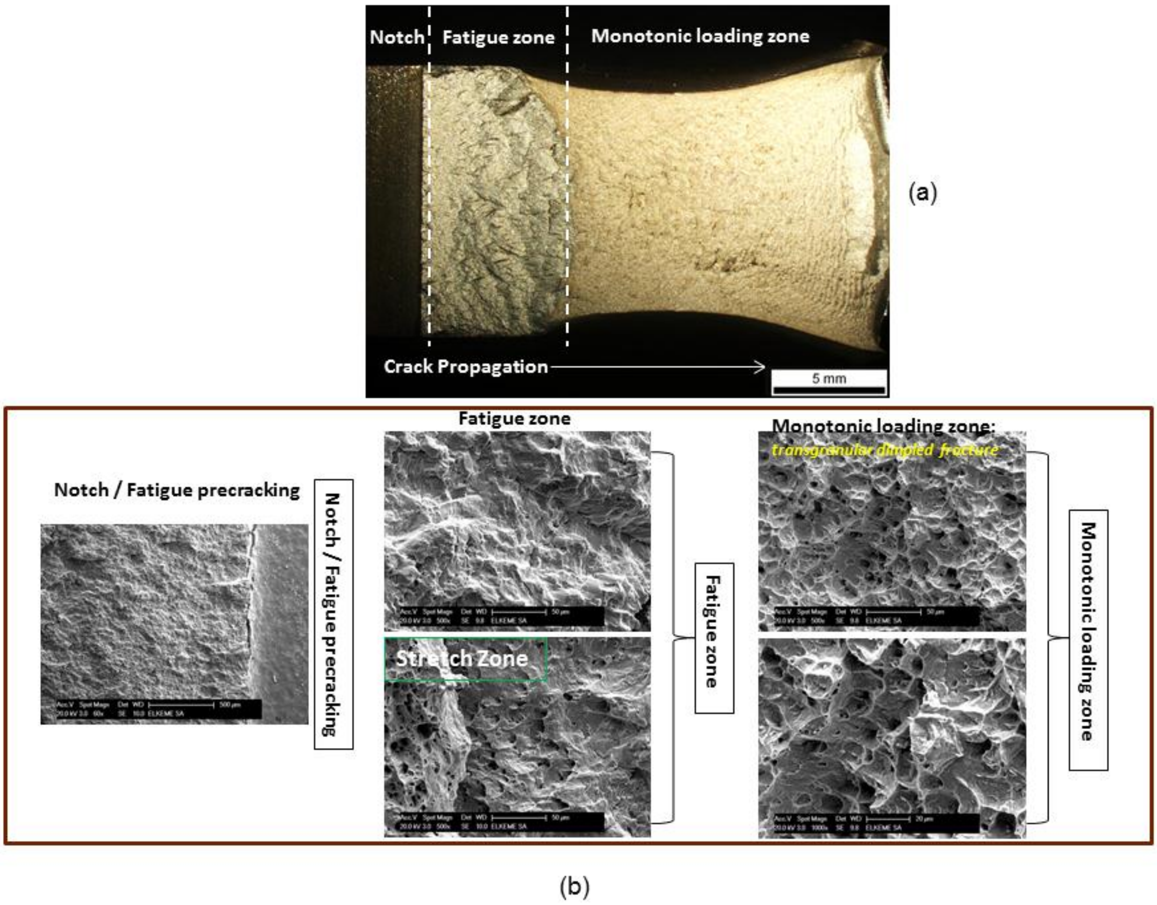

Fig. 6.10: Fractographic evaluation CTOD fracture of CW511L, as received condition: (a) optical stereomicrograph showing the entire fracture surface, (b) SEM micrographs showing details of the crack propagation history at the various transition zones (fatigue, stretch zone and monotonic loading).

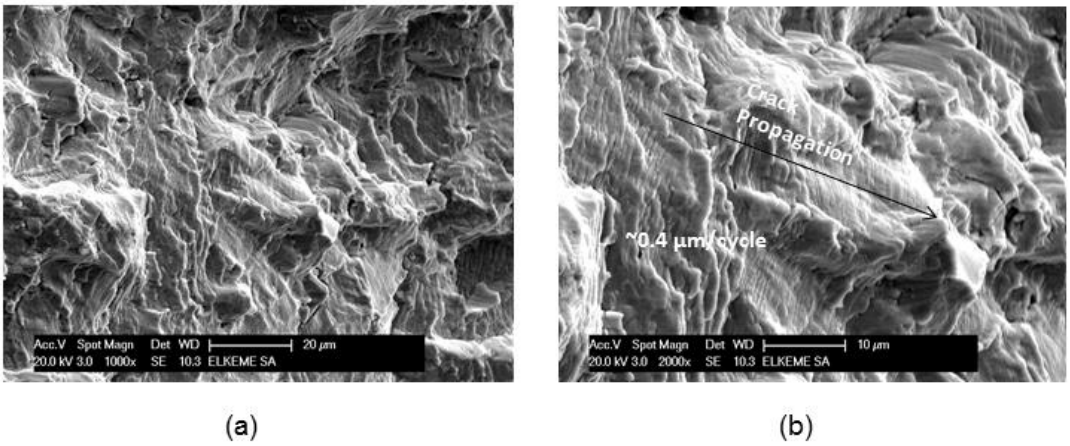

Fig. 6.11: Fractographic details of the fatigue crack propagation zone (CW511L, as received condition). Note the presence of typical fine fatigue striations denoting the localized *dα/dN*.

The crack propagation pattern remained qualitatively unaffected after “final heat treatment” of the CW511L brass alloy (Fig. 6.12). The main differences to the “as received” CW511L condition are summarized as follows: (i) a coarser fatigue striation spacing is measured, implying a faster crack propagation rate (2.8 μm/cycle), see Figure 6.13 and (ii) smaller dimple size governs the failure surface of the monotonic zone, signifying a lower amount of plastic deformation accounted during stable crack extension (compare Fig. 6.12b with Fig. 6.9b).

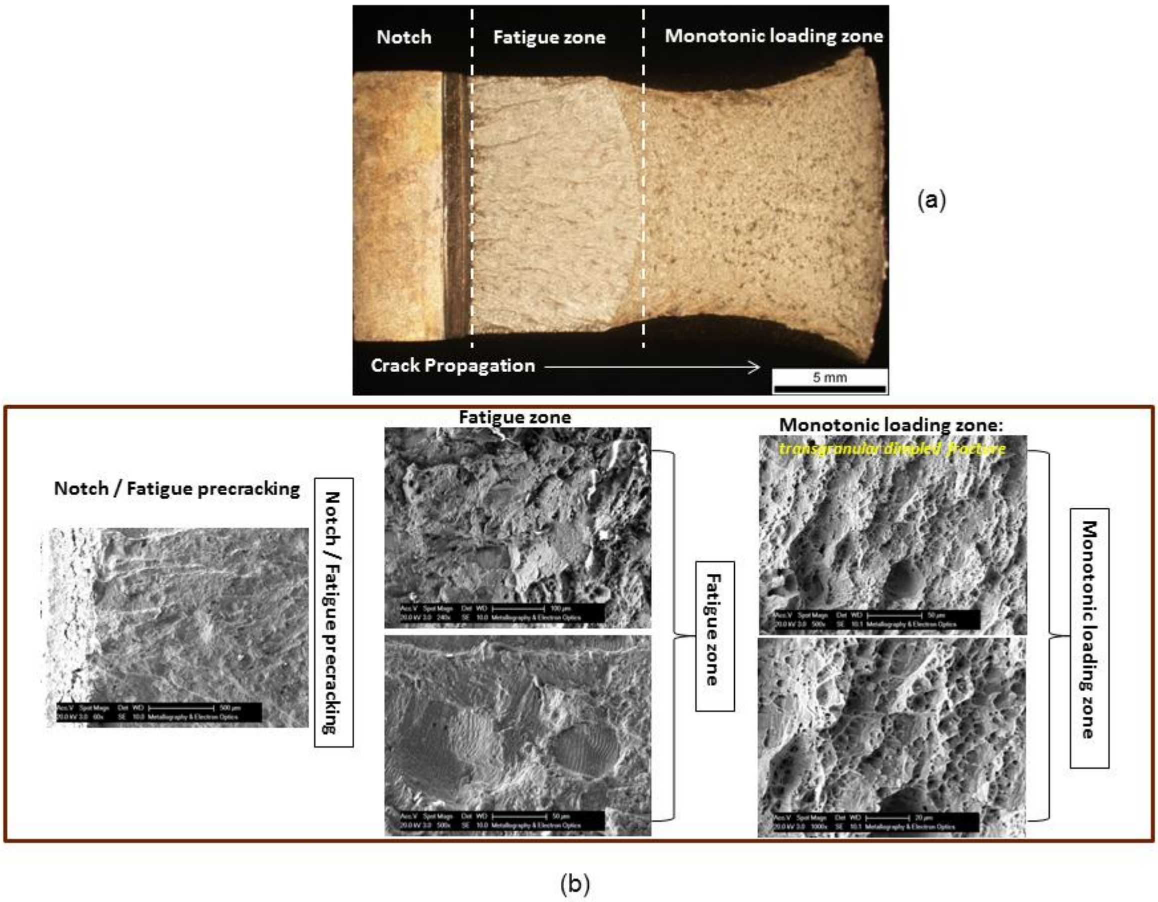

Fig. 6.12: Fractographic evaluation CTOD fracture of CW511L, after heat treatment: (a) optical stereomicrograph showing the entire fracture surface, (b) SEM micrographs showing details of the crack propagation history at the various transition zones (fatigue, stretch zone and monotonic loading).

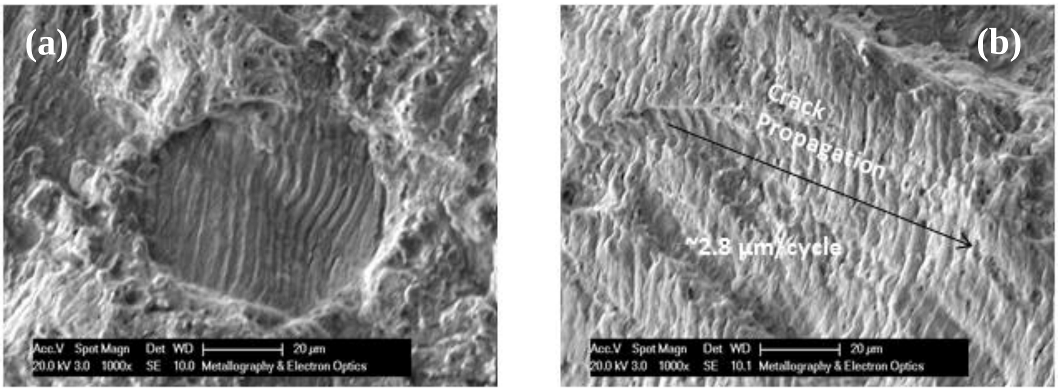

Fig. 6.13: Fractographic details of the fatigue crack propagation zone (CW511L, after heat treatment). Note the presence of typical fine fatigue striations denoting the localized *dα/dN*.

The fracture mechanics properties and failure mechanisms of CW510L and CW511L brass alloys under different manufacturing process conditions were studied ("as-received" and after "final heat treatment"). This study was mainly motivated by the findings presented in a previous paper, focused on the elaboration of final (post-processing) heat treatment as a manufacturing strategy to enhance the β-phase percentage and improve the machinability of such eco-friendly lead-free brass alloys [1]. In view of the performance optimization, the "fine tune" of the microstructure, in conjunction to the static mechanical properties mandated by the well-established technical specifications and customer's requirements, was among the main targets of this work [1]. However, preliminary fracture analysis undertaken in the former study, outlined alterations in failure mechanisms, alerting potential deterioration of fracture resistance of such components when working under adverse service conditions. In order to be able to ensure sound and reliable functionality of the (heat treated) brass alloys, a fracture mechanics study was launched to determine the variation in fracture toughness and the imminent failure mechanisms activated as a result of the proposed change in manufacturing process.

For CW510L brass alloy the "final heat treatment" condition shifted from dimpled transgranular to almost entirely macroscopic IG (intergranular) failure mode for impact and CTOD-tested samples (Figs. 6.3, 6.6 and 6.8). Ductile tearing and "staircase-type" transgranular fracture are considered as minor/secondary failure mechanisms (Fig. 6.4). It is noteworthy that the conventional CW614N-CuZn39Pb3 machinable leaded brass alloy possessed much lower fracture resistance, i.e. 9 J impact energy and 0.024 mm critical CTOD value at the regular manufacturing condition [3].

Similar failure modes (IG cracking) were identified after static tensile testing, as it was reported in a previous work [1]. A rather common cause, encountered as an IG fracture driver in brass alloy, is associated to *hot-shortness* and *liquid metal embrittlement (LME)*, especially in leaded brasses [8-9]. Pb diffusion provokes grain boundary decohesion and splitting, giving rise an IG failure mode. Hot tearing could be also assisted by extrusion conditions under high extrusion temperature and speed, where the application of axial stresses surpasses the material strength at the high temperature regime [10-11]. This fracture is usually of IG-type and it is normally connected to *hot shortness*. According to a review paper [12], the concentration of minor alloying elements (e.g. Bi, Pb, Sb) to the interface and grain boundaries is considered also as an embrittlement factor, especially at the temperature range between 300 and 600°C. In the embrittlement trough temperature range, the failure is again predominantly intergranular, and along the α-α and α-β grain boundaries which presented micro-voids (w- and r-type voids), similar to *brittle creep rupture,* as the major failure mechanism for 60-40 dual phase brass [13]. Also, the thermally activated Pb diffusion could diminish grain boundary and interface surface energy, promoting intergranular fracture, see Ref. [13].

The critical role of alignment of β-phase to the applied stress direction is also addressed in failure analysis and embrittlement of dual phase brass components [14]. However, in the former paper, there is an accompanied amount of plastic deformation and the fracture morphology differed significantly compared with that documented herein. In the current study, the absence of Pb and the ambient temperature testing conditions, rather excluded the possibility of the hot-shortness as the main cause of the observed IG fracture. No "molten pools" of low-melting constituents were also detected during high magnification imaging using Scanning Electron Microscopy, providing also an additional supporting evidence of the discount of the *hot-shortness* hypothesis.

The occurrence of IG fracture could be possibly interpreted taking into consideration the following parameters:

(a) Stress intensity range level (ΔK)
(b) Coarse β-*phase grain structure in relation to plastic zone size*
(c) High-angle grain boundaries

All the above parameters are considered as factors that could act individually or synergistically, promoting the IG crack propagation, in case of heat treated CW510L brass alloy. More specifically IG fatigue crack propagation has been observed in Ni-Al bronze valve and under slow fatigue crack growth regimes (10^{-7} mm/cycle), i.e. at low stress intensity level (ΔK) close to the threshold value [15].

Apart from the potential elements segregated at grain boundaries, the reasons for transition from transgranular to intergranular fracture near threshold ΔK_{th} values are not well clarified. A possible explanation is that slip processes adjacent to grain boundaries predominate especially at lower ΔK values and loading conditions, because grain boundaries are preferential sources of dislocation generation [15]. The validity of the above conceptual hypothesis could be further invigorated by the assumption of crack tip plasticity notion, in relation to the coarse β-phase grain structure. The plastic zone size is given by the following equations (1) and (2), for monotonic and cyclic loading conditions as a function of stress intensity – mode I (K_I), stress intensity range (ΔK) and proof strength $R_{p0.2}$ [6]. As it can be seen the cyclic plastic zone ($r_{p,cyclic}$) size is much lower than the corresponding monotonic ($r_{p,mono}$):

$$r_{p,mono} = \frac{1}{2\pi} \cdot \left[\frac{K_I}{(Rp_{0.2})}\right]^2 \qquad (1)$$

$$r_{p,cyclic} = \frac{1}{2\pi} \cdot \left[\frac{\Delta K}{(2.Rp_{0.2})}\right]^2 \qquad (2)$$

When the plastic zone size is higher than the grain size, then a multiple sets of slip systems are activated overcoming microstructural barriers and grain boundaries, promoting homogeneous plastic deformation and continuous crack propagation (Fig. 6.14).

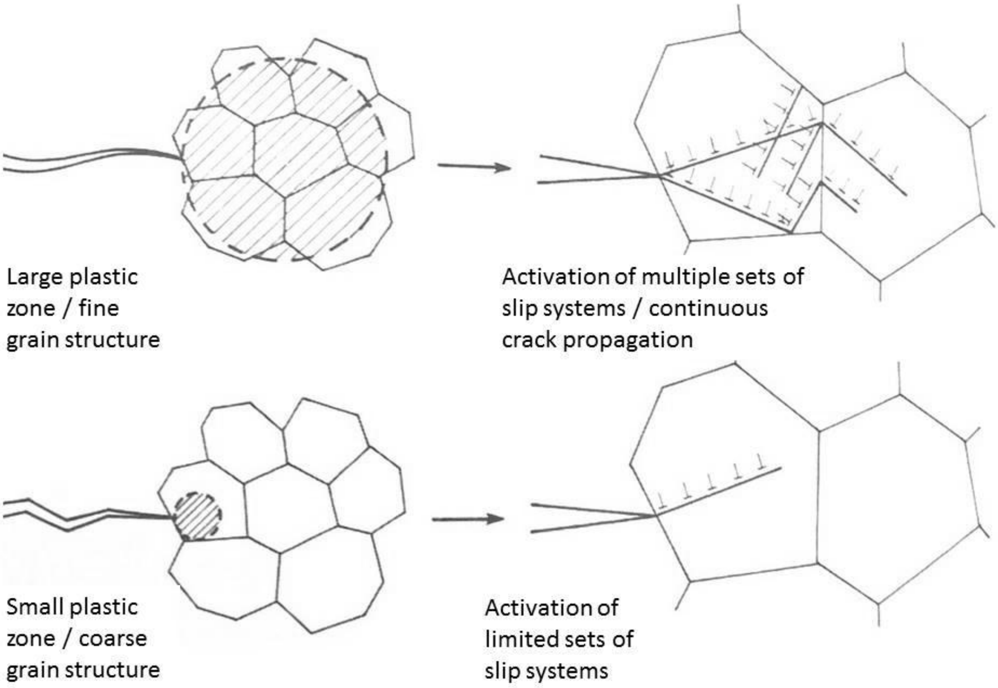

Fig. 6.14: Crack tip plasticity and grain size interactions.

On the contrary, as the grain size coarsens or the plastic zone size becomes comparable or less than the grain size, as in the current case, then only a few sets of slip systems are activated and dislocation emission is hindered by the existed microstructural barriers, causing dislocation pile-up to the activated slip systems. As plastic strain accommodation is ceasing, then threshold ΔK (ΔK_{th}) is approached [6]. A schematic representation of the interaction of plastic zone and grain size is presented in Figure 6.14 [6]. Generally, it can be stated that the coarse grain structure facilitated by high temperature heat treatment of CW510L in β-phase domain, results in a type of grain boundary sensitization leading to preferential IG cracking by microvoid coalescence (in case of monotonic loading conditions) or by micro-plastic deformation at the crack-tip region forming a typical striation pattern (in case of fatigue / cyclic loading conditions).

It is also known that grain boundaries have a significant influence on mechanical behaviour and can be considered as preferred sites for crack initiation and propagation. *High-angle grain boundaries* impede dislocation motion as a result of their high degree of misorientation, leading to dislocation pile-up and localized stress concentration that can induce failure [16]. Conversely, the slip systems of adjacent grains at low-angle grain boundaries are highly aligned, which allows the movement of dislocations inhibiting dislocation pile-up and accumulation and maintaining slip homogeneity across the boundary. Consequently, low-angle boundaries are resistant to intergranular (IG) fracture, which tends to propagate along *high-angle grain boundaries*. The strain incompatibilities and multiple slip system interactions at triple junctions arising from intersecting grain boundaries with varied structure, misorientation and defect content give birth to high stress fields in the triple junction region that promote crack nucleation. Triple junctions with *high-angle grain boundaries* are particularly prone to IG fracture [16].

The above parameters, namely *ΔK level, coarse* β*-phase structure and the formation of high-angle grain boundaries* constitute significant contributors of the outstanding IG failure mechanism activated in a broad range of loading conditions. This *unified concept of IG fracture* demonstrated by the finally heat treated CW510L is a salient hypothesis, highlighting the obscure role of the β-phase, possessing a bcc-lattice system which usually is prone to cleavage-transgranular rather than intergranular fracture. A synopsis of the fracture and failure analysis of the CW510L brass alloy is schematically shown in Figure 6.15.

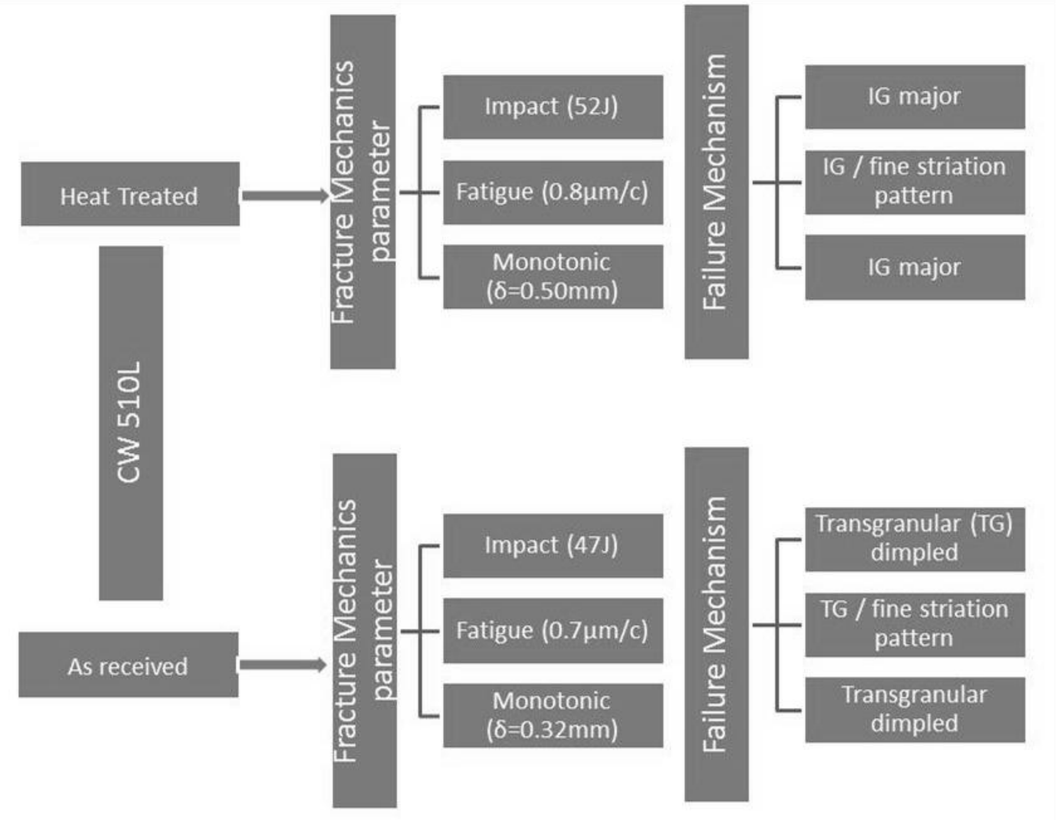

Fig. 6.15: Summary schematic of the fracture and failure analysis findings of the CW510L brass alloy under the “as-received” and “heat-treated” manufacturing conditions.

In case of CW511L heat treated brass alloy, no significant changes were identified concerning the emergent failure mechanism(s) under the diverse loading conditions (Figs. 6.5, 6.10 and 6.12). Nevertheless, minute changes in dimple size and distribution justified the slight deterioration of the plastic behaviour of heat treated CW511L brass alloy, giving rise to lower impact energy and critical CTOD values. Heat treatment of CW511L lead-free brass alloy at the high temperature range and for prolong period (850℃ for 120 min) resulted in the augmentation of β-phase percentage, but on the other hand in softening of the initial cold drawn (strain hardened) microstructure. This also resulted in decrease of hardness from 116 HV to 102 HV, as opposed to CW510L brass where hardness increase (from 127 HV to 138 HV) was mainly controlled by the massive β-phase transformation.

This could be a preliminary explanation concerning the different fracture toughness tendencies indicated by the two examined alloys. Further research pertaining to more in depth evaluation of microstructure and texture, as they considered critical contributors to fracture evolution, is suggested. However, the overall preservation of the ductile behaviour encourages the adoption of final heat treatment as a potential approach for machinability improvement.

In Figure 6.16, the findings of the fracture and failure analysis of the CW511L brass alloy are summarized.

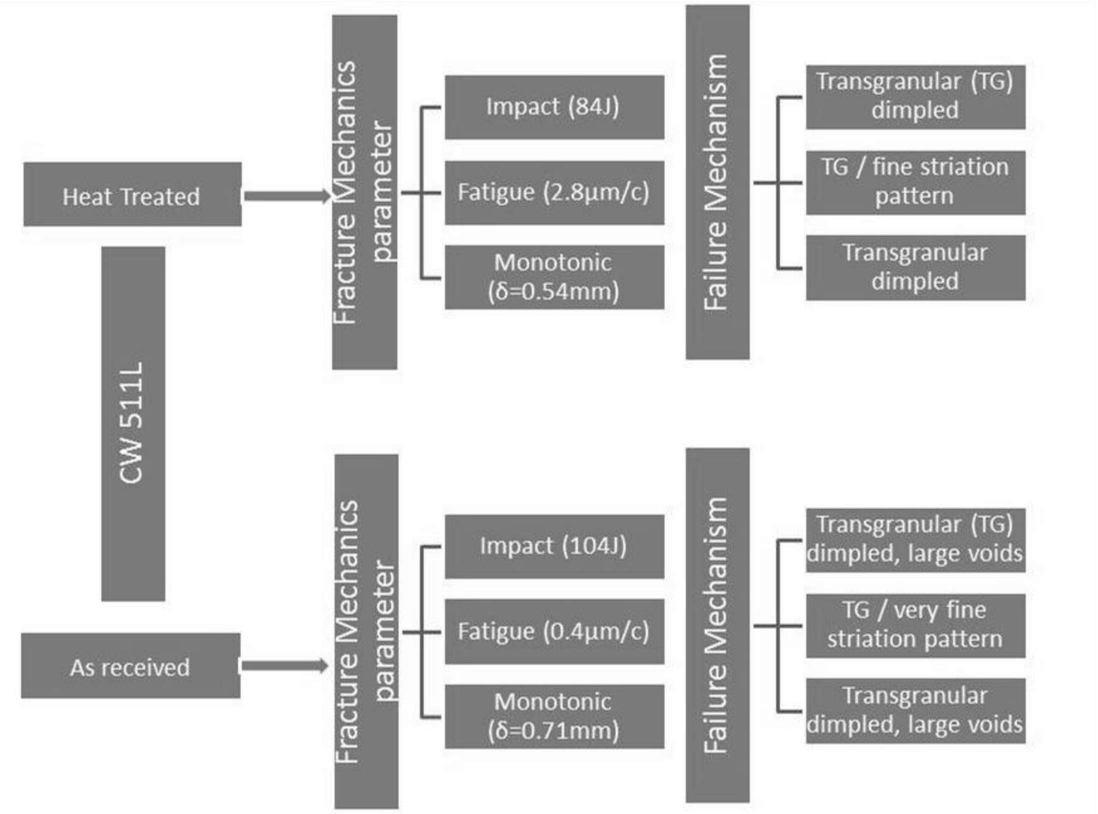

Fig. 6.16: Summary schematic of the fracture and failure analysis findings of the CW511L brass alloy under the “as-received” and “heat-treated” manufacturing conditions.

6.4. Section Conclusions

The optimum heat treatment conditions (775 °C, 60 min) of lead-free CW510L brass, caused an improvement of fracture toughness in terms of impact energy (from 47 J to 52 J) and critical CTOD (from 0.32 mm to 0.50 mm).

Failure mode at the various loading régimes for CW510L was governed by an intergranular fracture. Hot-shortness was excluded as the root-cause of the intergranular failure mechanism. The unification of intergranular failure mechanism constitutes a remarkable fracture mode and its interpretation could be based on the following concepts: ΔK-level, crack-tip plasticity zone/grain size interactions and high-angle grain boundaries notions.

Although, the heat treatment of lead-free CW511L brass, at 850 °C for 120 min, which was selected for machinability purposes, caused a slight deterioration of fracture toughness in terms of impact energy (from 104 J to 84 J) and critical CTOD (from 0.71 mm to 0.54 mm), the overall alloy ductility behaviour was maintained which was manifested via transgranular fracture by micro-void coalescence, resulting in a typical dimpled fracture surface.

6.5. References

[1] A. Toulfatzis, G. Pantazopoulos, A. Paipetis (2016) Microstructure and properties of lead-free brasses using post-processing heat treatment cycles. Materials Science and Technology 32: 1771-1781.

[2] G. Pantazopoulos, A. Toulfatzis (2012) Fracture modes and mechanical characteristics of machinable brass rods. Metallography, Microstructure, and Analysis 1: 106-114.

[3] A.I. Toulfatzis, G.A. Pantazopoulos, A.S. Paipetis (2014) Fracture behavior and characterization of lead-free brass alloys for machining applications. Journal of Materials Engineering and Performance 23: 3193-3206.

[4] A.I. Toulfatzis, G.A. Pantazopoulos, A.S. Paipetis (2017) Fracture analysis of eco-friendly brass alloys: comparison study and preliminary assessment. 14th International Conference on Fracture (ICF 14), June 18-23, Rhodes, Greece.

[5] W.F. Hosford (2013) Solid Mechanics. Cambridge University Press.

[6] M. Janssen, J. Zuidema, R. Wanhill (2004) Fracture Mechanics. 2nd edition, SPON Press.

[7] U. Zerbst, C. Klinger, R. Clegg (2015) Fracture mechanics as a tool in failure analysis-prospects and limitations. Engineering Failure Analysis 55: 376-410.

[8] G. Pantazopoulos, A. Vazdirvanidis (2008) Failure analysis of a fractured leaded-brass (CuZn39Pb3) extruded hexagonal rod. Journal of Failure Analysis and Prevention 8: 218-222.

[9] G. Pantazopoulos, A. Vazdirvanidis (2017) Fracture analysis and embrittlement phenomena of machined brass components. Procedia Structural Integrity 5: 476-483.

[10] R. Mannheim, J. Garin (2009) Hot tearing in extruded brass for machining applications. Revista de Metalurgia 45: 432-438.

[11] G.E. Dieter (1988) Mechanical Metallurgy. McGraw Hill, SI Metric Edition.

[12] V. Laporte, A. Mortensen (2009) Intermediate temperature embrittlement of copper alloys. International Materials Reviews 54: 94-116.

[13] D.J. Wolley, A.G. Fox (1988) The embrittlement of leaded and unleaded $\alpha+\beta$ (60-40) brasses in the temperature range 300 to 500°C. Journal of Materials Science Letters 7: 763-765.

[14] F. Felli, A. Brotzu, D. Pilone (2016) Analysis of the fracture criticality of biphasic brass. Procedia Structural Integrity 2: 2959-2965.

[15] R.T. Byrnes, S.P. Lynch (2015) An unusual failure of a nickel-aluminium bronze (NAB) hydraulic valve. Engineering Failure Analysis 49: 122-136.

[16] D. Bond, M.A Zikry (2017) Microstructural modeling of intergranular fracture in tricrystals with random low- and high-angle grain boundaries. JOM 69: 856-862.

Chapter 7: Final Heat Treatment as a Possible Solution for the Improvement of Machinability of Lead-Free Brass Alloys

7.1. Summary

The present work is an original contribution pertaining to the optimization of machinability of lead-free brass alloys (CuZn42, CuZn38As and CuZn36) after heat treatment. The current project possesses a unique advantage, since it aims to improve the machinability of conventional lead-free brass alloys, without altering the material chemistry. This can be also regarded as an attempt to change the metallurgical condition, and, on the other hand, to comply with the product European specification limits, as far as the chemical composition and mechanical properties are concerned, as opposed to the special alloy classes which referred to Refs [1-4]. A second, but also significant advantage of this "heat treatment" approach is the avoidance of detrimental hard secondary phases (such as κ-phase in Si-brasses), which accelerate cutting-tool wear [5].

To the best of our knowledge, no relevant studies have been published concerning the influence of microstructure after heat treatment on the machinability of lead-free brass alloys. In the frame of this work, chip morphology, power consumption, cutting force, and surface roughness were assessed before and after heat treatment to highlight the influence of the modified microstructure on the evolution of machinability quality parameters.

The examined machinability criteria were the following: chip morphology, power consumption, cutting force and surface roughness. All the above quality characteristics were studied in turning mode in "as received" and "heat treated" conditions for comparison purposes. The selected heat treatment conditions were set for CW510L (775°C for 60 min), CW511L (850°C for 120 min) and C27450 (850°C for 120 min) lead-free brass alloys, according to standard specification and customer requirement criteria. The results are very promising concerning the chip breaking performance, since the heat treatment contributed to the drastic improvement of chip morphology for every studied lead-free brass. Regarding power consumption, heat treatment seems beneficial only for the CW511L brass, where a reduction by 180 W (from 1600 to 1420 W), in relation to the as-received condition, was achieved. Furthermore, heat treatment resulted in a marginal reduction by 10 N and 15 N in cutting forces for CW510L (from 540 to 530 N) and CW511L (from 446 to 431 N), respectively. Finally, surface roughness, expressed in terms of the average roughness value

(*Ra*), seems that it is not affected by heat treatment, as it remains almost at the same order of magnitude. On the contrary, there is a significant improvement of maximum height (*Rt*) value of CW511L brass by 14.1 μm (from 40.1 to 26.0 μm), after heat treatment process performed at 850°C for 120 min.

7.2. Microstructure and Mechanical Properties

All the studied lead-free brass alloys exhibited a duplex phase microstructure consisting of α and β phases. Figure 7.1 depicts representative optical micrographs showing the microstructure of the CuZn42 (CW510L), CuZn38As (CW511L) and CuZn36 (C27450) lead-free brasses in "as received" (Fig. 7.1a–c) and in "heat treated" condition (Fig. 7.1d–f).

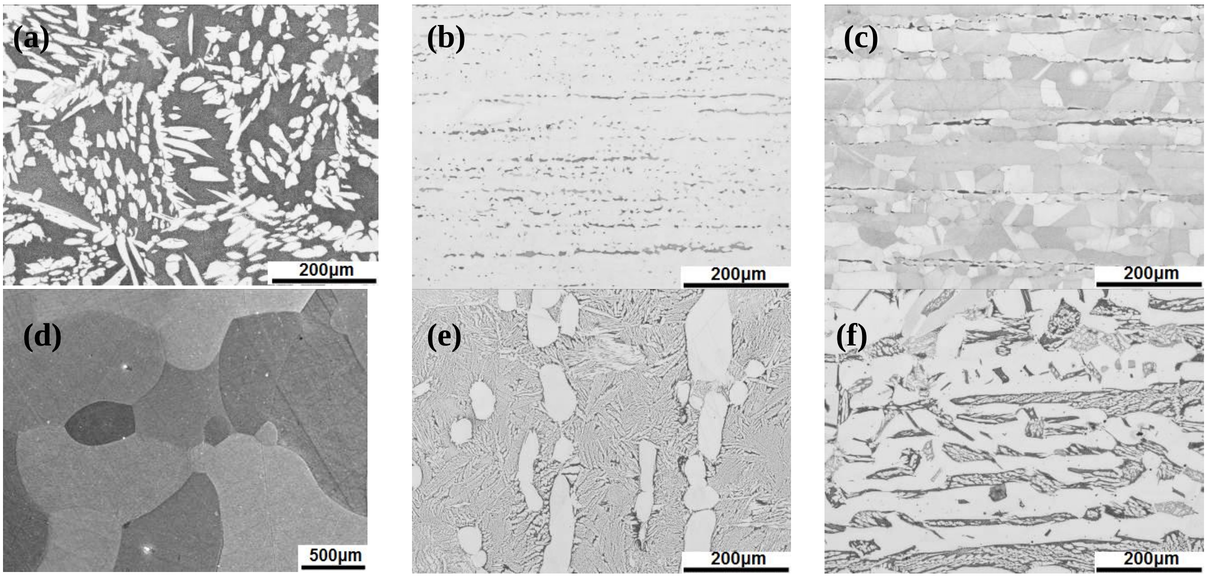

Fig. 7.1: Indicative optical micrographs showing the phase structure of longitudinal sections of "as received": (a) CW510L, (b) CW511L, (c) C27450 and "heat treated" conditions: (d) CW510L, (e) CW511L, (f) C27450 Pb-free brasses. Note that bright areas represent α-phase and dark areas represent β-phase regions.

Significant changes in phase structure were provoked after heat treatment (Fig. 7.1). More specifically, β-phase content was varied within 20–100% for the examined heat treatment conditions. In the case of CW510L brass, a massive β-phase transformation was achieved, leading to an almost 100% β-phase structure. In our previous research work, the alteration of microstructure of the lead-free brass alloys due to heat treatment and its influence on mechanical and fracture resistance was thoroughly analyzed [6-7]. More specifically, heat treatment contributed to the increased percentage of β-phase, also seriously modifying the mechanical properties and fracture toughness.

The increase of β-phase fraction resulted in alloy strengthening and elongation reduction (as a consequence of grain coarsening and β-phase dominance). The β-phase grain size was varied with respect to temperature and soaking time, as shown in Table 7.1.

Table 7.1: Average grain size of beta-phase as a function of soaking temperature and duration.

Temperature (°C)	Soaking Time (min)		
	15	60	120
700	Partial beta-phase formation	500–700 μm (~600 μm)	500–700 μm (~600 μm)
775	600–800 μm (~700 μm)	600–800 μm (~700 μm)	600–800 μm (~700 μm)
850	600–800 μm (~700 μm)	1000–1500 μm (~1250 μm)	1000–1500 μm (~1250 μm)

Temperature appeared to be the most significant parameter for grain size control. Machinability tests were subsequently performed for the "optimum" cases of heat treated brasses, where the mechanical properties were found in compliance with the relevant product specifications (Table 7.2). It was evidenced that the presence of β-phase (especially for CW510L brass alloy) stimulates the occurrence of intergranular fracture, a phenomenon which promotes the easy chip breaking and consequently the lower power consumption. After heat treatment, both CW511L and C27450 alloys, demonstrated fully plastic behaviour, resulting in a completely ductile dimpled fracture. The deeper and coarser dimples, which implied more severe plastic deformation was encountered for the heat treated C27450 brass alloy. Hence, the chip breaking of the two latter brass alloys (CW511L and C27450) is controlled by the maximum allowable plastic strain imposed on the cutting shear zone, which is required for the chip removal.

Characteristic scanning electron microscope (SEM) micrographs showing the phase structure of the heat treated lead-free brass alloys, under higher magnification, are presented in Figure 7.2. Except for phase content difference, the variations in phase morphology and distribution were found to be significant, a fact that could potentially affect both the mechanical properties and machinability. In a recently published work, an improvement of fracture toughness was reported for CW510L heat treated brass, in terms of impact energy and Crack-Tip-Opening-Displacement (CTOD) [7].

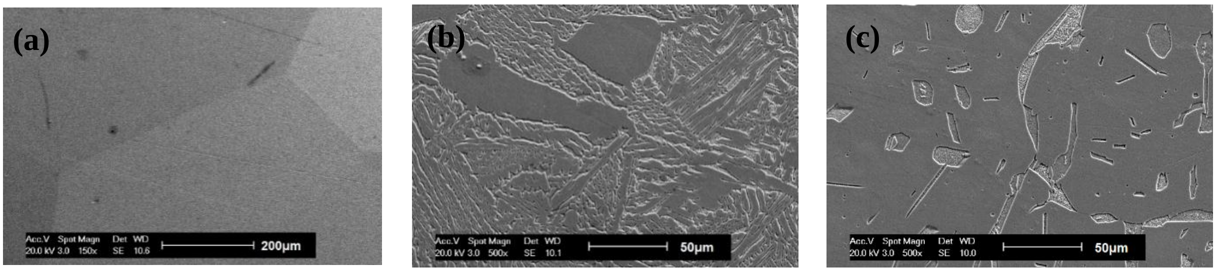

Fig. 7.2: Scanning electron microscope (SEM) micrographs of longitudinal sections showing the microstructures of (a) CuZn42 (CW510L), (b) CuZn38As (CW511L) and (c) CuZn36 (C27450), after selected heat treatment conditions.

Microstructure and mechanical properties, after the realization of the optimum heat treatment conditions, are summarized in Table 7.2, see also the results reported in a previous work [6].

Table 7.2: Phase structure and mechanical characteristics of heat treated lead-free brass alloys.

Brass Alloy	**Temperature (°C)**	**Soaking Time (min)**	**β-phase (%)**	$R_{p0.2}$ **(MPa)**	R_m **(MPa)**	A_{50} **(%)**	HV_1 **Midway**
CW510L	775	60	100	175	430	14	138
CW511L	850	120	35	136	396	44	102
C27450	850	120	20	118	364	47	88

7.3. Machinability Evaluation

In previous research works, machinability testing was performed in order to evaluate the chip morphology and power consumption, as well as the cutting force and the surface roughness [8-9]. In these studies, machining was conducted in three lead-free (CW510L, CW511L, C27450) brass alloys and one leaded (CW614N) brass alloy in the "as received" conditions and the optimum cutting parameters were defined by using Design of Experiments (DOE) statistical techniques [8-9].

In the present work, the selection of the machining parameters was based on the "worst" case scenario quality results. Table 7.3 shows the combinations of cutting parameters which resulted in the worst result for each specific quality characteristic (chip morphology, power consumption, cutting force and surface roughness) of the studied lead-free brass alloys, in the "as received" condition.

Therefore, the machining parameters which were applied to the heat-treated brasses, were properly selected from Table 7.3, in order to pursue a direct comparison with the "as received" material condition which exhibited the worst cutting performance, as far as the major quality characteristics were concerned.

Table 7.3: The "worst" combinations of cutting parameters for the quality characteristics (chip morphology, power consumption, cutting force, surface roughness-Ra) of studied lead-free brass alloys in "as received" condition [8-9]

Quality Characteristic	**Material**	**Cutting Speed (rpm)**	**Depth of Cut (mm)**	**Feed Rate (mm/min)**	**Average Value**
Chip Morphology (*CM*)	CW510L	1500	0.5	150	Class. 4*
	CW511L	2000	1.5	150	Class. 5*
	C27450	2250	2.0	150	Class. 5*
Power Consumption (*P*)	CW510L	1750	1.5	500	1900 W
	CW511L	1750	2.0	250	1600 W
	C27450	2000	1.0	500	1390 W
Cutting Force (*CF*)	CW510L	1750	1.5	500	540 N
	CW511L	1750	2.0	250	446 N
	C27450	1500	1.5	250	346 N
Surface Roughness (*Ra*)	CW510L	1750	1.5	500	8.0 μm
	CW511L	2250	0.5	500	4.3 μm
	C27450	2000	1.0	500	5.6μm

*Chip Morphology (*CM*) classification: 1 needle chip, 2 arc chips, 3 conical helical chips, 4 washer-type helical chips, 5 ribbon chips.

7.3.1. Chip Morphology

The results for the evaluation of chip morphology for each studied lead-free brass after the heat treatment process are depicted in Table 7.4. Overall, the turning operation before and after heat treatment resulted in the formation of different chip types from long and continuous chips (washer-type and ribbon) to short and discontinuous chips (arc and conical helical). Similar findings were obtained in a relevant study [10]. Figure 7.3 presents some of the chips obtained after the machining of the studied brass alloys, under the conditions illustrated in Table 7.4.

Table 7.4: Chip morphology results of lead-free brasses after the selected heat treatment processes.

Temp. (°C)	Soaking Time (min)	Cutting Parameters				*CM* (Class.) * As Received	*CM* (Class.) * Heat Treated
		Cutting Speed (rpm)	Depth of Cut (mm)	Feed Rate (mm/min)	Material		
775	60	1500	0.5	150	CW510L	4	2
850	120	2000	1.5	150	CW511L	5	3
850	120	2250	2.0	150	C27450	5	3

* Chip Morphology (CM) classification: 1 needle chip, 2 arc chips, 3 conical helical chips, 4 washer-type helical chips, 5 ribbon chips.

The chip morphology for CW510L brass alloy after heat treatment at 775°C for 60 min, was significantly improved, shifting from “Class. 4” (washer-type helical chips) to “Class. 2” (arc chips). Concerning heat treated CW511L brass alloy (850°C for 120 min), chip morphology was also substantially improved, as it moved from “Class. 5” (ribbon chips-snarled) to “Class. 3” (conical helical chips). Finally, regarding heat treated C27450 brass alloy (850°C for 120 min), the chip morphology changed from “Class. 5” (ribbon chips-short) to “Class. 3” (conical helical chips). All the above results are illustrated in Figure 7.3 and Table 7.4. As a common observation for all the studied brass alloys, an improvement of chip morphology ranking by two (2) classes after heat treatment was reported. An improved chip breaking capability is directly connected with lower cutting tool wear-rates. The width of the chips varies as a result of the different depth of cut (0.5, 1.5 and 2.0 mm) employed during the various machining experiments. Chip segmentation is of pivotal importance since it facilitates the machining ergonomics and scrap removal without damaging workpiece surface quality and ensuring the safety of the working personnel.

The highest hardness obtained for CW510L after heat treatment (Table 7.2) is directly related to a lower percent difference in hardness between the produced chip and the base metal, due to the lower strain hardening rate. This is also related to the lower extent of plastic deformation and hence the ease in chip fracturing and segmentation for the applied machining conditions [8]. Moreover, this argument is also in agreement with the lowest chip morphology obtained in the case of CW510L (Class. 2). The comparison between chip hardness of the as-received and heat treated brass alloys show systematically lower values (by 7–10%), as was anticipated by the limited degree of plastic strain imposed during machining under the final heat treatment condition (Fig. 7.4).

Fig. 7.3: Optimum conditions of chip morphology for the studied alloys after heat treatment (“AR”: as received, “HT”: heat treated). (a) CW510L - as received condition, (b) CW510L – heat treated condition, (c) CW511L – as received condition, (d) CW511L – heat treated condition, (e) C27450 – as received condition, (f) C27450 – heat treated condition.

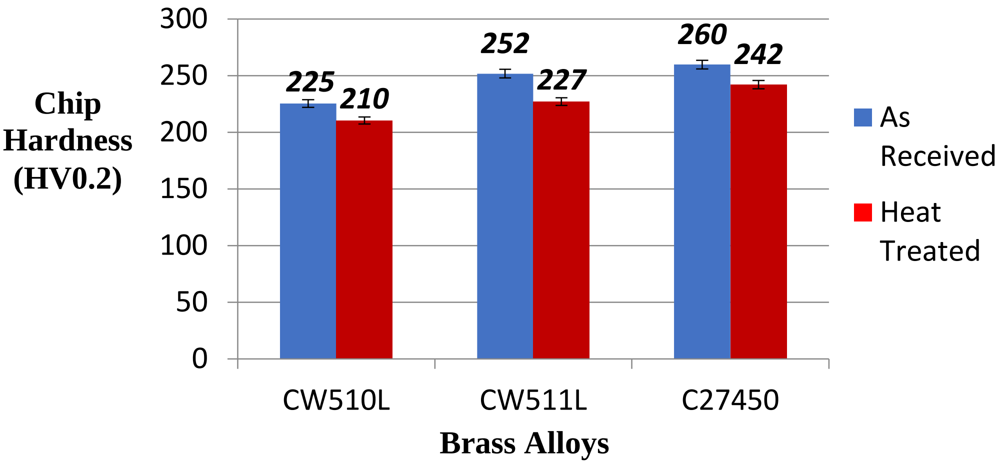

Fig. 7.4: Histograms showing the average chip hardness at the “as received” and “heat treated” conditions for the examined brass alloys.

Chip morphologies after heat treatment compared with the as received conditions were studied by optical microscopy for the three lead-free brass alloys (Fig. 7.5). It was observed that heat treatment has a beneficial effect leading to a highest extent of chip segmentation accompanied by a low degree of plastic deformation in the chip/rake face region (Fig. 7.5b, d, f) in relation to as received condition of lead-free alloys (Fig. 7.5a, c, e). Moreover, cracks seem to have evolved at the areas of intense shear band formation, see Figure 7.5b, d, f. This is in agreement with hardness differences found between chips originating from as-received and heat treated brass alloys, as illustrated in Figure 7.4.

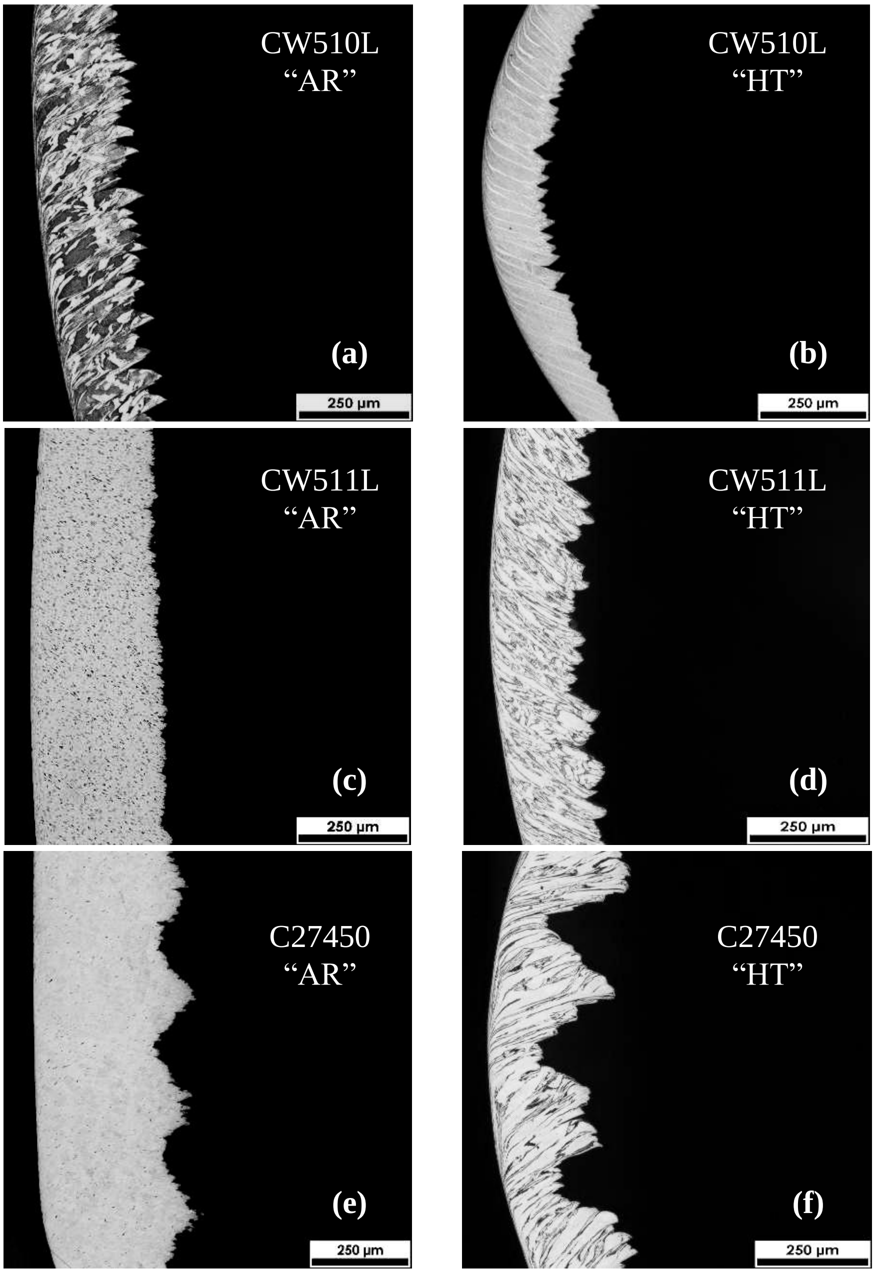

Fig. 7.5: Optical micrographs of chip morphologies: (a) CW510L, as received, (b) CW510L, heat treated, (c) CW511L, as received, (d) CW511L, heat treated, (e) C27450, as received, and (f) C27450, heat treated.

7.3.2. Power Consumption

Heat treatment at 850°C for 120 min of CW511L lead-free brass alloy yielded a beneficial result with regard to power consumption, where a reduction of 180 W (from 1600 W to 1420 W) compared to the as received condition was observed (Table 7.5). On the contrary, the power consumption for CW510L and C27450 brass alloys after heat treatment at 775°C for 60 min and 850°C for 120 min, respectively, did not show any improvement. More specifically, a moderate increase of 120 W (from 1900 W to 2020 W) and by 70 W (from 1390 W to 1460 W) in CW510L and C27450 brass alloys, respectively, was noticed. All the above results are presented in Table 7.5.

Also, using the present ranking, the highest power consumption was observed in the case of CW510L heat treated brass during turning, as it was also evidenced for the as-received condition. This could be attributed to the fact that the most influential parameter (depth of cut) did not change significantly, especially between the two first classes of brass alloys, i.e., CW510L and CW511L. The hierarchy of cutting process parameters of the three brass alloys (CW510L, CW511L and C27450), using the Taguchi-DOE technique, was studied and reported in a previous research paper [8].

Table 7.5: Power consumption results of lead-free brasses after the selected heat treatment processes.

Temp. (°C)	**Soaking Time (min)**	**Cutting Parameters**				***P* (W) As Received**	***P* (W) Heat Treated**
		Cutting Speed (rpm)	**Depth of Cut (mm)**	**Feed Rate (mm/min)**	**Material**		
775	60	1750	1.5	500	CW510L	1900	2020
850	120	1750	2.0	250	CW511L	1600	1420
850	120	2000	1.0	500	C27450	1390	1460

7.3.3. Cutting Forces

The evolution of cutting force during machining constitutes a common criterion used to evaluate machinability [11]. Cutting force results in the as received and heat-treated conditions are shown in Table 7.6. More specifically, in CW510L brass, cutting force is improved by 10 N (from 540 to 530 N) after heat treatment at 775°C for 60 min. In CW511L, there was also a higher reduction of cutting force by 15 N (from 446 to 431 N) after the application of heat treatment at 850°C for 120 min. Finally, the cutting force was increased by 27 N (from 346 to 373 N), in the case of C27450 brass, after heat treatment at 850°C for 120 min.

Table 7.6: Cutting force results of lead-free brasses after selected heat treatment processes.

Temp. (°C)	**Soaking Time (min)**	**Cutting Parameters**				***CF* (N) As Received**	***CF* (N) Heat Treated**
		Cutting Speed (rpm)	**Depth of Cut (mm)**	**Feed Rate (mm/min)**	**Material**		
775	60	1750	1.5	500	CW510L	540	530
850	120	1750	2.0	250	CW511L	446	431
850	120	1500	1.5	250	C27450	346	373

The cutting force results exhibited similar patterns compared with power consumption results (Table 7.5). Literally, heat treated CW511L brass alloy exhibited the highest reduction in both quality characteristics, while heat treated C27450 showed deterioration in cutting force as well as in power consumption. More specifically, the selected cutting parameters (1750 rpm cutting speed, 2.0 mm depth of cut and 250 mm/min feed rate), contributed to the improvement of cutting force quality characteristic (from 446 to 431 N) for the CW511L brass alloy. The same machining parameters which were used for power consumption measurements (as received vs. heat-treated CW511L alloy) resulted in the improvement of cutting power, from 1600 W to 1420 W. The similar behaviour manifested by the two quality characteristics, i.e., power consumption and cutting force, could be also attributed to their common most influential machining parameter (depth of cut) [9].

7.3.4. Surface Roughness

Figure 7.6 and Table 7.7, show the surface roughness and topography results for the studied alloys. It seems that heat treatment in comparison to the as received condition does not show improvement concerning the average roughness value (*Ra*) of the studied brass alloys.

Roughness average (*Ra*) is the primary indicator of surface roughness, but even completely different surfaces can still have the same *Ra* value. A surface with sharp spikes, deep pits, or general isotropy may yield the same average roughness value. *Ra* makes no distinction between peaks and valleys, nor does it provide information about spatial structure and topography. The surface roughness was also assessed in terms of *Rt* parameter to evaluate the surface quality after orthogonal cutting by turning operation [12]. *Rt* (maximum height—“Peak to Valley”) value is an important indicator of surface roughness which measures the vertical distance between the highest and lowest points in the evaluation length/area.

In this study, it seems that heat treatment of 850°C at 120 min, although it did not drive to an improvement in *Ra* values, it causes a substantial reduction in maximum height (*Rt*) values. This parameter was improved especially in the case of CW511L by 14.1 μm (from 40.1 to 26.0 μm). Heat treatment at 775°C for 60 min and 850°C for 120 min did not show any ameliorated results regarding the *Rt* value of CW510L and C27450 lead-free brasses, respectively. More specifically, the *Rt* value remained almost the same for CW510L brass (from 78.6 to 79.5 μm) and it increased for C27450 brass (from 49.2 to 59.4 μm). All the above results of *Ra* and *Rt* values are illustrated in Table 7.7.

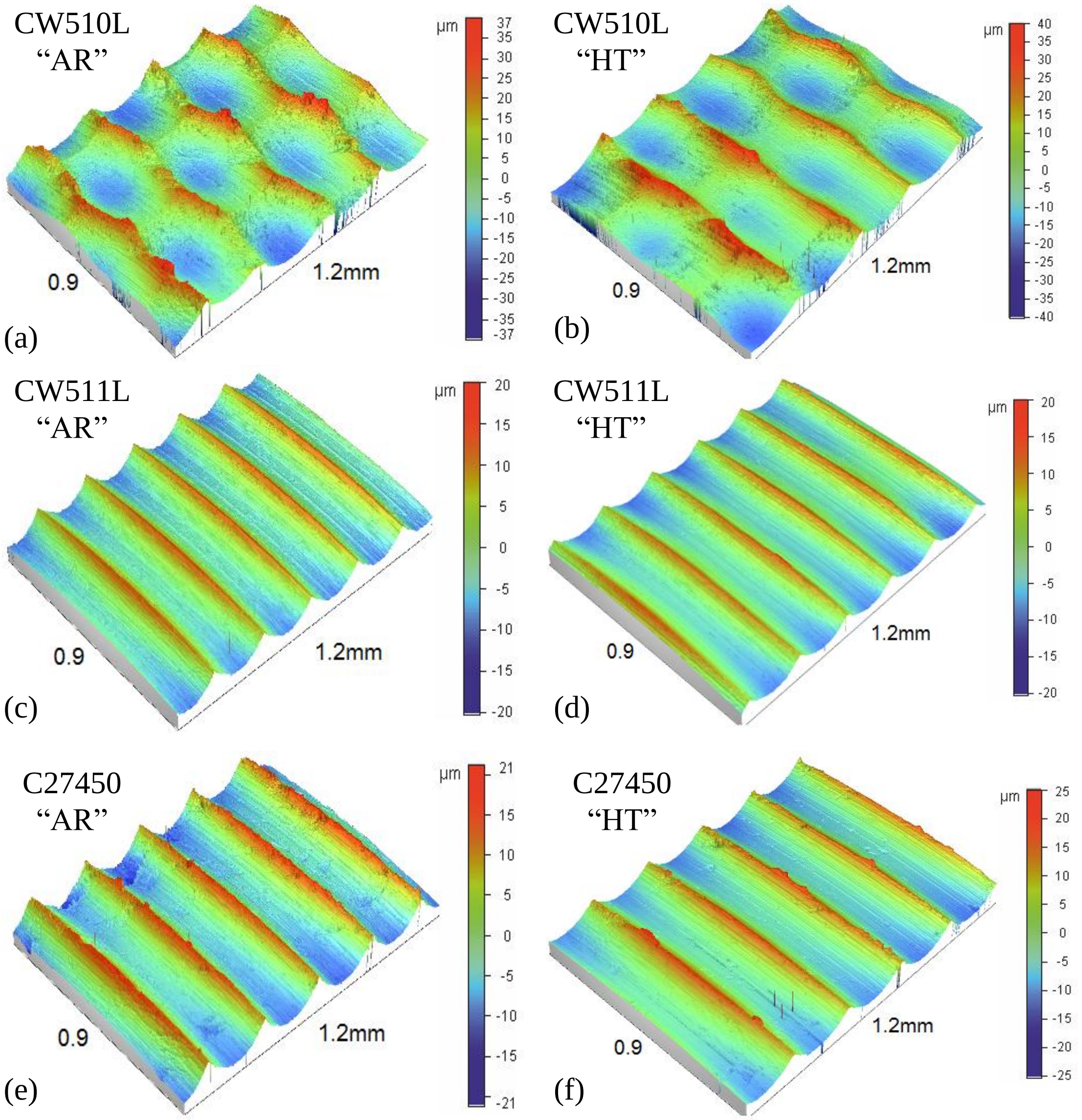

Fig. 7.6: Surface topography derived from profilometric measurements: (a) CW510L_As received, (b) CW510L_Heat treated, (c) CW511L_As received, (d) CW511L_Heat treated, (e) C27450_As received, and (f) C27450_Heat treated.

Table 7.7: Surface roughness results of lead-free brasses after selected heat treatment processes.

Temp. (°C)	**Soaking Time (min)**	**Cutting Parameters**				**SR-*Ra* (µm) As Received**	**SR-*Ra* (µm) Heat Treated**	**SR-*Rt* (µm) As Received**	**SR-*Rt* (µm) Heat Treated**
		Cutting Speed (rpm)	**Depth of Cut (mm)**	**Feed Rate (mm/min)**	**Material**				
775	60	1750	1.5	500	CW510L	8.0	8.5	78.6	79.5
850	120	2250	0.5	500	CW511L	4.3	4.3	40.1	26.0
850	120	2000	1.0	500	C27450	5.6	6.0	49.2	59.4

7.4. Section Conclusions

The heat treated lead-free brass alloys (at the optimum heat treatment process conditions) exhibited a significant improvement in chip breaking capability, reducing the chip morphology ranking by two (2) classes: (i) from “Class. 4” (washer-type helical chips) to “Class. 2” (arc chips) for CW510L and (ii) from “Class. 5” (ribbon chips) to “Class. 3” (conical helical chips) for both CW511L and C27450 brass alloys. Beneficial results in the power consumption were obtained only for the CW511L lead-free brass alloy, showing a reduction by 180 W (from 1600 W to 1420 W) in relation to as received condition. For the CW510L and C27450 lead-free brasses, the heat treatment process did not cause any further improvement.

A slight improvement in cutting forces (approximately by 2-3%) was recorded in case of heat treated CW510L and CW511L. CW511L cutting force reduction is consistent to the power consumption results. On the contrary, an increase in cutting forces (approximately by 8%) was evidenced for the heat treated C27450, as it was also dictated by the power consumption measurements. Surface roughness measurements, concerning the average roughness (Ra) values, seem that they were not affected by the selected heat treatment conditions. Conversely, an appreciable improvement in maximum height (Rt) value of the heat treated CW511L brass by 14.1 μm (from 40.1 to 26.0 μm) was achieved.

7.5. References

[1] Nobel. C, Klocke. F, Lung. D, Wolf. S (2014) Machinability enhancement of lead-free brass alloys. 6th CIRP International Conference on High Performance Cutting: 95-100.

[2] S. Li, K. Kondoh, H. Imai, H. Atsumi (2011) Fabrication and properties of lead-free machinable brass with Ti additive by powder metallurgy. Powder Technology 205: 242-249.

[3] H. Atsumi, H. Imai, S. Li, K. Kondoh, Y. Kousaka, A. Kojima (2011) High-strength, lead-free machinable α-β duplex phase brass Cu–40Zn–Cr–Fe–Sn–Bi alloys. Materials Science and Engineering A 529: 275-281.

[4] F. Schultheiss, D. Johansson, V. Bushlya, J. Zhou, K. Nilsson, J.E. Ståhl (2017) Comparative Study on the Machinability of Lead-Free Brass. Journal of Cleaner Production 149: 366-377.

[5] M.A. Taha, N. A. El-Mahallawy, R. M. Hammouda, T. M. Moussa, M. H. Gheith (2012) Machinability characteristics of lead free-silicon brass alloys as correlated with microstructure and mechanical properties. Ain Shams Engineering Journal 3: 383-392.

[6] A. Toulfatzis, G. Pantazopoulos, A. Paipetis (2016) Microstructure and properties of lead-free brasses using post-processing heat treatment cycles. Materials Science and Technology 32: 1771-1781.

[7] A. Toulfatzis, G. Pantazopoulos, A. Paipetis (2018) Fracture mechanics properties and failure mechanisms of environmental-friendly brass alloys under impact, cyclic and monotonic loading conditions. Engineering Failure Analysis 90: 497-517.

[8] A.I. Toulfatzis, G.A. Pantazopoulos, G.J. Besseris, A.S. Paipetis (2016) Machinability evaluation and screening of leaded and lead-free brasses using a non-linear robust multifactorial profiler. International Journal of Advanced Manufacturing Technology 86: 3241-3254.

[9] A. Toulfatzis, G. Pantazopoulos, C. David, D. Sagris, A. Paipetis (2018) Machinability of eco-friendly lead-free brass alloys: Cutting-force and surface-roughness optimization. Metals 8, 250, doi: 10.3390/met8040250.

[10] C. Vilarinho, J.P. Davim, D. Soares, F. Castro, J. Barbosa (2005) Influence of the chemical composition on the machinability of brasses. Journal of Materials Processing Technology 170: 441-447.

[11] N. Suresh Kumar Reddy, P. VenkateswaraRao (2006) Experimental investigation to study the effect of solid lubricants on cutting forces and surface quality in end milling. International Journal of Machine Tools and Manufacture 46: 189-198.

[12] H. Zein, O.M. Irfan (2018) Surface roughness investigation and stress modeling by finite element on orthogonal cutting of copper. Metals 8, 418: doi: 10.3390/met8060418.

Chapter 8: Final Conclusions and Suggestions for Further Work

8.1. Final Conclusions

In recent years, the enforced stricter regulations concerning allowable lead content levels in products, especially for drinking water applications, have encouraged the development of lead-free brass alloys. Brass alloys are widely used in industrial applications for the fabrication of final mechanical and electrical components such as bolts, nuts, hydraulic fittings, valves, switches, connectors, by machining. Therefore, the need for the design and development of eco-friendly (lead-free) brass alloys is imperative.

In this research work, the principal microstructural / mechanical characteristics and machinability behaviour of three special lead-free brass alloys (CW510L, CW511L and C27450), in relation to a typical leaded brass (CW614N) were studied. More specifically, this research was focused on the material characterization, cutting mechanisms (chip breaking), as well as the optimization of the machinability (Chip Morphology, Power Consumption, Cutting Force and Surface Roughness) of the aforementioned brass alloys. Also, in the frame of new alloy condition development, post-processing (extrusion and drawing) heat treatment cycles were scheduled and performed in experimental scale. The aim of this final heat treatment was to stimulate the formation of a microstructure with potential beneficial influence on machinability performance.

The main conclusions derived from the *Chapters* presented in this dissertation can be summarized as follows:

1. Regarding mechanical properties, CW510L lead-free brass alloy was found as a potential candidate (replacing conventional CW614N leaded brass), as it combines high tensile strength and fracture toughness, due to the prevalence of the β-intermetallic phase in the microstructure and the absence of lead particles at the grain boundaries. Fracture mechanics properties increased according to the following alloy order: CW614N < CW510L < CW511L < C27450. Dimpled ductile fracture was the dominant failure mechanism under impact loading for all tested brass alloys. The impact fracture surfaces of CW614N leaded brass and CW510L lead-free brass, revealed the shallowest and finest shear dimples, while the largest and deepest dimples were observed in the case of CW511L and C27450 brass alloys which absorbed the highest impact energy (*Chapter 2).*

2. Furthermore, a machinability optimization in turning for two quality characteristics, namely *Chip Morphology* (CM) and *Power Consumption* (P), was achieved using a joint screening technique with a four-level L_{16} (4^4) orthogonal array, in three special lead-free brass alloys (CW510L, CW511L and C27450) and a typical leaded brass (CW614N). The study revealed that the depth of cut and the alloy type were the two statistically predominant factors. The findings of the statistical evaluation were experimentally confirmed, validating the DOE approach (*Chapter 3).*

3. Concerning *Cutting Force* (CF) and *Surface Roughness* (SR), as quality characteristics of machinability during turning, a non-parametric optimization was attempted using data means, signal-to-noise (S/N) and ANOVA statistical techniques, in three special lead-free brass alloys (CW510L, CW511L and C27450) and a typical leaded brass (CW614N). It was deduced that the depth of cut and the feed rate were the most influential factors for the cutting force and surface roughness, respectively. Confirmation experiments are in close agreement to the main conclusions, validating the findings of the statistical evaluation (*Chapter 4).*

4. A variety of heat treatment cycles was chosen for each lead-free brass alloy, with a view to improving their machinability through the modification of the final microstructure, while keeping the mechanical properties within the standard specifications. The optimum selected heat treatment conditions (775°C / 60 min for CW510L, 850°C / 120 min for CW511L and 850°C / 60 & 120 min for C27450), led to a combination of increased β-phase percentage, along with mechanical properties conforming to standards, providing a promising ground for improved machinability performance, in the frame of the future design of production workflow (*Chapter 5*).

5. The optimum heat treatment condition for CW510L lead-free brass alloy resulted in an improvement of fracture toughness in terms of impact energy and critical CTOD. In case of heat treated CW511L a slight deterioration of fracture toughness concerning impact energy and critical CTOD was observed, while its overall ductility remained significant. The assessment of fracture mechanics properties and the fractographic information were closely connected to the dominant microstructure and loading regimes (e.g. ΔK-level, plastic zone size), which influence the crack propagation and the occurred failure mechanisms (*Chapter 6).*

6. Following a parametric machinability study, the results, after optimum heat treatment of lead-free brasses, were very promising concerning the chip breaking performance and morphology (by “2 classes” improvement according to ISO 3685) in relation to their as received condition (extruded and drawn). Regarding power consumption, heat treatment seems beneficial only for the CW511L brass while it has led to a marginal reduction in cutting forces for CW510L and CW511L lead-free brass alloys. Finally, surface roughness, expressed in terms of the average roughness value (Ra), seemed that it was not affected by heat treatment, as it remained almost at the same order of magnitude. On the contrary, there was a significant improvement of maximum height (Rt) value of CW511L lead-free brass after the optimum heat treatment process. The selection of the machining parameters was based on the “worst” case scenario for each quality criterion (Chip Morphology, Power Consumption, Cutting Force and Surface Roughness) presented in the previous *Chapters* 3 & 4 (*Chapter 7).*

Conclusively, the results of this work are considered promising, as they exhibit significant value due to the extended applications of these alloys in manufacturing industry. In addition, their reduced impact in the environment and human health provides an encouraging perspective towards the assurance of enterprise and society sustainable development.

8.2. Suggestions for Further Work

As a final note, post-processing heat treatment of lead-free brass alloys constitutes an interesting and innovative approach aiming to alter the machinability behaviour through microstructure modification, without changing the standard chemical composition, maintaining and even improving the mechanical properties without compromising the plastic behaviour. However, further experimental investigation is necessary to more precisely ascertain the heat treatment conditions and to transfer the process to the industrial scale, in order to design and implement an economically viable manufacturing process with minimum environmental impact.

The suggested further research will be focused:

(a) Simultaneous optimization of all quality characteristics (chip morphology, power consumption, cutting force and surface roughness) utilizing advanced statistical techniques, such as *Desirability Functions* (DFs) for the machinability of lead-free brass alloys.

Desirability Functions (DFs) play an important role for solving the optimization of process or product quality problems, having various quality characteristics in order to obtain a good compromise between these parameters. There are many alternative formulations to these functions and solution strategies suggested for handling their weaknesses and improving their strength.

(b) Electron Backscatter Diffraction (EBSD) analysis could be performed for better understanding of crystallographic orientations, texture analysis measurements and grain size/boundary types together with crack propagation relationships. This study could result in better understanding of the evolution of crystallographic texture during the various production stages of the lead-free brass alloys and to establish relationships with the evolved fracture micromechanisms.

(c) Design of new lead-free brass alloys, using special thermodynamics and phase diagram calculation software, such as CALPHAD (CALculation of PHAse Diagrams) could be further performed. Such thermodynamic simulation software could serve to the prediction of the microstructure and phase transformations under different states of equilibrium. In complex systems, CALPHAD is employed to model thermodynamic properties for each phase and simulate multicomponent phase behavior.

(d) Optimization and validation of the cutting conditions in industrial scale for the fabrication of exemplary final brass component by using complex machining operations (such as CNC machining center). Utilization of on-line monitoring techniques (e.g. vibration sensors) might be also employed to forecast the cutting tool durability and life time. In addition, the incurred cutting mechanisms could be further simulated using appropriate Finite Element Analysis (FEA) software.

Appendix A: Materials and Experimental Methods

A.1. Brass Rod Production Process

Three lead-free brass rods (CW510L – CW511L – C27450) and a leaded brass rod (CW614N) as a reference material, with a 35 mm nominal diameter, were employed for this study. Brass rods were produced by using classical casting and metal-forming operations, followed by heat treatment where necessary. A typical flow chart showing the sequence of the manufacturing operations of brass rods is showing in Figure A.1.

Continuous melting and casting was the first stage for the production of round brass billets. The next stage was hot billet extrusion. Preheating of the billets up to 650-700°C, depending on the alloy chemical composition and extrusion ratio (R), was required as the hot workability of the β-phase was increased. Subsequent pickling in sulfuric acid bath and rinsing in subsequent water baths was used for surface cleaning of the extruded bars. The dimensional tolerances and the hardness requirements are achieved by subsequent one-pass cold drawing with a reduction ratio (r_T) up to 10%, resulting in work hardening and subsequent surface strengthening, contributing to overall bar mechanical strength and also protecting the surface from mechanical damages (friction, abrasion, etc.).

Heat treatment, mainly stress relief (250-400°C), was necessary to eliminate the residual stresses originating mainly from cold metal forming. However, stress-relieving annealing is quite often required to prevent environmental failures like stress-corrosion cracking.

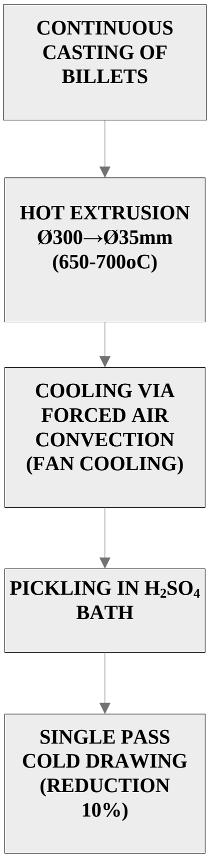

Fig. A.1: A simplified flow chart showing the production sequence of the CuZn39Pb3 (CW614N), CuZn42 (CW510L), CuZn38As (CW511L) and CuZn36 (C27450) brass rods.

A.2. Chemical Analysis

Chemical analysis was performed in brass alloys using optical emission spectrometry (OES) technique. Optical emission spectroscopy (OES) provides a non-evasive probe to investigate atoms, ions and molecules within plasma. It can provide information about properties, such as (excited state) species densities, electron-atom, atom-atom and ion-atom collisional effects, energy distribution of species, charge transfer between plasma constituents, and electric and magnetic fields to name a few. Its use as a diagnostic tool for emitting media has led to a greater understanding of very complex phenomena such as the evolution of stellar atmospheres and the study of fusion plasmas. Because the interpretation of OES observations is dependent on the source of emission and the understanding of the physical processes occurring within the source, care must be taken in the interpretation of these observations. Results of elemental chemical analysis of CuZn39Pb3 (CW614N), CuZn42 (CW510L), CuZn38As (CW511L) and CuZn36 (C27450) are presented in Table A.1 along with the corresponding tolerance limits foreseen by EN 12164 [1].

Table A.1: Chemical composition of the studied brass alloys (expressed in wt. %).

Alloy / (Spec.limits)	Cu	Sn	Pb	Fe	Ni	Al	Sb	As	Zn
CuZn39Pb3 (CW614N)	58.32	0.26	2.97	0.23	0.064	0.018	0.016	0.004	38.10
EN 12164 (CuZn39Pb3 / CW614N)	57-59	0.30 max	2.5-3.5	0.30 max	0.30 max	0.050 max	-	-	Rem.
CuZn42 (CW510L)	57.46	0.006	0.10	0.034	0.003	0.0002	0.003	0.001	42.38
EN 12164 (CuZn42 / CW510L)	57-59	0.30 max	0.20 max	0.30 max	0.30 max	0.050 max	-	-	Rem.
CuZn38As (CW511L)	62.04	0.004	0.09	0.019	0.001	0.0002	0.003	0.027	37.81
EN 12164 (CuZn38As / CW511L)	61.5-63.5	0.10 max	0.20 max	0.10 max	0.30 max	0.050 max	-	0.02-0.15	Rem.
CuZn36 (C27450)	63.38	0.014	0.21	0.024	0.003	0.025	0.003	0.001	36.32
Copper Development Association CDA (CuZn36 / C27450)	60-65	-	0.25 max	0.35 max	-	-	-	-	Rem.

A.3. Heat Treatment

A combination of nine (9) heat treatment schedules with rapid water quenching was implemented in each of the three studied leaded-free brass alloys (Table A.2). A total of twenty seven (27) heat treatments (3 temperatures x 3 times x 3 alloys) were performed in a Nabertherm electrical resistance furnace with air circulation and maximum temperature of 850°C (Fig. A.2**)**. The studied brasses, were placed in the preheated furnace of 700, 775 and 850°C and they were annealed for 15, 60 and 120 min (Fig. A.3). As is reported, 60 min heat treatment at 650^{o}C is known to cause stress recovery of strain hardened brass bar [2]. As aforementioned, the application of heat treatment process aimed at increasing β-phase percentage, leading potentially to the improvement of the machinability due to the intrinsic structure and hardness which characterizes this phase. At the same time, the alloy composition and mechanical properties' range should remain within the required standard specification limits.

The selection of heat treatment parameters was based on the “industrial workability window” and common practices. These depend on the engineering equipment tolerances, process optimization and alloy limiting conditions applied in order to avoid undesirable effects of severe surface oxidation and incipient melting.

Table A.2: Heat treatment schedule.

Heat Treatment	Brass Alloy	Temperature (°C)	Soaking Time (min)
AR 510	CW510L	As Received	
HT 1		700	15
HT 2		775	15
HT 3		850	15
HT 4		700	60
HT 5		775	60
HT 6		850	60
HT 7		700	120
HT 8		775	120
HT 9		850	120
AR 511	CW511L	As Received	
HT 10		700	15
HT 11		775	15
HT 12		850	15
HT 13		700	60
HT 14		775	60
HT 15		850	60
HT 16		700	120
HT 17		775	120
HT 18		850	120
AR 27450	C27450	As Received	
HT 19		700	15
HT 20		775	15
HT 21		850	15
HT 22		700	60
HT 23		775	60
HT 24		850	60
HT 25		700	120
HT 26		775	120
HT 27		850	120

*A triplicate of specimens were used for each condition

Fig. A.2: Nabertherm electrical resistance furnace.

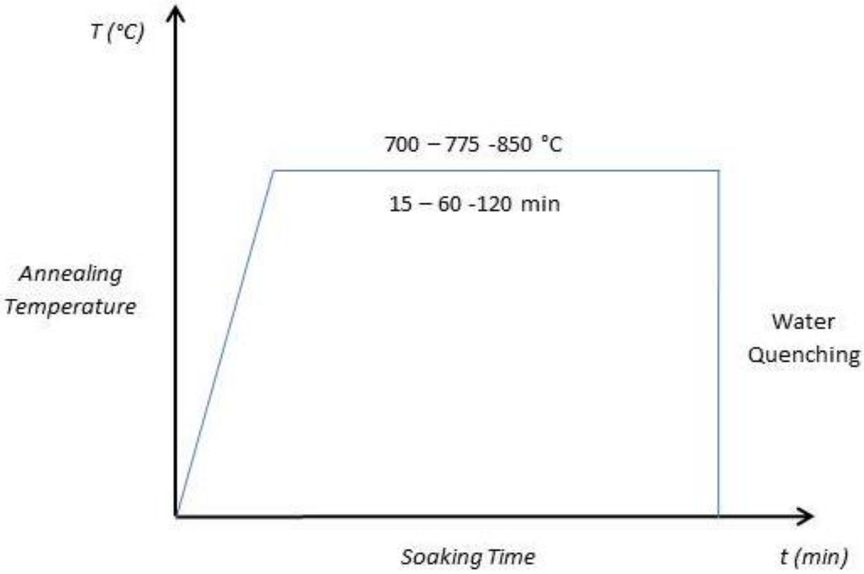

Fig. A.3: Indicative diagram showing the heat treatment procedure of CuZn42 (CW510L), CuZn38As (CW511L) and CuZn36 (C27450) lead-free brasses.

After the various heat treatments, microscopic characterization and mechanical testing were performed as was described below in Appendix A.4 and A.5, in order to identify the effect of heat treatment conditions on the microstructure and tensile properties.

A.4. Microstructure Characterization

The microstructural study was conducted in mounted sections (longitudinal and transversal to the extrusion direction) of the studied brass alloys. The hot mounted device used for mounting the CuZn39Pb3 (CW614N), CuZn42 (CW510L), CuZn38As (CW511L) and CuZn36 (C27450) brass alloys, was a Struers - Prontopress 20 (Fig. A.4).

Fig. A.4: Hot mounting device Struers - Prontopress 20.

Wet grinding and polishing were conducted in automatic grinding and polishing machine Struers - Rotopol 35 (Fig. A.5). Grinding was performed using successive abrasive SiC papers, followed by fine polishing using diamond and silica suspensions respectively. Rinsing in alcohol and drying in hot air stream were used as finishing procedures.

Fig. A.5: Automatic grinding and polishing machine Struers - Rotopol 35.

Finally, an immersion chemical etching was performed, using a $FeCl_3$ solution (8.3g $FeCl_3$ – 10ml HCl – 90ml H_2O), in the mounted specimens of CW614N and CW510L. For the mounted specimens of C27450 and CW511L a different solution of $FeCl_3$ (5g $FeCl_3$ – 50ml HCl – 100ml H_2O) was used according to the ASTM E407-07 standard [3]. Due to the higher percentage of zinc in the case of CW614N and CW510L, a different etching solution with lower concentration of HCL was used.

Lead particle dispersion as well as β-phase content were measured, in both longitudinal and transversal section of studied brass alloys**,** using the Image Pro Plus image analysis software and a metallographic inverted optical microscope Nikon Epiphot 300 (Fig. A.6).

Fig. A.6: Metallographic microscope Nikon Epiphot 300.

Lead-particle size and distribution parameters (Fig. A.7) include measurements as:

i) Measurement of maximum Lead-particle size.
ii) Measurement of mean size of Lead-particle size.
iii) Standard deviation in Lead-particle size measurement.
iv) Lead-particle density (particles / mm^2).

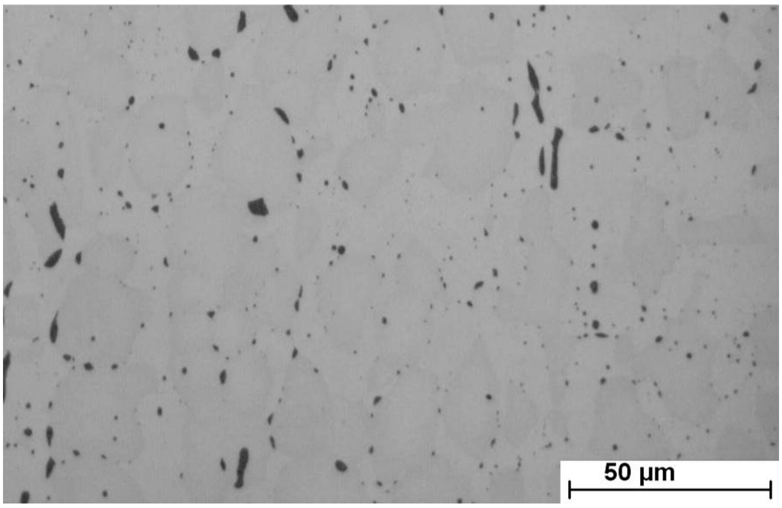

Fig. A.7: Lead particle distribution (Black spots).

The second category of measurements was the β-phase content (%). The phase structure consisted of α-phase crystals precipitated in a β-phase matrix as shown in Figure A.8. The β-phase had a higher contrast compared with the α-phase, as shown by means of bright field illumination light microscopy. The phase contrast was inverted under dark field illumination. The α/β interphase boundaries are high interfacial energy sites and, hence, potential lead distribution centers.

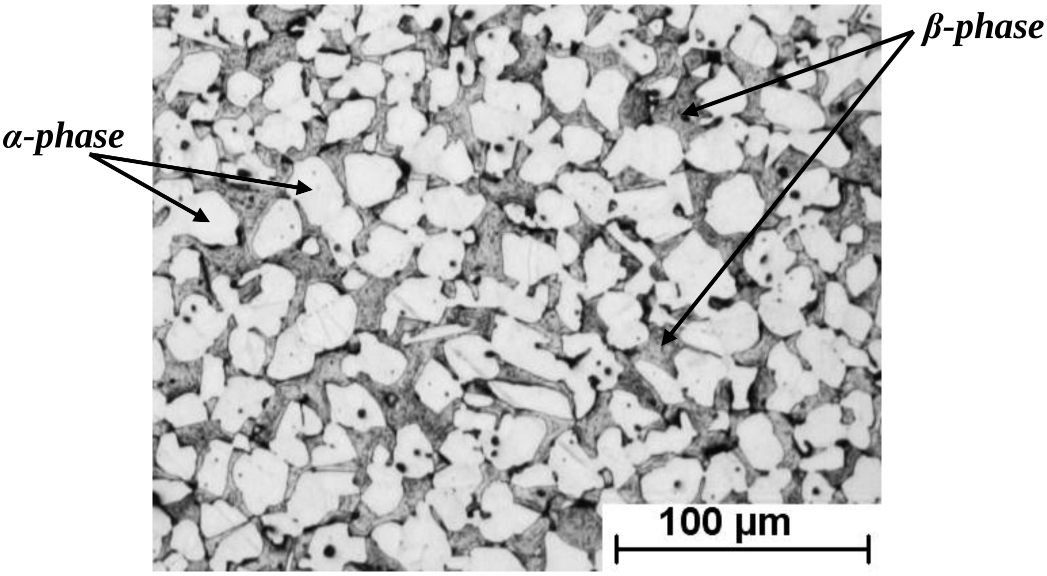

Fig. A.8: β-phase (dark areas).

A.5. Mechanical Testing

Tensile testing brass alloys specimens, were manufactured in a Computerized Numerical Control (CNC) lathe - EMCO PC TURN 155 as shown in Figure A.9.

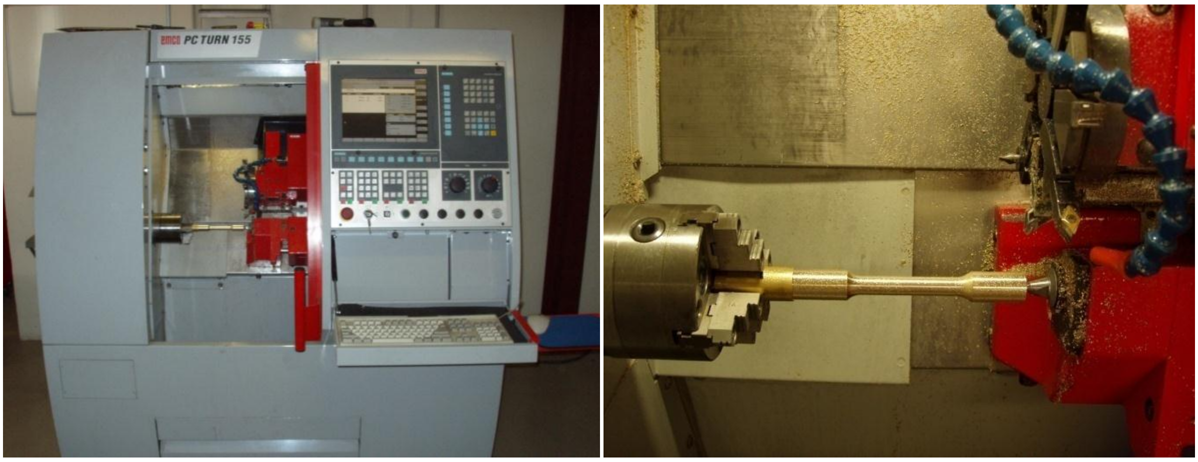

(a) (b)

Fig. A.9: (a) EMCO PC TURN 155, (b) Preparation of tensile testing specimens.

Tensile tests were performed on an Instron 8802 250 kN servohydraulic testing machine (Fig. A.10) at ambient temperature according to BS EN ISO 6892-1 standard [4].

Fig. A.10: Tensile testing machine Instron 8802.

Hardness tests were performed on a Instron Wolpert 2100 micro hardness tester (Fig. A.11a), using 1 kg (9.807 N) applied load, according to BS EN ISO 6507 standard [5]. Hardness tests were performed at the midway areas of transverse sections (Fig. A.11b) as dictated by EN 12164 standard [1].

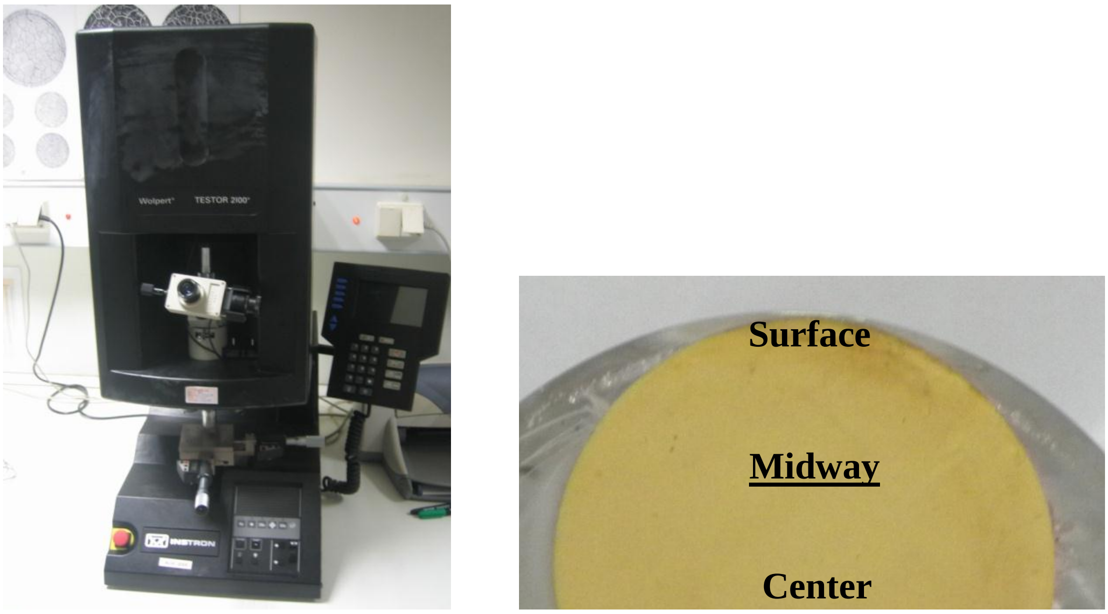

(a) (b)

Fig. A.11: (a) Hardness tester, Instron Wolpert 2100, (b) Hardness measurements positions.

Impact testing brass specimens, were manufactured in a CNC Mill (EMCO PC MILL 155) as shown in Figure A.12a, using a special device and a cutting mill tool which are shown in Figure A.12b.

(a) (b)

Fig. A.12: (a) EMCO PC MILL 155, (b) Tools for manufacturing impact specimens.

Dynamic bending loading was performed on an Instron Wolpert PW30 impact tester (Fig. A.13), using standard notched specimens with 10x10 mm^2 square section and 55 mm length, according to ISO 148-1 (Charpy V-notch tests) [6]; shear fracture and lateral expansion measurements were conducted according to ASTM A370 standard [7].

Fig. A.13: Instron Wolpert PW30.

Finally, the critical crack tip opening displacement (CTOD) was determined by three-point bending fracture toughness tests on the Instron 8802 machine (Fig. A.14) using standard single-edge notched bend (SENB) brass specimens (Fig. A.15) according to BS 7448: Part 1 standard [8]. The tests were carried out in displacement control with displacement rate 1 mm/min, bed-in amplitude 1 kN, modulus upper load 4 kN at a stable crack growth control mode rate within the range of 25 - 40 $MPa\cdot m^{1/2}$. During the fatigue pre-cracking stage (da/dN cycling process), crack length vs. cycles were also recorded and the load ratio (R) was prescribed equal to 0.1. The selected values for the frequency and the points/cycle were 25 Hz and 200, respectively.

The critical CTOD (δcrit) according to BS was given as the sum of elastic (δel) and plastic component (δpl) using the plastic hinge rotation model from crack-mouth opening displacement (CMOD), according to the following equation [8-9]:

$$\delta = \delta_{el} + \delta_{pl} = \left[\frac{S}{B} \cdot \frac{F}{W^{1.5}} \cdot g_1\left(\frac{a_o}{W}\right)\right]^2 \cdot \frac{1-v^2}{2R_{p0.2}\,E} + \frac{0.4\,(W-a_o)}{0.6a_o+0.4W+z}\ .V_p \tag{1}$$

Where,

S: span length between outer bending supports (100 mm)

F: load

B: specimen thickness (see Fig. A.15)

W: specimen width (see Fig. A.15)

g_1 (α_0/W): stress intensity factor

α_0: average original crack length

v: poisson’s ratio (0.3)

E: young’s modulus (105 GPa)

Vp: plastic component of CMOD

Z: knife edges thickness (1.5 mm)

$R_{p0.2}$: 0.2% proof strength (see Figs. 5.7a and 5.8a)

All the fracture mechanics tests were triplicated and the average value was extracted. The repeatability of the replicates was satisfactory, showing a very slight variation.

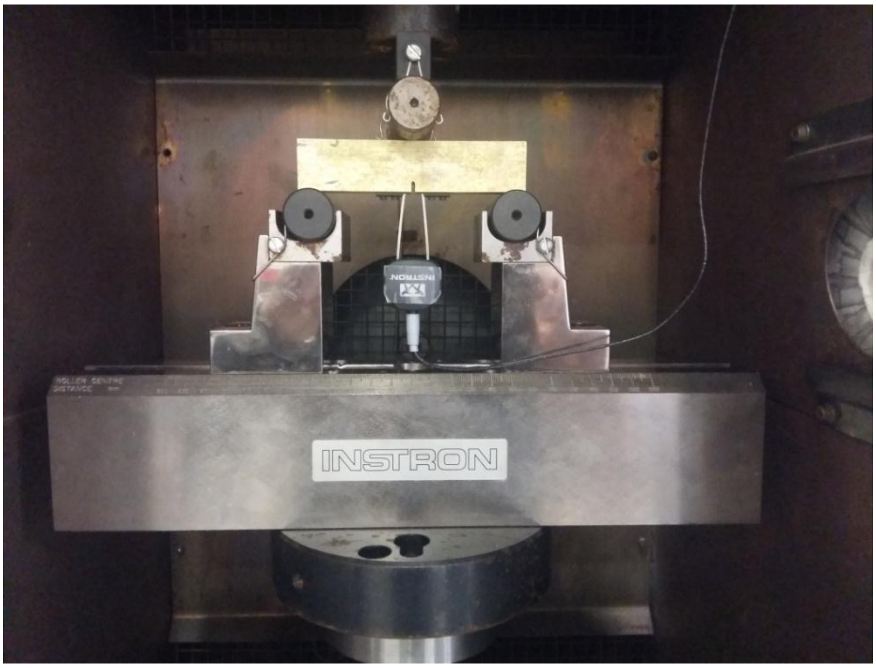

Fig. A.14: Three-point bending fracture toughness tests (CTOD).

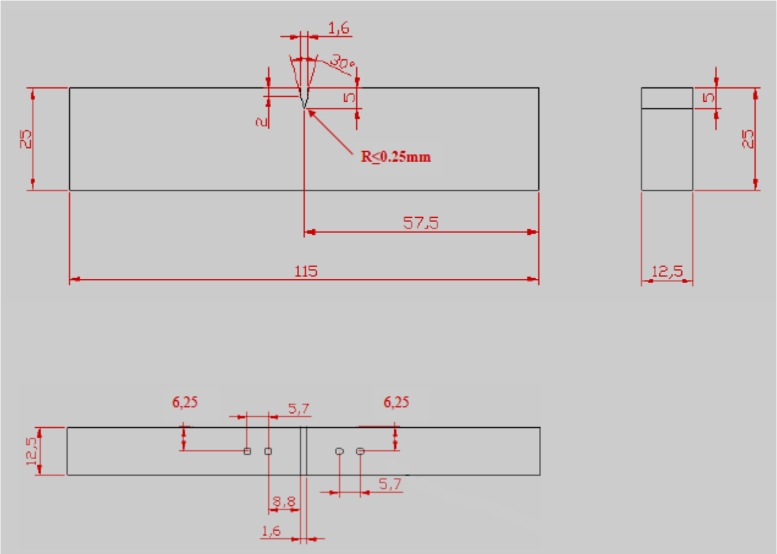

Fig. A.15: Standard single-edge notched bend (SENB) brass specimen.

A.6. Fracture Analysis

A Nikon SMZ 1500 stereomicroscope was employed for low-magnification observations of the fracture surface topography (macrofractography) (Fig. A.16a). High magnification observations of the fracture surfaces were conducted on ultrasonically cleaned specimens, utilizing a FEI XL40 SFEG scanning electron microscope (SEM), using both secondary electron (SE) and backscattered electron (BSE) signals under 20 kV accelerating voltage (Fig. A.16b). SEM was also used for high magnification observations of the microstructure before and after heat treatment.


(a) (b)

Fig. A.16: (a) Stereoscope Nikon SMZ 1500, (b) FEI XL40 SFEGSEM.

A.7. Machinability Testing

Machinability tests, concerning the chip morphology (CM) and power consumption (P), were performed in turning operation on a Computerized Numerical Control (CNC) lathe - EMCO PC TURN 155 (Fig. A.17a) according to ISO 3685 [10]. Chip morphology evaluation and classification was implemented according to the Table G.1 of ISO 3685. Table G.1 was employed as a reference, as an almost unlimited variety of chip types can be produced. As is recommended, a classifying system was established for each actual machining process.

In the studied process, five chip morphologies (from the total eight) were accounted for: i) needle chips, ii) arc chips, iii) conical helical chips, iv) washer-type helical chips and v) ribbon chips. Uncoated cemented Mitsubishi carbide cutting-tool inserts, with grade name HTi10, were used for the machinability tests (Fig. A.17b). The selected carbide grade is ideal for turning of non-ferrous metals, while it ensures high rigidity and wear resistance.

The length of machining, for each bar, was 150 mm and was kept constant throughout the machining tests, while the diameter of each bar was the same, 35 mm. The turning process was performed without lubrication. Tool wear was not selected as a criterion since there was not any measurable extent of flank wear after the machining experiments.

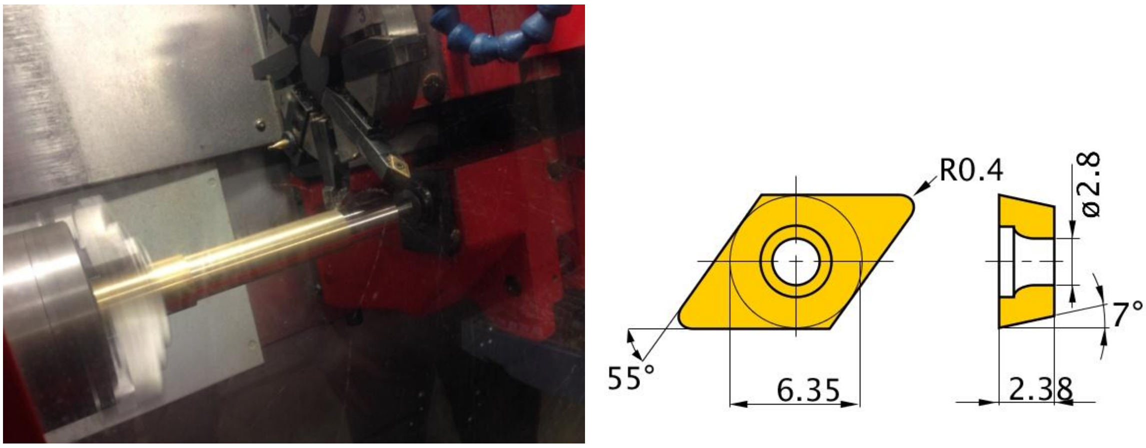

(a) (b)

Fig. A.17: (a) Representative view of a machining experiment in progress, showing also tool-workpiece arrangement and continuous chip formation, (b) Carbide cutting tool geometry and dimensions.

Chip morphology was studied by employing a Nikon SMZ 1500 stereo-microscope (Fig. A.16a). Power consumption was evaluated during the machining by a Power Logic PM750 recorder connected to the main rotor shaft of the CNC lathe. The average of two replicates, for each set of selected cutting parameters, was employed for this study.

Machinability tests, in terms of cutting force (CF) and surface roughness (SR) measurements, were performed in turning operation on a Computerized Numerical Control (CNC) lathe - DMG Alpha 500, according to the instructions of ISO 3685 standard. For the measurement of the cutting forces a specific setup, as illustrated in Figure A.18a, was employed. The cutting forces were acquired using a 3-axis dynamometer (Kistler 9257B) and an appropriate analog to digital device (NI PCI-MIO-16E - 1MHz) controlled by means of a GUI code developed under LabVIEW 11 software.

Figure A.18b illustrates the machining kinematics and the cutting force components that were measured in all experiments. The three cutting force components that arise due to the cutting process and the chip formation are: the main cutting force F_c, the passive force F_p and the feed direction force F_f. The magnitude of the main cutting force was dominant in comparison to the other force components and therefore the machinability study was focused specifically on this force component. As it is shown the main cutting force F_c is built up immediately at the entry of the cutting tool in the rotating specimen and it becomes both a static ($F_{c,st}$) and dynamic part ($F_{c,dyn}$) apparently.

The static part is stable throughout the whole measurement and determines the mean value of the main cutting force, which is taken into account in this study. Moreover, it expresses the specific cutting resistance of the machined material and therefore it is assumed as criterion of the machinability evaluation. Regarding the emerged dynamic part of the cutting force an amplitude distortion due to the chip formation, chip flow and chip segmentation was evident. In order to achieve reliable results, two repetitions of the turning tests were performed for each set of the selected cutting parameters and the average value of the measured main cutting force was considered in the subsequent evaluation analysis.

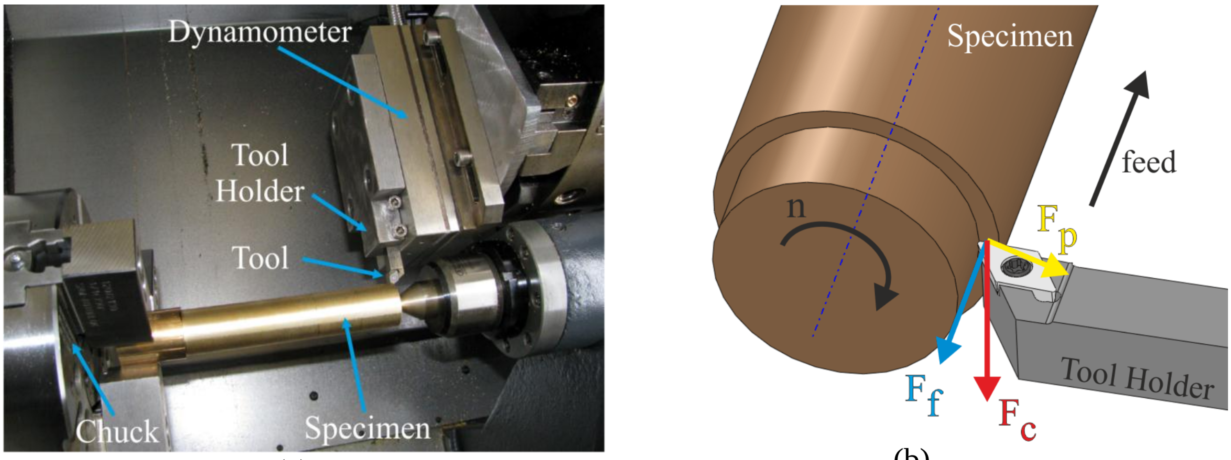

(a)

(b)

Fig. A.18: (a) Setup for the measurement of the cutting forces, (b) Machining kinematics and the cutting force components that were measured in all experiments.

A complete system for quantitative 3D Topography including Wyko NT1100 Optical Profiling system supported by Wyko Vision 32 analysis software was utilized for the evaluation of surface roughness (SR). It provides accurate, non-contact surface metrology based on white light interferometry to achieve high resolution of 3D surface roughness measurements of nanometer scale. In this study the three dimensional roughness average (Ra) over the entire measured area according to ASME. ANSI B46.1 standard [11] was evaluated.

Roughness average values (Ra) were selected as the most representative surface-roughness characteristic, used in case of industrial applications in brass component manufacturing. Although this is a partial surface-topography evaluation (other features of roughness were also retrieved, such as Rz, Rt, etc.), it is considered the most suitable parameter for such comparison measurements since it constitutes a very common quality criterion included in relevant customer specifications.

Figure A.19 illustrates the principle of 3D white light interferometry for surface roughness measurement, which was adopted as the most adequate technique for the scope of the current research. The surface analysis results comprise the 3D topographic map and 2D cross-sections, which show both the shape and the resulted roughness. Furthermore, all tribological data according to ANSI standard were calculated. As mentioned above, two repetitions were also exploited for each set of the selected cutting parameters and the average roughness value was deduced.

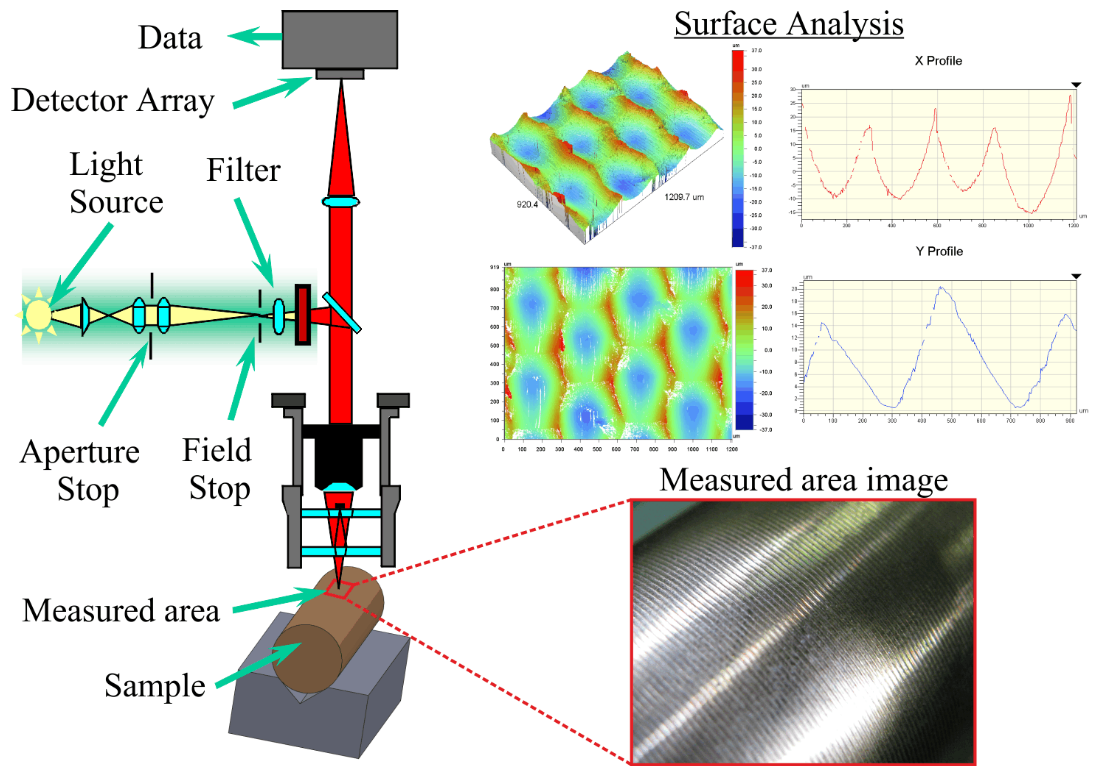

Fig. A.19: 3D white light interferometry for surface roughness measurement.

A.8 References

[1] BS EN 12164 (2011) Copper and copper alloys: Rod for free Machining Purposes. European Committee for Standardization (CEN), Brussels, Belgium.

[2] O. Zurita, V. Di Graci (2012) Surface integrity in turning of annealed brass: Hardness prediction. Journal of Materials Engineering and Performance 21: 1534-1538.

[3] ASTM E407 (2007) Standard practice for microetching metals and alloys. American Society for Testing and Materials (ASTM).

[4] BS EN ISO 6892-1 (2009) Metallic materials - Tensile testing - Part 1: Method of test at room temperature. European Committee for Standardization (CEN), Brussels, Belgium.

[5] ISO 6507-1 (2005) Metallic materials - Vickers hardness test - Part 1: Test method. International Organization for Standardization (ISO).

[6] ISO 148-1 (2009) Metallic materials – Charpy pendulum impact test - Part 1: Test method. European Committee for Standardization (CEN), Brussels, Belgium.

[7] ASTM A370 (2008) Standard test methods and definitions for mechanical testing of steel products. American Society for Testing and Materials (ASTM).

[8] BS 7448 (1991) Fracture mechanics toughness tests. Part 1: Method for determination of KIC, critical CTOD and critical J values of metallic materials. British Standard.

[9] T. Kawabata, T. Tagawa, T. Sakimoto, Y. Kayamori, M. Ohata, Y. Yamashita, E.-I Tamura, H. Yoshinari, S. Aihara, F. Minami, H. Mimura, Y. Hagihara (2016) Proposal for a new CTOD calculation formula. Engineering Fracture Mechanics 59: 16-34.

[10] ISO 3685 (1993) Tool-life testing with single-point turning tools. International Organization for Standardization (ISO).

[11] ASME. ANSI B46.1 (2009) Surface Texture (Surface Roughness, Waviness, and Lay); ASME: New York, NY, USA.

Appendix B: Robust Design Methods

B.1. Design of Experiments (DOE) - Taguchi Method

Business trends are incessantly leaning towards tighter budgets for research projects along with expeditious product introduction to the marketplace. Managing to predict the optimal behaviour of processes and products with minimal experimental effort becomes an operational necessity coupled of course with cost efficiency [1]. The quality of culture has permeated deep in the roots of engineering functions in many modern competitive companies. State-of-the-art business improvement initiatives such as the highly touted ‘Six Sigma’ have found worldwide acceptance as the right way to design and produce successful goods in short production cycles [2-3]. These initiatives maintain the early-time quality management credo that product improvement efforts ought to be focused primarily in the design phase in an attempt to lessen process control corrections after the full production is in effect [4].

During the ‘improve’ phase of the define-measure-analyse-improve-control (DMAIC) cycle of a ‘Six Sigma’ project, it is the design of experiments (DOE) that will set the tempo for optimising a selected quality characteristic or a group of them as it may be [5-6]. An up-to-date account of the state of affairs in the Six Sigma progress towards business improvement has been presented by Shahabuddin [7]. It turns out that there is a large body of knowledge today in DOE methods. Some brand of these methods was popularised by Dr. Genichi Taguchi in early ‘80s in the west when companies such as Motorola, AT&T, Ford and General Electric began to comprehend the usefulness of being able to interpret statistically product-controlling factors and noises in order to maximise their product quality.

To succeed in this, two rather simple conceptual things had to happen. First, product and design engineers had to eliminate controlling product factors proved to be statistically insignificant from an initial pool of parameters that were thought to be implicated after an in-depth departmental brainstorming session. Secondly, whatever factors were retained, they had to be adjusted at optimum settings (or levels), thus, leading to an optimum response prediction before the product proceeded through the scheduled process phases. The heavy reliance of Japanese industry on this type of experimental strategy became evident at that point through a host of case studies in critical areas of product development [8]. What also became clear was that most of the machinery that was needed to advance a DOE study was developed earlier in the west [9-10]. It also seemed that there was an apparent incompatibility in the west between statistical and engineering science from a professional perspective. It was hard to find engineers who were, in addition, savvy statisticians to shoulder the complicated data analysis.

Taguchi aided in bringing together practical statistical concepts packaged suitably for engineering use. DOE methods have become very important in any operational setting, targeting either manufacturing process improvement or product development.

Information modelling is a key ingredient in product and process design [11]. The basic steps usually are:

i) The defining of the optimisation problem at hand, which involves determining the quality characteristics (or responses) that would be sought to be improved along with the controlling factors and possibly the more obscure but still influencing noise variables.
ii) The sampling method that relies on a practical scheme.
iii) The execution of experiments.
iv) The statistical analysis of the generated data.
v) The determination of the statistical significant influences that leads to optimum factor settings.
vi) The confirmation of the optimum settings obtained from the previous step.

Sectors dedicated to consumer goods production have already a long-term experience with DOE methods. Nevertheless, optimisation is carried out in other areas other than the traditional product development. One such demanding area, for example, is the supply-chain inventory management where improvement modelling is incurred via genetic algorithms [12]. A simple search in any international journal engine would easily turn up reports on DOE applications that are of the order of a thousand articles.

Two trends become obvious in the current literature. Firstly, the most easily accessible techniques are developed for single quality characteristic optimisation. However, this is hardly the case in realistic production environments where several responses are expected to be ameliorated in a synchronous fashion. Secondly, when multi-response variables appear on an optimisation problem, then, the level of expertise in statistics as well as deep knowledge of linear and possible non-linear programming that is required to successfully resolve such problems is dramatically escalated. This makes such sophisticated methods hard to adopt by the operational personnel that need them the most. There is a need for a method that on one hand is statistically sound and on the other is convenient and efficient to use by any industrial practitioner. Thus, a simple Robust Method is proposed in this work appropriate for screening product improvement.

B.2. Orthogonal Arrays (OAs)

The non-linear behaviour of a group of quality characteristics against a group of controlling factors is of great interest in product development. The proposed methodology is benefited by the incorporation of an efficient test plan that belongs in the well-known Orthogonal Array (OA) family proposed by Taguchi and is based on Hadamard matrix transpositions. OAs belongs to the more general fractional factorial design family that have proved suitable and convenient for efficient, economical and balanced industrial trial planning. To demonstrate the capability of this new method, a provision is made to accommodate possible factor saturation to the desired sampling scheme. This aids product developers and manufacturing engineers to expand the applicability of the proposed method to real work situations where experimental runs have to be kept to a certain minimum. The proposed scheme is suitable for the added constraint of unreplication of the runs. Unreplicated designs are induced due to economic constraints or time limitations.

Another benefit reaped by this method is that there is essentially no need to rely on normal statistics theory. Data normality checks are often overlooked when small sample industrial experimentation is undertaken. Not accounting properly for it may lead to erroneous conclusions. The method outlined here is mainly intended for real product optimisation where the sample count for each factor setting is retained small usually in the neighbourhood of six or less. The statistical treatment attempted here is founded on the robust non-parametric test of Jonckheere-Terpstra [13]. It is worth mentioning that the coupling of non-linear OAs with non-parametric is unique. Advantages gained by this coupling are:

i) Test independence on the nature of the data distribution.
ii) Higher statistical power of non-parametric tests over normal-distribution related tests at low sample sizes.
iii) Computational simplicity of computing the test statistic.

Overall, the method eliminates the need for elaborate software and it may be carried out with an ordinary calculator [14]. The four-level L_{16} (4^4) Taguchi-type orthogonal array (OA) was selected to program the appropriate experimental recipes [15]. The motivation for resorting to a four-level OA was two-fold: i) there was a need to investigate four alloy materials, and ii) the team decided to verify the non-linearity of the effects by adding an extra level in the original three-level planner. Collected datasets were assessed after a duplication of the experimental scheme and if reproducibility was not satisfactory, additional replicates would be scheduled from then on until the significance of the dataset was stabilized at a level of 0.05.

To save time and costs from lead-free brass processing on the production line, it was decided that machinability screening and optimization took place in a single stage. Three machining parameters: i) cutting speed (CS), ii) depth of cut (DC), iii) feed rate (FR), along with the brass alloy material (M) were selected as the controlling factors. The tool type was not included in the parameters of this study which was performed under dry cutting conditions. The above factors were selected as controlling factors, since they constitute the principal cutting parameters in conventional machining. Several preliminary experiments were executed for the determination of the range of the cutting conditions. Table B.1 presents the final selection of process parameters and their levels. The experimental design which was arranged according to the L_{16} (4^4) OA is listed in Table B.2.

Table B.1: Process parameters and their levels

Parameters	Units	Level 1	Level 2	Level 3	Level 4
Cutting Speed	rpm (m/min)	1500 (165)	1750 (192)	2000 (220)	2250 (247)
Depth of Cut	mm	0.5	1.0	1.5	2.0
Feed Rate	mm/min	150	200	250	500
Material	-	CW510L	CW511L	C27450	CW614N

Table B.2: L_{16} standard orthogonal array for the experiments

Number of Experiment	Parameters			
	Cutting Speed (rpm)	**Depth of Cut (mm)**	**Feed Rate (mm/min)**	**Material**
1	1500	0.5	150	CW510L
2	1500	1.0	200	CW511L
3	1500	1.5	250	C27450
4	1500	2.0	500	CW614N
5	1750	0.5	200	C27450
6	1750	1.0	150	CW614N
7	1750	1.5	500	CW510L
8	1750	2.0	250	CW511L
9	2000	0.5	250	CW614N
10	2000	1.0	500	C27450
11	2000	1.5	150	CW511L
12	2000	2.0	200	CW510L
13	2250	0.5	500	CW511L
14	2250	1.0	250	CW510L
15	2250	1.5	200	CW614N
16	2250	2.0	150	C27450

B.3. Signal-to-Noise Ratio (S/N)

To check the reproducibility of the replicated data and confirm data adequacy, a prescreening was conducted by simply testing the tightness of their correlational fittings through regular linear regression. Once the number of replicates was settled, the response dataset for each characteristic was condensed using ranking operations. Signal to noise ratio is used to analyze the quality characteristics of the product or the process parameters. It is also called as statistical measure of performance and is used as an objective function for optimizing parameters. It is the ratio of the mean (signal) to the standard deviation (noise). Control factors are easily adjustable and are set by the manufacturer. These factors are the most important in determining the quality characteristics. Noise factors are difficult, impossible, or expensive to control (weather, temperature, humidity, etc.). Regardless of the category of the quality characteristic, process parameter settings with the highest S/N ratio always yield the optimum quality with minimum variance [16-21].

The following three types of S/N ratios are considered to be standard and are widely applied in the Taguchi method:

(i) “Smaller-is-better” criterion

$$S/N = -10\log\left(\frac{1}{n}\sum_{i=1}^{n} y_i^2\right) \tag{1}$$

(ii) “Nominal-is-best” criterion

$$\mathrm{S/N} = 10\log\left(\frac{\bar{\mathrm{y}}^2}{\mathrm{S}^2}\right) \tag{2}$$

(iii) “Higher-is-better” criterion

$$S/N = -10\log\left(\frac{1}{n}\sum_{i=1}^{n} \frac{1}{y_i^2}\right) \tag{3}$$

Where y_i corresponded to the performance value of the i-th experiment, n was the number of repetitions, $\bar{y}$ was the mean response and S was the standard deviation.

The “smaller-is-better” criterion was selected because of its applicability in cases where the minimization of the quality characteristics is targeted. In this study case, chip morphology, power consumption, cutting force and surface roughness were considered optimized if their values were minimized. All data were processed using the professional statistical Minitab 16 software.

B.4. References

[1] J.S. Oakland (1999) Total organizational excellence-achieving world-class performance. Butterworth-Heinemann, Oxford.

[2] J.R. Beatty (2006) The quality journey: historical and workforce perspectives and the assessment of commitment to quality. International Journal of Productivity and Quality Management 1: 139-167.

[3] M. Hu, B. Barth, R. Sears (2005) Leveraging six sigma disciplines to drive improvement. International Journal of Six Sigma and Competitive Advantage 1: 121-133.

[4] J. Kovach, B.R. Cho (2005) Development of product family-based robust design: a case study. International Journal of Six Sigma and Competitive Advantage 1: 403-419.

[5] K.R. Bhote, A.K. Bhote (2000) World class quality: Using design of experiments to make it happen. 2nd ed., AMACOM/American Management Association.

[6] F.W. Breyfogle (2003) Implementing six sigma: Smarter solutions using statistical methods. 2nd ed., John Wiley & Sons, NY.

[7] S. Shahabuddin (2008) Six sigma: issues and problems. International Journal of Productivity and Quality Management 3: 145-160.

[8] G. Taguchi (1986) Introduction to quality engineering. Asian Productivity Organization, Tokyo

[9] G.E.P. Box, W.G. Hunter, J.S. Hunter (2005) Statistics for experimenters: Design, innovation, discovery. 2nd ed., John Wiley & Sons, NY.

[10] D.C. Montgomery (2004) Design and analysis of experiments. 6th ed., John Wiley & Sons, NY.

[11] A. Hassan, J.Y. Dantan, A. Siadat (2007) Information modeling for variation risk management during product and process design. International Journal of Productivity and Quality Management 2: 221-240.

[12] P. Das, S. Chaudhury (2008) Optimisation of supply chain inventory for multi-retail and multi-item class consumer product problems using genetic algorithm. International Journal of Productivity and Quality Management 3: 33-73.

[13] E.L. Lehmann (2006) Nonparametric statistical methods based on ranks. 1st ed., Springer.

[14] G.J. Besseris (2009) Multi-response quality improvement by non-parametric DOE methods. International Journal of Productivity and Quality Management 4: 303-323.

[15] G. Taguchi, S. Chowdhury, Y. Wu (2004) Quality Engineering Handbook. Wiley-Interscience, Hoboken, NJ.

[16] G.J. Besseris (2012) Multi-response multi-factorial master ranking in non-linear replicated-saturated DOE for qualimetrics. Chemometrics and Intelligent Laboratory Systems 116: 47-56.

[17] G.J. Besseris (2013) Profiling effects in industrial data mining by non-parametric methods. European Journal of Operational Research 220: 147-161.

[18] G.J. Besseris (2015) Concurrent multi-response non-linear screening: Robust profiling of webpage performance. European Journal of Operational Research 241: 161-176.

[19] G.J. Besseris (2014) Multi-response non-parametric profiling using Taguchi's qualimetric engineering and neurocomputing methods: Screening a foaming process in a solar collector assembly. Applied Soft Computing 22: 222-237.

[20] G.J. Besseris (2015) Profiling multiple static and transient puff-pastry characteristics with a robust-and-intelligent processor. Journal of Food Engineering 164: 40-54.

[21] A. Mariajayaprakash, T. Senthilvelan (2014) Optimizing process parameters of screw conveyor (sugar mill boiler) through failure mode and effect analysis (FMEA) and Taguchi method. Journal of Failure Analysis and Prevention 14: 772-783.

Appendix C: List of Figures

Appendix D: List of Tables

Appendix E: List of Journal Papers and Conference Papers

Journal Papers

1. A.I. Toulfatzis, G.A. Pantazopoulos, A.S. Paipetis (2014) Fracture behavior and characterization of lead-free brass alloys for machining applications. Journal of Materials Engineering and Performance 23: 3193-3206.

2. A.I. Toulfatzis, G.A. Pantazopoulos, G.J. Besseris, A.S. Paipetis (2016) Machinability evaluation and screening of leaded and lead-free brasses using a non-linear robust multifactorial profiler. International Journal of Advanced Manufacturing Technology 86: 3241-3254.

3. A. Toulfatzis, G. Pantazopoulos, A. Paipetis (2016) Microstructure and properties of lead-free brasses using post-processing heat treatment cycles. Materials Science and Technology 32: 1771-1781.

4. A. Toulfatzis, G. Pantazopoulos, A. Paipetis (2018) Fracture mechanics properties and failure mechanisms of environmental-friendly brass alloys under impact, cyclic and monotonic loading conditions. Engineering Failure Analysis 90: 497-517.

5. A. Toulfatzis, G. Pantazopoulos, C. David, D. Sagris, A. Paipetis (2018) Machinability of eco-friendly lead-free brass alloys: Cutting-force and surface-roughness optimization. Metals, 8, 250, doi: 10.3390/met8040250.

6. A. Toulfatzis, G. Pantazopoulos, C. David, D. Sagris, A. Paipetis (2018) Final heat treatment as a possible solution for the improvement of machinability of Pb-free brass alloys. Metals, 8, 575, doi: 10.3390/met8080575.

Conference Papers

1. A. Toulfatzis, G. Pantazopoulos, A. Paipetis (2016) Study of heat treatment influence on microstructure and mechanical behaviour of lead-free extruded brasses for machinability improvement. Brass Alloys 2016, May 25-27, Stockholm, Sweden.

2. Α. Τουλφατζής, Γ. Πανταζόπουλος, Α. Παϊπέτης (2016) Μελέτη της μικροδομής και των μηχανικών ιδιοτήτων μη μολυβδούχων ορειχάλκων, κατόπιν θερμικής κατεργασίας, για την βελτιστοποίηση της κατεργασιμότητας. 6ο Πανελλήνιο Συνέδριο Μεταλλικών Υλικών, 07-09 Δεκεμβρίου 2016, Ιωάννινα, Ελλάδα.

3. A.I. Toulfatzis, G.A. Pantazopoulos, A.S. Paipetis (2017) Fracture analysis of eco-friendly brass alloys: comparison study and preliminary assessment. 14th International Conference on Fracture (ICF 14), June 18-23, Rhodes, Greece.

4. A.I. Toulfatzis, G.A. Pantazopoulos, C.N. David, D.S. Sagris, A.S. Paipetis (2017) Design of experiments for the optimization of cutting force and surface roughness of lead-free brass alloys. EUROMAT 2017, September 17-22, Thessaloniki, Greece.